Università degli Studi di Milano
Facoltà di Scienze Matematiche, Fisiche e Naturali
Corso di Laurea in Fisica

Time-Dependent CP-violating Asymmetries in B meson decay to $\eta' K^0_S$ with $K^0_S \to \pi^0\pi^0$ in the BaBar experiment at SLAC

Giordano Cerizza

Matricula 606046

P.A.C.S. Code 29.40

a. a. 2004-2005

Supervisor: Prof. F. Palombo, Dott. A. Lazzaro

Alla mia famiglia

Contents

Introduction

The goal of this thesis is realized at *BABAR* experiment in the asymmetric b-factory PEP-II at SLAC (Stanford Linear Accelerator Center, Stanford, USA). The history of CP violation is one of experimental discovery overturning untested assumptions. Observation of the $\theta - \tau$ puzzle in the early 1950s marks the inception of the discovery of the symmetry-violating properties of the weak interaction. Two spin-zero particles of the same mass and lifetime (now known to be charged kaons) were found to decay into different final states of opposite parity, one to two pions and the other to three, seemingly violating parity conservation. In 1956, Lee and Yang showed that parity conservation, while well-tested in strong and electromagnetic interactions, was not experimentally constrained for weak interactions, and proposed a list of experimental tests [1]. Shortly thereafter, C.S. Wu and collaborators performed one of these experiments, and showed that parity was not conserved in nuclear β decay, conclusively demonstrating the uniqueness of the weak interaction among the forces [2].[1] However, the combined CP transformation was still widely assumed to be a symmetry of nature due to the difficulty of explaining the weak interaction without it. The discovery eight years later of CP violation in neutral K mesons by Christenson, Cronin, Fitch and Turlay provided the basis for both far-reaching insight (the Kobayashi-Maskawa prediction of a third family of quarks and leptons, a year before even the charm quark was discovered, and 4 years before the b) [3, 4].

Before 1964, no one realistically expected CP symmetry to be violated. Accomodating CP violating involves a significant increase in the complexity of weak interaction theory that was just not motivated at the time, as only the first 3 quarks had been discovered at that moment. Fitch later remarked that "not many of our colleagues would have given credit for studying CP violation, but we did so anyway" [5]. The beam that was used contained pure K_2^0 (= K_L^0) mesons. A two-arm spectrometer was

[1] Note however that parity conservation is still poorly experimentally constrained in gravity.

used in order to detect the decay products. After two months of data taking, a significant peak was indeed observed for a $\pi^+\pi^-$ decay of the K_2^0. If mass eigenstates and CP eigenstates were equivalent, K_2^0 would be the purely CP-odd (and slightly heavier) counterpart to the CP-even K_1^0 (= K_S^0). But the $\pi^+\pi^-$ final state is CP-even, thus the (presumably) CP-odd K_2^0 should not be able to decay into it *unless CP were violated*. Fitch and Cronin observed a significant peak for a $\pi^+\pi^-$-hypothesis decay at the K_2^0 mass, consisting of 45 ± 9 two-pion events out of a total of 22,700 K_2^0 decays. Although the experiment did result in a slowly increasing acceptance in the physics community that CP was violated, immediately following the measurement strong disbelief did exist. Alternative explanations were proposed, including regeneration of K_1^0, a non-bosonic version of the pion as the actual decay product, and violation of exponential decay laws. These alternatives were at least as unpleasant for theory as the violation of CP itself, and successive experiments refuted their possibility, eventually eliminating all but the Kobayashi-Maskawa quark mixing picture as the description of Cronin and Fitch's results. Thirty-seven years of experimental study of the kaon sector after CP violation was discovered has yielded only recently the observation of direct CP violation, and has merely helped to confirm the counterintuitive picture of a small complex coefficient in a 3 x 3 unitary matrix as the source of the CP asymmetry. The smallness of CP violating effects in the kaon system is an impediment to progress in that sector, although the potential remains for measurements of the decays $K^+ \rightarrow \pi^+\nu\overline{\nu}$ and $K_L^0 \rightarrow \pi^0\nu\overline{\nu}$, which directly probe the imaginary part of the coefficient. The present and near future lie in B decays, which, as shown by *BABAR* and Belle[2], exhibit significant CP asymmetries, as is predicted by the Standard Model. However, the predictions of the Standard Model regarding CP have yet to be fully examined experimentally, and, as seen above, one cannot take untested ideas for granted. Many well-motivated theoretical extensions of the Standard Model produce strikingly different predictions for CP violation; and the manifest baryon asymmetry of the universe poses great difficulty for reconciliation with the small amount of CP violation predicted by the Standard Model. Such tests are the primary purpose of the *BABAR* experiment — the goal was to either confirm or refute the Standard Model picture of CP violation.

B meson decay channels useful for CP violation studies have a very little branching fractions, in the order of 10^{-4} or less, with a $\Upsilon(4\mathrm{S})$[3] cross section of 1.2 nb. To

[2] similar experiment to *BABAR* in the KEK-B accelerator (Tsukuba, Japan).

[3] $\Upsilon(4\mathrm{S})$ is a resonance composed by a quark couple $b\overline{b}$ with mass 10.58 GeV and decades in a couple

observe CP violation a high luminosity collider is necessary (a so called b-factory[4]). Time dependent measurements of asymmetries depend on the ability of evaluating decay vertices of the two B mesons coming from $\Upsilon(4\mathrm{S})$ meson decay. In *BABAR* experiment the measurement of this vertices is due to asymmetric collider (e^- with 9 GeV and e^+ with 3.1 GeV) where Υ mesons are produced with impulse in the laboratory frame. The B mesons boosts make distances run by particles measurable.

The Milan group studies hadronic charmless B meson decays. These processes are manifestations of suppressed penguin or tree diagrams and are very sensitive to new physics; fondamental measurements of parameters, joined with CP violation, are linked to this decay channels studies. In this thesis work will be describe the study of B meson decays in $\eta' K$ in the final quasi-two body states composed by η' and K mesons, for subchannels with η' in $\rho^0\gamma$ and $\eta\pi\pi$, with η in $\gamma\gamma$ and $\pi^+\pi^-\pi^0$ and with K meson in $K^0_S \to \pi^0\pi^0$ and K^+. Analysis has been done on a on-peak $\Upsilon(4\mathrm{S})$ resonance data sample of 210.9 fb^{-1} (232.0 x 10^6 $B\overline{B}$ pairs). An unbinned multivariate maximum likelihood (ML) analysis is the analysis tecnique. In the first step we wrote modules for the reconstruction of real and MC events and we used different kinds of variables both topological and kinematical. The events are selected with cuts on variables and then we proceeded with definition of PDFs (probability density function) for variables used in fits. After that, we evaluated systematic errors, due to analysis program tecnique and fitting dependent parameters of PDFs. All the results obtained have been discussed and added to standard channels[5].

of mesons $B\overline{B}$ (50% neutral $B\overline{B}$ and 50% charged $B\overline{B}$). Quantum numbers of this resonance are J^{CP}=1^{--}.

[4] b-factory is usual expression to describe an accelerator that is able to produce a large number of B mesons (greater than 10^7 B for year).

[5] Please see Chapter 7-8.

Chapter 1

CP Violation in the B Meson System

1.1 Overview of CP Violation

1.1.1 Discrete Symmetries

The set of operators on the Hilbert space of state functions on the quantum field contains both discrete and continuous transformations that preserve the Minkowski interval $t^2 - \vec{x}^2$. The set of continuous transformations that preserve this interval are the familiar Lorentz transformations, comprised of the product space of rotations, translations, and Lorentz boosts. The three independent discrete transformations that also preserve $t^2 - \vec{x}^2$ are the charge conjugation operator (C), the parity operator (P), and the time-reversal operator (T). These form a complete set of discrete Minkowski interval-preserving transformations of the Hilbert space. Although other discrete interval-preserving transformations exist in the Standard Model (SM) [6, 7, 8], all can be formed from C, P, T, and the group of continuous Lorentz and gauge rotations.[1] The action of the three discrete transformations on, as an example, the special case of a spin 1/2 (Dirac) field, is discussed below.

Parity

The parity operator $\mathcal{P}$ reverses the signs of the 3 spatial elements of a four-vector: $(t, \vec{x}) \rightarrow (t, -\vec{x})$ and $(E, \vec{p}) \rightarrow (E, -\vec{p})$. One can easily visualize parity as a mirror-

[1] For example, consider the set of discrete transformations $M_{\hat{n}}$, which takes the mirror image of space with respect to a plane defined by a unit vector $\hat{n}$. This is simply parity combined with a rotation of π about $\hat{n}$. Minimal supersymmetry adds a single independent Lorentz-invariant transformation (R-parity), of which the symmetry is broken at observable energy levels, producing mass differences.

image plus an 180-degree rotation normal to the plane of the mirror (which works for any mirror angle) — this reverses the momentum of a particle but leaves its spin unchanged:

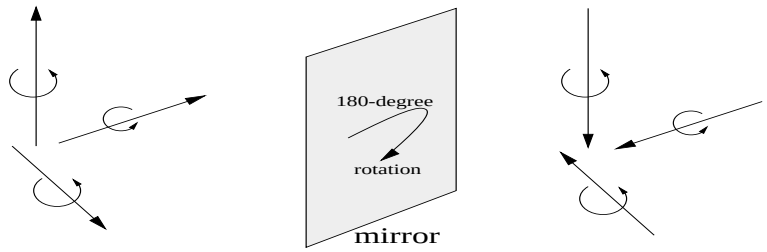

Figure 1.1: Effects of P symmetry

Consider the action of parity on the particle and antiparticle annihilation operators of the Dirac field $a^s_{\vec{p}}$ and $b^s_{\vec{p}}$. Parity should transform the states $a^s_{\vec{p}}|0\rangle$ and $b^s_{\vec{p}}|0\rangle$ to $a^s_{-\vec{p}}|0\rangle$ and $b^s_{-\vec{p}}|0\rangle$ as shown in the figure above. This implies

$$\mathcal{P}a^s_{\vec{p}}\mathcal{P}^{-1} = \eta_a a^s_{-\vec{p}} \qquad \text{and} \qquad \mathcal{P}a^s_{\vec{p}}\mathcal{P}^{-1} = \eta_b b^s_{-\vec{p}} \tag{1.1}$$

where η_a and η_b are phases. Since $\mathcal{P}^2 = \mathbf{1} \Rightarrow \eta_a, \eta_b$ must equal ± 1 (the parity group, as with the other two discrete operators, is idempotent, *ie.* $\mathcal{P}^{-1} = \mathcal{P}$, so the equation above could just as easily have been written $\mathcal{P}a^s_{\vec{p}}\mathcal{P}$, etc.). To find the matrix representation of $\mathcal{P}$ and the phases η_a and η_b, consider the action of $\mathcal{P}$ on $\phi(x)$. Decomposing ϕ into eigenstates of spin and momentum gives:

$$\mathcal{P}\phi(x)\mathcal{P}^{-1} = \frac{1}{\sqrt{2E_{\vec{p}}}} \int \frac{d^3p}{(2\pi)^3} \sum_s \left(\eta_a a^s_{-\vec{p}} u^s(p) e^{-ipx} + \eta_b^* b^{s\dagger}_{-\vec{p}} v^s(p) e^{ipx} \right) \tag{1.2}$$

The key is to change variables to (not surprisingly) $p' = (p^0, -\vec{p}) \Rightarrow p \cdot x = p' \cdot (t, -\vec{x})$ and $p' \cdot \sigma$ (where σ is the four-vector of 2×2 Pauli matrices) $= p \cdot \sigma^\dagger \gamma^0$ (where γ^0 is the 0-th Dirac matrix) $= p \cdot \overline{\sigma}$, where

$$\overline{\sigma} \equiv \sigma^\dagger \gamma^0 \tag{1.3}$$

Thus the four-spinors $u(p)$ and $v(p)$ can be written as:

$$u(p) = \begin{pmatrix} \sqrt{p\cdot\sigma}\varsigma \\ \sqrt{p\cdot\overline{\sigma}}\varsigma \end{pmatrix} = \begin{pmatrix} \sqrt{p'\cdot\overline{\sigma}}\varsigma \\ \sqrt{p'\cdot\sigma}\varsigma \end{pmatrix} = \gamma^0 u(p')$$
$$v(p) = \begin{pmatrix} \sqrt{p\cdot\sigma}\varsigma \\ -\sqrt{p\cdot\overline{\sigma}}\varsigma \end{pmatrix} = \begin{pmatrix} \sqrt{p'\cdot\overline{\sigma}}\varsigma \\ -\sqrt{p'\cdot\sigma}\varsigma \end{pmatrix} = -\gamma^0 v(p') \tag{1.4}$$

where ς is a generic two-component spinor. Thus (1.2) can be written as:

$$\mathcal{P}\phi(x)\mathcal{P}^{-1} = \frac{1}{\sqrt{2E_{\vec{p'}}}}\int\frac{d^3p'}{(2\pi)^3}\sum_s \quad \left(\eta_a a^s_{\vec{p'}}\gamma^0 u^s(p')e^{-ip'\cdot(t,-\vec{x})}\right.$$
$$\left. - \eta_b^* b^{s\dagger}_{\vec{p'}}\gamma^0 v^s(p')e^{ip'\cdot(t,-\vec{x})}\right) \tag{1.5}$$

But,

$$\phi(t,-\vec{x}) = \frac{1}{\sqrt{2E_{\vec{p'}}}}\int\frac{d^3p'}{(2\pi)^3}\sum_s \quad \left(a^s_{\vec{p'}}u^s(p')e^{-ip'\cdot(t,-\vec{x})}\right.$$
$$\left. + b^{s\dagger}_{\vec{p'}}v^s(p')e^{ip'\cdot(t,-\vec{x})}\right) \tag{1.6}$$

$\Rightarrow \eta_a = 1$, $\eta_b = -1$, and

$$\mathcal{P}\phi(t,\vec{x})\mathcal{P}^{-1} = \gamma^0\phi(t,-\vec{x}) \tag{1.7}$$

Time Reversal

The time reversal operator reverses momentum and spin and also flips the sign of the time component of a state. Therefore we want the transformation of the Dirac particle and antiparticle annihilation operators to be:

$$\mathcal{T}a^s_{\vec{p}}\mathcal{T}^{-1} = \eta'_a a^{-s}_{-\vec{p}} \qquad \text{and} \qquad \mathcal{T}b^s_{\vec{p}}\mathcal{T}^{-1} = \eta'_b b^{-s}_{-\vec{p}} \tag{1.8}$$

We can start to compute the transformation of the fermion field ϕ:

$$\mathcal{T}\phi(t,\vec{x})\mathcal{T}^{-1} = \frac{1}{\sqrt{2E_{\vec{p}}}}\int\frac{d^3p}{(2\pi)^3}\sum_s \mathcal{T}\left(a^s_{\vec{p}}u^s(p)e^{-ipx} + b^{s\dagger}_{\vec{p}}v^s(p)e^{ipx}\right)\mathcal{T}^{-1} \tag{1.9}$$

However, if $\mathcal{T}$ were to only act on the operators a and b, the situation would be the same as with parity and the spatial coordinates would flip sign instead of time (also the operators would reverse spin but not the spinors, which would be an unphysical nonlinearity). $\mathcal{T}$ therefore must act on more than just the operators.

The solution is to let $\mathcal{T}$ act on complex numbers in addition to operators. Let

$$\mathcal{T}z = z^*\mathcal{T} \quad \forall z \,\mathrm{in}\, \mathcal{C} \tag{1.10}$$

Thus (1.9) becomes

$$\frac{1}{\sqrt{2E_{\vec{p}}}} \int \frac{d^3p}{(2\pi)^3} \sum_s \left(\eta_a'^* a^{-s}_{-\vec{p}} (u^s(p))^* e^{ipx} + \eta_b'^* b^{-s\dagger}_{-\vec{p}} (v^s(p))^* e^{-ipx} \right) \tag{1.11}$$

We need to find a constant matrix $\mathcal{M}$ such that $\mathcal{M}u^{-s}(p') = (u^s(p))^*$ (and similarly for $v^s(p)$) — then we can change variables to p' and $(-t, \vec{x})$ so that we can obtain an answer for the action of the transformation in terms of $\phi(-t, \vec{x})$.

We can see that:

$$(u^s(p))^* = \begin{pmatrix} \sqrt{p\cdot\sigma^*}\varsigma^{s*} \\ \sqrt{p\cdot\overline{\sigma}^*}\varsigma^{s*} \end{pmatrix} = \begin{pmatrix} \sigma^2 & 0 \\ 0 & \sigma^2 \end{pmatrix} \begin{pmatrix} \sigma^2 & 0 \\ 0 & \sigma^2 \end{pmatrix} \begin{pmatrix} \sqrt{p\cdot\sigma^*}\varsigma^{s*} \\ \sqrt{p\cdot\overline{\sigma}^*}\varsigma^{s*} \end{pmatrix} = -\gamma^1\gamma^3 \begin{pmatrix} -i\sigma^2\sqrt{p\cdot\sigma^*}\varsigma^{s*} \\ -i\sigma^2\sqrt{p\cdot\overline{\sigma}^*}\varsigma^{s*} \end{pmatrix} \tag{1.12}$$

and can then use the identity

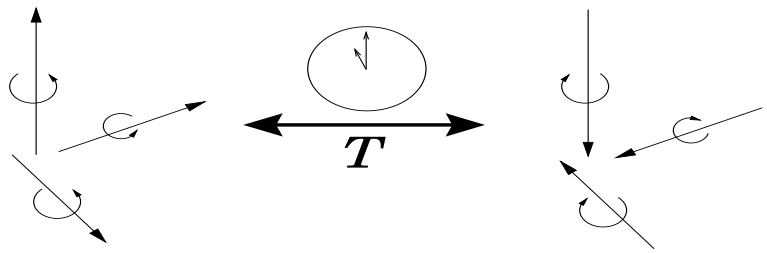

Figure 1.2: Effects of T symmetry

$$\sigma^2\sqrt{p\cdot\sigma^*} = \sqrt{p'\cdot\sigma}\,\sigma^2 \tag{1.13}$$

and the fact that

$$-i\sigma^2\varsigma^{s*} = \begin{pmatrix} 0 & 1 \\ -1 & 0 \end{pmatrix}\begin{pmatrix} \varsigma^{1*} \\ \varsigma^{2*} \end{pmatrix} = \begin{pmatrix} \varsigma^{2*} \\ -\varsigma^{1*} \end{pmatrix} = \varsigma^{-s} \tag{1.14}$$

to obtain for (1.13):

$$-\gamma^1\gamma^3\begin{pmatrix} \sqrt{p'\cdot\sigma}(-i\sigma^2\varsigma^{s*}) \\ \sqrt{p'\cdot\overline{\sigma}}(-i\sigma^2\varsigma^{s*}) \end{pmatrix} = -\gamma^1\gamma^3\begin{pmatrix} \sqrt{p'\cdot\sigma}\varsigma^{-s} \\ \sqrt{p'\cdot\overline{\sigma}}\varsigma^{-s} \end{pmatrix} = -\gamma^1\gamma^3 u^{-s}(p') \tag{1.15}$$

and similarly for $(v^s(p))^*$. Thus (1.15) becomes

$$\begin{aligned} -\gamma^1\gamma^3\frac{1}{\sqrt{2E_{\vec{p'}}}}\int\frac{d^3p'}{(2\pi)^3}\sum_s \quad & \left(\eta_a'^* a^{-s}_{\vec{p'}}u^s(p')e^{-ip'\cdot(-t,\vec{x})}\right. \\ & \left. + \eta_b'^* b^{-s\dagger}_{\vec{p'}}v^s(p')e^{ip'\cdot(-t,\vec{x})}\right) \quad \Rightarrow \\ \mathcal{T}\phi(t,\vec{x})\mathcal{T}^{-1} &= -\gamma^1\gamma^3\phi(-t,\vec{x}) \end{aligned} \tag{1.16}$$

Charge Conjugation

The charge conjugation operator is defined to be the transformation of a particle into its antiparticle without changing momentum or spin. Thus,

$$\mathcal{C}a^s_{\vec{p}}\mathcal{C}^{-1} = \eta_a'' b^s_{\vec{p}} \qquad \text{and} \qquad \mathcal{C}b^s_{\vec{p}}\mathcal{C}^{-1} = \eta_b'' a^s_{\vec{p}} \tag{1.17}$$

so the transformation of the Dirac field is

$$\mathcal{C}\phi(x)\mathcal{C}^{-1} = \frac{1}{\sqrt{2E_{\vec{p}}}}\int\frac{d^3p}{(2\pi)^3}\sum_s\left(b^s_{\vec{p}}u^s(p)e^{-ipx} + a^{s\dagger}_{\vec{p}}v^s(p)e^{ipx}\right) \tag{1.18}$$

We want to find what this is in terms of $\overline{\phi} = \phi^\dagger\gamma^0$, so we need a relation between $u^s(p)$ and $v^{s*}(p)$, and between $v^s(p)$ and $u^{s*}(p)$:

$$u^{s*}(p) = \begin{pmatrix} \sqrt{p\cdot\sigma^*}\varsigma^{s*} \\ \sqrt{p\cdot\overline{\sigma}^*}\varsigma^{s*} \end{pmatrix} = \begin{pmatrix} \sqrt{p\cdot\sigma^*}\varsigma^{s*} \\ \sqrt{p\cdot\overline{\sigma}^*}\varsigma^{s*} \end{pmatrix} = \begin{pmatrix} i\sqrt{p\cdot\sigma^*}\sigma^2\varsigma^{-s} \\ i\sqrt{p\cdot\overline{\sigma}^*}\sigma^2\varsigma^{-s} \end{pmatrix} \tag{1.19}$$

However, from the identity (1.13) we can see that:

$$\begin{aligned} \sqrt{p\cdot\sigma^*}\sigma^2 &= \sigma^2\sqrt{p\cdot\overline{\sigma}} \qquad \text{and} \\ \sqrt{p\cdot\overline{\sigma}^*}\sigma^2 &= \sigma^2\sqrt{p\cdot\sigma} \end{aligned} \tag{1.20}$$

Thus,

$$u^{s*}(p) = \begin{pmatrix} i\sigma^2\sqrt{p\cdot\overline{\sigma}}\varsigma^{-s} \\ i\sigma^2\sqrt{p\cdot\sigma}\varsigma^{-s} \end{pmatrix} = \begin{pmatrix} 0 & -i\sigma^2 \\ i\sigma^2 & 0 \end{pmatrix} \begin{pmatrix} \sqrt{p\cdot\sigma}\varsigma^{-s} \\ -\sqrt{p\cdot\overline{\sigma}}\varsigma^{-s} \end{pmatrix} = -i\gamma^2 v^s(p). \tag{1.21}$$

Similarly, $v^{s*}(p) = -i\gamma^2 u^s(p)$, so (1.18) becomes:

$$\begin{aligned} \mathcal{C}\phi(x)\mathcal{C}^{-1} &= \frac{1}{\sqrt{2E_{\vec{p}}}}\int \frac{d^3p}{(2\pi)^3}\sum_s \left(i\gamma^2 b^s_{\vec{p}} v^{s*}(p)e^{-ipx} + i\gamma^2 a^{s\dagger}_{\vec{p}} u^{s*}(p)e^{ipx}\right) \\ &= i\gamma^2\phi^*(x) = i(\overline{\phi}\gamma^0\gamma^2)^T \end{aligned} \tag{1.22}$$

CPT

The combination $\mathcal{CPT}$ operator has a rather special property: it is guaranteed to be a fundamental symmetry of nature, with only the basic assumptions of Lorentz invariance, locality, and the spin-statistics relation.[2] A proof for the restricted case of the Dirac field follows.

It's summarized and shown in the Table 1.1 how scalars, pseudoscalars, vectors, pseudovectors, and tensors are affected by the discrete symmetries:

The Lagrangian $\mathcal{L}$ is a Lorentz scalar, and as we can see above, any contraction of indices to form a Lorentz scalar must result in an eigenstate with a +1 $\mathcal{CPT}$ eigenvalue.

[2]Note that the spin-statistics relation itself is implied from Lorentz invariance, positive energies, positive norms, and causality.

	$\mathcal{C}$	$\mathcal{P}$	$\mathcal{T}$	$\mathcal{CP}$	$\mathcal{CPT}$
Scalar	+1	+1	+1	+1	+1
Pseudoscalar	+1	-1	-1	-1	+1
Vector	$-\vec{1}$	$\begin{pmatrix} +1 \\ -1 \\ -1 \\ -1 \end{pmatrix}$	$\begin{pmatrix} +1 \\ -1 \\ -1 \\ -1 \end{pmatrix}$	$\begin{pmatrix} -1 \\ +1 \\ +1 \\ +1 \end{pmatrix}$	$-\vec{1}$
Pseudovector	$+\vec{1}$	$\begin{pmatrix} -1 \\ +1 \\ +1 \\ +1 \end{pmatrix}$	$\begin{pmatrix} +1 \\ -1 \\ -1 \\ -1 \end{pmatrix}$	$\begin{pmatrix} -1 \\ +1 \\ +1 \\ +1 \end{pmatrix}$	$-\vec{1}$
Tensor	-1	$\begin{pmatrix} +1 & -1 & -1 & -1 \\ -1 & +1 & +1 & +1 \\ -1 & +1 & +1 & +1 \\ -1 & +1 & +1 & +1 \end{pmatrix}$	$\begin{pmatrix} -1 & +1 & +1 & +1 \\ +1 & -1 & -1 & -1 \\ +1 & -1 & -1 & -1 \\ +1 & -1 & -1 & -1 \end{pmatrix}$	$\begin{pmatrix} -1 & +1 & +1 & +1 \\ +1 & -1 & -1 & -1 \\ +1 & -1 & -1 & -1 \\ +1 & -1 & -1 & -1 \end{pmatrix}$	$+1$
Derivative Operator	$+\vec{1}$	$\begin{pmatrix} +1 \\ -1 \\ -1 \\ -1 \end{pmatrix}$	$\begin{pmatrix} -1 \\ +1 \\ +1 \\ +1 \end{pmatrix}$	$\begin{pmatrix} +1 \\ -1 \\ -1 \\ -1 \end{pmatrix}$	$-\vec{1}$

Table 1.1: Summary of discrete symmetries for scalars, pseudoscalars, vectors, pseudovectors and tensors.

1.1.2 CP

The CP transformation properties of the fermion field bilinears are listed in the column next to CPT. As we can see, if we restrict our attention to scalars, pseudoscalars, vectors, and the derivative operator, a Lagrangian formed from only such quantities must remain CP-invariant. Thus a massless spin 1/2 field with real coupling constants cannot violate CP. This is in fact true for quantum fields of any spin. Charge conjugation ensures that the fields themselves transform to their Hermitian conjugates (we have seen this above for the special case of spin 1/2). However, particle masses and coupling constants do not transform under CP (as complex numbers such as these are only transformed by, of the discrete operators, $\mathcal{T}$, as previously seen). If any of these quantities is not purely real, it will suffer a phase shift relative to the quantities that are transformed by CP, thus potentially violating CP symmetry.

Such phase differences must be robust against gauge modifications in order to manifest themselves as CP violation. If simple redefinitions of the phases of any of

the fields can remove overall phases in each field coupling, the theory remains CP-conserving. As will be shown in Section 1.4, if only two fermion generations are present, such a redefinition always exists, hence the Kobayashi-Maskawa prediction of a third generation. The effect of irreducible CP-violating phases will be elucidated in the following sections.

1.2 Mixing and Time Evolution of Neutral Mesons

The four pairs of conjugate neutral mesons that decay weakly, K^0, D^0, B^0, and B_s, can each mix with their respective antiparticle via a pair of box diagrams:

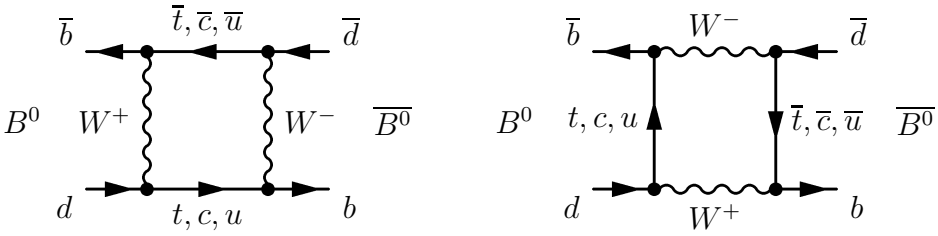

Figure 1.3: Feynman diagrams mixing $B^0 - \overline{B}^0$.

The ability to mix implies that the flavor eigenstates may not be equivalent to the mass eigenstates; the observed presence of mixing (into conjugate flavor-specific decays) implies that the mass and flavor eigenstates are in fact different.

Lack of CP symmetry implies a third set of eigenstates, CP eigenstates, which can differ from the mass and flavor eigenstates, as will be seen below.

1.2.1 Mixing of a "Generic" Neutral Meson

Consider a weakly-decaying neutral meson X^0 (which could be any of K^0, D^0, B^0 or B_s). An arbitrary linear combination of the flavor eigenstates

$$\alpha|X^0\rangle + \beta|\overline{X}^0\rangle \tag{1.23}$$

mixes according to the time-dependent Schrödinger equation

$$i\frac{\partial}{\partial t}\begin{pmatrix}\alpha\\ \beta\end{pmatrix} = \mathcal{H}\begin{pmatrix}\alpha\\ \beta\end{pmatrix} \equiv \begin{pmatrix} m_{11}-\frac{1}{2}i\gamma_{11} & m_{12}-\frac{1}{2}i\gamma_{12}\\ m_{21}-\frac{1}{2}i\gamma_{21} & m_{22}-\frac{1}{2}i\gamma_{22}\end{pmatrix}\begin{pmatrix}\alpha\\ \beta\end{pmatrix} \tag{1.24}$$

The m and γ parts represent the mixing and decay parts, respectively, of the time dependence. Each of the off-diagonal elements can be complex: the angle in the complex plane of m_{12} represents the phase of the mixing, and γ_{12} represents the (complex) coupling to common decay modes of X^0 and $\overline{X}^0$ (for example, $B^0/\overline{B}^0 \to J/\psi K^0_S$ or $\pi^+\pi^-$). We can see that CPT invariance guarantees that $m_{11} = m_{22}$ and $\gamma_{11} = \gamma_{22}$, and that $m_{21} = m^*_{12}$ and $\gamma_{21} = \gamma^*_{12}$ — the CPT-conjugate pairs of equations are:

$$\begin{aligned} i\frac{\partial\alpha}{\partial t} &= (m_{11}-\frac{1}{2}i\gamma_{11})\alpha + (m_{12}-\frac{1}{2}i\gamma_{12})\beta\\ i\frac{\partial\beta}{\partial t} &= (m_{21}-\frac{1}{2}i\gamma_{21})\alpha + (m_{22}-\frac{1}{2}i\gamma_{22})\beta \end{aligned} \tag{1.25}$$

and

$$\begin{aligned} i\frac{\partial\beta}{\partial t} &= (m_{11}-\frac{1}{2}i\gamma_{11})\beta + (m^*_{12}-\frac{1}{2}i\gamma^*_{12})\alpha\\ i\frac{\partial\alpha}{\partial t} &= (m^*_{21}-\frac{1}{2}i\gamma^*_{21})\beta + (m_{22}-\frac{1}{2}i\gamma_{22})\alpha \end{aligned} \tag{1.26}$$

which must be equivalent. Thus, setting m_{11} and m_{22} to m and γ_{11} and γ_{22} to γ, we have:

$$i\frac{\partial}{\partial t}\begin{pmatrix}\alpha\\ \beta\end{pmatrix} = \begin{pmatrix} m-\frac{1}{2}i\gamma & m_{12}-\frac{1}{2}i\gamma_{12}\\ m^*_{12}-\frac{1}{2}i\gamma^*_{12} & m-\frac{1}{2}i\gamma\end{pmatrix}\begin{pmatrix}\alpha\\ \beta\end{pmatrix} \tag{1.27}$$

The mass eigenstates are the eigenvectors of the Hamiltonian:

$$\begin{aligned} |X_L\rangle &= p|X^0\rangle + q|\overline{X}^0\rangle\\ |X_H\rangle &= p|X^0\rangle - q|\overline{X}^0\rangle \end{aligned} \tag{1.28}$$

where $|X_L\rangle$ and $|X_H\rangle$ are the lighter and heavier mass eigenstates,

$$q = \sqrt{\frac{m_{12}^* - \frac{1}{2}i\gamma_{12}^*}{m_{12} - \frac{1}{2}i\gamma_{12}}}p \tag{1.29}$$

$$\text{and} \qquad |p|^2 + |q|^2 = 1. \tag{1.30}$$

The difference in the magnitude of q/p from 1 is reponsible for CP-violation that is purely due to mixing — this will be discussed in section 1.3.2. The mass difference $\Delta m = m_H - m_L$ and decay width difference $\Delta\Gamma = \Gamma_H - \Gamma_L$ can also be obtained by diagonalizing the "mixing matrix" shown in Equation 1.27. Let

$$\alpha = |m_{12}|^2 - \frac{1}{4}|\gamma_{12}|^2, \qquad \beta = \mathcal{R}e(m_{12}\gamma_{12}^*) \tag{1.31}$$

then,

$$\Delta m = \sqrt{2\alpha - 2\sqrt{\alpha^2 - \beta^2}} \tag{1.32}$$

and

$$\Delta\Gamma = 4\beta/\Delta m \tag{1.33}$$

An initially pure $|X^0\rangle$ state will, therefore, time evolve as a superposition of the mass eigenstates $|X_L\rangle$ and $|X_H\rangle$. Equation 1.29 may thus also be expressed as

$$q = \left(\frac{\Delta m - \frac{i}{2}\Delta\Gamma}{2(m_{12} - \frac{1}{2}i\gamma_{12})}\right)p \tag{1.34}$$

1.2.2 The Neutral K System

Mixing between the two neutral K weak eigenstates K^0 and $\overline{K}^0$ was first predicted in 1955 by Gell-Mann and Pais [9]. The two physical states, $|K_1\rangle = \frac{1}{\sqrt{2}}(K^0 + \overline{K}^0)$ and $|K_2\rangle = \frac{1}{\sqrt{2}}(K^0 - \overline{K}^0)$, would thus be CP eigenstates with eigenvalues $+1$ and -1. The dominant decay of neutral K mesons is $\pi^+\pi^-$, due to helicity constraints and the fact the 3-body phase space is strongly suppressed at these mass scales (due to the well-known $(\Delta m)^5$ scaling rule). However, $\pi^+\pi^-$ is itself a CP eigenstate with eigenvalue $+1$. Thus, if CP were exactly conserved, *only the* $|K_1\rangle$ *physical state could decay into it*.

The limited phase space to decays other than $\pi^+\pi^-$ forces the lifetime of the eigen-

state with opposite CP K_2, to be far larger (3 orders of magnitude) than the lifetime of the K_1, thus the nomenclature K_S^0 and K_L^0 (for short and long lifetimes) is used. The lifetime difference is very convenient since it allows for simple experimental separation of the two physical states.

In 1964, Fitch and Cronin made their discovery that K_L^0 can in fact decay into $\pi^+\pi^-$ with a branching fraction of 2×10^{-3} (see the Introduction). Since CP is thus not strictly conserved, the general formalism detailed in the previous subsection must be used. Thus we have

$$\begin{aligned} |K_S\rangle &= p|K^0\rangle + q|\overline{K}^0\rangle \\ |K_L\rangle &= p|K^0\rangle - q|\overline{K}^0\rangle \end{aligned} \tag{1.35}$$

where p and q are commonly parametrized as:

$$p = \frac{1+\epsilon}{\sqrt{2(1+|\epsilon|^2)}}; \qquad q = \frac{1-\epsilon}{\sqrt{2(1+|\epsilon|^2)}} \tag{1.36}$$

The real part of ϵ is a measure of CP violation purely in mixing whereas the imaginary part is a measure of CP violation in the interference between mixing and decay (see the following section). The former is simplest to measure experimentally and was the effect seen in the orginal 1964 discovery. Since, in the K system, $\Delta\Gamma$ is of the same order as Δm, these effects are of similar magnitude, quite unlike the neutral B system, where the latter is far more prevalent.

1.2.3 The Neutral B System

In the case of neutral B mesons, in contrast with the neutral K system, the lifetime difference $\Delta\Gamma$ between the two mass eigenstates is *small* compared with the mixing frequency due to the difference in masses Δm. This difference in behavior of the K and B is due to the larger mass of the B meson and thus far greater phase space for flavor-specific decays in the B system, which dominate the partial width (in contrast to the K system) and give equivalent contributions (by CPT symmetry) to the width of both neutral B eigenstates. The resulting lack of decay suppression of either eigenstate implies nearly equivalent lifetimes.

Due to this simplification in formalism, the time evolution of neutral B mesons

which are initially created (at time $t = 0$) as pure flavor eigenstates can be written as:

$$|B^0_{phys}(t)\rangle = f_+(t)|B^0\rangle + (q/p)f_-(t)|\overline{B}^0\rangle \tag{1.37}$$

$$|\overline{B}^0_{phys}(t)\rangle = f_+(t)|B^0\rangle + (q/p)f_-(t)|\overline{B}^0\rangle \tag{1.38}$$

where

$$f_+(t) = e^{-imt}e^{-\Gamma t/2}\cos(\Delta m t/2) \tag{1.39}$$

$$f_-(t) = e^{-imt}e^{-\Gamma t/2}i\sin(\Delta m t/2) \tag{1.40}$$

This approximation holds up to the condition that

$$\Delta\Gamma \ll \Delta m \tag{1.41}$$

Since $\Delta\Gamma = \mathcal{O}(10^{-3})\Delta m$ in the B system, corrections to it are not considered in CP asymmetry measurements with the current statistics (furthermore, *BABAR* will have the capability of measuring $\Delta\Gamma$ as statistics of reconstructed B decays increase).

1.3 Three Types of CP Violation

Three types of CP violation can potentially be observed at B physics experiments:[3]
1) CP violation in decay (often referred to as direct CP violation): this occurs when multiple amplitudes with different weak phases as well as different strong phases contribute to a given final state, the result is visible as differing magnitude of the amplitude to a decay versus its CP conjugate.
2) CP violation purely in mixing: this occurs when the mass eigenstates of a neutral meson are different from the CP eigenstates.
3) CP violation in the interference between decays of mixed and unmixed mesons: this occurs for decays which are common to a neutral meson and its antiparticle.

1.3.1 CP Violation in Decay (Direct CP Violation)

Direct CP violation manifests itself as a difference in the magnitude of the amplitude to a given decay as compared with its CP conjugate, thus resulting in differing rates to

[3]There can be other manifestations of CP violation, *e.g.* CP violation in interaction, however observable CP violation at B-factories can all be classified into the 3 categories.

the two elements of the CP conjugate pair. It can occur for both neutral and charged decays.[4] Amplitudes from B^0 and $\overline{B}^0$ to a final state and its CP conjugate may be written as

$$A_f = \sum_i A_i e^{i(\phi_i+\delta_i)} \qquad \text{and} \qquad \overline{A}_{\overline{f}} = \eta_f \sum_i A_i e^{i(-\phi_i+\delta_i)} \tag{1.42}$$

where η_f is the CP eigenvalue (multiplied by a convention-dependent phase) if f is a CP eigenstate, ϕ are the weak phases, and δ are the strong phases. CP violation can only occur when the different weak phase contributions also have different strong phases (or else a simple rotation can remove the strong phase and thus the ratio would clearly have unit magnitude). It can also only occur when weak phases are nontrivial, *i.e.* when exists a relative phase between them (that is therefore irreducible by a rotation of the Lagrangian). Only when both different weak phases *and* different strong phases are present can one have the condition:

$$|\overline{A}_{\overline{f}}/A_f| \neq 1 \tag{1.43}$$

This is CP violation in decay. CP violation in decay has been observed in the kaon system and recently in the B system too. Since the strong phases that enter into measurements of CP violation in decay involve hadronic uncertainties, the relation of such measurements to CKM factors (see next section) cannot be calculated from first principles, but the strong phases may themselves be measured if the CKM factors are known from other measurements. These strong phase measurements can then be used as inputs to other measurements which have equivalent strong phases (thus allowing the extraction of other parameters), and thus measurements of CP violation in decay can (indirectly) provide a useful handle on fundamental quantities.

1.3.2 CP Violation Purely in Mixing

From section 1.2.1, recall that the mass eigenstates of the neutral meson system are the eigenvectors of the Hamiltonian

$$|X_L\rangle = p|X^0\rangle + q|\overline{X}^0\rangle$$

[4] For charged decays, it is the *only* potential manifestation of CP violation.

$$|X_H\rangle = p|X^0\rangle - q|\overline{X}^0\rangle \tag{1.44}$$

where

$$q = \sqrt{\frac{m_{12}^* - \frac{1}{2}i\gamma_{12}^*}{m_{12} - \frac{1}{2}i\gamma_{12}}}p \tag{1.45}$$

If q and p have different magnitudes, the CP conjugates of the mass eigenstates clearly will differ from the mass eigenstates themselves by more than a trivial phase. Thus the mass eigenstates will not be CP eigenstates and CP violation will be manifest. CP violation from

$$|q/p| \neq 1 \tag{1.46}$$

is purely an effect of mixing and is independent of decay mode. Thus it may be referred to as CP violation purely in mixing.

In neutral B decays, as discussed in section 1.2.2, this effect is expected to be very small. Since

$$\Delta m = \mathcal{O}(10^3)\Delta\Gamma \tag{1.47}$$

this implies that

$$|m_{12}| \gg |\gamma_{12}| \tag{1.48}$$

and thus the factor in equation 1.34 simplifies to a near-phase. CP violation purely in mixing should thus only enter the neutral B system at the 10^{-3} level. An asymmetry in the measurements of the overall rate to flavor tagged B^0 vs. $\overline{B}^0$would be a signature of CP violation purely in mixing. With greater statistics, evidence for this may be seen; at present, experimental limits exist. It has been clearly observed, however, in the neutral kaon system (where it is the prevalent effect); the discovery of CP violation in 1964 was a detection of CP violation purely in mixing (see Section 1.2.2).

1.3.3 CP Violation in Interference Between Decays of Mixed and Unmixed Mesons

Final states which may be reached from either B^0 or $\overline{B}^0$ decays can exhibit a third type of CP violation, which results from the interference between the decays of mixed and of unmixed neutral B mesons which both decay to the final state. Consider the

CP-violating asymmetry in rates between B^0 and $\overline{B}^0$ as a function of time:

$$a_{CP}(t) = \frac{\Gamma(B^0_{phys}(t) \to f) - \Gamma(\overline{B}^0_{phys}(t) \to f)}{\Gamma(B^0_{phys}(t) \to f) + \Gamma(\overline{B}^0_{phys}(t) \to f)} \tag{1.49}$$

To calculate each of the time-dependent rates $\Gamma(t)$, one can form the inner product of equations 1.37 and 1.38 with the final state f and then take the magnitude squared of the resulting amplitudes:

$$\begin{aligned}
&\Gamma(B^0(t) \to f) \propto \\
&|\langle f|\mathcal{H}|B^0(t)\rangle|^2 = \quad e^{-\Gamma t} \quad &\left\{\cos^2\left(\frac{\Delta m t}{2}\right)|\langle f|\mathcal{H}|B^0\rangle|^2\right. \\
&&+\sin^2\left(\frac{\Delta m t}{2}\right)\left|\frac{q}{p}\right|^2|\langle f|\mathcal{H}|\overline{B}^0\rangle|^2 \\
&&-\frac{i}{2}\left|\frac{q}{p}\right|e^{-2i\phi_M}\sin(\Delta m t)\langle f|\mathcal{H}|B^0\rangle\langle f|\mathcal{H}|\overline{B}^0\rangle^* \\
&&\left.+\frac{i}{2}\left|\frac{q}{p}\right|e^{2i\phi_M}\sin(\Delta m t)\langle f|\mathcal{H}|B^0\rangle^*\langle f|\mathcal{H}|\overline{B}^0\rangle\right\}
\end{aligned} \tag{1.50a}$$

$$\begin{aligned}
&\Gamma(\overline{B}^0(t) \to f) \propto \\
&|\langle f|\mathcal{H}|\overline{B}^0(t)\rangle|^2 = \quad e^{-\Gamma t} \quad &\left\{\cos^2\left(\frac{\Delta m t}{2}\right)|\langle f|\mathcal{H}|\overline{B}^0\rangle|^2\right. \\
&&+\sin^2\left(\frac{\Delta m t}{2}\right)\left|\frac{p}{q}\right|^2|\langle f|\mathcal{H}|B^0\rangle|^2 \\
&&+\frac{i}{2}\left|\frac{p}{q}\right|e^{-2i\phi_M}\sin(\Delta m t)\langle f|\mathcal{H}|B^0\rangle\langle f|\mathcal{H}|\overline{B}^0\rangle^* \\
&&\left.-\frac{i}{2}\left|\frac{p}{q}\right|e^{2i\phi_M}\sin(\Delta m t)\langle f|\mathcal{H}|B^0\rangle^*\langle f|\mathcal{H}|\overline{B}^0\rangle\right\}
\end{aligned} \tag{1.50b}$$

where $2\phi_M$ is the phase of q/p. Since, as shown above, for the B system $|q/p| \approx 1$, we can thus write

$$\langle f|\mathcal{H}|\overline{B}^0(t)\rangle = \eta e^{-2i\phi_D}|\lambda|\langle f|\mathcal{H}|B^0(t)\rangle \tag{1.51}$$

where ϕ_D is the phase of the decay, η is the CP eigenvalue of f, and

$$\lambda = \frac{q}{p}\frac{\langle f|\mathcal{H}|\overline{B}^0\rangle}{\langle f|\mathcal{H}|B^0\rangle} = |\lambda|e^{-2i(\phi_M+\phi_D)}, \tag{1.52}$$

the expressions simplify greatly:

$$|\langle f|\mathcal{H}|B^0(t)\rangle|^2 = A^2e^{-\Gamma t}\{1 - \mathrm{C}\cos(\Delta mt) - \mathrm{S}\sin(\Delta mt)\} \quad \text{and} \tag{1.53}$$

$$|\langle f|\mathcal{H}|\overline{B}^0(t)\rangle|^2 = A^2e^{-\Gamma t}\{1 + \mathrm{C}\cos(\Delta mt) + \mathrm{S}\sin(\Delta mt)\} \tag{1.54}$$

where $A^2 = |\langle f|\mathcal{H}|B^0\rangle|^2$ and

$$\mathrm{C} = \frac{1-|\lambda|^2}{1+|\lambda|^2} \qquad \text{and} \qquad \mathrm{S} = \eta\frac{-2\sin(2(\phi_M+\phi_D))}{1+|\lambda|^2} \tag{1.55}$$

Thus the time-dependent asymmetry

$$a_{CP}(t) = \frac{\Gamma(B^0_{phys}(t)\to f) - \Gamma(\overline{B}^0_{phys}(t)\to f)}{\Gamma(B^0_{phys}(t)\to f) + \Gamma(\overline{B}^0_{phys}(t)\to f)} = \mathrm{C}\cos(\Delta mt) + \mathrm{S}\sin(\Delta mt) \tag{1.56}$$

In the absence of CP violation, S and C must both go to zero, since they occur only when weak phases do not cancel. C is only nonzero when the ratio of the amplitude norms differs from unity, which is the signature of direct CP violation (detailed in section 1.3.1). S, however, represents a distinct type of CP violation that can occur even in the absence of CP violation purely in decay or in mixing. It results from the interference of the decays of mixed mesons with those of unmixed mesons; if the mixing contains a phase that is not cancelled by the decay itself, this observable time-dependent asymmetry above will result. Unlike CP violation in decay, no nontrivial strong phases are required.

As will be seen in the next section, CP violation in interference between decays of mixed and unmixed mesons is a large effect in the Standard Model picture of the neutral B system. Since this is a measurement of an asymmetry rather than an absolute rate, many experimental and model-dependent uncertainties (such as reconstruction efficiency) that would otherwise contribute to experimental error, instead cancel out in the ratio. Thus it provides an excellent mechanism for precision measurements of CP violation and the study of the Standard Model picture of CPV.

1.4 CP Violation in the Standard Model

CP violation within the context of the Standard Model $SU(2) \times U(1)$ electroweak symmetry was introduced by Kobayashi and Maskawa in 1973 via the postulation of a third family of quarks. This occurred a year prior to the discovery of charm; only 3 quarks existed at the time, so the prediction was quite prescient. The b-quark was then first observed in 1977. The prediction of additional quarks did not occur entirely without precedent, however. Theoretical interpretation of quark mixing via the weak interaction has closely followed experimental result, and the development of the 3 x 3 CKM matrix and its CP violating phase was a steady and piecewise process.

1.4.1 Weak Interactions and the CKM Matrix

The observed suppression of flavor-changing neutral current decays indicates that the quark sector is separated into families, similar to the lepton sector. However, lepton flavor is conserved,[5] whereas quark generation is manifestly violated (*e.g.* in weak decays of kaons). However, strangeness-changing decays have an additional suppression compared with strangeness-conserving weak decays. This "Cabibbo factor" may be accounted for by considering that, similar to neutral mesons, the quark mass eigenstates differ from the weak eigenstates. Thus a mixing matrix describing transitions between quark generations is necessary.

Such a matrix must be unitary since quark number is manifestly conserved.[6] With 2 generations, a unitary matrix can be described by a single parameter Θ_c:

$$\begin{pmatrix} d_{mass} \\ s_{mass} \end{pmatrix} = \begin{pmatrix} \cos\Theta_c & \sin\Theta_c \\ -\sin\Theta_c & \cos\Theta_c \end{pmatrix} \begin{pmatrix} d \\ s \end{pmatrix} \tag{1.57}$$

where d_{mass} and s_{mass} are the mass eigenstates nearest to the flavor eigenstates d and s respectively.

The same matrix (experimentally) holds for the (u, c) quark pair (although the c quark was of course discovered afterwards in 1974, four years after its prediction via the GIM mechanism that required charm to explain the absence of weak flavor-changing neutral currents[10]). The Cabbibo angle Θ_c is thus a full description of 2-generation mixing.

[5] Discounting, for the purposes of this document, recently discovered neutrino oscillations and thus lepton mixing.

[6] in contrast with the number of neutral mesons

More generally, we can write the charged-current coupling j_{cc} with 2 generations as

$$j^{\mu}_{cc} = \left(\begin{array}{cc} \overline{u} & \overline{c} \end{array} \right) \gamma^{\mu}(1-\gamma^5) \left(\begin{array}{c} d_{mass} \\ s_{mass} \end{array} \right) = \left(\begin{array}{cc} \overline{u} & \overline{c} \end{array} \right) \gamma^{\mu}(1-\gamma^5) \, V_{ij} \left(\begin{array}{c} d \\ s \end{array} \right) \qquad (1.58)$$

where V_ij is the 2 x 2 Cabbibo matrix parametrized by Θ_c above. With an arbitrary number of generations, the charged current ($W^{\pm}$) Lagrangian becomes:

$$\mathcal{L}_W = \frac{g}{\sqrt{2}} \left\{ \overline{u}^L_i \gamma^{\mu} W^+_{\mu} \, V_{ij} \, d^L_j + \overline{d}^L_i \gamma^{\mu} \, W^-_{\mu} \, V^*_{ij} u^L_j \right\} \qquad (1.59)$$

with u^L_i representing the vector of up-type quarks and d^L_i representing the down-type quarks. Applying the CP operation to the Lagrangian, one obtains:

$$\mathcal{L}_W = \frac{g}{\sqrt{2}} \left\{ \overline{d}^L_i \gamma^{\mu} W^-_{\mu} \, V_{ij} \, u^L_j + \overline{u}^L_i \gamma^{\mu} \, W^+_{\mu} \, V^*_{ij} d^L_j \right\} \qquad (1.60)$$

which is exactly the same except for the complex conjugation of V. Thus, if we can find a basis for which V (as well as the quark masses) are real, then CP is a symmetry.

Unitary matrices of dimension N form a group, the Lie group $SO(N)$. Elements of $SO(N)$ may be specified by $N^2 - 2N + 1$ real parameters. With 2 quark generations, V is defined by a single real parameter, the Cabibbo angle Θ_c. However, with 3 quark generations, 4 parameters are required. The real rotations may be taken to be the 3 Euler angles, but this leaves an extra parameter. The extra parameter is an *irreducible* complex phase. If this phase is nonzero, one can no longer find a basis for which V is real. Thus CP would cease to be a symmetry, and indeed that is the case in nature.

1.4.2 Unitarity Conditions and the Unitarity Triangle

Unitarity of the CKM matrix V requires that

$$V^{\dagger} V = V V^{\dagger} = 1 \quad \Rightarrow \quad \sum_j V^*_{ji} \, V_{jk} = \sum_j V_{ij} \, V^*_{kj} = \delta_{ik} \qquad (1.61)$$

With a 3-generation CKM matrix

$$V = \begin{pmatrix} V_{ud} & V_{us} & V_{ub} \\ V_{cd} & V_{cs} & V_{cb} \\ V_{td} & V_{ts} & V_{tb} \end{pmatrix} \tag{1.62}$$

this results in 9 independent equations, 3 of which (for the diagonal of the product unit matrix) equal one and 6 of which equal zero. The equations for the off-diagonal elements, each containing a sum of 3 complex numbers which equals 0, will each describe a triangle in the complex plane:

$$V_{cd}V_{ud}^* + V_{cs}V_{us}^* + V_{cb}V_{ub}^* = 0 \tag{1.63a}$$
$$V_{cd}V_{td}^* + V_{cs}V_{ts}^* + V_{cb}V_{tb}^* = 0 \tag{1.63b}$$
$$V_{ud}V_{td}^* + V_{us}V_{ts}^* + V_{ub}V_{tb}^* = 0 \tag{1.63c}$$
$$V_{us}^*V_{ud} + V_{cs}^*V_{cd} + V_{ts}^*V_{td} = 0 \tag{1.63d}$$
$$V_{ub}^*V_{us} + V_{cb}^*V_{cs} + V_{tb}^*V_{ts} = 0 \tag{1.63e}$$
$$V_{ub}^*V_{ud} + V_{cb}^*V_{cd} + V_{tb}^*V_{td} = 0 \tag{1.63f}$$

The differences between these 6 triangles are purely empirical. There is no theoretical motivation at present for the fact that 4 of them are nearly degenerate and only 2 describe triangles that have each of their sides being the same order of magnitude in length — the 4 parameters that describe the CKM matrix are not predicted by the Standard Model and can only be determined experimentally. It is emprically the case that only equations 1.63c and 1.63f above describe triangles which are not nearly degenerate. Of these, the last equation, 1.63f, is the one that is typically used to pictorially represent the irreducible CP violating phase and is referred to as the Unitarity Triangle.

They exist many CKM parametrizations. The standard one uses θ_{12}, θ_{23}, θ_{13} and a phase δ_{13}, called PDG [**?**] parameterization, given by

$$\mathsf{V} = \begin{pmatrix} c_{12}c_{13} & s_{12}c_{13} & s_{13}e^{-i\delta_{13}} \\ -s_{12}c_{23} - c_{12}s_{23}s_{13}e^{i\delta_{13}} & c_{12}c_{23} - s_{12}s_{23}s_{13}e^{i\delta_{13}} & s_{23}c_{13} \\ s_{12}s_{23} - c_{12}c_{23}s_{13}e^{i\delta_{13}} & -c_{12}s_{23} - s_{12}c_{23}s_{13}e^{i\delta_{13}} & c_{23}c_{13} \end{pmatrix} \tag{1.64}$$

with c_{ij}=cosθ_{ij} and s_{ij}=sinθ_{ij} for quark families labelled with i,j=1,2,3. The empirical

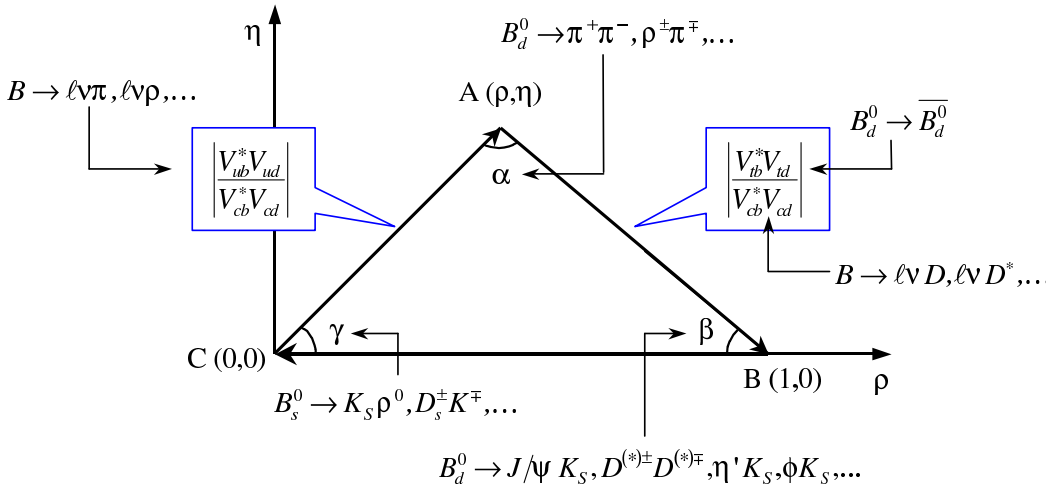

Figure 1.4: Unitary triangle and main decays to measure the sides and the angles.

fact that 4 of the triangles are nearly degenerate allows for a convenient parametrization of the CKM matrix via an expansion around the order parameter $\lambda \equiv s_{12} (= 0.2205 \pm 0.0018)$[7], sinus of Cabibbo's angle and function of real parameters A, λ and complex parameter ρ+iη :

$$V = \begin{pmatrix} 1 - \frac{\lambda^2}{2} & \lambda & A\lambda^3(\rho - i\eta) \\ -\lambda & 1 - \frac{\lambda^2}{2} & A\lambda^2 \\ A\lambda^3(1 - \rho - i\eta) & -A\lambda^2 & 1 \end{pmatrix} + \mathcal{O}(\lambda^4) \qquad (1.65)$$

with (λ, A, ρ, η) as the 4 real parameters describing the CKM matrix, the latter 3 being of order 1. This approximate parameterization, first proposed by Wolfenstein.

Unitary triangle obtained by (1.63f) can be rotated and scaled choosing a conventional phase in a way that $V_{cb}^* V_{cd}$ is real, and so aligning related side to real axis, and dividing lenght of all sides for $|V_{cd} V_{cb}^*|$ so lenght is normalized to 1. Obtained triangle (show in figure 1.4) will have two fixed vertexes at (0,0) and at (1,0) and coordinates of remaining vertex will depends by (ρ,η) corresponding to Wolfenstein's parameters; leghts of complex sides become:

$$R_u \equiv \left|\frac{V_{ub} V_{ud}}{V_{cb} V_{cd}}\right| = \sqrt{\rho^2 + \eta^2}, \qquad R_t \equiv \left|\frac{V_{tb} V_{td}}{V_{cb} V_{cd}}\right| = \sqrt{(1-\rho)^2 + \eta^2}. \qquad (1.66)$$

[7] Note that this Cabibbo parameter $\lambda \equiv \sin\Theta_c$ differs from the time-dependent asymmetry parameter λ detailed in Section 1.3.3.

The three angles of out unitary triangle, denoted with α, β and γ, are:

$$\alpha \equiv \arg\left[-\frac{V_{td}V_{tb}^*}{V_{ud}V_{ub}^*}\right], \quad \beta \equiv \arg\left[-\frac{V_{cd}V_{cb}^*}{V_{td}V_{tb}^*}\right], \quad \gamma \equiv \arg\left[-\frac{V_{ud}V_{ub}^*}{V_{cd}V_{cb}^*}\right]. \tag{1.67}$$

These quantities are physical and can be measured from CP asymmetries in B decays. Consistency among different experimental values help in Standard Model verification. Particularly, β angle yields, with a good approximation, Standard Model phase between mixing amplitude of neutral B and their decay amplitude.

1.4.3 Measurement of CKM parameters

We show in the following lines the measurement of CKM parameters and fixing, briefly, processes to evaluate them. More informations can be found in [11].

$|\boldsymbol{V_{ud}}|$: analysis has been done using nuclear β decays:

$$|V_{ud}| = 0.9738 \pm 0.0005. \tag{1.68}$$

$|\boldsymbol{V_{us}}|$: they used semileptonic decays of kaons and hyperons:

$$|V_{us}| = 0.2200 \pm 0.0026. \tag{1.69}$$

$|\boldsymbol{V_{cd}}|$: due to charm neutrino-antineutrino pairs production:

$$|V_{cd}| = 0.224 \pm 0.012. \tag{1.70}$$

$|\boldsymbol{V_{cs}}|$: from ratio between hadronic decays of W and leptonic decays, measured by LEP:

$$|V_{cs}| = 0.996 \pm 0.013. \tag{1.71}$$

$|\boldsymbol{V_{cb}}|$: with exclusive semileptonic decays and inclusive charm B meson becays:

$$|V_{cb}| = 0.0413 \pm 0.0015. \tag{1.72}$$

$|\boldsymbol{V_{ub}}|$: value has been obtained combining measurement with exclusive method (from

$B^0 \to \rho^- \ell^+ \nu_\ell$ channel) with an inclusive method (from $b \to u \ell^- \overline{\nu}_\ell$):

$$|V_{ub}| = 0.00367 \pm 0.00047. \tag{1.73}$$

$|\boldsymbol{V_{tb}}|$: with hypotesis on unity of triangle:

$$|V_{tb}| = 0.94^{+0.31}_{-0.24}. \tag{1.74}$$

All informations on absolute values of CKM elements evaluated both with direct measurements and unitariety conditions can be summed up as:

$$|V| = \begin{pmatrix} 0.9739 - 0.9751 & 0.221 - 0.227 & 0.0029 - 0.0045 \\ 0.221 - 0.227 & 0.9730 - 0.9744 & 0.039 - 0.044 \\ 0.0048 - 0.014 & 0.037 - 0.043 & 0.9990 - 0.9992 \end{pmatrix} \tag{1.75}$$

All the values of CKM matrix parameters founded so far, of angles and sides of unitary triangle, let us determinate an area in which we had to find the position of the third vertex. In the figure 1.5 we can see a possible triangle, where we have the area (dots on white field) in which it is possible to find vertex with a confidence level of 95%.

1.4.4 Penguin and tree processes

Direct CP violation depends both weak phases difference and strong phases difference. So, we need to distinguish which diagrams give a contribution to total amplitude with different phases. In Standard Model meson decays, composed by a heavy quark happen through charged interactions described by Lagrangian [12]. Generally, amplitudes are divided in two classes, so called *tree* and *penguin*. If all complications due to long distance strong interactions or final state interactions or hadron-hadron interactions are negligible, this split is easily explained through weak diagrams. So called penguin diagrams are ones with W boson is emitted and reabsorbed in the same line of emitter quark (figure 1.6), while tree diagram, that havo no loop in weak diagram (figura 1.7). Tree diagrams are further split in *spectator* (light quark is disconnected by starting meson in the weak diagram), *exchange* (W boson is swapped between starting meson quark) and *annihilation* (starting meson quarks are annihilated to make W).

This separation between different kinds of tree diagram is not important in CP

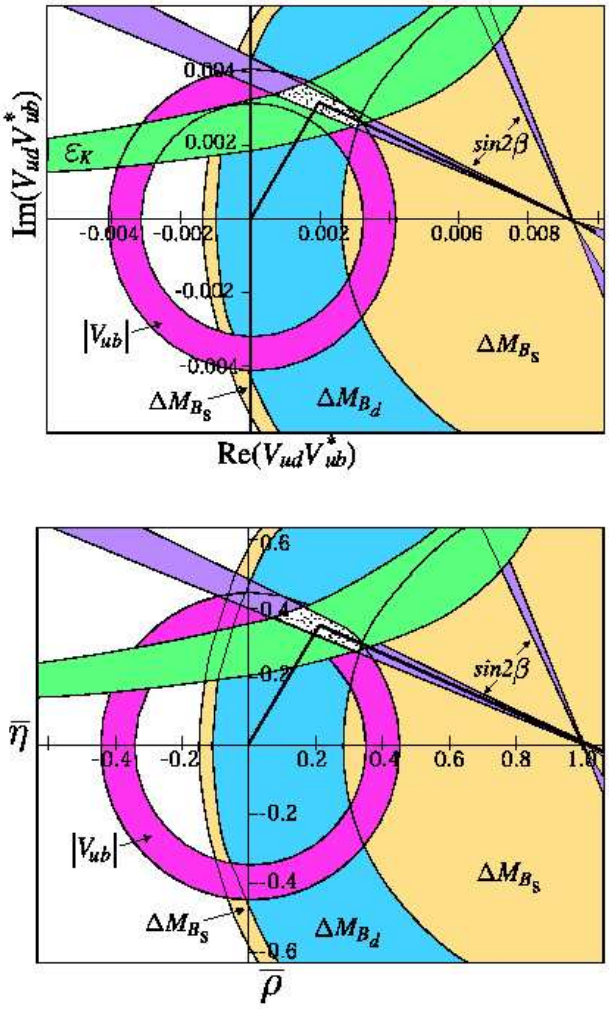

Figure 1.5: Constraint from the text on the position of the apex, A, of the unitarity triangle following from $|V_{ub}|$, B mixing, ϵ and $\sin 2\beta$. A possible unitarity triangle is shown with A in the preferred region.

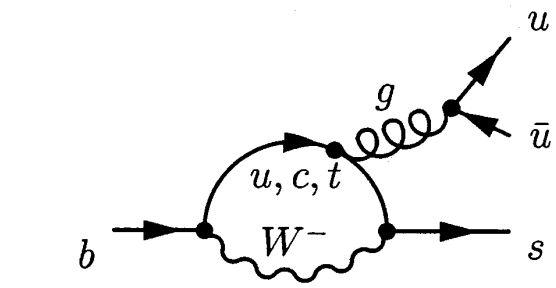

Figure 1.6: Penguin diagram for $b \to sg^*$ process.

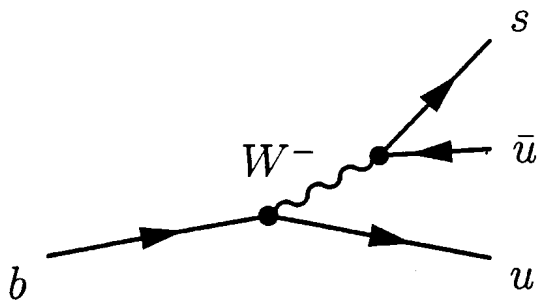

Figure 1.7: Tree diagram for $b \to uW^-$ process.

violation cause two kinds of diagrams, that contribute to decay amplitude, have same CKM matrix element and so the same weak phase. Different from tree diagram, in $b \to q$ with $q = d, s$ process, penguin terms contribute with different combinations of CKM elements depending by the quark within loop $i = u, c, t$:

$$v_{iq} = V_{ib}^* V_{iq}. \tag{1.76}$$

So weak phase differences in the asymmetry are the ones due to penguin and tree contributions; it becomes important to know intensity and weak phases related to both diagrams. In penguin diagram are considered strong interactions too. The quark in the loop emits a gluon to compensate for mass difference between initial and final quark. Gluon can produce a quark-antiquark pair o be reabsorbed and re-issued from other gluons that can be found in this kind of process. When we evaluate direct CP

asymmetry, strong phase differences are caused by penguin diagrams.

1.4.5 Measurement of angles of unitary triangle

The simplest way to see relationship between measurement of asymmetry $a_{f_{CP}}$ and angles of unitary triangle α, β e γ is due to decays dominated by only one amplitude with particular final states, CP eigenstates. In this case, relationship that links asymmetry with angles is simply. In B mesons system we have, in first approximation (neglecting $\Delta\Gamma_B$):

$$\left(\frac{q}{p}\right)_B \simeq -\frac{M_{12}^*}{|M_{12}|} = \frac{(V_{tb}^* V_{td})^2}{|V_{tb}^* V_{td}|^2} = \frac{V_{tb}^* V_{td}}{V_{tb} V_{td}^*} = e^{2i\beta}. \tag{1.77}$$

Combinations of CKM parameters can be seen directly from box diagram in figure 1.3: in Standard Model they are responsible of not-diagonal elements of mass matrix defined on flavour eigenstates. Box diagrams, where mixing happens through u and c quarks, are negligible for many cases.

To avoid hadronic uncertainties, we need to choose decay modes dominated by only one diagram. Most of channels, instead, has contributions both penguin and tree diagrams. There are three cases in which CP violation is caused by phase: tree diagrams dominate penguin ones because they are forbidden; tree diagrams are forbidden and so penguin diagrams dominate; both diagrams have same weak phase.

Dominant tree diagrams

Tree diagrams are dominant when CKM parameters of penguin diagrams are not greater than tree ones, or when this condition is verified:

$$\left|\frac{V_{tb} V_{td}^*}{V_{q'b} V_{q'q}^*}\right| \leq 1 \tag{1.78}$$

An example of dominating tree diagram is $B \to \pi\pi$ decay that corresponds to $b \to u\overline{u}d$ where CKM parameters of this penguin and tree process are in the order of λ^3. So, tree diagram results dominant in a good approximation. In this case, we measure α angle and from (1.77) we obtain

$$\lambda_{\pi\pi} = \frac{q}{p}\frac{\overline{A}}{A} \simeq \frac{V_{tb}^* V_{td}}{V_{tb} V_{td}^*}\frac{V_{ub} V_{ud}^*}{V_{ub}^* V_{ud}} = e^{2i\alpha} \tag{1.79}$$

that corresponds to first equation of (1.67). Hadronic uncertainties rise from penguin diagrams contribution, estimated about 10% and it can be reduced.

Forbidden tree diagrams

In the Standard Model they expect flavour changing decays but not decaying quark charge: in this case tree diagrams are forbidden. An example of these decays is $B \to \phi K_S$ or $b \to s\overline{s}s$ at quark level. Because we have a K meson we had to consider kaons mixing too that involves an addition of a factor

$$\left(\frac{q}{p}\right)_K \simeq \frac{V_{cs}V_{cd}^*}{V_{cs}^*V_{cd}} \tag{1.80}$$

to λ expression that becomes:

$$\lambda_{\phi K_S} = \left(\frac{q}{p}\right)_B \left(\frac{q}{p}\right)_K \frac{\overline{A}}{A} \simeq \frac{V_{tb}^*V_{td}}{V_{tb}V_{td}^*}\frac{V_{cs}V_{cd}^*}{V_{cs}^*V_{cd}}\frac{V_{tb}V_{ts}^*}{V_{tb}^*V_{ts}} = e^{-2i\beta} \tag{1.81}$$

Diagram with only one weak phase

$B \to \psi K_S$ decay, $b \to c\overline{c}s$, is representative in the case which a single weak phase dominates. Neglecting corrections in the order of λ^4 we have $V_{tb}^*V_{ts} = -V_{cb}V_{cs}^*$, where first CKM elements combination is related to penguin diagram while second one is related to tree diagram. In this way, with a good approximation, we can assume same phase for both diagrams.

$$\lambda_{\psi K_S} = \left(\frac{q}{p}\right)_B \left(\frac{q}{p}\right)_K \frac{\overline{A}}{A} \simeq \frac{V_{tb}^*V_{td}}{V_{tb}V_{td}^*}\frac{V_{cs}V_{cd}^*}{V_{cs}^*V_{cd}}\frac{V_{cb}V_{cs}^*}{V_{cb}^*V_{cs}} = -e^{-2i\beta} \tag{1.82}$$

Hadronic uncertainties are estimated about 10^{-3}.

1.5 Rare B meson decays

All B meson decays that not happen through $b \to c$ reaction are known as rare B decays. Due to little value of $|V_{ub}|$, $b \to u$ are suppressed, so, we expect observable contributions from other diagrams for some hadronic decay channel.

There are many processes that contribute to rare B decays. B mesons can decay with or without strangeness change. ($|\Delta S| = 1$ or 0). Rare decays with $|\Delta S| =$

1 produce, in their final state, strange mesons (K or K^*), and they happen through a process with a Cabibbo-suppressed spectator quark $b \to u\overline{u}s$ and a gluonic loop (penguin) $b \to sg^*$. In these decays penguin diagrams are dominant. In these diagrams the favourite side from CKM matrix, that corresponds to $b \to s$ transition, should be rare decays amplitude in final states with one or three s quarks.

Viceversa, for decays with $|\Delta S| = 0$, we expect a dominant Cabibbo-favoured spectator quark process $b \to u\overline{u}d$, because $b \to dg^*$ is suppressed by V_{td}, but it shouldn't be negligible for decays in final states without s or c quarks. A significant contribution of $b \to dg^*$ would mean presence of so called *penguin pollution*. We can note loop diagram is more significative for B meson decays rather than D decays because $b \to s$ loop is sensitive for strong coupling of t quark through V_{tb} and V_{ts}, while corresponding $c \to u$ loop contributions are suppressed cause of weak V_{cb} and V_{ub} coupling and due to small s and d masses [13].

1.6 Formalism for $B\overline{B}$ coherent states

B^0 and $\overline{B}^0$ mesons produced by $\Upsilon(4\mathrm{S})$ decay can be found in a coherent quantum state with $L = 1$ (*p wave*). In this state two particle form one system that can be considered as one B meson evolving in time with two mesons propagating in the space with the same phase between them. This means that for every time the state is composed exactly by B^0 and $\overline{B}^0$. When one of two particles decays, we will be able to have events with B^0 and $\overline{B}^0$ whose decay probabilities are controlled by time difference of two decays.

Two mesons produced in $\Upsilon(4\mathrm{S})$ decay are identified with θ angle that form with electron beam in Υ frame. Coherent state is described by antisymmetric function:

$$\begin{aligned} S(\tau_1,\tau_2) \quad &= \tfrac{1}{\sqrt{2}}\{B^0_{phys}(\tau_1,\theta,\phi)\overline{B}^0_{phys}(\tau_2,\pi-\theta,\phi+\pi) \\ &\quad -\overline{B}^0_{phys}(\tau_1,\theta,\phi)B^0_{phys}(\tau_2,\pi-\theta,\phi+\theta)\}\sin(\theta) \end{aligned} \tag{1.83}$$

and replacing 1.37 and 1.38, we can write as

$$\begin{aligned} S(\tau_1,\tau_2) \quad &= \tfrac{1}{\sqrt{2}}e^{-(\Gamma/2+im)(\tau_1+\tau_2)}\{\cos[\Delta m_B(\tau_1-\tau_2)/2](B^0_1\overline{B}^0_2-\overline{B}^0_1B^0_2) \\ &\quad -i\sin[\Delta m_B(\tau_1-\tau_2)/2](\tfrac{p}{q}B^0_1B^0_2-\tfrac{q}{p}\overline{B}^0_1\overline{B}^0_2)\}\sin(\theta_1). \end{aligned} \tag{1.84}$$

where τ_1 is B_1 own time, which we identify with B meson decaying forward ($\theta_1 < \pi/2$), and τ_2 is B_2 own time moving in the opposite direction. Cause in Υ frame two B mesons have same but opposite momenta, we can consider, until one of two meson will decay, $\tau_1 = \tau_2$ and in this case the equation (1.84) contains B^0 and $\overline{B}^0$. When one of the two particles decays, its own timer stops, so proportional terms $\sin[\Delta m_B(\tau_1 - \tau_2)/2]$ assume importance.

From equation (1.84) it's possible the following result: decays amplitude in which one of two mesons decays in a final state f_1 at t_1 time while the other one decays in a state f_2 at t_2 time is obtained in this way

$$\begin{aligned} A(t_1,t_2) \;&= \tfrac{1}{\sqrt{2}} e^{-(\Gamma/2+im)(t_1+t_2)} \zeta(t_1,t_2)\{cos[\Delta m_B(t_1-t_2)/2](A_1\overline{A}_2 - \overline{A}_1 A_2) \\ &\quad -i\sin[\Delta m_B(t_1-t_2)/2](\tfrac{p}{q}A_1A_2 - \tfrac{q}{p}\overline{A}_1\overline{A}_2)\}\sin(\theta_1), \end{aligned} \tag{1.85}$$

where A_i means B^0 decay amplitude in a f_i state, $\overline{A}_i$ is $\overline{B}^0$ decay amplitude in the same state f_i.

A particular B decay state that allows us to identify such flavour meson (*tagging decays*) has one of two amplitudes A_f or $\overline{A}_f$ equal to zero. In the equation (1.85) we introduce following brief notation to mantain same signs with (1.84)

$$\zeta(t_1,t_2) = \begin{cases} +1 & t_1 = \tau_1,\ t_2 = \tau_2 \\ -1 & t_1 = \tau_2,\ t_2 = \tau_1 \end{cases}$$

but this factor vanishes in decay rate calculation.

We can evaluate production rate of combined states f_1 and f_2, that results time dependent:

$$\begin{aligned} &R(t_1,t_2) = Ne^{-\Gamma(t_1+t_2)}\{(|A_1|^2+|\overline{A}_1|^2)(|A_2|^2+|\overline{A}_2|^2) - 4\mathrm{Re}(\tfrac{q}{p}A_1^*\overline{A}_1)\mathrm{Re}(\tfrac{q}{p}A_2^*\overline{A}_2) \\ &-\cos(\Delta m_B(t_1-t_2))[(|A_1|^2-|\overline{A}_1|^2)(|A_2|^2-|\overline{A}_2|^2) + 4\mathrm{Im}(\tfrac{q}{p}A_1^*\overline{A}_1)\mathrm{Im}(\tfrac{q}{p}A_2^*\overline{A}_2)] \\ &+2\sin(\Delta m_B(t_1-t_2))[\mathrm{Im}(\tfrac{q}{p}A_1^*\overline{A}_1)(|A_2|^2-|\overline{A}_2|^2) - (|A_1|^2-|\overline{A}_1|^2)\mathrm{Im}(\tfrac{q}{p}A_2^*\overline{A}_2)]\} \end{aligned} \tag{1.86}$$

In this formula, it was estimated an integral on all possible directions of both B mesons so we could delete angular dependence and showing a normalization factor N. We used also this approximation $|q/p| = 1$.

To measure CP asymmetry we seek for events in which a B (B_{CP}) decays in a CP eigenstate f_{CP} at $t_{f_{CP}}$ time, while other meson (B_{tag}) decays in a way that allows us to identify its flavour, so called *tagging* mode, at t_{tag} time. For example, it's possible to

consider a way to tag with $A_2 = 0$, $\overline{A}_2 = \overline{A}_{\rm tag}$. This identifies B meson decaying in a CP eigenstate as a B^0 at $t_1 = t_{\rm tag}$ time in with the tagging decays. Furthermore we had to underline how this it is true when tagging decay happens afterwards the decay in CP eigenstate. In this case, B_{CP}, for every time $t_1 < t_{\rm tag}$, is described by a state evolving in a way to be tagged as B^0 at $t_1 = t_{\rm tag}$ time. So, the expression with two times it is reduced to

$$\begin{aligned} R(t_{\rm tag}, t_{f_{CP}}) = N e^{-\Gamma(t_{\rm tag}+t_{f_{CP}})} |\overline{A}_{\rm tag}|^2 |A_{f_{CP}}|^2 \{1 + |\lambda_{f_{CP}}|^2 \\ + \cos[\Delta m_B (t_{f_{CP}} - t_{\rm tag})](1 - |\lambda_{f_{CP}}|^2) \\ -2\sin[\Delta m_B (t_{f_{CP}} - t_{\rm tag})]{\rm Im}(\lambda_{f_{CP}})\} \end{aligned} \tag{1.87}$$

with $\lambda_{f_{CP}}$ defined in 1.52.

If final tagging state has $\overline{A}_2 = 0$, $A_2 = A_{\rm tag}$, that identifies B_{CP} as a $\overline{B}^0$ at $t_{\rm tag}$ time, usually it is used an expression similar to equation (1.87) where signs of cosinus and sinus terms are opposite. Hypotesis $|q/p| = 1$ guarantees us amplitudes for opposite tags are same. With these rates, we can evaluate time dependent CP asymmetry that results to be equal to expression 1.56, where $t = t_{f_{CP}} - t_{\rm tag}$.

Expression (1.87) is function of two temporal variables $t_{\rm tag}$ and $t_{f_{CP}}$ representing respectively passed time from $B^0\overline{B}^0$ pair creation for B_{CP} and $B_{\rm tag}$. This requires reconstruction of pair creation time but it's pratically impossible to realize it. So to solve this problem, we replace variables

$$\{t_{\rm tag}, t_{f_{CP}}\} \rightarrow \{s = t_{\rm tag} + t_{f_{CP}}, \Delta t = t_{f_{CP}} - t_{\rm tag}\}$$

with these new ones, assuming values:

$$\begin{aligned} -\infty < \Delta t < +\infty \\ |\Delta t| < s < +\infty \end{aligned} \tag{1.88}$$

Integrating on s, we obtain relationship between decay rate and $B_{CP} \rightarrow f_{CP}$ to Δt:

$$R(\Delta t) \propto e^{-\Gamma|\Delta t|}[1 \pm S\sin(\Delta m_B \Delta t) \mp C\cos(\Delta m_B \Delta t)] \tag{1.89}$$

where C and S are defined, respectively, in 1.55 and signum $+$ $(-)$ refers to $B_{\rm tag}$ when we have B^0 ($\overline{B}^0$). Necessity of the Δt measurement is main cause of contruction of asymmetric collider (please see Chapter 2 for more details).

1.7 Latest results on CP violation measurements

BABAR has already published the results on the measurement of time-dependent CP-violating asymmetries in the neutral B mesons decays. The results was obtained using analyzed data corresponding to 232 millions $B\overline{B}$ pairs acquired in the period 1999-2004. The selected events are the ones with a neutral B completely reconstructed in a charmonium final state, while the flavour of the other B is determined through decay products. Asymmetry amplitude, proportional to $\sin 2\beta$ in the considered decays, comes from lifetime distributions of these events. The result obtained is:

$$\sin 2\beta = 0.722 \pm 0.040_{stat} \pm 0.023_{syst}$$

It has been also determined $|\lambda|$ value:

$$|\lambda| = 0.950 \pm 0.031_{stat} \pm 0.013_{syst}$$

consistent with the absence of direct CP violation, according with the Standard Model results for these decay modes. Furthermore *BABAR* for the first time has measured the direct CP asymmetry in the decay $B^0 \to K^+\pi^-$ [43] with the following result:

$$A_{K\pi} = -0.133 \pm 0.030_{stat} \pm 0.009_{syst}$$

Also Belle collaboration at KEKB (Tsukuba, Japan) has published measurements on CP violation, obtained with a statystics of 152 millions $B\overline{B}$ pairs:

$$\sin 2\beta = 0.728 \pm 0.056_{stat} \pm 0.023_{syst}$$

$$|\lambda| = 1.007 \pm 0.041_{stat} \pm 0.033_{syst}$$

The results founded by *BABAR* and Belle are in a good agreement with the Standard Model prediction.

Chapter 2

The BaBar Detector

2.1 Overview — B-Factories

Exploring CP violation in the B system and its potential impact on the Standard Model, baryogenesis, and cosmology, requires copious production of B mesons, accurate measurement of the B flight time and flavor, and reasonably low background for reconstruction. There are several potential options for experiments which can fulfill these criteria:

1. Hadron colliders ($\overset{(-)}{p}p$): The cross section for $B\overline{B}$ production at TeV hadron colliders is very high compared with e^+e^- B factories, approximately 100 μb vs. 1.2 nb. This large advantage does compete with several disadvantages, however. Hadronic collisions have far more background, making reconstruction of final states which do not contain a J/ψ very challenging. Purely hadronic final states with non-negligible background in e^+e^- colliders at the $\Upsilon(4\mathrm{S})$, such as $D\overline{D}$ or $\pi^0\pi^0$, may be extremely difficult at a hadronic collider and it is not clear that it will be possible to reconstruct such decays. Nevertheless, these experiments do have a statistical advantage and also have the potential for observing CP violation in the B_s system, which is beyond the reach of $\Upsilon(4\mathrm{S})$ experiments. LHC-b at CERN is a new experiment currently under construction.

2. Fixed target proton beam experiments: Fixed-target experiments also offer the potential of a higher rate of B production, but have even greater levels of backgrounds, superimposed interactions, and boost which compresses all tracks in a small solid angle. A significant effort was undertaken at DESY to build such an

experiment, HERA-B.

3. e^+e^- colliders at the Z-pole: The Z-pole presents a relatively clean environment for B-physics with a relatively large cross section ($\sim$ 6 nb). However, the luminosities achieved at this energy are low, the only two colliders in the world which can reach it, LEP and SLD, are both dismantled, and the cost of building new experiments at this energy prevents this from being a viable option.

4. Symmetric and asymmetric e^+e^- B-factories: The $\Upsilon(4\mathrm{S})$ resonance provides a very clean environment for B reconstruction. Asymmetric e^+ and e^- beams provide a boost to the B meson pair that is produced, allowing for reconstruction of B flavor as a function of flight time through the separation of the B vertices in the lab frame, Δz . Statistical limitations, of which luminosity is the critical factor, are the dominant source of error for time-dependent CP asymmetries. Two asymmetric B-factories have been built and are currently producing physics: PEP-II/*BABAR* and KEK-B/Belle. Previously, the symmetric B-factory CLEO (at the CESR ring at Cornell) was able to produce precision B physics results, however the symmetric design precluded measurement of time-dependent CP-violating asymmetries.

Figures 2.2 and 2.3 show the *BABAR* and Belle detectors. The experiments are very similar, with the following important differences: the KEK B factory has a nonzero beam crossing angle (4.2 mr) at the interaction point (IP), whereas the PEP-II/*BABAR* B factory has a more traditional collinear IP. The KEK design potentially allows a greater number of beam bunches to be stored in the ring, due to absence of parasitic crossings at $\pm$ 1m, as are present in the PEP-II design. However KEK-B is a highly non-traditional design; concerns over higher-order mode resonances at the IP led the PEP-II B factory to use a collinear crossing. So far, both KEK-B and PEP-II have performed well. At the time of writing, PEP-II has integrated 254.6 fb^{-1}and KEK-B has integrated 443.2 fb^{-1}.

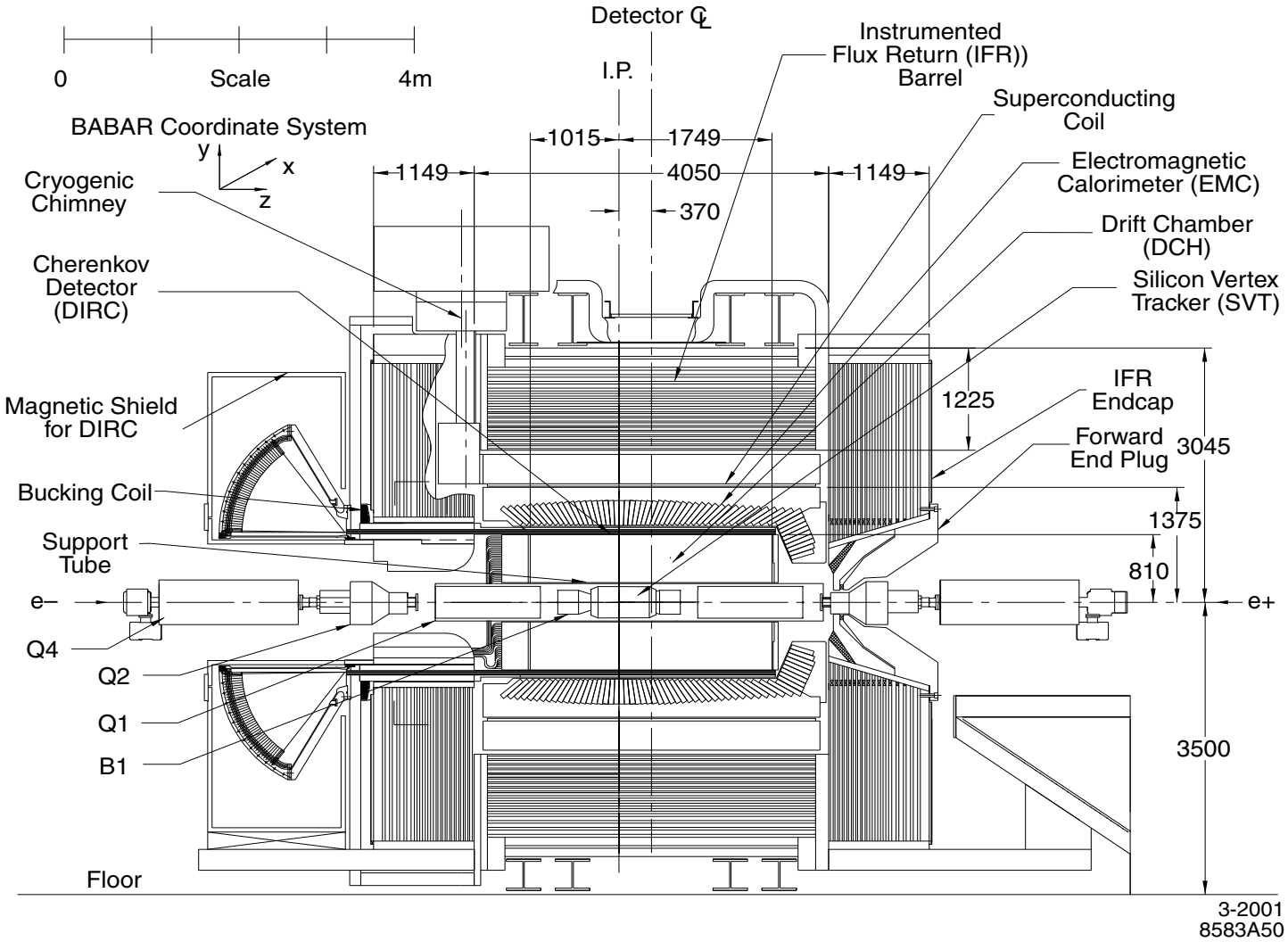

Figure 2.1: *BABAR* detector longitudinal section.

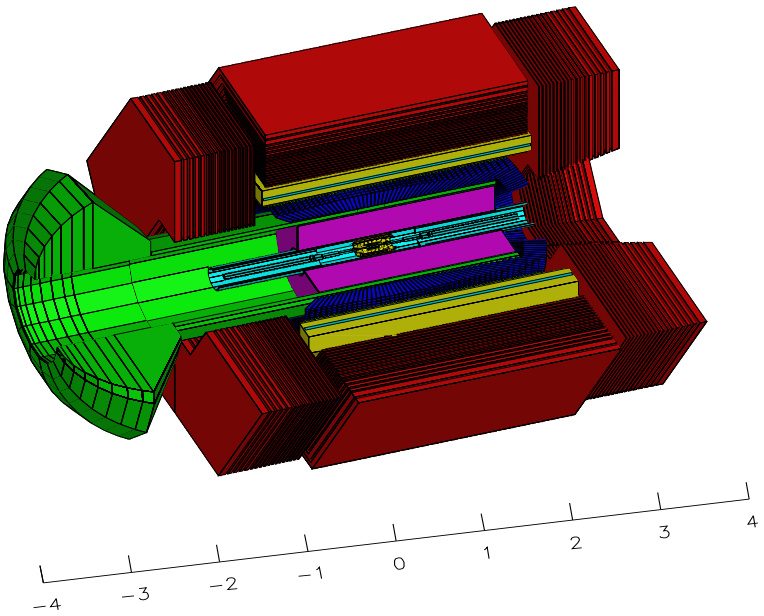

Figure 2.2: *BABAR* detector cutout diagram.

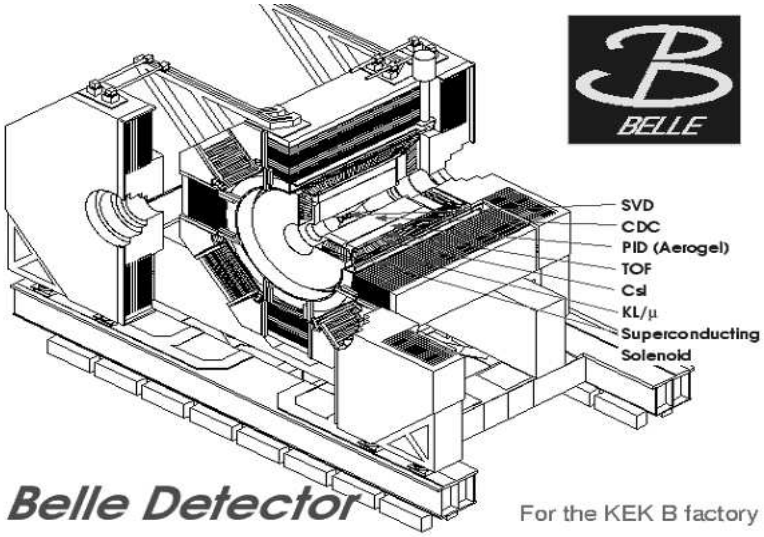

Figure 2.3: Belle detector cutout diagram.

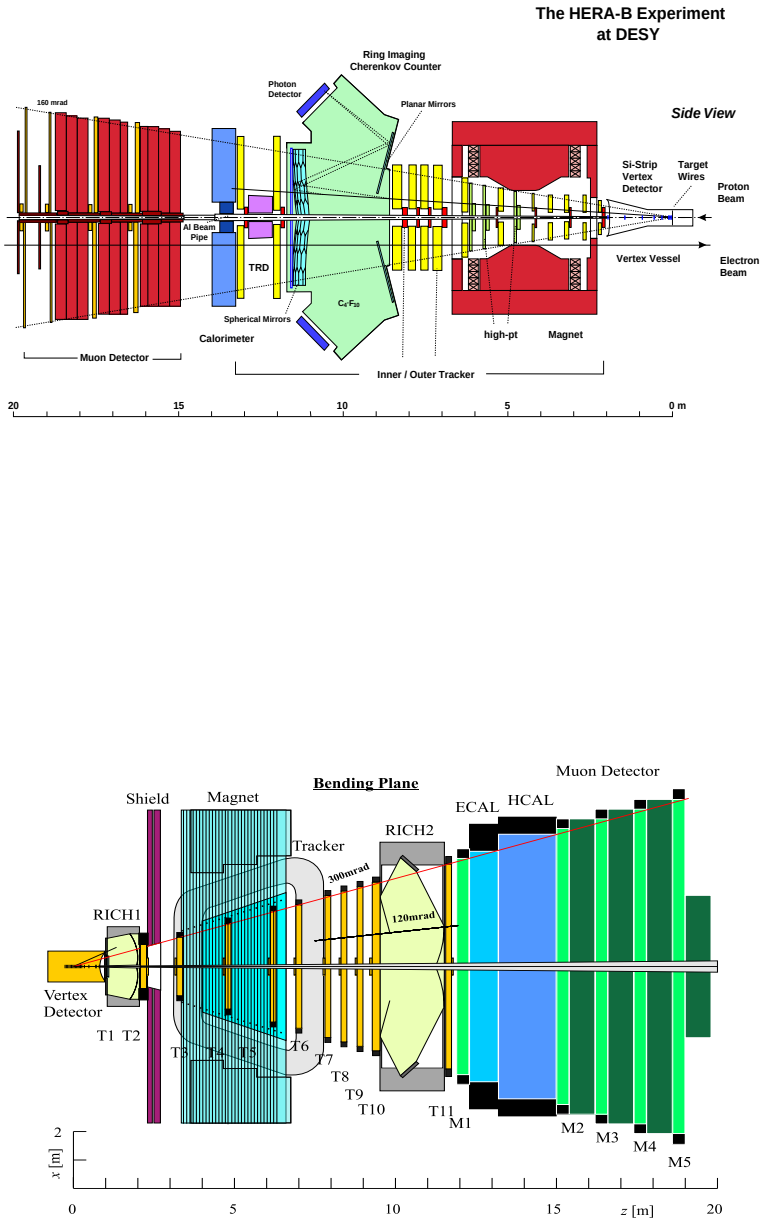

Figure 2.4: Diagrams of: (*top*) the HERA-B detector (at DESY, first beam in 2000) and (*bottom*) the LHC-b detector (CERN, to be completed in 2007).

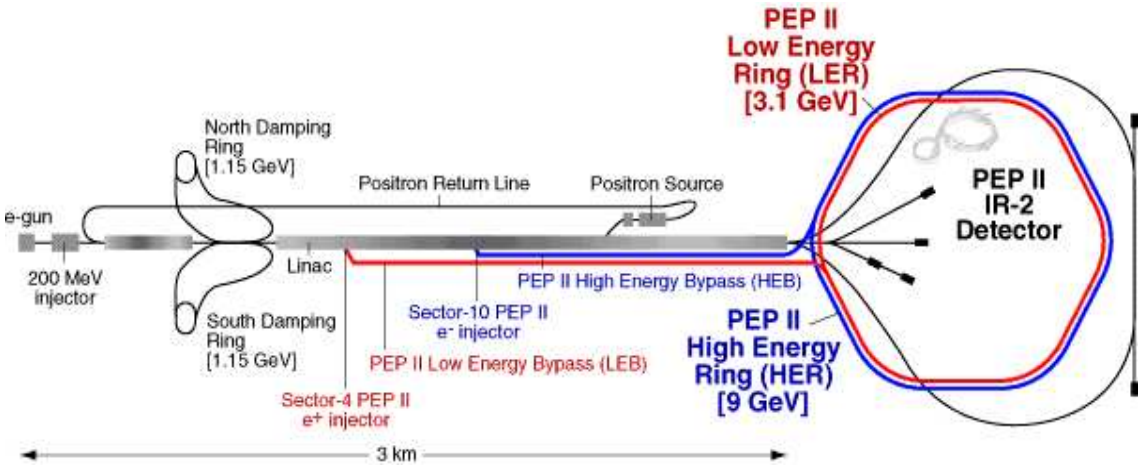

Figure 2.5: The PEP-II asymmetric storage ring and the SLAC linear accelerator. The SLAC linac is the injector for PEP-II. The single interaction point of PEP-II is at Interaction Region 2, where *BABAR* is situated.

The particle identification method also differs between *BABAR* and Belle: as will be described in Section 2.6, *BABAR* uses quartz bars to internally reflect Cerenkov light to a backward-mounted detector (the DIRC), whereas Belle uses an aerogel Cerenkov detector. In addition, *BABAR* has a 5-layer silicon vertex detector (SVT, see section 2.3) that can do standalone tracking (important for $D\overline{D}$), whereas Belle uses a 3-layer silicon vertex detector.

Figure 2.4 shows the design of the HERA-B and LHC-b experiments. Each of these experiments uses hadron beams, with, in the case of HERA-B, a fixed (tungsten wire) target in the beam halo, and, for LHC-b, colliding proton beams. Hadrons do present a challenging (but potentially very rewarding) environment for B physics.

2.2 The PEP-II Asymmetric Collider

The design of PEP-II is shown in figure 2.5. The 9 GeV electrons and 3.1 GeV positrons are injected from the SLAC linac via bypass lines in the linac gallery. The beam parameters are listed in Table 1. PEP-II has surpassed design goals both in instantaneous and in average integrated luminosity.

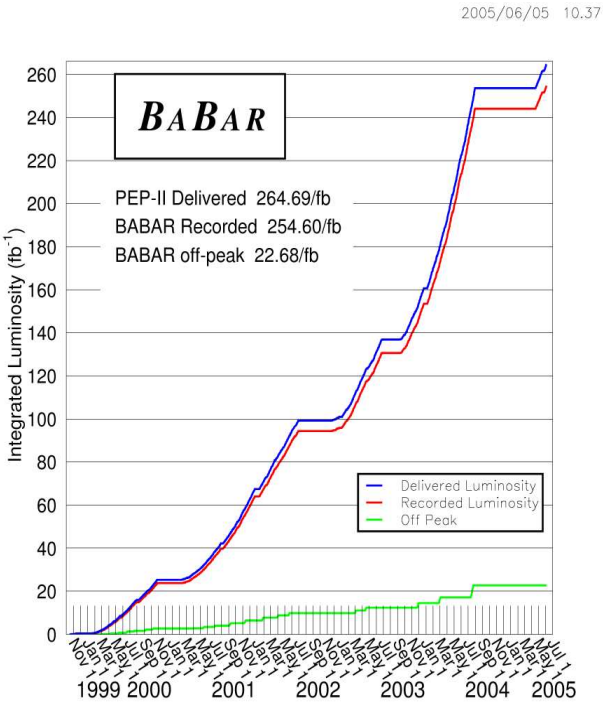

Figure 2.6: PEP-II -*BABAR* integrated luminosity since startup.

Parameters	Design	Typical
Energy HER/LER (GeV)	9.0/3.1	9.0/3.1
Current HER/LER (A)	0.75/2.15	1.21/2.04
# of bunches	1658	889
Bunch spacing (ns)	4.2	4.2-8.4
σ_{Lx} (μm)	110	110
σ_{Ly} (μm)	3.3	4.1
σ_{Lz} (mm)	9	9
Luminosity ($10^{33}\,\mathrm{cm}^{-2}\mathrm{s}^{-1}$)	3	8-9
Luminosity (pb^{-1}/d)	135	423

Table 2.1: PEP-II beam parameters. Values are given for the design and for colliding beam operation at time of writing. HER and LER refer to the high energy e^- and low energy e^+ ring, respectively. σ_{Lx}, σ_{Ly}, and σ_{Lz} refer to the R.M.S. horizontal, vertical, and longitudinal bunch size at the IP.

Most of the data is taken at the $\Upsilon(4S)$ resonance (10.58 GeV), however approximately 12% are taken at 40 MeV below the resonance to allow studies of non-resonant background in data. A plot of PEP-II integrated luminosity as a function of time is in figure 2.6.

2.3 Overview of Experimental Technique at the $\Upsilon(4S)$

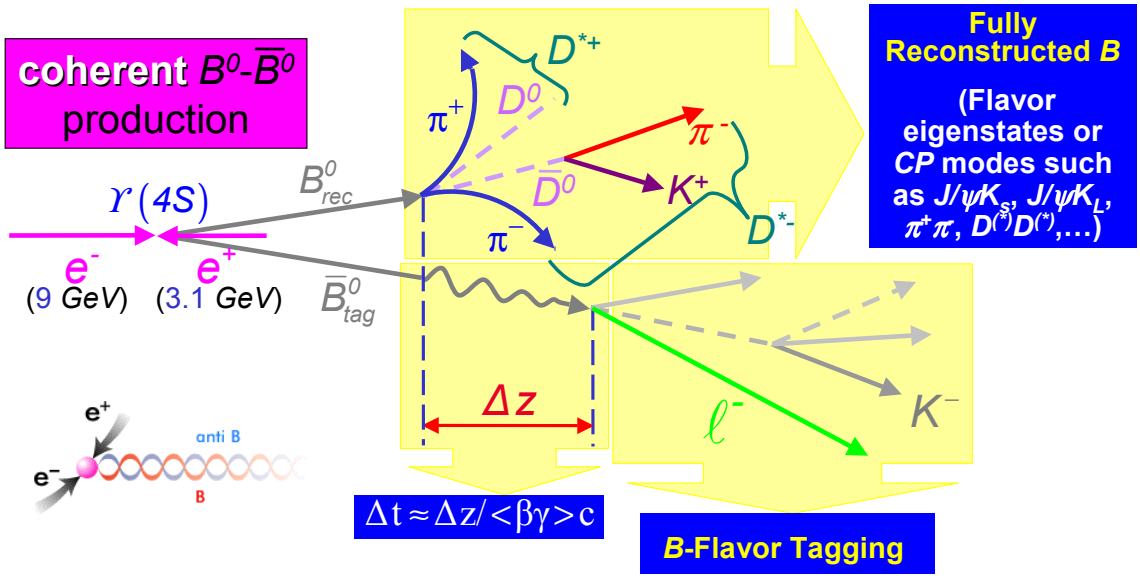

Figure 2.7: Experimental reconstruction technique used for measuring time-dependent CP-violating asymmetries at an $\Upsilon(4S)$ asymmetric collider. A coherent $B\overline{B}$ pair is produced from the $\Upsilon(4S)$ decay, which allows determination of reconstructed neutral B flavor as a function of decay time.

In order to measure time-dependent CP-violating asymmetries at the $\Upsilon(4S)$, one must (of course) first reconstruct a neutral B decay mode that can exhibit CP violation, such as $B^0 \to D\overline{D}$ or $B^0 \to J/\psi K^0_s$. However, that is merely the first step. After signal event reconstruction, the additional tracks in the event (which correspond to the decay products of the other B [the "tag side B"]) must be used to determine whether the other B in the event was a B^0 or $\overline{B}^0$, due to the fact that the CP asymmetry is opposite for B^0 and $\overline{B}^0$ (see equations 1.53 and 1.54).

After both the event reconstruction and the flavor tagging are completed, the difference

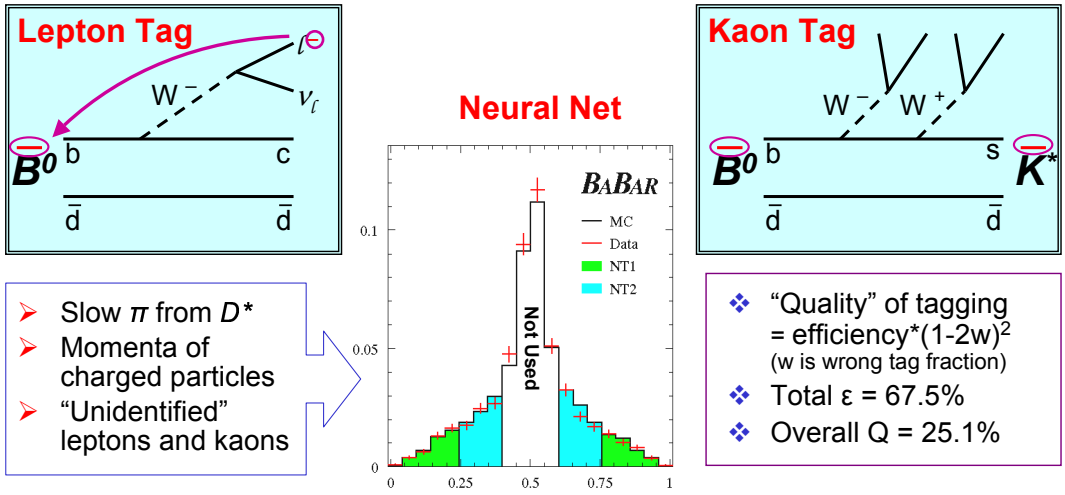

Figure 2.8: Technique used for tagging the flavor of the opposite-side B. Lepton and kaon charge is correlated with the flavor of the B. For events with no obvious lepton or kaon, a neural net is used to attempt to extract the flavor.

in vertex z-position[1] between the reconstructed B vertex and the tag side B vertex must be determined. This difference, Δz, is (very nearly) proportional to the decay time difference Δt between the two B decays. Δt is the time measurement over which the CP-violating asymmetry can occur, and is input (as t) in equations 1.53 and 1.54. Figure 2.7 gives an overview of this reconstruction method.

Figure 2.8 briefly describes the technique used for flavor tagging. The sign of charged leptons and kaons in the event (which are not part of the reconstructed B) is correlated with the flavor of the tag side B. A cut-based selector using *BABAR*'s electron, muon, and kaon identification capabilities is used to select signal events with a lepton or kaon on the tag side, and from this determine the flavor of the tag side B. For events which are not cleanly tagged by the cut-based selector, a neural net algorithm is used to extract the flavor of the tag side B. The neural net uses information including slow pion charge, jettiness of the tag side tracks, and recovery of leptons and kaons which are not cleanly identified in order to reconstruct the tag side flavor. The overall efficiency of tagging is 74.0% and the fraction of tagged events which are given an incorrect tag is 16.8%. The error on time-dependent asymmetries is proportional to $Q = \epsilon(1-2w)^2$ where ϵ is the efficiency and w is the wrong-tag fraction. This quality

[1]The z-axis in *BABAR* is along the direction of the beam line, with electrons (and the center-of-mass boost) pointing toward $+z$ in the lab frame.

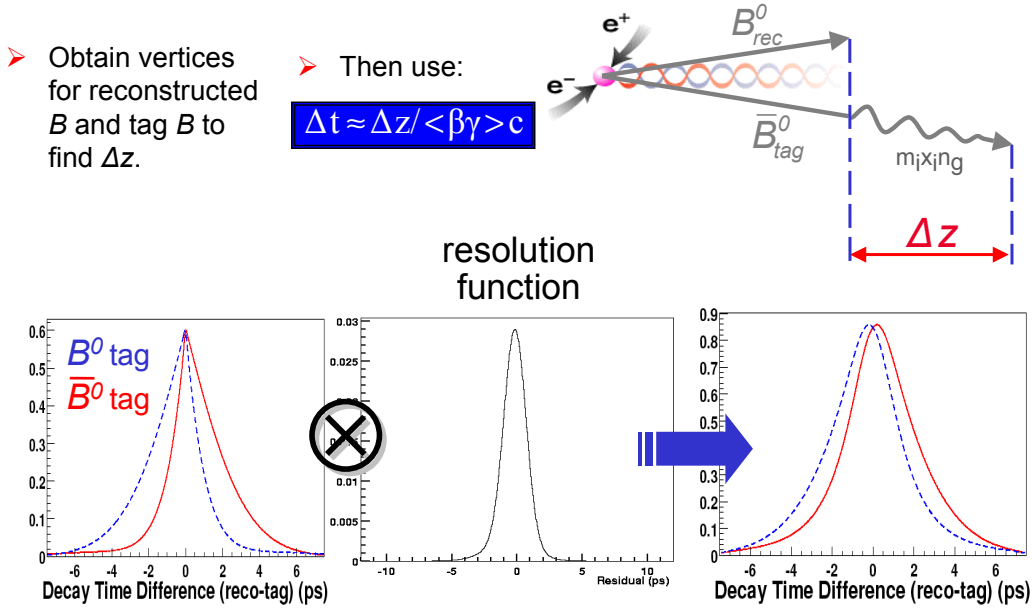

Figure 2.9: Δt measurement and resolution function. The difference in reconstructed z-position of the tag and reconstructed B decay vertices is used to determine the time difference Δt.

factor Q is 29.7% for *BABAR*'s tagging algorithm.

Figure 2.9 briefly describes the Δt measurement and resolution function. A clustering algorithm is used to determine the vertex position for the tag side B decay; the error on this position dominates the resolution. CP violation evinces itself as a difference in Δt distribution depending on whether the flavor tag is B^0 or $\overline{B}^0$, but this decay time distribution is convoluted by the error of Δt. Fully reconstructed B events which have definite flavor (such as $B^0 \rightarrow D^{*+}\pi^-$ or $D^{*+}\rho^-$) are used to determine both the mistag fractions and the parameters of the resolution function (which is modelled as a triple gaussian) in data (for more details please see Section 7.4.2).

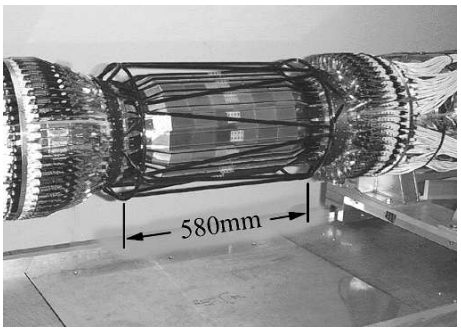

Figure 2.10: Fully assembled SVT. The silicon sensors of the outer layer are visible, as is the carbon-fiber space frame (black structure) that surrounds the silicon.

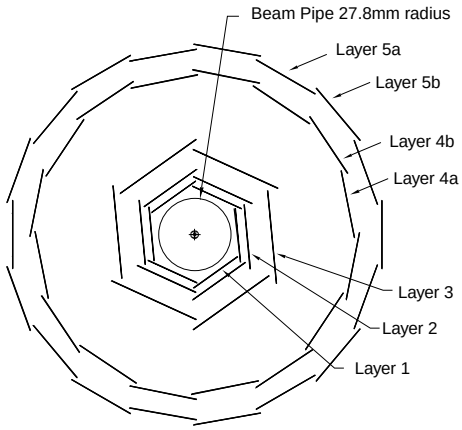

Figure 2.11: Transverse section of the SVT.

2.4 The Silicon Vertex Tracker (SVT)

The SVT contains 5 layers of silicon, double sided with conductive strip sensors. Strips on the opposite sides of each layer are orthogonal: ϕ strips run parallel to the beam axis and z strips run transverse to the beam direction.

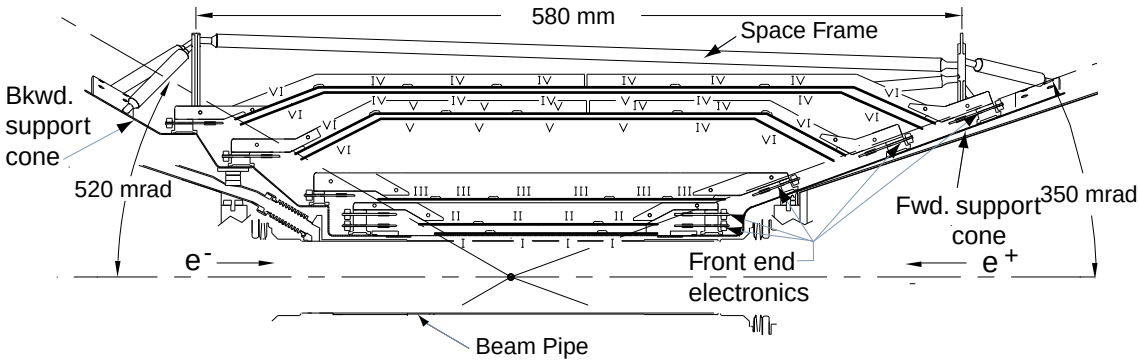

Figure 2.12: Longitudinal section of the SVT.

Together, the SVT and the central tracking drift chamber (DCH) form the charged particle tracking system (see also the following 2 sections). Precise and efficient measurement of track 4-momentum is necessary for full reconstruction of B meson decays, which tend to have multiple charged decay products. In addition, good vertex (and Δz) resolution and accurate extrapolation to the outer subdetectors is essential for reconstruction and background subtraction. Thus, accurate charged particle tracking and vertexing is required.

The 5 layers and relatively long radial separation between SVT detector layers provide both standalone track pattern recognition and refinement of drift chamber tracks via addition of SVT hits. The necessity of precise measurements close to the interaction point for Δz measurement and for background rejection using vertex quality, and for efficient reconstruction of low momentum tracks (such as slow pions from D^*decays), drive the requirements for the SVT.

The SVT silicon is composed of n-type substrate with p^+ and n^+ strips on opposite sides. The bias voltage ranges from 25-35 V. The layers of the SVT are divided radially into modules, shown as line segments in Figure 2.11. The modules in the inner 3 layers are straight along the z-axis, while those in layers 4 and 5 are arch-shaped, as shown in Figure 2.12. The arch design was selected to minimize the amount of silicon as well as increase the angle of incidence of tracks originating at the IP which cross the arch "lampshades" near the edges of acceptance. The total active silicon area is 0.96 m^2.

The strip pitch (width) varies from 50 to 210 μm depending on the layer (inner layers are more closely bonded). The strips are AC-coupled to the electronic readout. Only approximately half the strips are read out; most have an unconnected "floating strip" between each pair of active strips (to reduce cost of readout electronics without adversely impacting performance). Digitization is performed by an ATOM ("A Time-Over-Threshold Machine") chip at the end of each set of 128 strips, which amplifies, digitizes, and buffers the signal from each channel. The ATOM chip compares the charge accumulated on each strip with an (adjustible) threshold of 0.95 fC, and records the time in clock intervals (30 MHz for the SVT) for which each strip is over threshold. This information is then delivered to a computer farm for further processing upon an accept signal from the Level 1 Trigger (see section 2.9).

A variety of monitoring checks and calibrations must be performed on the SVT to maintain data quality. Perhaps the most important of these from an avoidance-of-equipment-damage perspective is radiation protection. Currently, twelve silicon PIN

diodes surround the support cones and monitor both instantaneous radiation and accumulated dose. The beam is automatically aborted if radiation levels are above 1 Rad/ms threshold. So far, the SVT is well below the operational limit of 4 MRad integrated dose. The silicon PIN diodes have a temperature-dependent leakage current that increases with absorbed radiation dose. Due to absorbed doses of over 2 MRad in some diodes, the leakage current in these diodes is much higher than the current induced by the radiation. The temperature is monitored very precisely but it is a challenge to correct for the temperature dependence of the leakage current, and the annealing and reverse-annealing effects due to radiation damage. During the 2005 summer shutdown it will be installed a system of diamond sensors inside the SVT. Diamond sensors grown by chemical vapor deposition (CVD) have no significant leakage current and are much more radiation hard than silicon PIN diodes. With a bias voltage of 500V applied across a 500-μm-thick polycrystalline CVD diamond sensor, the size of the signal due to a minimum-ionizing particle is more than 50% of that for a signal from a 300-μm-thick silicon sensor. The existing twelve silicon PIN diodes are mounted on the outside of support rings at the small end of each of the SVT support cones. We are assuming that the SVT will not be disassembled for replacement of SVT modules in the summer of 2005 and hence we will not have access to the existing PIN-diode sensors. However, we are assuming that the SVT will be removed from the beam-pipe so that we have access to the inside of the support cones for installation of diamond sensors. The diamond sensors will then augment (rather than replace) the existing silicon PIN-diode radiation sensors. For data quality calibration, channel gains and noise must be individually calibrated, and these are done online via an integrated pulse generator and calibration electronics. The offline reconstruction has the responsibility for calibration of the alignment of each SVT module. Alignment is critical for accuracy of vertexing and of tracking reconstruction, and is done in two steps. The local SVT alignment uses dimuon and cosmic ray events to calibrate the relative position of each of the 340 wafers. The global alignment then determines the overall position and rotation of the SVT with respect to the DCH.

The SVT has performed according to design essentially since its inception. A combined hardware and software hit-finding efficiency greater than 95% is observed, excluding the 4 (out of 208) readout sections which are defective. Single hit resolution for tracks originating from the IP averages 20 μm in both z and ϕ for hits on the inner 3 layers and 40 μm in z and 20 in ϕ for hits in the outer 2 layers. Before the summer

2002 shutdown there were 9 readout sections out of 208 that were not used in the DAQ. During the shutdown it was recabled the SVT and there was the possibilty to inspect closely all the modules with problems. This allowed us to fix 5 of the 9 problems and the last 4 sections do not have significantly impact on performances.

2.5 The Drift Chamber (DCH)

The DCH contains 40 layers of gold-coated tungsten-rhenium sense wires and gold-coated aluminium field wires in a mixture of 80% helium and 20% isobutane gas. There are a total of 7,104 sense wires and 21,664 field wires, with one wire per electronics channel. Wires are each tensioned (30 grams for sense wires, 155 grams for field wires) and pass through the aluminium endplates via feedthroughs made from Celenex insulating plastic around a copper wire jacket. The layers are grouped by four into 10 superlayers, with the wires in each superlayer oriented as either axial (directly parallel to the z-axis) or "stereo" (at a small angle in ϕ with respect to the z-axis, in order to obtain longitudinal position information). 6 of the 10 superlayers are stereo, and the other 4 are axial.[2] The DCH is asymmetric in z about the interaction point, as shown in Figure 2.15, to accommodate the forward boost of the center of mass of physics events.

[2]The arrangement is, from inner to outer, AUVAUVAUVA (A = axial, U = u stereo ($+\phi$), V = v stereo ($-\phi$)).

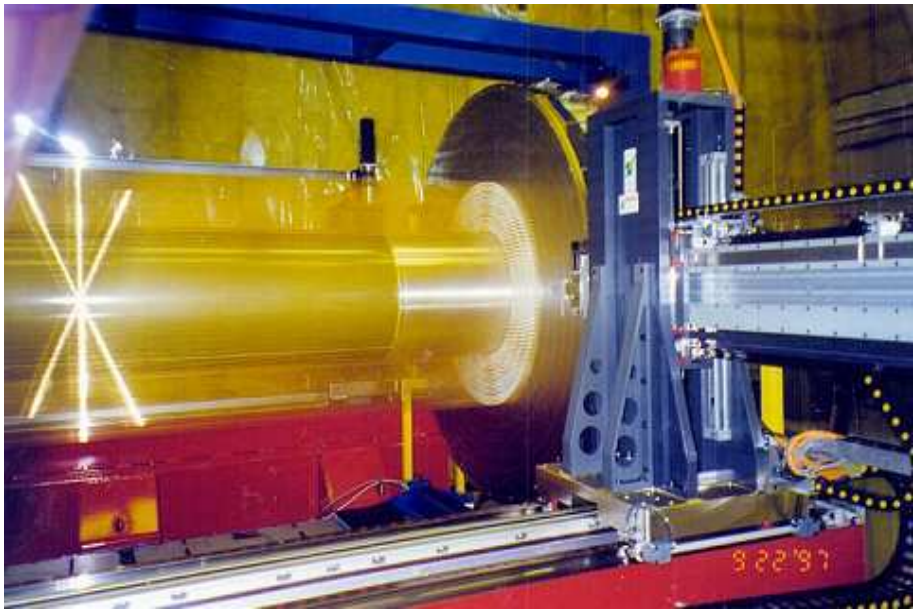

Figure 2.13: DCH wire stringing at TRIUMF (September 1997).

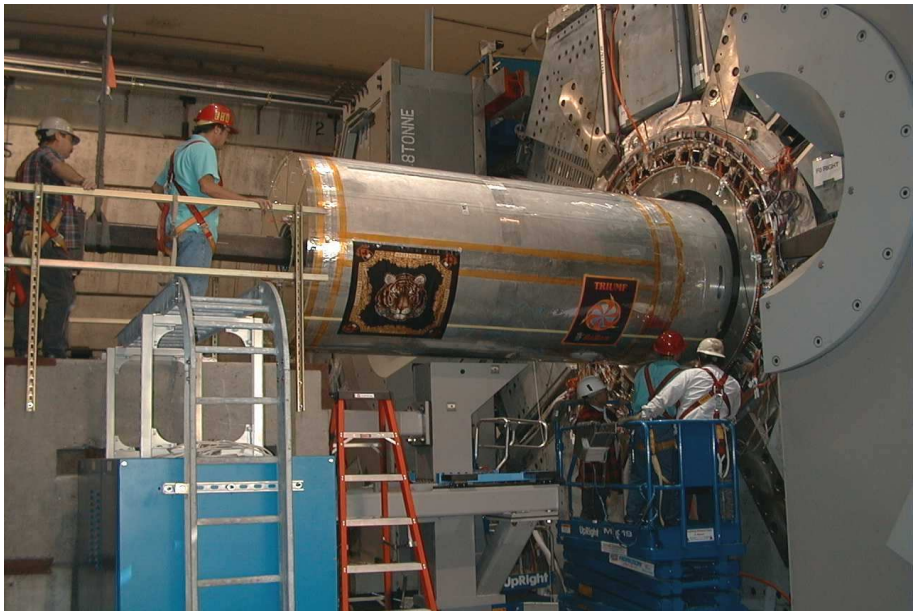

Figure 2.14: DCH installation (August 1998).

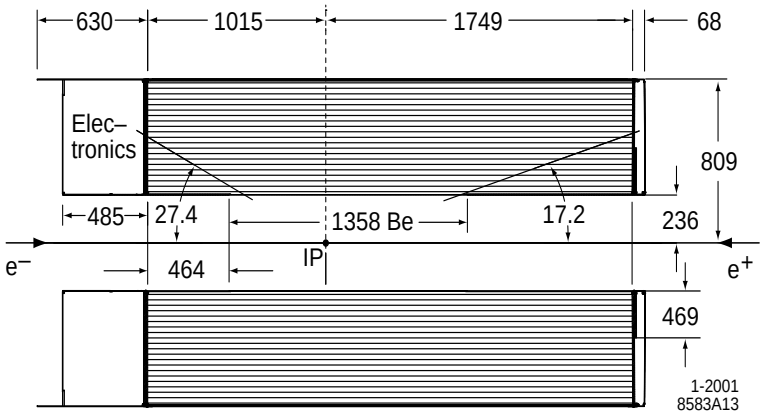

Figure 2.15: Longitudinal section of the drift chamber.

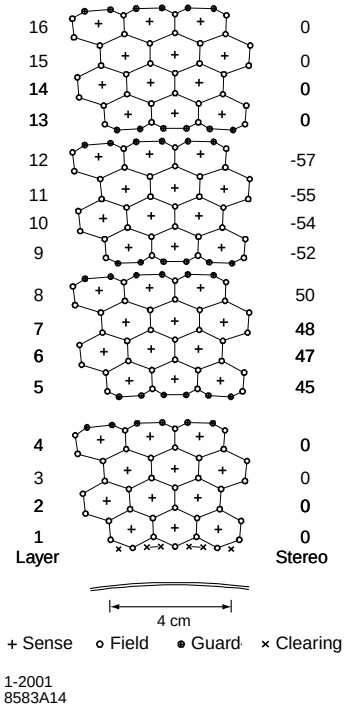

Figure 2.16: DCH cell pattern (for a section of the inner 16 [of 40] layers).

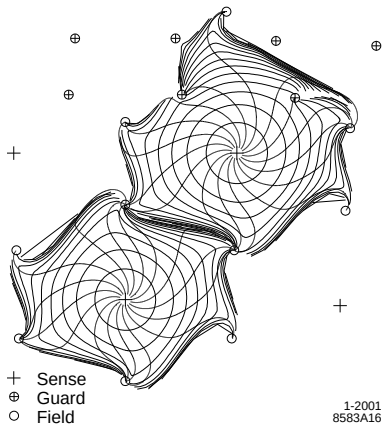

Figure 2.17: DCH cell drift isochrones for cells in layers 3 and 4 (axial). Isochrones are at 100 ns intervals.

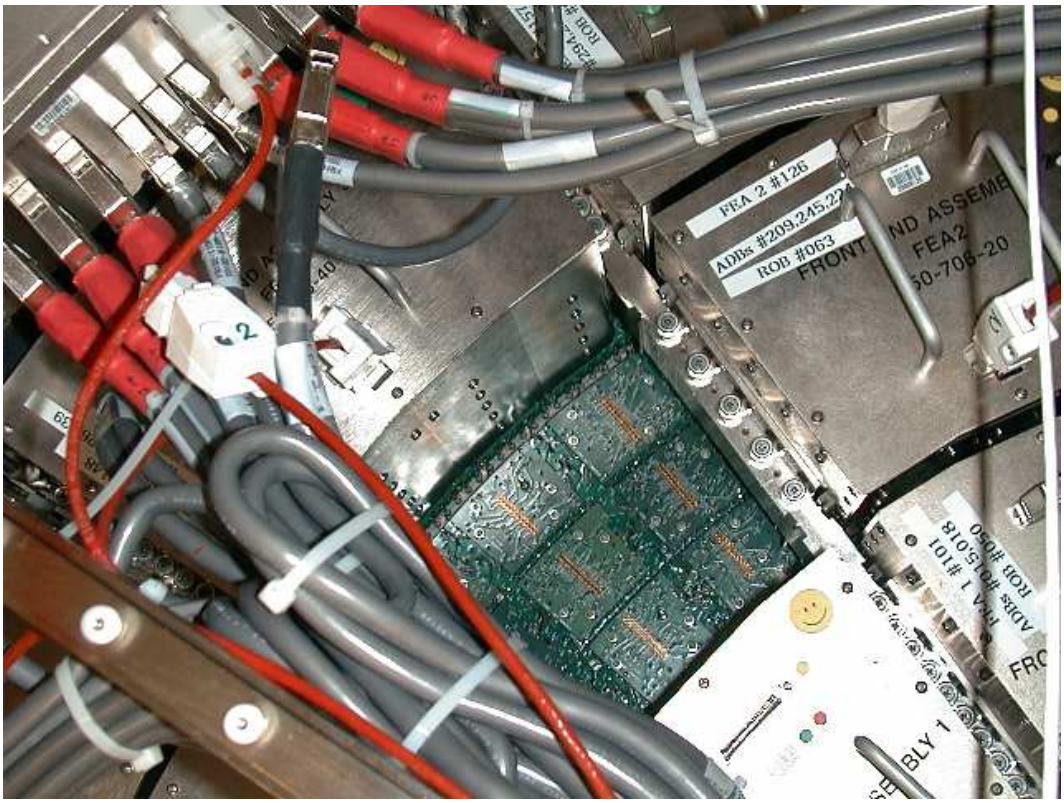

Figure 2.18: Partial view of drift chamber front-end electronics.

The endplates are 24mm thick aluminium, except for the outer 33.1 cm of the forward endplate, which is reduced to 12 cm to minimize the amount of material in front of the forward calorimeter endcap. The inner cylinder is fabricated from beryllium (to minimize the multiple scattering for the section of inner cylinder within the tracking fiducial volume) and aluminium (for the rest). The outer cylinder is 1.6 mm carbon fiber on 6 mm thick honeycomb Nomex core. The total thickness of the DCH is 1.08% X_0.

The cells are arranged in a hexagonal pattern, each with a sense wire at the center and field wires at the corners, as shown in figure 2.16. Cells on a superlayer boundary have a slightly different arrangement, with two guard wires taking the place of a single field wire. The nominal operating voltage is 1930 V. Isochrones and drift paths, calculated using the GARFIELD simulation, are shown in figure 2.17.

The DCH electronics are designed to provide accurate measurements of signal time and integrated charge (as well as providing information to the Level 1 Trigger,

see Section 2.9). Service boards plug directly onto the wire feedthroughs on the rear endplate. These boards distribute the high voltages as well as pass signal and ground to the front-end electronics assemblies. The front-end assemblies (FEAs) plug into the service boards and amplify, digitize, and buffer (for 12.9 μs) the signals. A view of the front-end electronics including (enclosed) front-end assemblies and service boards below can be seen in figure 2.18. The digital data is sent, upon receipt of a level 1 trigger accept signal, via 59.5 MHz serial link to a data I/O module which transmits the signal to the external electronics via fiber-optic cable. Extraction of hit time and integrated charge from the digital waveform takes place in the readout modules (ROMs) in external electronics.

Online calibrations of channel gain and threshold are performed daily via internal pulse generation. The data are monitored online to check for FEA or other electronics failure or for miscalibrated output. Monitoring and control of high voltage, radiation protection (using silicon PIN diodes similar to the SVT, as well as RadFETs for integrated dose measurement), the gas system, and temperature are performed, similar to other subsystems, via a slow control system based on EPICS.

Offline calibrations of the time-to-distance relation within cells, as well as of the deposited charge used for particle identification via dE/dx measurement, are performed. The time-to-distance relation is determined from two-prong events (Bhabha scattering events and dimuons) and is fit to a sixth-order Chebychev polynomial for each cell layer, with separate fits to right and left sides of wires (to account for $E \times B$ asymmetries). A correction for time-to-distance variations as a function of track entrance angle to the cell is detemined via simulation (not calibration) and added to the calibrated entrance-angle-averaged relation. The energy loss per unit length of tracks, dE/dx, contains particle type information due to the dependence of dE/dx on particle velocity (Bethe-Bloch relation), and is derived from measurements of integrated charge deposited in each cell along the track path. An overall multiplicative correction to the charge measurements due to gas pressure and temperature variations is performed once per run; additional calibrations due to variations with track entrance angle in ϕ and in θ are performed only when high-voltage settings are changed.

The design goal for the average drift distance resolution was 140 μm. An average resolution of 110 μm is achieved. The drift distance resolution as a function of drift distance can be seen from the offline monitoring plot shown in figure 2.19 (left side). Particle identification using the drift chamber provides significant information up to

high momenta, as can be seen in figure 2.19 (right side).

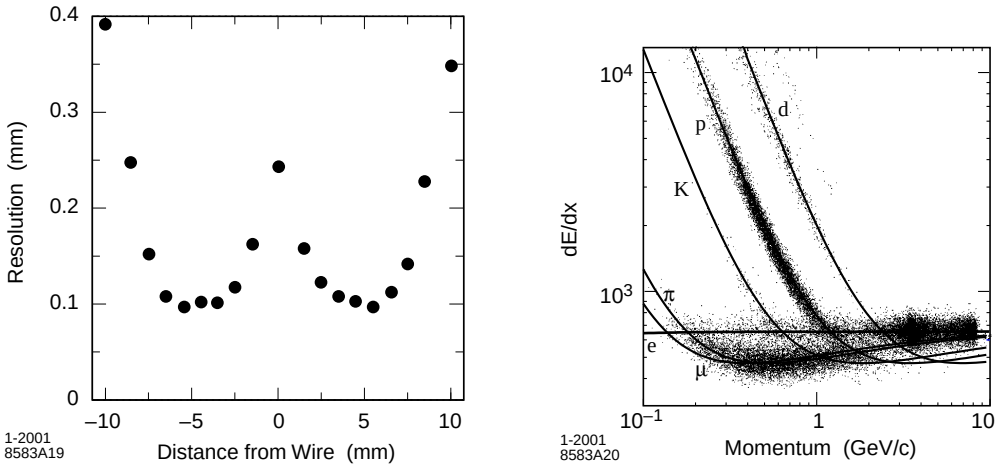

Figure 2.19: DCH drift distance resolution as a function of the drift distance in the cell (left); DCH particle identification as a function of momentum using dE/dx (right).

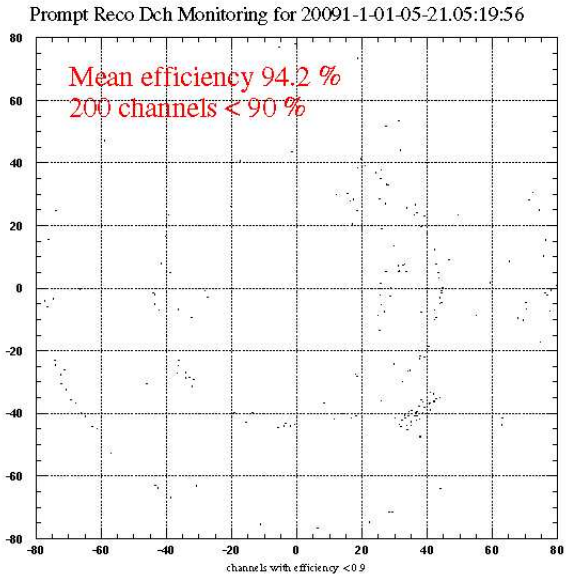

Figure 2.20: DCH channel efficiency.

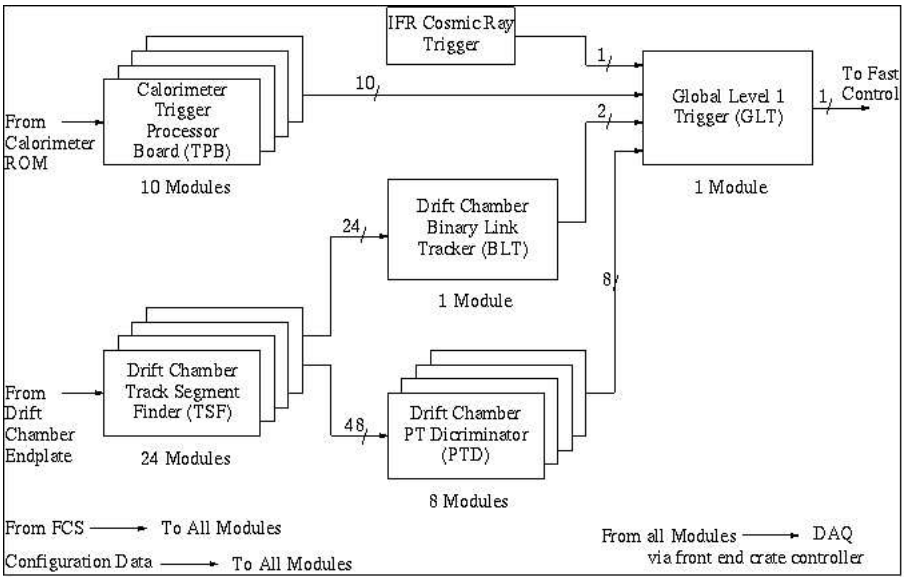

Figure 2.21: Trigger L1 scheme.

Cell-by-cell channel efficiency is also monitored; typical efficiency is 90-95%, as may be seen in figure 2.20 (including a small region damaged from a high-voltage accident early in the commissioning phase, this can be seen towards the lower right of the figure as a higher concentration of points).

2.6 The Trigger and the Tracks Reconstruction

The *BABAR* trigger needs to provide high efficiency that is well-understood and stable for physics events. Since the events which pass the trigger must be fully reconstructed in the offline event reconstruction, the output rate must be no higher than 120 Hz to satisfy computing limitations of the offline processing farm. Since events with either a DCH track or a > 100 MeV EMC cluster occur at 20 kHz, the trigger is responsible for scaling this rate down by a factor of > 150 while accepting over 99% of B events, over 95% of hadronic continuum, and over 90% of $\tau^+\tau^-$ events. It also must be flexible enough to deal with changing background conditions, as this can happen at any given time at *BABAR*, without impact on physics or increase in online dead time (which must be $< 1\%$). The *BABAR* trigger is implemented in two levels, a Level 1 hardware trigger (called L1), and a Level 3 software trigger (called L3); a Level 2 trigger is used in some other high energy particle physics experiments, but was not needed for *BABAR*.

The Level 1 trigger consists of four subsystems: the Drift Chamber Trigger (DCT)

a trigger for charged particles, the Calorimeter Trigger (EMT) for neutral particles, an IFR Trigger used for calibration and works as cosmic trigger (IFT), and global electronics for producing the final L1 accept signal (GLT stands for Global Level Trigger). The DCT and EMT receive information from the Drift Chamber and Calorimeter detectors, respectively, process it, and send condensed data to the Global Trigger. The GLT attempts to match the angular locations of calorimeter towers and drift chamber tracks, and flexibly generates Level 1 triggers and sends them on to the Fast Control and Timing system (FCTS), based on the results of the processing. The GLT also uses the IFT information to independently trigger on cosmic ray and mu-pair events. The Level 1 trigger has been upgraded since 2004 with a new DCT system which performs 3D tracking using stereo wire information from the Drift-Chamber to obtain $\sim 4cm$ resolution in track Z (along beamline) coordinates of tracks to imporve background rejection. The Level 1 trigger rates are typically 2.5 Khz at a luminosity of of $L = 8 \times 10^{33} cm^{-2} s^{-1}$. The various stages of the L1 system operate at 4Mhz to 15MHz intervals with a total L1 trigger latency of ~ 11 microseconds.

The Level 3 then analyzes the event data from the Drift-Chamber and Calorimeter sub-systems in conjunction with the L1 trigger information to further reduce background events. Besides the physics filters. L3 trigger also performs Bhabha veto, selection of various calibration events and critical general online monitoring tasks. The L3 operates on an online farm which consists of 28 Dell 1650 (dual Pentium-III 1.4 GHz) computers with fast algorithms processing at $\sim 4ms$ per event. The L1 triggers are reduced by typically a factor of ~ 10 after the L3 filtering, before logging to the data storage system

The DCT is further subdivided azimuthally into Track Segment Finders (TSF), a binary link tracker for producing tracks from the segments (BLT), and a p_t discriminator (PTD). The set of TSF modules received 7104 "hit" signals originating in the 7104 cells of the drift chamber. The search for track segment is organized in terms of pivot cells. Physically, pivot cells are the cells in the third layer, called pivot layer, of each superlayer. Each pivot cell and seven neighboring cells constitute a pivot group. Some of the cells are shared with other pivot groups, but each pivot group has one unique pivot cell (see Fig. 2.22): Each segment finder engine reeives continuous digital-discriminator signals from the eight cells of the pivot group assigned to that engine. The cells in a pivot group are numbered 0 through 7, as shown in Fig. 2.22 (cell 4 is the pivot cell). Note that if the pivot group template (the black circles in the figure)

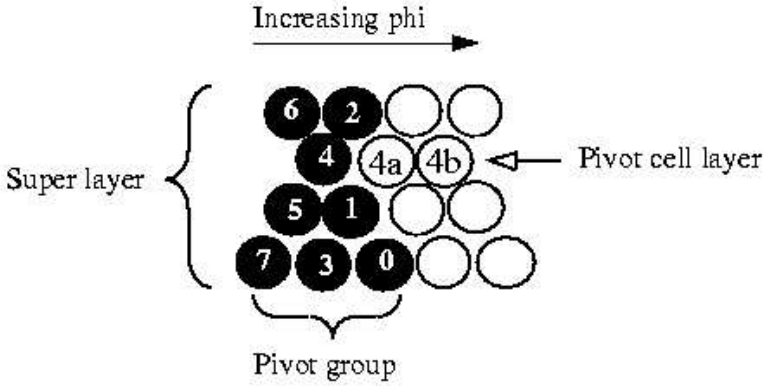

Figure 2.22: Showing the definitions of pivot cell and pivot group. Numbers indicate the cell number within a pivot group; the pivot cell is number 4. 4a and 4b indicate adjacent pivot cells.

were to move one cell to the right, a new pivot cell (cell 4a) and a new pivot group would be defined. Note also that the signals from some cells are needed for more that one engine. In particular, cells labeled “7”, “3” and “0” are associated with two other pivot groups.

The complete Segment Finder consists of 1776 track segment finder engines, one of each of the 1776 pivot cells (pivot groups). Each engine processes data from the eight cells in its assigned pivot group to find valid track segment that pass through its pivot cell and other cells in the pivot group. The engine can be programmed to require a hit in each of the four layer (4/4), or in at least three of the four layers (3/4), to accept a track segment as valid. Typically, valid segment patterns consist of hits, close together in time and in three of four layers, that could represent acceptable tracks which fall within a pre-defined range of azimuthal angles. Sets of valid segment patterns are stored in a pattern memory within each engine.

A two-bit counter is associated with each wire (cell). When a segment is hit its counters start being incremented at regular time intervals. At any given time the 16 bit pattern formed by the counters gives the segment address. A lookup table (LUT) is written to the read-out modules of each configure transition from the database. The LUT is calibrated to translate segment addresses to track ϕ position estimates and “weights”. Five bits are available for ϕ. ϕ=0 corresponds to weight 0 and values 29-31

are not used. ϕ, therefore, ranges between 1 an 28 and the integer values correspond to:

- 01-07: half of the left neighboring segment
- 08-14: left half of the segment
- 15-21: right half of the segment
- 22-28: half of the right neighboring segment

In this numbering scheme the pivot wire is at 14.5, the segment boundaries are at 7.5 and 21.5 and the neighboring pivot wires are at 0.5 and 28.5.

The weight ranges between 0 and 3. For the LUT used at the time of this writing the meaning of the weight is the following:

- 0 - pattern is not in the LUT. ϕ is set to 0.
- 1 - no ϕ to estimate for the pattern (ϕ is set to 14), or ϕ lies outside the segment.
- 2 - ϕ inside the segment.
- 3 - ϕ inside the segment, better resolution that weight 2.

L3 tracking algorithms do not use weight 0 segments. For weight 1 the pivot wire position is used as the track ϕ coordinate. For weight 2 and 3 segments integer ϕ estimates are converted to absolute track ϕ position estimates.

Considering a pattern of hits in a superlayer, all the wires in the pattern can be attributed to one TSF segment (delineated with a solid line). However, this segment shares wires with a neighboring segment (delineated with a broken line), therefore, there will be hits in two TSF segments for this pattern. Once the principal segments (typically with higher weight) have been used to find a track pattern, remaining ghost segments can form another track pattern to produce an additional "ghost" track, as may be seen in Fig.2.23

The binary link tracker (BLT) receives this information and detemines whether segments lie in a road defined by "supercells," which are sectors of a superlayer covering to 1/32 of the DCH in ϕ. Patterns of segment-containing supercells that appear to correspond to tracks (according to the BLT look-up table) are output to the L1 global trigger. In parallel with the BLT, the p_t discriminator (PTD) checks TSF segments in

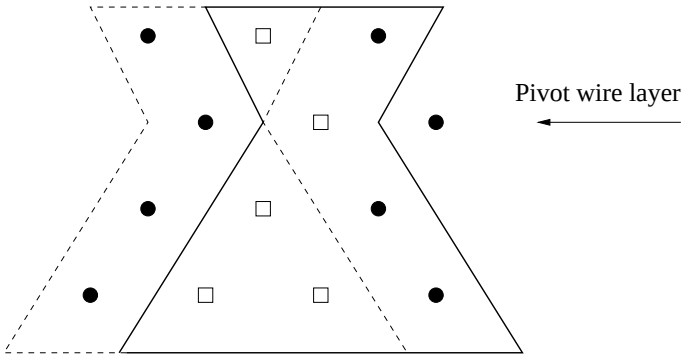

Figure 2.23: Ghost segment.

axial superlayers to see if they are consistent with a track having a greater p_t than a configurable minimum cutoff value. This information is also output to the GLT.

The level 1 calorimeter trigger (EMT) divides the EMC into 280 "towers" of 24 crystals each (22 for the endcap). All crystal energies within a tower which are above a 20 MeV threshold are summed and supplied to the EMT trigger processor boards (TPBs). The TPBs digitally filter the energy deposition (to smooth the output waveform of noise) and compare neigboring towers to look for clusters which span more than one tower. Trigger line "primitives" (bytes corresponding to trigger type and information) are output to the GLT corresponding to the energy and placement of found clusters.

The global level 1 trigger (GLT) receives the trigger line primitives from the EMT and DCT, along with information from an IFR trigger (IFT) which is used for cosmic ray and dimuon calibration purposes, and performs timing alignment to reduce jitter. The GLT does some rudimentary matching between DCT tracks and EMT clusters, and performs a logical AND of the input trigger primitives, which defines the output trigger line. The combined L1 trigger efficiency is $> 99.9\%$ for generic $B\overline{B}$events, 99% for continuum, and 94.5% for $\tau^+\tau^-$ events.

Complete reconstruction of B decays (in addition to other major *BABAR* analysis techniques, such as tagging) requires precise and efficient charged particle tracking. As will be seen later, separation of decays in these modes from combinatoric background requires precise determination of mass and energy, which in turn requires precision measurement of track momentum. The majority of other modes are just as dependent on charged particle tracking. Data from the DCH and SVT is combined to satisfy the stringent charged particle tracking requirements of *BABAR*.

Charged tracks are parametrized by the 5 variables $d_0, \phi_0, \omega, z_0, \tan\lambda$ and their

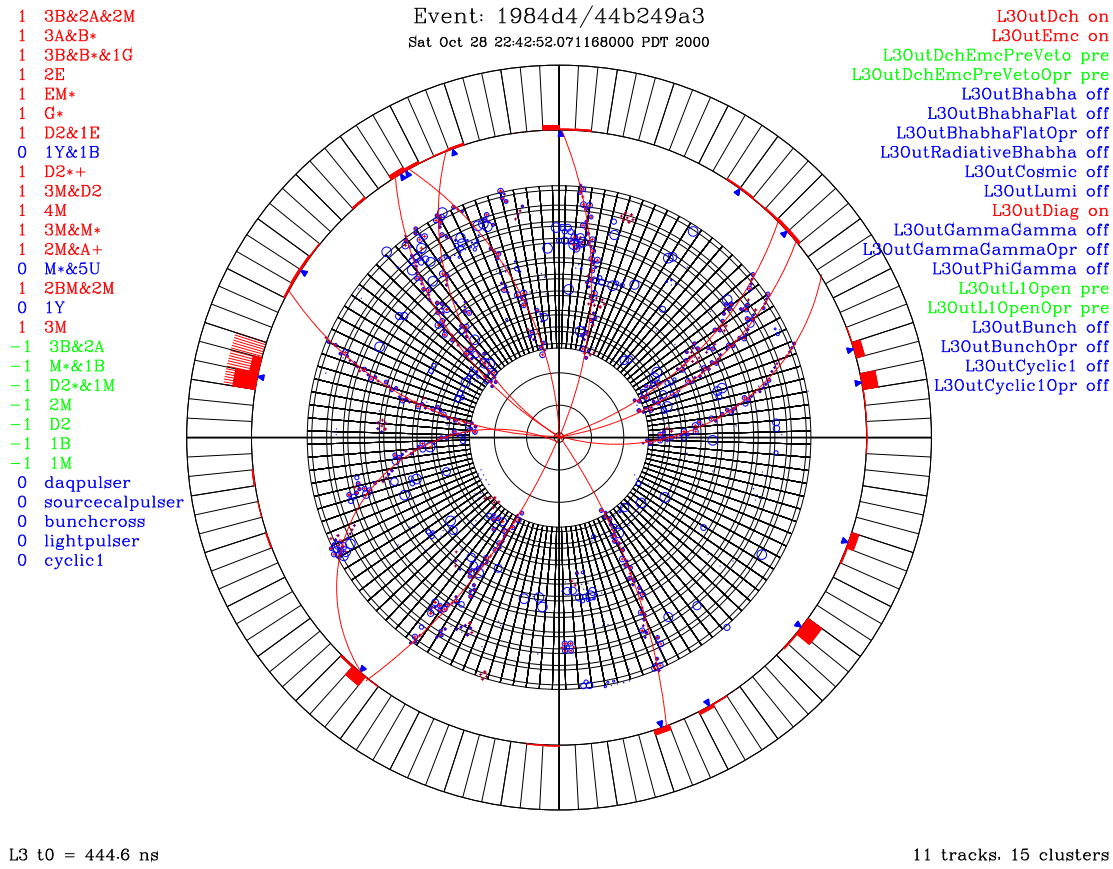

Figure 2.24: A level 3 trigger event display for a multihadron event.

error matrix. The parameters are defined as: d_0 is the distance of the track to the z-axis at the track's point of closest approach to the z-axis, z_0 is the distance along the z-axis of that point to the origin, ϕ_0 is the azimuthal angle of the track at that point, λ is the dip angle with respect to the transverse plane, and ω is the curvature of the track and is proportional to $1/p_t$. After tracks are recognized by the pattern recognition alorithms, these 5 variables are fitted, and error matrices are extracted. Offline track reconstruction begins with tracking and event time information from the L3 Trigger.

2.6.1 t_0 Reconstruction

L3 provides both tracks and an estimate of the time at which the interaction occured (with a resolution of approximately 5 ns), referred to as the t_0.[3] Reconstruction of the event interaction time, or t_0, is necessary for both fitting DCH tracks (since the DCH time-to-distance relation is necessary for position information of a track within a given cell, a time must be provided as input) and for rejecting out-of-time hits within the SVT to reduce background. t_0 reconstruction takes place in several steps, iterated with track pattern recogition since the two are interdependent, during offline reconstruction. The value of t_0 is used for drift time to drift distance conversion. The drift distances are used in track fits, therefore, t_0 finding and tracking efficiency and resolution are directly related. For example, tracks coming from the interaction point will be missed if t_0 finding latches on background hits, or a cosmics track instead. Beam background typically produces clusters of adjacent TSF segment hits. These are looked for and removed from t_0 finding. Note, that for an ioninzing particle the time-of-flight in the DCH (of order of several ns) is much smaller than typical ionization drift time (of order of $500\,\mathrm{ns}$). Only segments belonging to track patterns found in event are used for initial t_0 finding. The initial t_0 estimate is obtained by subtracting a constant value of $220\,\mathrm{ns}$ from the drift time average for all the wires in those segments. Time-of-flight is not taken into account.

If no track patterns have been found $500\,\mathrm{ns}$ is used as the initial guess, but t_0 finding will very likely fail. The initial t_0 estimate is iteratively improved. Iterations are stopped after 5 iterations or if the time estimate changes from iteration to iteration by less than $5\,\mathrm{ns}$. If t_0 finding fails on first iteration on second the initial time estimate is incremented by $200\,\mathrm{ns}$. If t_0 finding fails again on third iteration initial time estimate is decremented by $200\,\mathrm{ns}$. t_0 estimates calculated are only calculated for TSF segments in which all 4 wires (2, 3, 4, 5) or (4, 5, 6, 7) (Fig. 2.22) are hit. t_0 finding efficiency could possible be improved if other patterns are also used. Time-of-flight is crudely taken into account by assuming that the particle's flight length is equal to the radius of the pivot layer. (A better estimate of the flight length could be obtained for TSF segment belonging to tracks, by using track parameters). TSF segment time estimates are accumulated in a histogram. (Two binnings are used to avoid splitting a peak into two bins.) If no bin contains 3 entries or more -20000 is returned, otherwise the average of entries in the highest bin is returned.

[3] The e^+e^- interaction time is referred to as the "bunch t_0," often shortened to "t_0."

Inefficiency in t_0 finding for these events directly translates into tracking inefficiency. t_0 finding algorithm should be modified to use more hit configurations for segments and use associated track information, if available. This should allow to recover t_0 for most of these events. t_0 finding efficiency then could be as high as 93%.

2.7 Track fitting

Before tracks are fitted a second pass of track pattern finding is done. However, this time a fit is attempted to every track pattern found. For a successful fit hits will be removed from the hit map for the cells used in the fit. Because the hit map is cleared of hits in a different manner track patterns found in pass two will in general be different from those found in pass one.

Fitting for track parameters is done by a least squares minimization of

$$\chi^2 = \sum \left(\phi_{\text{ipt}}(k, d_0, \phi_0, t, z_0) - \phi_{\text{est}}\right)^2$$

The sum runs over DCH superlayers, ϕ_{est} are the estimates for TSF segments and ϕ_{ipt} are track intercepts that have a non-linear dependence on the track parameters. The system is solved iteratively. Given a seed track the expression for ϕ_{ipt} is linearized around seed track parameters using track intercept derivatives to obtain an easily solvable linear system. The iterations are described below.

The seed track corresponding to a track pattern is used to perform prefitting. TSF ϕ estimates are used for the prefit. d_0 and z_0 are fixed to zero and the other 3 track parameters are allowed to vary. The fitted track is used as the seed track in the next fit. Fits 1 - 4 are 5 parameter fits, each iteratively improving on the previous one. For each intercepted cell two cells to the left and two to the right are considered. The one with the ϕ estimate for TSF segment closest to the intercept is selected. Fitting fails if fewer than 6 TSF segments are available, of if for seed track $P_t < 225\,\text{MeV}$ or $|d_0| > 15\,\text{cm}$. For each layer ϕ errors are estimated and outlier hits (beyond 3 ϕ errors) are counted. If there are no outliers and 10 segments were used for the fit it is declared successful. For fit number 4 it's only required that there be no outliers.

Finally if the fit does not succeed after 4 iterations a final fit is done where segments used in fit number 4 are refitted using with the fit number 4 output used as the seed track.

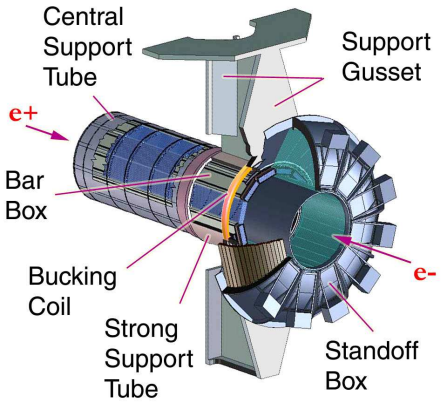

Figure 2.25: View of DIRC mechanical stucture.

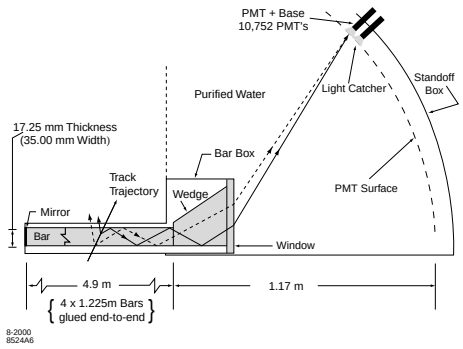

Figure 2.26: DIRC schematic showing the principle behind PID measurements. The Cerenkov angle is preserved through specular internal reflection.

The L3 tracking efficiency is about 95% above 2 GeV/c in transverse momentum, sinks to about 80% for 1 GeV/c and further down for lower transverse momenta until it reaches 0 for a transverse momentum of 180 MeV. This is the transverse momentum of a track which curls in the drift chamber.

2.8 The DIRC

BABAR has stringent requirments for $\pi - K$ separation over a large momentum range. At the lower end of the range, primarily at momenta < 1 GeV, flavor tagging using kaons from cascade decays is an efficient way of determining B flavor. At the high end of the range, reconstructing $B^0 \rightarrow \pi^+\pi^-$ and $B^0 \rightarrow K^{\pm}\pi^{\mp}$ requires separation at momenta up to 4.2 GeV in the lab frame. At intermediate energies, reducing background in charm decays such as $D^0 \rightarrow K\pi$ is necessary for $B^0 \rightarrow D\overline{D}$ reconstruction. The particle identification device must exhibit sufficient $\pi - K$ separation throughout this wide range of momentum with a minimum of material in order to avoid adversely impacting calorimeter resolution.

The DIRC (Detector of Internally Reflected Cerenkov light) principle uses internal reflection within quartz bars to propagate Cerenkov light to readout phototubes while preserving the Cerenkov angle. This requires extremely flat surfaces in order to avoid

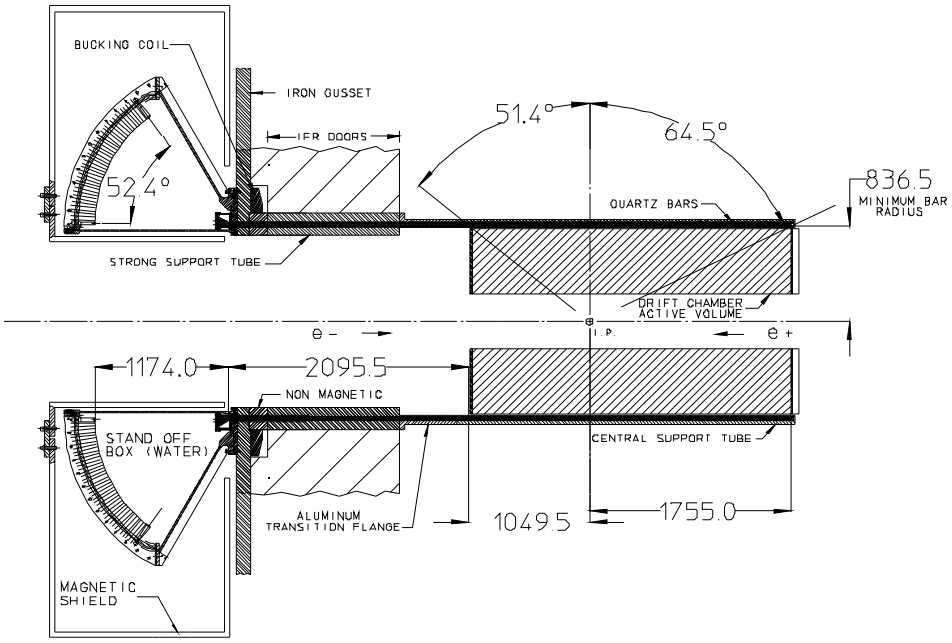

Figure 2.27: Longitudinal section of the DIRC. Length units are mm.

dispersing the reflected angles. Fused, synthetic silica quartz is used due to the excellent optical surface it allows through polishing, as well as other favorable properties such as long attenuation length, low chromatic dispersion, small radiation length, and radiation hardness. As shown in figure 2.26, the light is internally reflected down to a wedge to reflect photons into a water-filled "standoff box." The standoff box is enclosed by an array of 10752 photomultiplier tubes, which are each 29 mm. in diameter. The Cerenkov light from a particle passing through the DIRC forms a ring (essentially a conic section) imaged on the phototubes. The opening angle of this conic section contains information on particle type via the typical relation $\cos\theta_c = 1/n\beta$, with β being the particle velocity normalized to the speed of light, and n being the mean index of refraction (= 1.473 for fused silica).

Both efficiency and the timing of the electronics are critical for DIRC performance. Timing is critical for two reasons: one, for background hit rejection, resolving ambiguities, and separation of hits from differing tracks within an event; and two, timing gives information on the photon propagation angles, allowing an independent measurement of the Cerenkov angle. The intrinsic timing resolution of the PMTs is limited to 1.5 ns by transit time spread. Data from the phototubes is read out to front-end electronics, which performs the amplification, digitization, and buffering. Reduction of data from

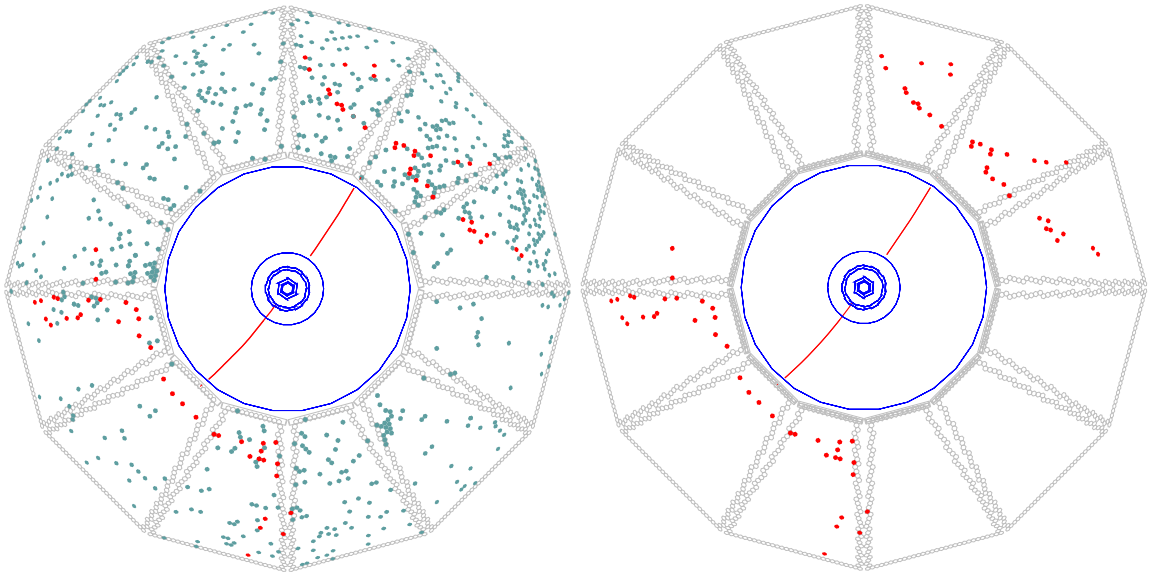

Figure 2.28: Display of an $e^+e^- \rightarrow \mu^+\mu^-$ event reconstructed in *BABAR* with two different time cuts. On the left, all DIRC PMTs with signals within the $\pm$300 ns trigger window are shown. On the right, only those PMTs with signals within 8 ns of the expected Cherenkov photon arrival time are displayed.

out-of-time or noisy PMTs is performed in in the external electronics and reduces the data volume by 50% using rough timing cuts. Online calibration of PMT efficiency, timing response, and electronics delays uses a light pulser system which generates precise 1 ns flashes from blue LEDs inside the SOB.

The DIRC has performed well throughout *BABAR*'s operational lifetime: 99.7% of PMTs are operating with design performance. The measured time resolution is 1.7 ns, very close to the intrinsic resolution of the PMTs. The Cerenkov angle resolution for dimuon events is 2.5 mrad, close to the design goal of 2.2 mrad. This results in $\pi - K$ separation at 3 GeV of 4.2σ. The mean kaon selection efficiency and pion misidentification for a "loose" selection are 96.2% and 2.1% respectively, as can be seen in figure 2.29. This results in dramatic background rejection with little signal loss for charm reconstruction, as may be seen in figure 2.30.

2.9 The Electromagnetic Calorimeter (EMC)

The design parameters for the *BABAR* EMC are driven by the requirements of precisely measuring energies over a spectrum from 20 MeV to 9 GeV in a 1.5 T magnetic field

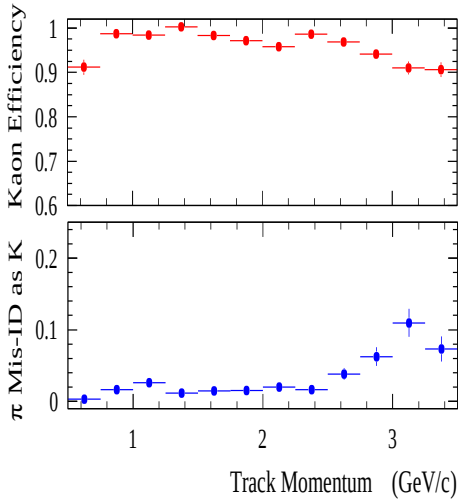

Figure 2.29: Kaon selection efficiency and misidentification probabilities as a function of momentum.

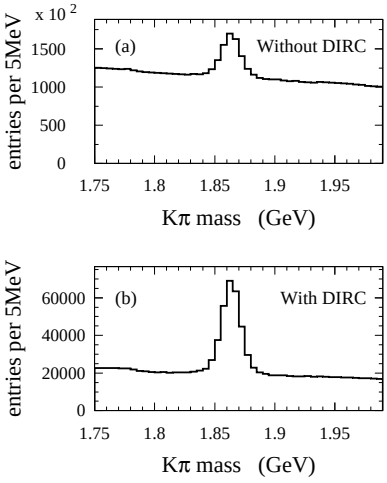

Figure 2.30: Inclusive $K\pi$ invarant mass spectrum (a) without and (b) with the use of the DIRC for kaon identification.

and a high radiation environment. At the high end of the spectrum, measurements of QED processes such as Bhabha and two-photon scattering, as well as (at slightly lower energies) photons from the critical physics processes $B^0 \rightarrow \pi^0\pi^0$ and $B^0 \rightarrow K^*\gamma$ decays, present the motivating incentive. The need for efficient detection of photons from high multiplicity B decays containing π^0's determines the requirement for the low end of the spectrum. *BABAR* uses a thallium-doped cesium iodide (CsI(Tl)) crystal calorimeter in order to achieve the necessary energy and angular resolution to meet these physics requirements.

The EMC contains a cylindrical barrel and a conical endcap containing a total of 6580 CsI(Tl) crystals. The crystals have nearly square front and rear faces with a trapezoidal longitudinal cross-section. They range in length from 29.6 to 32.4 cm with a typical front face dimension of 4.7 x 4.7 cm. A diagram can be seen in figure 2.31. The crystals are mounted in thin (300 μm) carbon-fiber composite housings which are mounted on an aluminium strong-back (see figure 2.32). Although light incident on the crystal boundary is internally reflected, the small part that is emitted is reflected back with a coating of white reflective TYVEK on the outer surface. Surrounding that are thin layers of aluminium and mylar to act as RF shielding and electrical insulation respectively. On the rear face of the crystal, two 1 cm^2 silicon PIN diodes with quantum efficiency of 85% for CsI(Tl) scintillation light are mounted via transparent

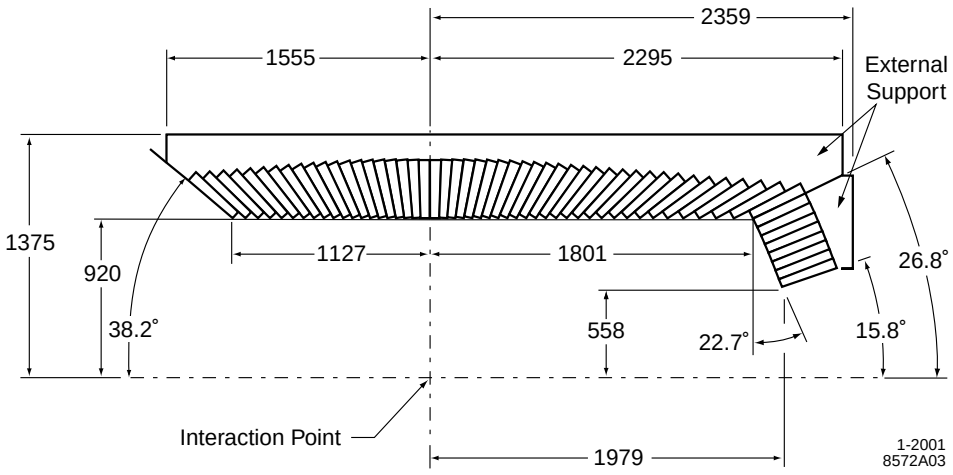

Figure 2.31: Longitudinal section of the EMC. Length units are mm.

polystyrene substrate.

Each diode is connected to a low-noise preamplifier which shapes and amplifies the signal by a factor between 1 and 32. The signal is then transmitted to mini-crates at the end of the barrel (see figure 2.32) where a digitization CARE ("custom auto-range encoding") chip provides an additional variable amplification factor. Unlike other subsystems (except for the IFR), the EMC does not buffer the data on front-end electronics; rather it outputs the full digital datastream to the read-out modules in external electronics, which perform, on receipt of a level 1 accept signal, a parabolic fit to the digitally filtered datastream to derive energy and time measurements.

A variety of online calibrations and checks is performed, including a neutron source which produces a monoenergetic 6.13 MeV calibration signal and a xenon flash light pulser system. Offline energy calibrations are necessary for higher energy corrections. The relation between polar angle and energy of Bhabha and radiative Bhabha scattering events is used to calibrate the 0.8-9 GeV range. The middle range is covered by π^0 calibration, which constrains the mass of a sample of π^0's to the known value, extracting correction coefficients.

The clustering pattern recognition uses a seed crystal algorithm to establish energy clusters. Local energy maxima within a cluster are used (if there are more than 1) to separate the cluster into bumps. Charged particle tracks are associated with bumps using a χ^2 consistency cut. In an average hadronic event, 15.8 clusters are detected, of which 10.2 are not associated to a track.

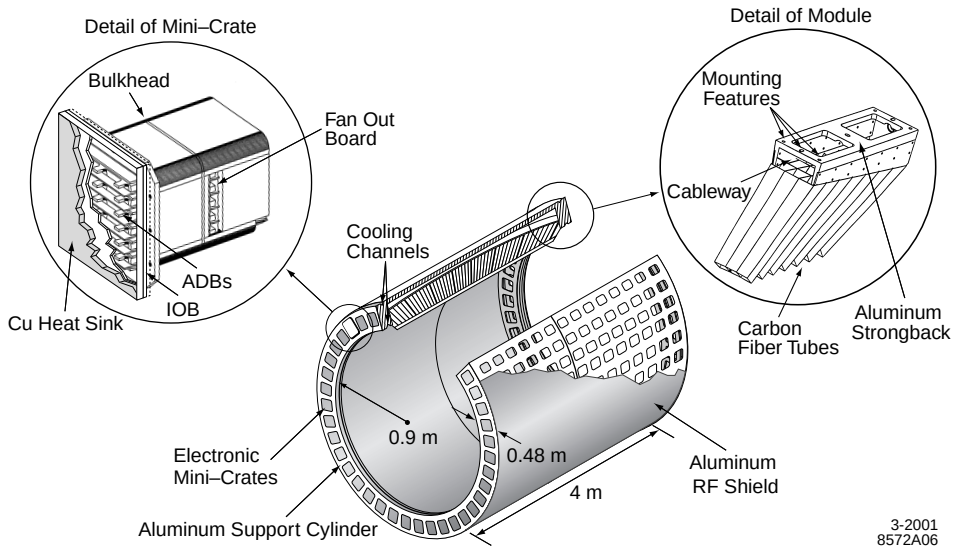

Figure 2.32: The EMC barrel support structure, modules, and mini-crates.

Energy resolution is determined using $ChitoJpsig$ and Bhabha scattering events to be

$$\frac{\sigma_E}{E} = \frac{(2.32 \pm 0.30)\%}{\sqrt[4]{E(\,\mathrm{GeV})}} \oplus (1.85 \pm 0.12)\% \tag{2.1}$$

and angular resolution is determined using π^0 and η decays to be

$$\left(\frac{3.87 \pm 0.07}{\sqrt{E(\,\mathrm{GeV})}} + 0.00 \pm 0.04 \right) \text{mrad.} \tag{2.2}$$

As can be seen in figure 2.33, the reconstructed π^0 average width is 6.9 MeV. The separation of electrons from charged hadrons using the ratio of shower energy to track momentum (E/p) and other variables may be seen in figure 2.34:

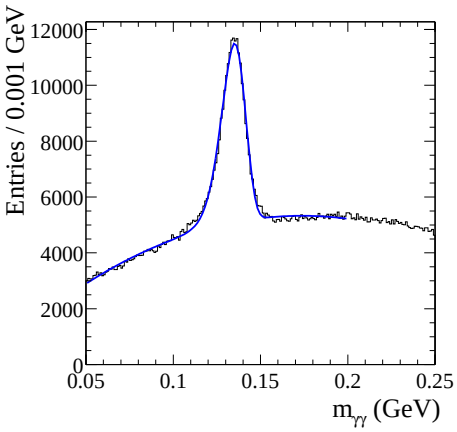

Figure 2.33: Two photon invariant mass, using photons between 30 and 300 MeV.

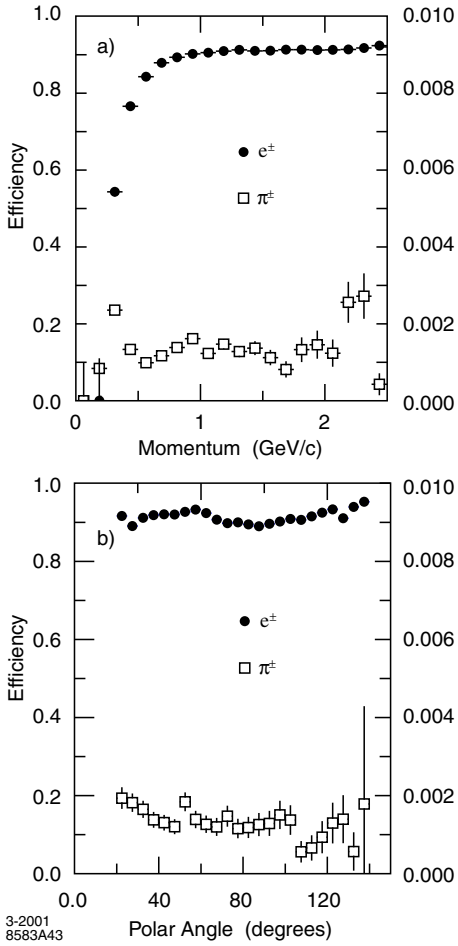

Figure 2.34: Electron efficiency and misidentification as a function of (a) momentum, and (b) polar angle.

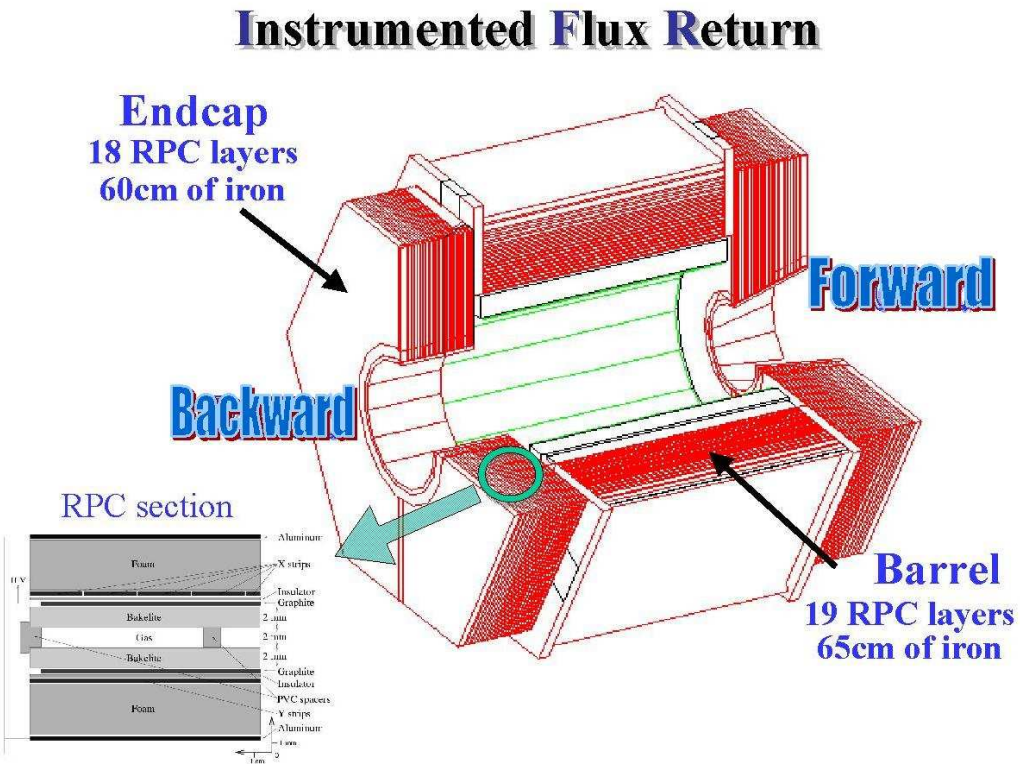

Figure 2.35: The instrumented flux return modules, structure, and RPCs.

2.10 The Instrumented Flux Return (IFR)

Detection of neutral hadrons (primarily K_L^0's) and muons is necessary for several *BABAR* analyses and analysis techniques. Muons provide a very clean B flavor tag, extremely useful for increased efficiency in tagging the opposite-side B for time-dependent CP violation measurements. Muons are also necessary for reconstructing $J/\psi \rightarrow \mu^+\mu^-$, as well as for measuring semileptonic branching fractions, required for extracting magnitudes of CKM elements. K_L^0 reconstruction is critical for the $B^0 \rightarrow J/\psi\, K_L^0$ channel. Initially, *BABAR* used an Instrumented Flux Return (IFR) composed of layers of resistive plate chambers (RPCs) and steel plates in order to provide enough material to separate pions and kaons from muons and to efficiently detect the presence and position of both μ and K_L^0 over a large solid angle. As shown in figure 2.35, the IFR consists of layers of planar RPCs in a barrel and endcap (red lines) as well as 2 layers of cylindrical RPCs (green lines) between the EMC and the magnet. Between the RPC layers are steel plates of thickness varying between 2 cm (inner plates) to 10 cm (outer plates). The total mass of the IFR is 870 metric tons. Planar

RPCs contain a 2 mm Bakelite gap with $\sim$ 8 kV across it. Ionizing particles which cross the gap create streamers of ions and electrons in the gas mixture (which is typically 56.7% Argon, 38.8% Freon, and 4.5% isobutane) which in turn creates signals via capacitive coupling on the "x-strips" and "y-strips" on opposite sides of the RPC. Strip width varies between 16 mm and 38.5 mm. The 2 mm gap is kept constant using polycarbonate spacers spread at 10 cm intervals and glued to the Bakelite. The Bakelite surface is smoothed with an application of linseed oil. Cylindrical RPCs are composed of a special thin and flexible plastic, rather than Bakelite, and have no linseed oil or other surface treatment. They are laminated to cylindrical fiberglass boards. In 2003 they decided to replace the present RPCs in the gap of the *BABAR* IFR with plastic Limited Streamer Tubes (LST). After testing, they were persuaded that LST's are the most straightforward, practical and reliable detectors among the various options to instrument the barrel region, access to which has been and will be continue to be difficult and in some cases impossible. A "standard" LST configuration consists of a silver plated wire 100 μm in diameter, located at the centre of a cell 9x9mm^2 section. A plastic (PVC) extruded structure, or "profile", contains 8 such cells, open on one side 2.36.

The profile is coated with a resistive layer of graphite, having a typical surface resistivity between 0.2 and 1 MΩ/square. The profiles, coated with graphite and strung with wires, are inserted in plastic tubes ("sleeves") of matching dimensions for gas containment. The signals for the measurement of one coordinate can be read directly from the wires, but it has become customary instead to read both coordinates with strip planes, thereby avoiding the complications of feedthroughs and DC-blocking capacitors. For such tubes the operating voltage is typically 4.7kV; the efficiency plateaus are at least 200V wide; the signals on the wire are of the order of 200/300mV (into 50Ω), typically 50ns at the base, sometimes with an afterpulse. The gas mixtures are strongly quenching: the original one (25% Ar, 75% n-pentane) being explosive has been replaced in accelerator use by a non-flammable one based on CO_2.

The LST geometrical efficiency is limited by the ratio of active versus total volume in the cell. The effect is mitigated by the fact that most tracks do not impinge perpendicularly. In the gap between iron slabs is wide enough, the inefficiency can be greatly reduced by using larger cells or, alternatively, a double-layer geometry.

The LST tubes are somewhat fragile mechanically so careful design, handling, and operation are of paramount importance in preventing failures. The "mortality" of the

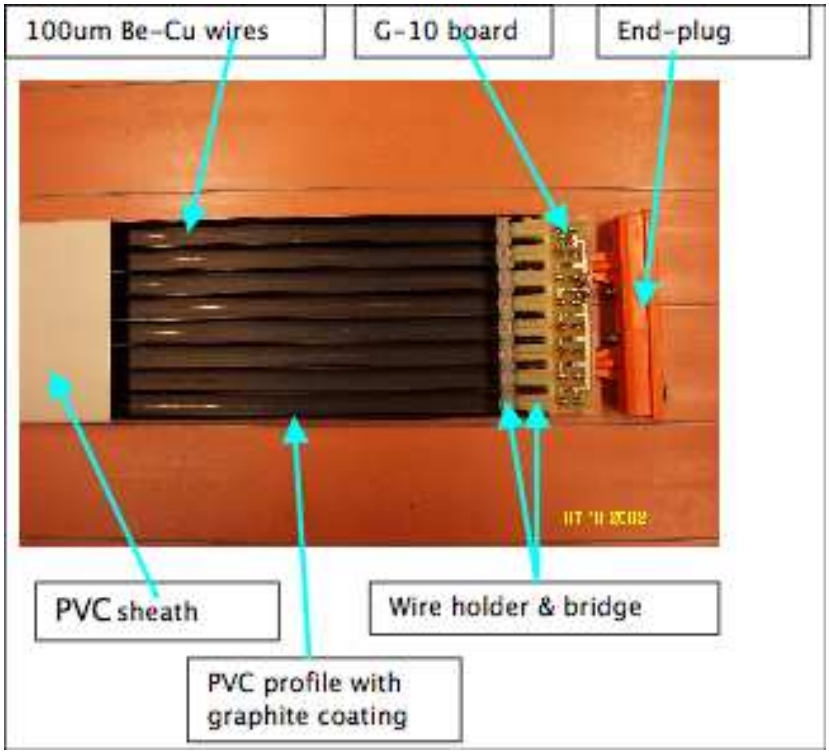

Figure 2.36: Photo of a standard LST, partially inserted in the sleeves

LST's depends on the cell size, on the care and attention given during construction and installation, and on the strictness of the acceptance tests. If we consider the performance isses, we have:

- minimize dead spaces. These include the profile walls, separation between tubes, dead areas at the tube ends, both inside the sleeves and outside, for electronics, gas and cabling

- reduce tube mortality and/or introduce redundancy to decrease its effect on detector efficiency

- arrange tubes into modules that can be extracted and replaced without removing corner pieces

- feed each tube with one or more independent HV channels

- locate HV distribution boxes and front end electronics on the outside of the detector to avoid having to doors to repair.

The cell efficiency was studied by a simple Monte Carlo simulation, reproducing tracks going through standard-cell LST and it's esistimated around 5-10%. Results from measurements made with cosmic rays on stardard tubes and on the first batch of double layer prototypes are consistent with these numbers. In addition the overall efficiency of the detector depends on the dead space at both ends of the LST and in between the LST.

Instead of recycling the existing IFR Front End Cards (FEC), it has been decided to build a new FEC. The new FEC's have a different input section but with the same interface to the existing IFR-FIFO boards, which is used for the readout of the LST's and are well integrated in the *BABAR* Data Acquisition (DAQ). The data format will be the same as it was in the RPC system. This choice allows us to use the present DAQ software and electronics also with the LST system. Compared to the old FEC's, two new functions are provided: front-end amplification and a settable threshold. The electronics is located just outside the detector in a set of 12 crates. The new system will be based on boards which serve 64 channels: 4 input connectors, 64 amplifiers and comparators, and a Field Programmable Gate Array (FPGA) which will contain all the digital logic (delay, gate with the trigger, latch) for the 64 channels. The baseline plan is to route the utilities (gas, HV) to the detector layers of a sextant, as well as

the signals from the z cathode strip planes thorughout 2 dedicated conduits located at the backward end of each sextant. The Φ-strip signals will be routed throughout 2 dedicated conduits located at the forward end of each sextant. The baseline plan includes suitable fixtures to the LST endplugs to help in an orderly routing of the utilities and the signal cables at the detector layer. These structures will occupy about 8cm at the backward end and 3cm at the forward end.

Reconstruction of clusters proceeds via two methods: a standalone method where groups of hits along 1 dimension within a module are joined to form one-dimensional clusters, which are then combined with opposite-side hits to form two-dimensional clusters, and then with other modules to form 3D clusters; and a "swimmer" method, where charged tracks are propagated to the IFR — 1D clusters within 12 cm. of the expected path are combined to form 2D or 3D clusters. Clusters which are not matched to a charged track are considered as neutral clusters. Muon identification uses variables such as number of expected vs. actual interaction lengths tranversed and the χ^2 match to the charged track.

Chapter 3

BaBar software

3.1 Introduction

In this and in the following chapters will be presented framework and software tools used during this thesis work. This section includes a presentation of the simulation and the reconstruction programs used in *BABAR* collaboration.

The system includes two parts: *online* system (data acquisition, checking and monitoring) and *offline* system (reconstruction, simulation and data analysis). It is implemented on PC with commercial Unix operative systems (SunOS e OSF/1) and Linux.

3.2 Programming choices

In the *BABAR* experiment it is used a software developped using *Object Oriented* programming implemented on Unix machines.

We have a big choice in using object oriented codes [17]; among all possibilities, in *BABAR* collaboration C++ has been choosen for its specific demands: for example, large disponibility for compilers, distributed with free open-source licenses, compatibility with different platforms, efficiency of the code and tools for development and debugging and large disponibility of libraries.

3.2.1 Object oriented programming

The main feature of object oriented coding can be simplified through a analogy with real world: utilization of an object is not linked to knowledge, for an user, of its internal

operation. For example, to drive a car we hadn't to know how engine is and how it functions, but this (substantial) difference doesn't influence our driving.

This is an example of separation between *what* an object offers in functionality terms and *how* it realizes this functionality; the way to interface with an user should be costant in the time, but system can be modified, expanded and optimized. This feature is fundamental in complex software system codes, as used in *BABAR*.

In C++, tool that allows us to use object oriented programming is *class*, data types defined by programmer; they are composed of a public interface that give us functions to operate on contained data, and a hidden, private, structure that tipically includes both internal data representation and utility functions to operate on themselves. This way to hide effective implementation is called *encapsulation* and it's tipical for object oriented programming.

So, classes can be thought as boxes that speak each other with messages: we can operate on data for a class (that is most the interesting thing for an user) only through some function in public interface; these functions are called *methods*.

Such a way to operate can give us some advantages cause we can shield data from illegal operations and verify finished operations (verification on variation interval of a quantity, as in data input stage). Much more, it allows a re-utilization of the code (for example, a classes set to operate on vectors and matrices with usual addition, product and convolution operations etc.) and it reduces the development and software debugging times.

Another object oriented feature is objects hierarchy, illustrable with a real world example: it's possible to define some abstract data types with certain very general properties; in fact we are able to think to abstract objects, like a particle, and derive from these ones other objects with more definite properties, "boson or fermion?". Continuing in this hierarchy, we can specify more detailed properties, "if fermion: lepton or quark?" and reach up for more internal levels maintaining general class properties, leaving them as before or modifying parts of them. This feature is called *heredity* and we can have single heredity (if it derived by only one more general class) or multiple heredity (if derived by more classes).

Polymorphism is a concept strictly linked to heredity: it is the language ability to use some specific objects (derived by more or less generic classes) as if they were like generic class objects: for example, I could want a list with all particles with a fixed momentum, independently if they are bosons or leptons, and I'd want to use them in a

uniform way (for a fixed particles class definition).

3.3 Object oriented database

Recently, *BABAR*'s data storage has changed to a completely new system. The new model is called *CM2* ("Computing Model 2").

The original *BABAR* Event Store used two data-storage formats. The *Objectivity* database was a large object-oriented database with several levels of detail stored for each event. It could be used for almost any analysis or detector study. *Kanga* ("Kind ANd Gentler Analysis") datasets stored only the micro (see below) level information in ROOT-type files (architecture for object oriented data analysis developped by CERN) [18]. This is the level of detail required for most physics analysis jobs, and avoided the complication of interacting the full Objectivity database and the complications that often arose with it. The idea was to have Objectivity as the main database, and use Kanga files at remote sites.

The Objectivity database had four levels of detail: *raw*, *reco*, *micro* and *nano* (or "tag"). *Raw* and *reco* were very big databases that kept virtually all of the details from every event. *Micro* was a smaller, more user-friendly database that kept only information likely to be useful for physics analyses, rather than detector studies, or more refined analysis tasks. *Nano* ("tag") contained even less detail, and was used only to skim data for a few given key characteristics to save loading in the whole event information for each event (a time-consuming process). The original idea was to keep *raw* and *reco* information for jobs like detector studies. *Raw* and *reco* were infrequently used, and only a small part of the information was ever accessed.

The new CM2 Event Store has just one database, the *Mini*. The *Mini* database is basically an extended version of the *micro*, however with the additional capability to store information written into "skims" by users ("user data", see below). The *Mini* contains all of the information from the old *Micro* database, plus the small part of *Raw* and *Reco*. The new data storage format is more like *Kanga* than anything else, so we may refer to the CM2 Mini database as "CM2 Kanga," "new Kanga" or (since old-kanga is obsolete) just "kanga". Another difference between the CM2 Mini and the old database system is that the CM2 Mini allows for the storage of "user data": user-defined composite candidate lists and user-calculated quantities.

Here's a summary table of the differences between the old Objectivity/Kanga sys-

tem and the new CM2/Mini system:

	Old Objectivity/Kanga	New CM2/Mini/Kanga
Level of detail	Objectivity: high detail Old Kanga: low detail	Mini: intermediate detail
Portability	Objectivity: central Old Kanga: portable	Mini: central, but easily skimmed to make portable collections
User data	Objectivity: None (central database) Old Kanga: Lots (small, user-defined collections)	Mini: some user data in central database

Table 3.1: Differences between the old system and CM2.

3.4 Code organization

BABAR software is accessible to all registered users through NFS system file (*Networked File System*) or AFS (*Andrew File System*), mounted on every UNIX workstation at SLAC.

The scheme is replied in all calculus labs in the countries that collaborate in this experiment: USA, France, England, Italy and Germany.

Analysis presented in this thesis work has been developped only on SLAC PCs.

3.4.1 BaBar Framework

BABAR software is organized like a framework for the event reconstruction coming from detector. For example to figure out what programming inside a framework means, it's possible to compare it with reality: in every home we find water, electricity, telephones, etc. and these services are supplied without worrying about how they realized them.

In software engineering, a framework supplies base services as I/O, graphic management, data scheme management. The obvious advantage is: low-level function problems have already been solved and generally in a very efficient way with few faults. So, the user can only work in his specific domain; in this way, it is favoured a re-use of a work (a well written code can so be re-used to solve similar problems even if not identical). A drawback can be operating inside the framework, but this stiffness can be considered not significant if framework has been planned cunningly.

3.4.2 Package

BABAR software is completely modular, and his base element is the *package*, defined as a classes set planned to solve certain exact problems very closer among them (for example a selectors package, or planned classes that assign a specific identity to a candidate particle). In every package we can find classes with same tasks, that differ for chosen approach or chosen operative tecnique. Many dozen of packages are avalaible, to cover a large spectrum of possibilities and requests coming from reconstruction and event analysis.

3.4.3 Release

We define *release* the set of all packages, each defined in his specific version. Like packages are updated with new classes added, releases are updated with new packages. Particularly, we can divide release in two parts: ones with a testing function for code implementation and ones considered stable, used for official analyses.

For this work it has been used the official stable release tagged with 12.5.2 (so called `analysis-21`), using Linux 7.2 platforms.

3.4.4 Module

BABAR framework base unity is defined as *module* and it can be or a package class or a user defined class based on other packages classes. The modules hold code that draws data from every event, runs specific algorithms and it can eventually give back results in the event in a such way that they can be used in next phases.

An executable analysis program is formed by one or more compiled and linked modules; each of them can be enabled or disabled during execution if it is useful in data processing.

Framework functionality management is left to TCL (*Tool Command Language*) language that has two features: it can interpret and so it can be an interface among user and framework, and for that, it can be used as a scripting language to check exactly the operations for every module, in a similar way with a Unix shell. It can be used on many platforms and it is a big advantage.

Modules can be added in a *sequence* in which they are executed in apparition order. Modules and sequences can be combined in a *path*, completed sequences start with an input module and finish with an output module.

The presence of particular filter modules can allow that a path will be finished before exiting and so a processed event won't reach output module. Multiple paths can be specified and each of them can be enabled or disabled.

3.5 Online system

BABAR Online software comprehend detector check and monitoring systems, processes related to data flow from front-end electronics to storaging in database or run checking programs. These tasks are solved by main Online system components: *Data Flow*,

Run Control, *Online Event Processing* (OEP) and *Prompt Reconstruction*. Another component exists, *Detector Control*, and it's not joined to event: it checks software and hardware detector components (for example DCH high tension system).

3.5.1 Online Data Flow (ODF)

Data acquisition system has a software and a hardware component; first one is called *Data Flow* while the hardware one is called *Platform*. Often, we refer to both of them as *BABAR Data Flow* [19].

Data Flow has task of joining all the data coming from front-end electronics, processing them in a preliminar way (so called *feature-extraction*) and delivering them to OEP.

Main platform elements are: checking masters that form trigger interface and distribute clock and command system, read-out modules (ROM), particular modules that catch data from front-end electronics and execute feature-extraction, and *bulk data fabric* that transport data inside-outside the platform.

Every platform needs a clock and an external trigger system; it has 32 input lines for the trigger that produce level 1 trigger acceptance signal (L1 accept) and then it propagates overall the platform. A platform can manage electronics for more than one sub-detector and they are able to operate independently, can't be independent because they are on a same platform. To maximize resources, such platforms are *partitioned*: in this way operations related to different detectors are done in parallel.

Data Flow platform has been drawn considering rigorous conditions due to experiment for dimensions and events frequency.

Components are organized in a hierarchy that permits to execute operations with a high-grade of parallelism.

3.5.2 Online Event Processing (OEP)

OEP receives completed events from Data Flow's Event Builder, executes level 3 trigger algorithms, checks data quality through so called *Fast Monitoring processes* and develops other tasks as supporting functions to calibration activities. Furthermore, OEP allows avalaible events for the reconstruction to *Prompt Reconstruction*.

Work done by OEP is distributed among knots of a farm composed by Unix machines. On every machine are solved identical processes parallelly.

3.5.3 Prompt Reconstruction

Prompt Reconstruction task is to reconstruct, in short times, all events that passed level 3 trigger filter, to furnish calibration constraints and informations on data quality. This allows us to diagnose immediately detector problems in such a way that they can be solved without losing integrated luminosity. This function has been specially important in the preliminar phases of the experiment. Many calibration constraints, like pedestals and electronics component gain, are evaluated through special runs, others, like DCH time-distance relationship and relative corrections of alignment between chamber and vertex detector, need a large number of reconstructed events. Prompt Reconstruction receives these quantities from a previous (but recent) dataset and applies to current data. Generated constraints by every reconstructed events block are storaged in Condition Database to be read again during following reconstruction block.

The Prompt Reconstruction results are monitored by *Prompt Monitoring* that checks for example chamber performances, data quality and reconstruction and calibration algorithms of reconstruction. Unlike Fast Monitoring, Prompt Monitoring analyzes reconstucted events and has a large numbers of informations on tracks.

3.6 Simulation

Completed simulation of the detector is formed by three parts: events generation, particles tracing through the detector and detector reply simulation.

3.6.1 Generators

Simulation process starts with event generation, using one of available different generators, of $B\overline{B}$ events with the corresponding decay channels, $q\overline{q}$ with $q = u$, d, s, c background events, e^+e^- diffusion events, and other backgrounds linked with accelerator operation. Furthermore, energies beams and interaction point position smearing are simulated; for each beam is used a single gaussian with width 5.5 MeV for the high energy beam, and 3.1 MeV for the low energy beam. Smearing for interaction point is in the x and y coordinates, respectively 160 μm and 6 μm, and it's simulated, for each coordinate, with a single gaussian. The z beam position is modelled on a flat distribution 1 cm long.

Most important events generator for $B\overline{B}$ is EvtGen. This generator furnishes a

scheme in which specific decay channels can be implemented as modules. Such modules, called EvtGen *patterns*, can solve different functions; for example, they can evaluate decay amplitudes. EvtGen introduces mixing, generating $\Upsilon(4\mathrm{S})$ decays in a user defined proportion of $B^0\overline{B}^0$, $\overline{B}^0\overline{B}^0$ and B^0B^0 final states with correct Δt distributions; CP asymmetries are generated in modules which modify producted B mesons mean life distributions. They are available generic patterns to simulate two body decays in a scalar mesons pair, a scalar and a vectorial mesons, a tensorial and a scalar mesons or a vectorial mesons pair. Decay features (branching ratio, numbers of sons and patterns) are planned in a ASCII file called `DECAY.DEC`.

Generator manages only exclusive final states; for quarks to hadrons fragmentation we use Jetset7.4, and for this reason it is used for $q\overline{q}$ background generation, $c\overline{c}$ states and weak baryons decays. Jetset7.4 decay table has been updated to latest measurements.

3.6.2 BOGUS

BOGUS simulator (*Babar Object-oriented Geant4-based Unified Simulation*), using Geant4 package developped by CERN, allows us an unified simulation, in the sense that permits a completed and a faster simulation.

Geant includes tools to simulate detector geometry, charged and neutral tracks revelation through the detector, interactions and decays of every kind of particle, magnetic field and detector reply.

BOGUS is structuralized in some packages, one for every underdetector, in each of them are contained standard routines recalled in different simulation phases. Geometries of all under detectors are re-created starting from parameters hold in a format ASCII data bank, in which they are specified materials, dimensions, positions and orientations for every enabled and disabled under detectors and also the quantities for materials concerned an enabled detector.

Monte Carlo tracks hits are called in the *BABAR* terminology *GHits*. These contain all needed informations to obtain in a second phase detector reply simulation. *GHits* are written, with Monte Carlo truth, on an output file.

3.6.3 Detector reply

Tracks hits digitalization happens in another process called *SimApp*. This process is added as *GHit* input information and produces digitalized data as output in the same format of those producted by real detector. At the end of such a process, Monte Carlo data are processed by same code of real data. This code is organized like a subsystems packages set. These packages contain routines to give simulated data sample as most similar as data coming from detector.
Another function of SimApp packages code is to add background hits: rather than simulate background in the detector, it is preferred to catch a random trigger sample and mix (using correct luminosity factors) them with Monte Carlo simulated events.

3.7 Reconstruction software

We already gave prominence to packages as base element of *BABAR* software; in the following sections will be described main *packages* used for analysis done.

3.7.1 `Beta` package

`Beta` is a data analysis program developed for *BABAR*, and it is the base interface for data reconstruction. `Beta` main task is to furnish a solid and simple basement to write detailed physical analysis programs; to do that it gives needed tools to particles identification, tagging, vertexes reconstruction, etc.

All the `Beta` structure, and so the reconstruction mechanism, is based on four fundamental concepts:

- *Candidate*. A candidate is the representation that `Beta` gives to the particle that could be existed in the considered event. There are many kinds of candidates: for example a charged track, reconstructed thanks to vertex detector and DCH, can be a π candidate, while calorimeter neutral cluster can be a photon candidate. The important thing is that all candidates have same interface (they are `BtaCandidate` objects) and they can be used in a general way.

- *Operator*. An operator acts on one or more candidates, combining them in new candidates (for example defining a mother particle by two charged tracks) or extracting informations as mass, charge etc. by them.

- *Selector*. A selector is a particular structure that creates candidates with certain features starting by avalaible candidates. For example a selector for π^0 selection can seek among photons candidates pairs the ones with invariant mass close to nominal π^0 mass and combine them with a right operator in π^0 candidates. Selectors can be generic or destined to a specific physical analysis, and they can be used in different analyses (for different decay channels) without modifying anything.

- *Combiner*. It creates an agreement between two candidates. For example, reconstructed candidates can be combined to respective Monte Carlo generated candidates and so on.

For every *BABAR* event, reconstructed `BtaCandidate` objects are gathered in lists. Each list has a different identity hypothesis and different selection criteria. In table 3.2 are listed some default lists avalaible in the Micro database level.

3.7.2 `CompositionTools` package

This package [20] contains functions for the creation of `BtaCandidate` lists that describe a fixed decay reaction, for example $\pi^0 \rightarrow \gamma\gamma$, starting by `BtaCandidate` existing lists (for a little example, lists described in table 3.2). Candidates obtained are tree-like decay. For these trees we can impose kinetical and geometrical constraints. So, composite candidates are decay trees that combine tracks, neutral clusters, PID and fitting. In this way, using all the informations given by detector, `CompositionTools` is the package for reconstruction of every kind of composite particle.

In the package there are base modules for particles composition through a specific decay channel like `CompositeSelector` that offers a common interface, while for other decays and for every particles it creates a module called `CompositeSelector`, derived by the selector (cfr. 3.7.1).

- we can give at maximum six input lists (parameters are modifiable through file.tcl, but default lists are `ChargedTrack`);

- it has a `BtaCandidate` list as output;

- we can impose masses, energies, momenta, composite candidate reconstruction probability and reconstruction daughters chain cuts.

Name of the list	Description
`ChargedTracks`	Candidates with charge not equal to zero. Pion mass hypotesis is assigned.
`CalorNeutral`	Candidates are single bumps not associated to any tracks. Photon mass hypotesis is assigned.
`CalorClusterNeutral`	Candidates that correspond to multi-bump neutral or single bumps not associated to any cluster related to a track.
`NeutralHad`	Candidates that correspond neutral clusters in hadronic calorimeter not associated to any tracks.
`GoodTrackLoose`	`ChargedTracks` list candidate with: • Min momentum: 0.1 GeV • Max momentum: 10 GeV • DCH min # hit: 12 • Max DOCA in XY plane: 1.5 cm • Min Z DOCA: -10 cm • Max Z DOCA: 10 cm
`GoodPhotonLoose`	`CalorNeutral` list candidate with: • Min energy: 0.030 GeV • Min # of crystals: 0 • Max “lateral momentum”: 0.8 Gev

Table 3.2: Main avalaible lists in Micro database.

- we can impose kinematical and geometrical constraints on reconstruction chains and fit and evaluate vertexes;
- the name of `CompositeSelector` we want to create is given as constructor argument.

Chapter 4

Statistical tecnique and software for physical analysis

4.1 Introduction

In this chapter it will be described the developed software to do analysis presented in this thesis work. In the first part it will be shown the analysis tecnique based on unbinned maximum likelihood fit, that *BABAR* collaboration chosen as the official one. This kind of analysis shows a better efficiency, the possibility of consider errors with a better precisions and correlations between variables. Then it will be presented the procedures that allow us to pass through reconstructed events to the ones which we fit, starting from identification of the problems and showing identified solutions; in the end, it will be described fitting software, illustrating features and functionalities. To develop analysis software has been choosen an object oriented coding technique (C++ language); we also use ROOT framework classes and a particular classes package developed by *BABAR*, called RooFit. We'll briefly present features of both.

4.2 Maximum Likelihood analysis

Analysis has been done using EML, *Extended Maximum Likelihood*, through a program that does an unbinned fit.
Now we consider a x casual variable distributed with a distribution function $f(x;\theta)$. We suppose the expression $f(x;\theta)$ well-known, but at least a parameter value θ (or parameters $\theta = (\theta_1, \ldots, \theta_n)$) should be unknown. So, $f(x;\theta)$ expression represents,

after normalizing it, hypotized probability density function (PDF) for x variable. Maximum likelihood method is a technique to estimate parameters value given a finite data sample. Furthermore, we suppose to perform an experiment where a measurement has been repeated N times, supplying $x_1, \ldots, x_N$ values, where x can represent a multidimensional casual vector, the probability of x_i included between the interval $[x_i, x_i + dx_i]$ for every i is

$$P = \prod_{i=1}^{N} f(x_i; \theta) dx_i \tag{4.1}$$

If the hypotized expression $f(x; \theta)$ for PDF and the parameters θ are correct, this probability will have an large value for measured data. While, a parameter value very different by real one gives us a small probability for realized measurements. Cause dx_i doesn't depend with parameters, same considerations can be effected for the function $\mathcal{L}$, defined as:

$$\mathcal{L}(\theta) = \prod_{i=1}^{N} f(x_i; \theta) \tag{4.2}$$

called likelihood function. It is clear that to estimate parameter value we had to maximize this function. We should underline that x_i values are well-known and so $\mathcal{L}$ only depends by parameters we want to fit.

Often it happens that number of measurements N is a random variable following a Poisson distribution with a mean value n. So, experiment result can be understand as N number and N values $x_1, \ldots, x_N$. In this case likelihood function is given by Poisson probability product to evaluate N for the function (4.2)

$$\mathcal{L}(n, \theta) = \frac{e^{-n}}{N!} \prod_{i=1}^{N} n f(x_i; \theta) \tag{4.3}$$

This function is called extended maximum likelihood. In this case to evaluate parameters values and n value it needs to determinate corresponding parameters that maximize the function.

Now we see how extended maximum likelihood technique allows us to measure the number of signal events and the number of background events in a data sample where every measurement has constituted by observable quantities.
We suppose that parameters we have to evalutate are the number of events $n_1, \ldots, n_s$, each one corresponding to a particular species of events (signal, continuum background, non-continuum background...), where s is index of such a species. To dis-

tinguish the events of each species between them, we determine the variables distributions that present an high discriminant power between those species. We fit these distributions with corresponding PDFs, indexed with $f_1^j, \ldots, f_h^j$ ($j = 1, \ldots, s$) where h is the number of PDFs for each species. When observations are independent (if no, we should consider correlation terms), extended maximum likelihood function becomes:

$$\mathcal{L} = \frac{e^{-\sum_{j=1}^{s} n_j}}{N!} \prod_{i=1}^{N} \sum_{j=1}^{s} n_j \mathcal{P}_j(x_i) \tag{4.4}$$

where

$$\mathcal{P}_j(x_i) = \prod_{l=1}^{h} f_l^j(x_i) \tag{4.5}$$

The evaluation of maximum for the extended maximum likelihood $\mathcal{L}$, or equivalently the minimum of $\chi^2 = -2\ln(\mathcal{L})$, can be done in a numeric way.

4.3 ROOT

BABAR software uses ROOT, an object oriented framework dedicated to scientific data analysis [18]. The project was born in CERN in the middle of '90s to furnish tools for data analyses that would offer a better stability with respect to FORTRAN traditional tools. At the same time, many people needs the necessity of a programming that allow them to manage quickly big projects, realized by huge and mixed groups, using advanced software programming tecniques: it has been chosen the object oriented programming, that in the 90s stood out as optimal choice to realize complex projects.

Several of the most used ROOT components are fitting and hystogramming for statistical analysis and for 2D and 3D graphics.

ROOT framework has been developed using a liberal and informal style where it is necessary an interaction between developers and users, roles very similar and often superimposed: this allows to maintain a continuous evolving project.

ROOT architecture is really portable: released version for more common commercial Unix versions (SunOS/Solaris, IBM AIX, HP-UX, SGI IRIX, Compaq/DEC OSF1), for Linux, for Windows NT and for MacOs are avalaible. Furthermore avalaibility of the source code give adaption to specific necessities of operative system possible.

The ROOT basic structure is formed by a hierarchy of over 300 classes, divided in 14 categories and organized as a tree with one common root, or a large part of classes

inherits from common class *TObject*. Among categories we find:

- *container classes* that implement a series of complex data structures as vectors, lists, sets and maps used very often in ROOT
- *histogram classes* and *minimization* procedure that offer advanced functionalities for statistical data analysis as histograms in one, two or three dimensions, profiles, fitting, minimization and evaluation of mathematical formulas
- *tree classes* and *ntuple* that estend potentialities of PAW[1] n-tuples, 2D and 3D graphical classes and classes for both graphical and textual interface for the user
- *operative system interface* that represents the only link with Operative System (OS) and favoures framework portability, classes for the documentation that allows a careful and complete documentation generation during project developments.

ROOT is based on C/C++ interpreter called CINT [21]; his goal is to process programs (*script*) which not need high performance but they are important for a quick development. CINT supports about 95% of ANSI C code and about 85% of C++.

ROOT version used for the analysis described in this thesis is 3.10/02 con CINT 5.15.115.

4.4 RooFit

RooFit package is formed by a set of classes constructed on ROOT framework dedicated to unbinned maximum likelihood fit, and uses a natural and intuitive notation, that not needs a direct knowledge of ROOT programming[22, 23].

RooFit is composed by two packages: RooFitModels e RooFitCore. Former contains all the classes for the PDFs definition and complex models (as sum or product of PDFs). Latter puts at everybody disposal a set of classes to define a fitting model and fitting methods; it extends ROOT graphical functions allowing to project fitting models in function of several parameters; it allows data and both discrete and continuous variables management.
RooFit scripts are executed inside ROOT, loading external library in the initialization phase.

[1] Framework for statistical analysis developed in FORTRAN[**?**]

4.4.1 Main classes

Variables: *RooRealVar* and *RooCategory*

The first operation we have to do when we create a fit model is to define variables and parameters: it is not done a type distinction between them because they are all objects of *RooRealVar* class. A *RooRealVar* object is featured with a value, a minimum and maximum limit, an error, a name, an unit of measurement, a description and other attributes (for example, to establish if the object defines a constant or a variable).

The *RooRealVar* objects can be used to construct more complex structures as vectors, matrices or lists in the traditional way but RooFit already offers a container class adapted to multidimensional structures called *RooArgList* and *RooArgSet*. It allows to create a list of different variables to use them with other classes (for example as PDFs parameters).

If *RooRealVar* are used to describe continuous variables, *RooCategory* permits to manage discrete variables. Examples of discrete variables can be the B tagging, numbers of run of the events or a naive identification between different sub-channels in a combined fit. The *RooCategory* is important in the fits for the time dependent CP-violating parameters cause it allows to do simultaneous fits (in this case for B^0 and $\overline{B}^0$ and for the different tagging categories) splitting fitting data in subsets.

Data sets: *RooDataSet*

A class useful to manage a complex data structure to fit is called *RooDataSet*. It permits to organize the data as a matrix, in which single variables are represented in columns while in the other the single events. For rows the constructor allows to initializate an object in a direct way through a number of *RooRealVar* (from one to five) or with a arbitrary number of variables using a *RooArgList*. This way is more flexible but much more complicate to manage due to the presence of a middle structure.

Data are read through `read()` method. This method allows to access to both text-like files (ASCII) and binary-like ones with ROOT *tree* format.

Distributions: *RooAbsPdf*

The distributions used are the most common for the physics analyses, so we can use a gaussian (*RooGaussian*), an asymetric gaussian (*RooBifurGauss*), polinomials (*RooPolynomial*), an Argus [24] function (*RooArgusBG*), a Breit-Wigner function

(*RooBreitWigner*), an exponential (*RooExponential* and *RooLifetime*) and some others. The single classes inherits from the abstract class *RooAbsPdf* and we can define new functions in a quick and simple way.

The *RooAbsPdf* class puts at the people's disposal a series of generic methods to the events random generation based on a *try–reject* technique that can be redefined in a more efficient way for the subclasses. This class offers a fundamental method defined `fitTo(RooDataSet *data,...)` that effects a fit creating a specific object *TMinuit*; it is possible to set up some options to perform a binned fit or to minimize the likelihood function with a certain algorithm (`MIGRAD, MINOS, HESSE`). It offers some other options for plotting and drawing [25].

It's useful to note that *RooAbsPdf* distributions are automatically normalized (with unitary area).

Furthermore we can compose single PDFs through sum (*RooAddPdf*), product (*RooProdPdf*) and convolution (*RooConvPdf*). Single classes inherit from the same abstract class *RooAbsPdf*.

The *RooAddPdf* class permits to declare a model obtained with the sum of an arbitrary number of PDFs, each weighted with a parameters. This model furnishes the basis for the declaration of the extended maximum likelihood function.

4.5 Software for the cut optimization: Selector

The variables determined during the event reconstruction are saved in ROOT files (`.root`) contained in particular structures called *tree*. These files represent the output of the event reconstruction process; during this stage loose cuts are applied on several variables that caracterized our event. To discriminate signal from background. This permits to reduce files dimension because we save only the events that pass cuts (*preliminary* cuts). After the reconstruction we can optimize the values of such cuts (obviously, using tighter cuts). To do that it's necessary a program that allows us to read values of the variables held in the *tree* to establish the number of these ones passing the applied cuts. ROOT realizes that with a solid and flexible method: *selector*. This procedure is based on the realization of a user's personalized class (depending on the analyses to realize) that is derived from the *TSelector* class. These following methods are implemented in it:

- `TSelector::Begin`: This function is called every time we start to read val-

ues of the variables of the tree. It's possible to furnish a configuration parameter that permits to effect several kind of operations for a fixed selector. For example, the selector used for the analysis in this thesis work allows to prepare input to the fitting program, to perform cut and count analysis, to draw variables distributions, to select a number of events and much more. Configuration parameter is only a alfanumeric string: reading of this parameter and the identification of the operation requested is performed in this function `Begin`.

- `TSelector::Process`: This function is called for every single event. Inside, they are defined the cuts to apply on the variables values. After every cut, we have a counter that allows us to determine the number of the events that pass them. If an event is analyzed and its variables pass all the cuts, this event passes to the following procedures. In this case the event is counted in all the counters. If, viceversa, a determined cut is not respected, the event is rejected and the counting operation is interrupted in the last passed cut. All the operations requested are done with the configuration program, as saving on a file or filling a histogram.

- `TSelector::Terminate`: This function is called at the end of variables reading of all the events. It performs the conclusive operations as closing a file, drawing histograms, showing at screen the number of the events after all the cuts and so on.

Cause different analyses differ essentially for the variables and for the cut values on them, from the description given for the methods, we can guess that the method that should be much more personalized is `Process`. For all the other functions is possible to realize a model for the selector which we can refer to.

4.6 Fitting program: MIFIT

As we said in the previous sections, we use an unbinned extended maximum likelihood (ML) fit in our analysis. After the events selection describer in the section 4.5, we prepare an input file (in .root format) to the ML program with the events we want to fit. This program, developed in Milan group by Alfio Lazzaro in C++, is called MIFIT. It uses the ROOT and RooFit classes, but it is a standalone executable code. For the work of this thesis we have used MIFIT version 3.0. Essentially, the main goal of

the program is to provide a very simple interface to perform several operations used in the different analyses. It is not requested any skills about ROOT and RooFit, but any configuration of the program is given using an intuitive configuration text files: mipdf.cfg and mifit.cfg. The first file is used when we make the PDF plots of the variables while the second one for any other function of the program. The structure of the two files is very similar but to avoid any confusion about them we decide to consider the operation of PDF plots as different from the other ones and therefore we use two different files.

MIFIT is based on four main classes:

1. MFConfiguration: the goal of this class is to read the configuration file (mipdf.cfg or mifit.cfg) and to interpret it line by line. If no errors occur (there is a syntax spelling and declarations consistence check), it provides to other classes the necessary informations to declare objects requested in the configuration reading. The configuration file is divided in different parts:

   - *config*: they are fixed some features as title for each PDF, best candidate choice selection criteria, number of $B\overline{B}$ pairs, blind procedure parameters
   - *embedded tree*: some tests (called toy experiments) require the generation of a sample of data from PDFs, so, we add some events taken by an external sample. In this part we declare these MC samples and the number of events to embed to the generated sample.
   - *input*: they are listed all fitting variables. Definition sintax is given by: name (same name of the variable in the ntuple), description, definition interval used to normalize the PDF and eventually unity of measurement.
   - *category*: there are written the discrete variables used for tagging informations (tag and category) and indices of different sub-decays.
   - *correction*: the PDFs obtained fitting on MC data have small discrepancies with respect to what we could obtain from the real data. This is due to a not good MC simulation. For example, in some cases the resonances masses have a small difference in the central value and in the width. Using a control sample, we study this effect and we take it in account applying corrections to the parameters. In some cases, this corrections are run-dependent, i.e. they are different for each run of data. In this part of the configuration file we declare these run-dependent corrections.

- *pdfparam*: here we consider the declared PDFs parameters fixed in the fit. Sintax is: name of the variable, fixed value, error value and eventually the unity of measurement.
- *floatpdfparam*: we consider the declared PDFs parameters floating in the fit. There are some options that we can consider for each parameter declared here: *constant*, if we want that the parameter didn't change from the initial value, and *blind*, if we want that parameter was blinded.
- *KEYSpdf*: in this section we declare the KEYSpdf (aka "Kernel Estimating Your Shapes") is a non-parametric PDF that describes a distribution empirically, without referring to any model of the expected shape. In some cases it is difficult to fit a distribution with a standard PDF so this kind of PDF helps us in doing it.
- *pdf*: here we define the PDFs used to fit variables. They exist several kind of avalaible PDF: more common used ones are gaussians (single, double and triple), asymetric gaussians, polinomial and Chebychev polinomial (first, second and third) and combinations of these (for example gaussian plus a first degree polinomial). For each PDF we must give the name of the variable to fit (declared in *input* section) and the names of the parameters (declared in *pdfparam* and in *floatpdfparam*). In this section we declare also the resolution models for Time-Dependent analysis.
- *CPpdf*: here we declare the PDFs for the Time-Dependent analysis. These are special PDF because they have as input parameters also the B tagging discrete variable (declared in *category* section) and the resolution model (declared in *pdf*).
- *yieldvar*: we declare here the variables which correspond to the numbers of the events for each species (signal and background).
- *extendedpdf*: in this section we consider the product of the PDFs declared in *KEYSpdf* or *pdf* section to obtain the total PDF for each species (signal and background) times the correspondent yield variable, declared in *yieldvar*.
- *fitpdf*: the PDFs declared in *extendedpdf* are summed to obtain tht final extended PDF for the fit.

- *simfitpdf*: in this sectionwe declare special PDFs for simultaneous fit, i.e. fit of different categories of events or different sub-decays. It is possible, using a discrete variable (called label), to assign a different label value to a *fitpdf* PDF. It is also possible to have a simultaneous PDF of simultaneous PDFs and so on.

2. MFDataFile: this class performs the reading of input events from the ROOT files. It verifies the correspondence between declared variables in input and category sections and the variables of the tree in the ROOT file. If no errors occur, it performs final cuts on such input variables, the best candidate choice selection (if requested) fpr events with multiple candidates (we can make a random selection or using a best χ^2 selection), calculate the correlation matrix for the input variables, write in an output file two sample: first one after the applied cuts and the other one after best choice selection (corresponding to the final sample for the fit).

3. MFModels: this class instances all PDFs declared in the section *KEYSpdf*, *pdf*, *CPpdf*, *extendedpdf*, *fitpdf*, and *simfitpdf*. It controls if the number of parameters for each PDF is correct. This class performs also the generation of events from PDF and the drawing of one PDF.

4. MFFits: the goals of this class is to perform ML fits for one variable or extended ML fits for yield extraction. In this class we also have defined the toy experiment procedures, upper limits calculations, likelihood function plots, contour plots of the likelihood function, and output of the fit results.

Now we will describe some functions of MIFIT. Further description can be found in the web page

`http://pcbabar4.mi.infn.it/lazzaro/MiFit`

4.6.1 Making PDFs

After launching MIFIT executable, the program shows a text menu. The option "1" allows us to perform a fit of the distribution of one variable. After reading the configuration file (in this case mipdf.cfg), if no errors occur during the configuration file reading, the program asks which variable we want to use in the fit. At the end of the

fit, the plot is visualized for the fitted variable, with overimposed the PDF, the values of the PDF parameters and the χ^2 value. We can choose the number of bins for the distribution (just a graphical reason because the fit is unbinned) and the logarithmic scale for the y-axis. The parameters of the PDFs can be copied in the file mifit.cfg to perform the rest of the analysis.

4.6.2 Making Fit

The option "2" of MIFIT is used to perform extended ML fit for the determination of the number of events for every hypothesis. Of course in the fit we can determine other parameters of the PDFs which are floating (like S and C). After choosing the option "2", MIFIT asks (in order):

- if we want to apply correction for MC/data matching. This facility is requested if in the configuration file we have declared PDF parameters with MC/data corrections.
- if we want the results of the fit in blind or unblind mode.
- the extended PDF (declared in fitpdf or simfitpdf) to use.

When the fit is completed, the results are shown.

4.6.3 Making Toy Experiments

The third option of MIFIT is useful to study the causes for biases and correlations with respect to the results. In other words, we want to verify all the hypotheses done on the PDFs and the lack of knowledge on the parameters. That's why we use a statistical technique called "toy experiments" generation. In this method we generate several samples of data (with the data generated from PDFs or taken from MC samples) and we fit on them. Cause we know the composition of the sample (how many signal and background events are inside it), we expect that the distribution of the results of the fits should be a Gaussian distribution with central value as used in the generation of the events. Eventually, biases in the mean of the Gaussian used to fit the distributions of the results are considered as systematic effects. We can decide also to correct the final results in the fit on real data to take in account these biases. These studies are applied to the number of events and to the parameters S and C.

4.6.4 Making Projections

The option “4” of MIFIT allows to draw projections of variables. In this case is necessary to work in two steps. First of all, if we want to project a variable x, we need to emphasize the signal in the data sample with respect to the background. For this reason we apply a cut on likelihood function L, evaluated without the x variable. So, the first step consists in the evaluation of the cut value on L: we use a sample of signal events and a sample of background events to optimize this cut. After that, the second step is to apply the cut to the data and then show the distribution of the variable with the signal and background PDFs superimposed.

Chapter 5

Event reconstruction

5.1 Particles identification and reconstruction

To study B^0 meson decay in $\eta' K$, with η' decaying in $\rho\gamma$ and $\eta\pi^+\pi^-$ (η in $\gamma\ \gamma$ and η in $\pi^+\pi^-\pi^0$), are very important a correct photons identification and charged tracks reconstruction. In the following paragraphs it will be shown methods used to verify the detector reply and to identify particles inside *BABAR*.

5.1.1 Control Sample

A "control sample" is a high statistics data sample useful to study resonances. Data coming from "control sample" have been used to some goals:

- study of the reply for the subdetectors,
- evaluate the performance of the algorithms for the particles identifications,
- estimate systematic uncertainties.

Pure samples of a particle are selected using only kinematical informations. For example, a pure pions sample is selected using

$$K_S^0 \rightarrow \pi^+\pi^-$$

decay channel and applying tighter cuts on several variables as: angle between K_s^0 candidate direction and the direction of the decay vertex, the distance of the vertex from interaction point and the mass of reconstructed K_s^0 candidate.

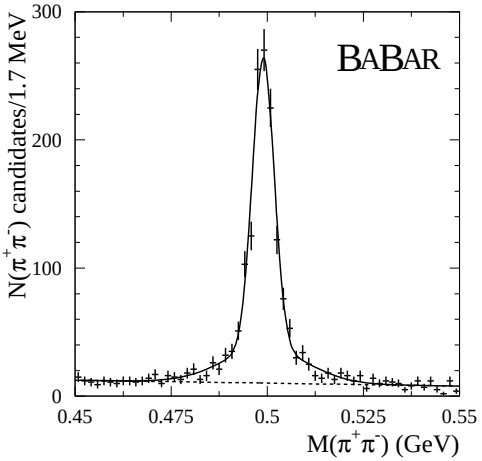

Figure 5.1: Mass distribution for K^0_S candidates used to select pions control sample.

Invariant mass distribution of $\pi^-\pi^+$ pairs is shown in the Fig. 5.1: purity of the sample is greater than 99%.

For a K mesons data sample with a very high purity, we can use selected tracks coming from the decay chain

$$D^{*+} \rightarrow \pi^+ D^0,\ D^0 \rightarrow \pi^+ K^-$$

and its charge conjugation. In the Fig. 5.2 it's shown the distribution of the mass difference between $K\pi\pi$ and $K\pi$, $0.139 < \Delta M < 0.162$ GeV/c^2. With a tight cut on this variable, the combinatorial background is equal to 13% for a kaons sample with 90% of purity.

5.1.2 Track reconstruction

Please see Sec. 2.6 for more details.

5.1.3 Electrons

Inside *BABAR* detector, electrons are mainly divided by charged hadrons through energy, lateral momentum of the shower and tracks momentum. To obtain a better precision, we have to check that energy loss dE/dx in the drift chamber and the Cherenkov angle of DIRC will be consistent with electron hypotesis. One of the most important variables for hadrons discrimination is the ratio between the energy left in the calorimeter and track momentum (E/p).

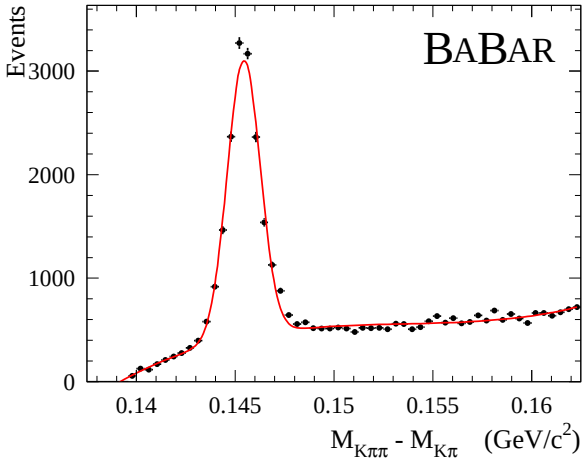

Figure 5.2: Distribution of mass difference for D^* and D^0 candidates, used to select kaons control samples.

Fig. 5.3 shows efficiency for the electrons identification and probability of an uncorrect pions identification; both of them are function of the momentum and the polar angle, measured in the lab frame. Efficiency for electrons identification has been studied using electrons coming from radiative Bhabha and events $\gamma\gamma \to 4e$. Probability of an uncorrect pions identification is measured using τ three body decays and charged pions coming from K^0_S decay.

Selection criterium *tight* has an average efficiency of 94.8% in the momentum interval $0.5 < p < 2$ GeV/c while probability of an uncorrect identification is $\sim 0.3\%$. With *very tight* criterium, the efficiency is 88.1% with an average uncorrected pions identification of 0.15%.

5.1.4 Muons

Muons identification is performed almost completely in the IFR, other detectors furnish only additional informations. Charged particles are reconstructed in the SVT and DHC; μ candidates should satisfy criteria for particles at minimum ionization energy in the EMC. Charged tracks, reconstructed in the drift chamber, are founded using a detailed map of the not uniform magnetic field and evaluating the expected average energy loss. The average position of the intersections with active plans of the detector is calculated including the uncertainty due to multiple scattering.

To divide muons from charged hadrons, mainly pions, it's applied several selection

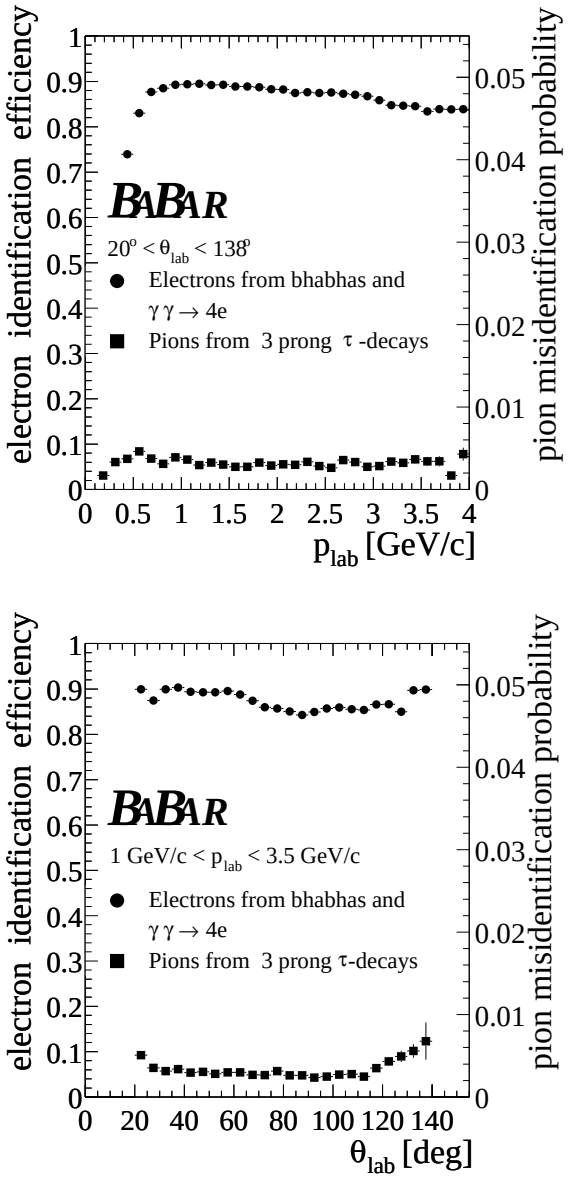

Figure 5.3: Efficiency of the electrons identification and probability of a uncorrect pions indentification vs momentum (top) and polar angle (bottom).

criteria. First of all, found hits in every reading plan, within a maximum distance from studied intersection point, are linked with charged tracks. Then, inside acceptance of the calorimeter, we usually cut on left energy, asking for such a loss of consistence with the expected one for a particle at minimum ionization energy. It's requested the presence of a signal in at least two *layers* in the IFR, and then we apply a cut on total number of interaction lenghts run in every subdetectors; we have to compare this value with the number of interaction lenghts given by a muon with same momentum and angle. Mean value and r.m.s.[1] for the *strip pattern* through different layers furnish the μ/π discriminant power.

Muon selector performances have been evaluated on real data sample; for muons have been considered $\mu\mu ee$ processes and $\mu\mu\gamma$ in the final states, instead for pions sources, τ three body decays and $K^0_S \rightarrow \pi^+\pi^-$. Selection of the control sample is based on kinematical variables and not on used variables for muons identification. The selector with *loose* criterium reaches an efficiency of 90% in the momentum interval $1.5 < p < 3.0$ GeV/c with an uncorrect pions identification of 6-8%. Tighter selection criteria halves uncorrect hadrons identification and give us an efficiency for muons of 80%.

5.1.5 Photons

Photons identification is performed inside EMC. Usually an electro-magnetic shower is distributed on many adjacent crystals forming a *cluster* of a certain left energy. We can distinguish two kind: single *cluster* with a single energy maximum and *merged cluster* where we have more local energy maxima called *bumps*. The reconstruction and the identification algorithm has been developed in a way to identify efficiently the *clusters*, distinguish them from *bumps* and determine if they are generated by a neutral or charged track.

A *cluster* has at least one crystal with energy greater than 10 MeV and the adjacent crystals are considered part of a *cluster* if their energy exceeds the 1 MeV threshold. To establish the local energy maxima inside a *cluster* it's requested that candidate crystal would have an energy, $E_{LocalMax}$, greater than every adjacent crystal. Furthermore it must be verified the following condition: $0.5(N - 2.5) > \frac{E_{NMax}}{E_{LocalMax}}$ where E_{NMax} is the maximum energy for N adjacent crystals with energy greater than 2 MeV. All the clusters are divided in many *bumps* in the same number of local maxima. The energy

[1] Root mean square (standard deviation).

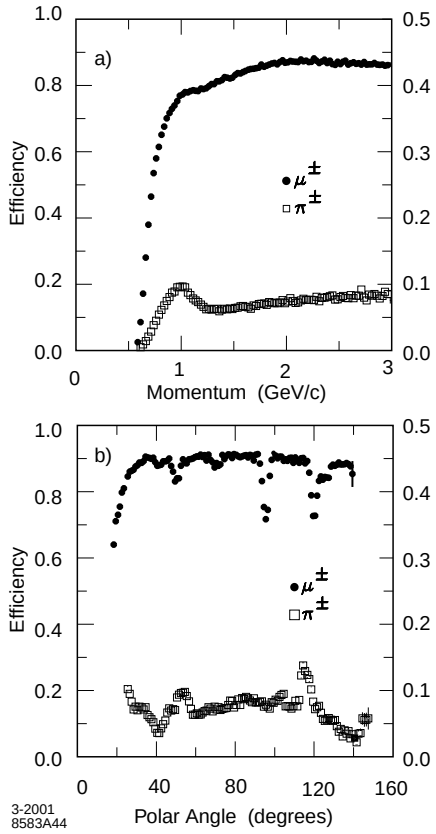

Figure 5.4: Efficiency for muons identification and probability of an uncorrect pions identification with *loose* selection criterium versus momentum (top) and polar angle (bottom) with $1.5 < p < 3.0$ GeV/c.

for every crystal is associated with each *bump* with a simultaneous adjustment, starting from the shape of electro-magnetic shower, the centers and energies of the *bumps*. Then all the reconstructed charged tracks in the tracking volume are estrapolated until the EMC entrance and for every track-bump pairs is evaluated the association probability. All the *bumps* with a low probability are considered photons candidates. A little percentage of these candidates is rejected if the shape is not compatible with the one expected for an electro-magnetic shower.

In this analysis have been used photon candidates with a total energy left in the EMC greater than 50 MeV in the $\eta \to \gamma\gamma$ decay while greater than 100 MeV in $\eta' \to \rho\gamma$.

5.1.6 Mesons π^0 and η reconstruction

Neutral pions and η mesons are formed starting from photons pairs (or three pions in the case of $\eta \to \pi^0\pi^+\pi^-$) and we assume as their origin the primary interaction point. The spectrum of the invariant mass for the $\gamma\gamma$ pairs is shown in Fig. 5.5 for different E_γ and $E_{\gamma\gamma}$ ranges; it's possible to distinguish peaks for π^0 and η. The mass resolution for π^0 is 6.9 MeV in the multi-hadronic events while 6.5 MeV for $\tau\tau$ events.

The detector segmentation and the spatial resolution allow to reconstruct π^0 with the EMC photons separation until 5cm without a significative worsening in the mass resolution. The little fraction of high energy π^0 in which we cannot separate the photons, about 10% in the 4-6 GeV region, are distinguished through single photons with the help of the cluster shape.

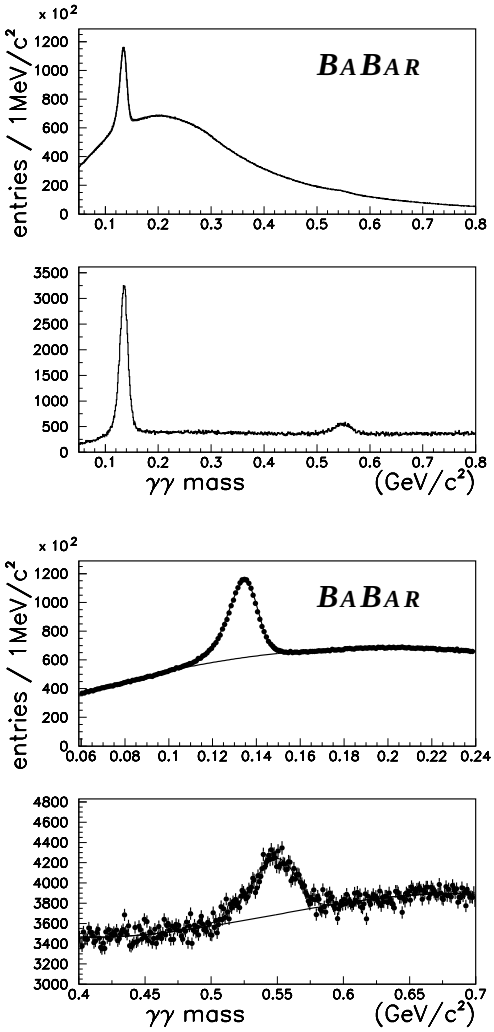

Figure 5.5: Mass spectrum for $\gamma\gamma$ pairs in the hadronic events in the π^0 and η regions. $E_\gamma > 30$ MeV, $E_{\gamma\gamma} > 300$ MeV (top), $E_\gamma > 100$ MeV, $E_{\gamma\gamma} > 1$ GeV (bottom).

5.2 $B^0 \to \eta' K$ event reconstruction

All event selections make use of *BABAR*'s `Q2Body` user package. The results are obtained with the `analysis-21`. Charged tracks and electromagnetic showers identified by the detector are combined to form particle candidates using tools from the `CompositionTools` package.

5.2.1 π^0

Two photons taken from the `GoodPhotonLoose` list are combined to form a π^0 candidate, kinematically fitted to the true pion mass, using the standard tool `Pi0ToGG_DefaultMass`. We made a cut on unfitted mass between 0.100 and 0.155 $\mathrm{GeV/c^2}$.

5.2.2 ρ^0

The ρ^0 mesons have been reconstructed using the standard tool `Rho0ToPiPi_Default`. As input list we used `GoodTracksLoose` with all the charged particles considered as pions. ρ^0 candidate mass was required to be between 0.470 and 1.000 $\mathrm{GeV/c^2}$.

5.2.3 $\eta_{\gamma\gamma}$

The η mesons have been reconstructed in $\eta \to \gamma\gamma$ decay channel by using the standard tool `EtaToGG_DefaultMass`. Input list is the `GoodPhotonLoose` for the two photons. The $\eta_{\gamma\gamma}$ mass is kinematically fitted to the true η mass, and the unfitted mass is cut between 0.470 and 0.620 $\mathrm{GeV/c^2}$.

5.2.4 $\eta_{3\pi}$

The η mesons have been reconstructed in $\eta \to \pi^+\pi^-\pi^0$ decay channel by using the `EtaToPiPiPi0_Default` module. Input list for charged tracks is the `GoodTracksLoose` list with all the charged particles considered as pions. The $\eta_{3\pi}$ mass was cut between 0.470 and 0.620 $\mathrm{GeV/c^2}$.

5.2.5 $\eta'_{\rho\gamma}$

The η' mesons have been reconstructed in $\eta' \rightarrow \rho^0\gamma$ decay channel by using the `EtaPToRho0G_Default`. The photons have been taken from `GoodPhotonLoose` list. The $\eta'_{\rho\gamma}$ candidate is accepted if the mass is in the interval 0.900 – 1.010 $\mathrm{GeV/c^2}$.

5.2.6 $\eta'_{\eta\pi\pi}$

The η' mesons have been reconstructed in $\eta' \rightarrow \eta\pi^+\pi^-$ decay channel with $\eta \rightarrow \gamma\gamma$ or $\eta \rightarrow \pi^+\pi^-\pi^0$ by using the `EtaPToPiPiEta_Default`. Input list for charged tracks is the `GoodTracksLoose` list with all the charged particles considered as pions. The $\eta'_{\eta\pi\pi}$ candidate is accepted if the mass is in the interval 0.900 – 1.010 $\mathrm{GeV/c^2}$.

5.2.7 $K^0_S \rightarrow \pi^+\pi^-$

The $K^0_S \rightarrow \pi^+\pi^-$ candidates come from the `KsDefault` input list. Beam spot is used in the selector, three dimensional flight distance from the event primary vertex > 2 mm and two-dimensional angle between the line-of-flight and momentum vectors < 40 mrad. We applied a cut of 0.010 $\mathrm{GeV/c^2}$ around the nominal mass of K^0_S (0.488 – 0.508 $\mathrm{GeV/c^2}$) (See Fig. 5.6).

5.2.8 $K^0_S \rightarrow \pi^0\pi^0$

The $K^0_S \rightarrow \pi^0\pi^0$ candidates come from `KsToPi0Pi0Loose` list (input list was `GoodPhotonLoose` for gammas and `Pi0ToGGDefaultMass` for pions).
For the $K^0_S \rightarrow \pi^0\pi^0$ the decay point is chosen at the origin, the angles between gammas are understimated which leads to too low invariant masses, so the K^0_s decay vertex is fitted along a line of the initial momentum using a decay position of η' as a geometrical constraint using the `WalkFit` vertexing algorithm. We applied a cut of 0.030 $\mathrm{GeV/c^2}$ around the nominal mass of K^0_S (0.468 – 0.528 $\mathrm{GeV/c^2}$) (See Fig. 5.6).

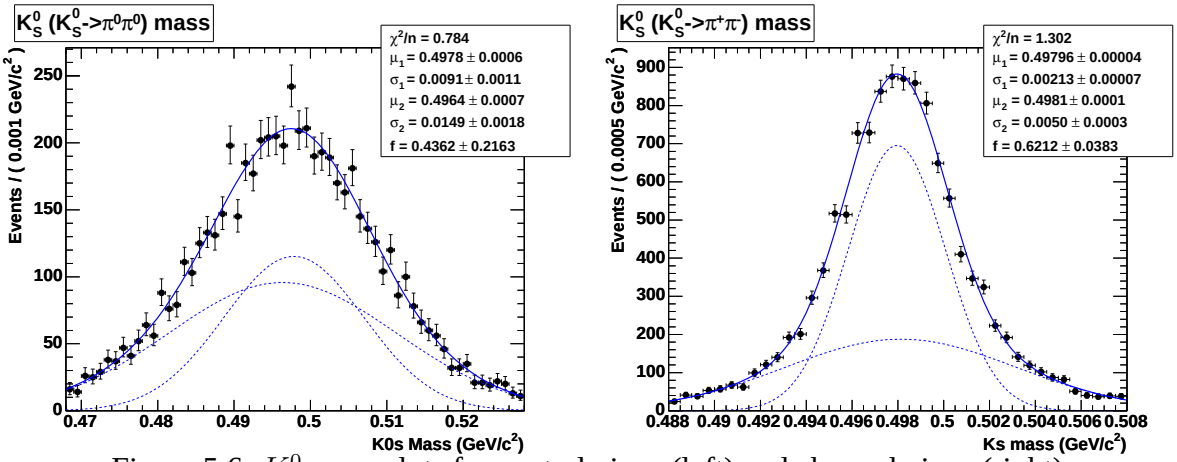

Figure 5.6: K^0_S mass plots for neutral pions (left) and charged pions (right).

5.2.9 B candidates

The neutral $B^0 \rightarrow \eta' K^0_S$ candidates have been formed combining η' and K^0_S candidates and for the charged $B^{\pm} \rightarrow \eta' K^{\pm}$ combining η' with a charged track form the `GoodTrackLoose` list. For the B selection we made some preliminar cuts specific for a quasi-two body analysis: a cut between 1.9 $\mathrm{GeV/c}$ and 3.1 $\mathrm{GeV/c}$ on the momentum of the B daughters (η' and K mesons) in the B rest frame and a cut on B mass between 4.7 $\mathrm{GeV/c^2}$ and 5.7 $\mathrm{GeV/c^2}$. Other cuts will be described in detail in the Chapter 7 after describing the discriminant variables used in the analysis.

Chapter 6

Discriminating variables

6.1 Introduction

In this chapter it will be described the discriminating variables used to separate signal from background events.
It will be considered kinematical and topological variables linked with spatial structure of the events. This analysis present two different kind of background: continuum background $e^+e^- \rightarrow q\overline{q}$ ($q = u, d, s, c$) and the background coming from $e^+e^- \rightarrow b\overline{b} \rightarrow B\overline{B}$ events with charm or charmless final states.
At $\Upsilon(4\mathrm{S})$ resonance energy, we have a number of $e^+e^- \rightarrow q\overline{q}$ events abouth three times with respect to $B\overline{B}$ events. The $q\overline{q}$ continuum background can be studied using collected data under the resonance (*off-peak* data), while the study of $B\overline{B}$ background using simulated data with Monte Carlo method.
Topological variables furnish a separation between $B\overline{B}$ events and the continuum background ones; kinematical variables allow us to discriminate signal from $B\overline{B}$ background and further by the continuous one.

6.2 Topological variables

From the kinematical study of $e^+e^- \rightarrow q\overline{q}$ we deduce that background and signal events have a different geometry. Cause beam energy in the center of mass (CM) is equal to 10.580 GeV, kinetical energy at $c\overline{c}$ or $u\overline{u}$, $d\overline{d}$, $s\overline{s}$ (uds) pairs' disposal is very high: the event jets will be almost anti-parallel between them. In the case of a

process $e^+e^- \rightarrow \Upsilon(4\mathrm{S}) \rightarrow B\overline{B}$ the kinetical energy for B mesons will be low, so, the event will be much more isotropic. Topological variables used in the background discrimination are:

- cosine of the thrust angle, $\cos\theta_{\mathrm{T}}$

- Fisher discriminant

6.2.1 The θ_{T} angle

The thrust axis is defined as the following expression:

$$T = max_{|\vec{n}|=1}\frac{\sum_i |\vec{n}\vec{p}_i|}{\sum_i |\vec{p}_i|}. \tag{6.1}$$

with p_i, particles momenta used to calculate it and $\vec{n}$ is versor that maximizes the value of thrust T. θ_{T} is the angle between the thrust axis of the B candidate and the thrust axis of the rest of the event, calculated in CM frame. The $\cos\theta_{\mathrm{T}}$ variable has a nearly flat distribution for B candidates while is sharply peaked at ± 1 for continuum background events (Fig. 6.1). The $|\cos\theta_{\mathrm{T}}| < 0.9$ condition has been applied in the cuts during the events reconstruction. This cut allows us to lose a big amount of continuum background with a loss of signal event efficiency of 10%.

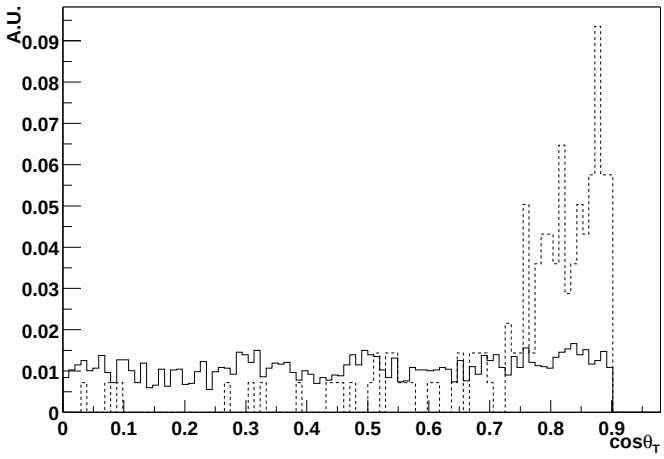

Figure 6.1: $|\cos\theta_{\mathrm{T}}|$: comparison between *off-peak* data and Monte Carlo signal events.

6.2.2 Fisher discriminant

For every reconstructed event we need to decide if it agrees better with signal or background hypotesis. To do that, we introduce a *statystical test* **t(x)**, function of several **x** event variables. Such a function will have different distributions for those two hypoteses.

The simplest choice is represented by Fisher discriminant that is a linear combinations of more variables:

$$\mathcal{F} = \sum_i \alpha_i x_i \tag{6.2}$$

where α_i coefficients are chosen in the way to maximize the separation between $\mathcal{F}$ distributions in signal and background hypoteses. In the variables choice we consider quantities that furnish us informations on spatial shape of the event.

For the CP time-dependent analysis we used a $\mathcal{F}$ Fisher discriminant with four variables: the absolute value of the cosine of the angle between the B direction and the beam axis, the absolute value of the cosine of the angle between the thrust axis of the B candidate and the beam axis, the two monomials L_0 and L_2 with L_n defined as [26]:

$$L_n = \sum_{i=ROE} p_i \times |\cos(\theta_i)|^n \tag{6.3}$$

where the sum is over the list of the rest of event (all tracks and neutrals which do not belong to the B candidate), p_i is the momentum of particle i, and θ_i is the angle between the direction of particle i and the thrust axis of the B candidate. We called this variable $\mathcal{F}_{LGD}$ ("Legendre Fisher"). It was noticed that $\mathcal{F}_{LGD}$ is correlated with the tagging category. The Tag04 tagging algorithm is designed to tag the flavor of the B in two stages: first of all the information relative to a particular physics precess are combined in a Neural Network to obtain a sub-tagger; then all the sub-taggers are combined in a larger Neural Network that determines the probability for the entire event. Based on the output of the various neural nets, each event is assigned to a physics category. The algorithm uses 9 input sub-taggers and has 6 output Physics Categories:*Lepton, Kaon I, Kaon II, Kaon&Pion, Pion, Others* . *Lepton* contains the events in which flavor identification is possible through a lepton identification or if present a kaon. Events with kaons or weak pions with opposite charge but similar flight direction are assigned to *Kaon I* category. Events with only a kaon tag are assigned to *Kaon I* or *Kaon II* category following the probability of an uncorrected identification. *Kaon II* category contains the residual events with a weak pion. *Kaon&Pion* category

has events where both a charged kaon and a slow pion candidates are present. Tag is assigned by requiring a kaon and a slow pion tag with agree (i.e. the kaon and the slow pion candidate must have opposite charge) and additionally exploiting the angular correlation between the two tracks. Events coming from slow pions are assigned as *Pion* category. All the other events are assigned to *Others* category or excluded *no Tag* if the probability of an uncorrected identification is too high. In order to remove this correlation, a new variable ($\mathcal{F}_{T04}$, "Legendre-Tagging-Category Fisher") was defined as a linear combination of $\mathcal{F}_{LGD}$ and the tagging categories. This variable was used in the analysis whose results was sent to ICHEP04 [15]. For the published results [16] we have decided to use a new definition of $\mathcal{F}_{T04}$ (called $\mathcal{F}'_{T04}$) where the category is not in combination but it is based on a category by category correction.

Definition of $\mathcal{F}_{T04}$

The purpose of $\mathcal{F}_{T04}$ is to remove to first order the correlation between the shape of the Fisher distribution and the tagging category. The correlation is illustrated in

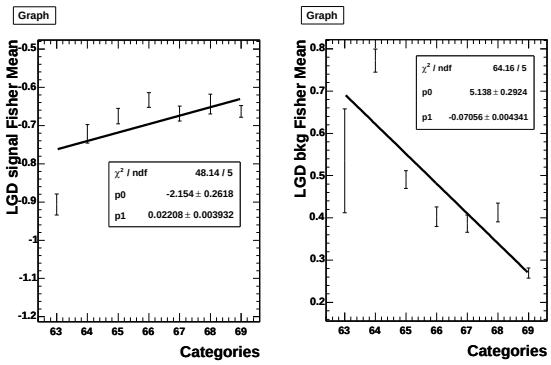

Figure 6.2: Variation of the mean of a bifurcated Gaussian fitted to the $\mathcal{F}_{LGD}$ distribution for each Tag04 tagging category, for signal MC (left) and onpeak sidebands (right). Category 69 is the untagged category.

Fig. 6.2 for the mode $B^+ \to \eta'_{\rho\gamma} K^+$. The plots show the fitted mean of a bifurcated Gaussian to the $\mathcal{F}_{LGD}$ distribution for each Tag04 tagging category, for signal and continuum background. A polynomial of degree 1 is fitted to the distributions, showing the different slope for signal Monte-Carlo and background (defined here as the onpeak sidebands: $M_{ES} < 5.27$ GeV/c^2 or $0.1 < |\Delta E| < 0.2$ GeV).

Since the data sample is dominated by continuum background events, the correlation in continuum is most important to remove. We therefore use the parameters

from the onpeak sideband to reduce the effect. We checked that the slope of the fit to the variation of the mean is compatible among all four $B \to \eta' K$ modes ($\eta'_{\eta\pi\pi} K^+$: -0.077 ± 0.019, $\eta'_{\rho\gamma} K^+$: -0.062 ± 0.004, $\eta'_{\eta\pi\pi} K^0$: 0.052 ± 0.027, $\eta'_{\rho\gamma} K^0$: 0.056 ± 0.007). We take the weighted average as our correction value: -0.0604 ± 0.0036.

Finally, we define the new Fisher variable $\mathcal{F}_{T04}$ as

$$\mathcal{F}_{T04} = \mathcal{F}_{LGD} + 0.0604 \cdot \mathrm{Cat(Tag04)} - 4.06, \tag{6.4}$$

where $\mathrm{Cat(Tag04)}$ is the Tag04 category of the candidate ($\mathrm{Cat(Tag04)} = 63 - 68$ for tagged events, and is set to 69 for untagged events), and the constant -4.06 is an arbitrary factor.

Properties of $\mathcal{F}_{T04}$

We describe here checks that were made to validate the new $\mathcal{F}_{T04}$. We checked that the correlation between the $\mathcal{F}_{T04}$ mean and the tagging category was indeed reduced for continuum. Fig. 6.3 shows the fitted mean of a bifurcated Gaussian to the $\mathcal{F}_{T04}$ distribution versus the Tag04 tagging category. The correlation for continuum is clearly small compared to $\mathcal{F}_{LGD}$. The increase in the correlation for signal was checked to be negligible for the purpose of the ML-fit [27], and this will be checked again with toy Monte-Carlo sample.

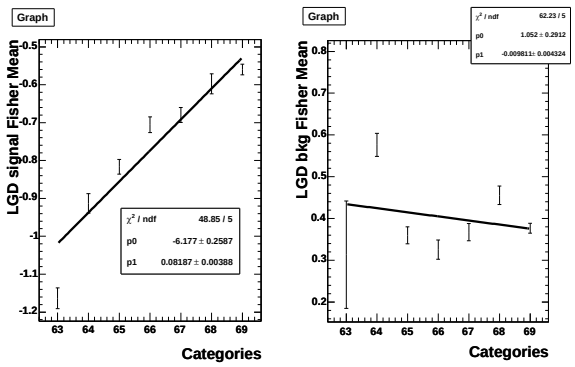

Figure 6.3: Variation of the mean of a bifurcated Gaussian fitted to the $\mathcal{F}_{T04}$ distribution for each category, for signal MC (left) and onpeak sidebands (right).

Finally, we determined directly from the data the correlation between $\mathcal{F}_{T04}$ and the Tag04 tagging category. For all $\eta' K$ modes, we obtain the raw correlations given in Table 6.1. For comparison, we show both the correlations for $\mathcal{F}_{LGD}$ and $\mathcal{F}_{T04}$, and

for signal MC (SIGMC) and onpeak side-bands (ON-SB).

Table 6.1: Correlation between $\mathcal{F}_{LGD}$, $\mathcal{F}_{T04}$ or $\mathcal{F}'_{T04}$ and the tagging category $\mathrm{Cat(Tag04)}$, for signal (SIGMC) and onpeak sidebands (ON-SB).

Mode	Data	Correlation of $\mathrm{Cat(Tag04)}$ and $\mathcal{F}_{LGD}$	$\mathcal{F}_{T04}$	$\mathcal{F}'_{T04}$
$\eta'_{\eta\pi\pi}K^0_S$	SIGMC	%	%	%
	ON-SB	-12.1%	$+5.9\%$	$+3.1\%$
$\eta'_{\rho\gamma}K^0_S$	SIGMC	$+1.6\%$	$+21.5\%$	$+14.8\%$
	ON-SB	-13.7%	$+2.6\%$	$+1.0\%$
$\eta'_{\eta\pi\pi}K^+$	SIGMC	$+1.3\%$	$+21.0\%$	$+14.6\%$
	ON-SB	-17.1%	$+0.2\%$	-2.1%
$\eta'_{\rho\gamma}K^+$	SIGMC	$+0.3\%$	$+20.0\%$	$+13.9\%$
	ON-SB	-15.4%	$+1.1\%$	-0.2%

We conclude that the dominant correlation between the Fisher discriminant and the tagging category is removed for continuum with the variable $\mathcal{F}_{T04}$.

Definition of $\mathcal{F}'_{T04}$

Like for $\mathcal{F}_{T04}$, the purpose of $\mathcal{F}'_{T04}$ is to remove to first order the correlation between the shape of the Fisher distribution and the tagging category. The correction is done on a category by category basis. For each tagging category, we shift the value of $\mathcal{F}_{LGD}$ such that the distribution for all category have the same average.

We define the new Fisher variable $\mathcal{F}'_{T04}$ as

$$\mathcal{F}'_{T04} = \mathcal{F}_{LGD} + \delta(\mathrm{Cat_{Tag04}}), \tag{6.5}$$

where

$$\begin{aligned}
\delta(\mathrm{Cat_{Tag04}} = 0) &= +0.106,\\
\delta(\mathrm{Cat_{Tag04}} = 63) &= +0.010,\\
\delta(\mathrm{Cat_{Tag04}} = 64) &= -0.294,\\
\delta(\mathrm{Cat_{Tag04}} = 65) &= -0.070,\\
\delta(\mathrm{Cat_{Tag04}} = 66) &= -0.005,\\
\delta(\mathrm{Cat_{Tag04}} = 67) &= -0.024,
\end{aligned}$$

$$\delta(\mathrm{Cat}_{\mathrm{Tag04}} = 68) \quad = +0.008.$$

Properties of $\mathcal{F}'_{T04}$

We checked that the correlation between the $\mathcal{F}'_{T04}$ mean and the tagging category was reduced for continuum. Fig. 6.4 shows the fitted mean of a bifurcated Gaussian to the $\mathcal{F}'_{T04}$ distribution versus the Tag04 tagging category. The correlation for continuum is clearly small compared to that of $\mathcal{F}_{LGD}$, and the mean is also more constant over categories than it is for $\mathcal{F}_{T04}$. The residual variations come from the fact that the plot shows the mean of a fitted bifurcated gaussian while the correction was determined from the average of the distribution for each category.

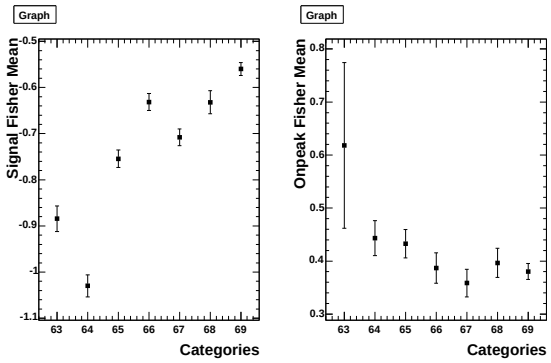

Figure 6.4: Variation of the mean of a bifurcated Gaussian fitted to the $\mathcal{F}'_{T04}$ distribution for each category, for signal MC (left) and onpeak sidebands (right).

Finally, we determined directly from the signal and onpeak sideband data the correlation between $\mathcal{F}'_{T04}$ and the Tag04 tagging category. For four $\eta' K$ modes, we obtain the raw correlations given in Table 6.1. The correlations for both signal and onpeak sidebands are improved relative to that for $\mathcal{F}_{T04}$.

We conclude that the dominant correlation between the Fisher discriminant and the tagging category better removed with the variable $\mathcal{F}'_{T04}$. Furthermore, the correlations in signal are significantly reduced relative to $\mathcal{F}_{T04}$ ($\sim 14\%$ VS $\sim 21\%$).

6.3 Kinematical variables

The B candidates, coming from $e^+e^- \rightarrow \Upsilon(4\mathrm{S}) \rightarrow B\overline{B}$ reaction, have been characterized kinematically by ΔE and M_{ES} . The invariant ΔE is defined as the difference

between B candidate energy and beam energy, calculated in the CM:

$$\Delta E = \frac{2q_{\Upsilon(4S)}q_B - s}{2\sqrt{s}} \tag{6.6}$$

where $q_{\Upsilon(4S)}$ and q_B are four-momenta of the $\Upsilon(4S)$ and the B candidate. In the Fig. 6.5 we can see that ΔE presents a gaussian distribution for the signal events while linear for the continuum background.

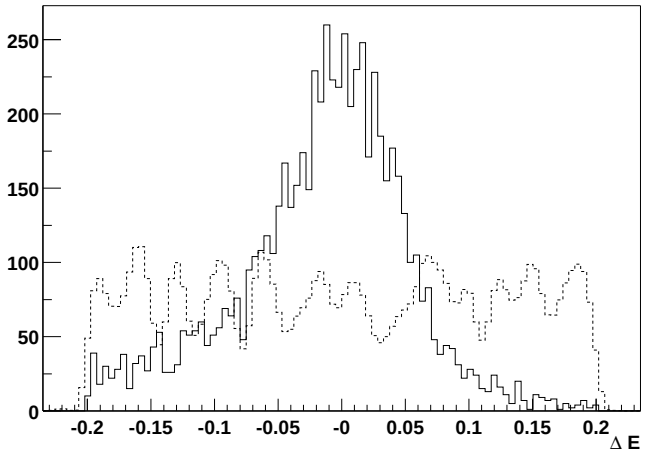

Figure 6.5: ΔE : comparison between continuum background (off-peak) and Monte Carlo signal events.

Other kinematical variable is the B candidate mass that has a little correlation with ΔE . The M_{ES} is the beam-energy substituted mass, computed in the LAB frame and independent of mass hypotheses assigned to B candidate daughters:

$$M_{ES} = \sqrt{\frac{(s/2 + \vec{p}_{\Upsilon(4S)} \cdot \vec{p}_B)^2}{E^2_{\Upsilon(4S)}} - \vec{p}_B^{\,2}} \tag{6.7}$$

where $s \equiv (q_{\Upsilon(4S)})^2$ is the square of the CM energy, $p_{\Upsilon(4S)}$ and p_B are three-momenta of the $\Upsilon(4S)$ and the B candidate in the LAB frame and $E_{\Upsilon(4S)} \equiv q^0_{\Upsilon(4S)}$ is the energy of the $\Upsilon(4S)$ in the LAB frame. The comparison between M_{ES} distributions for signal and background are shown in Fig. 6.6; in the background events M_{ES} has been described through ARGUS [24] function:

$$F(x) = Cx\sqrt{1-(M_{ES}/E^*_{fascio})^2}\ e^{-\xi(1-(M_{ES}/E^*_{fascio})^2)}. \tag{6.8}$$

where C is a normalization factor and ξ is a shape parameter.

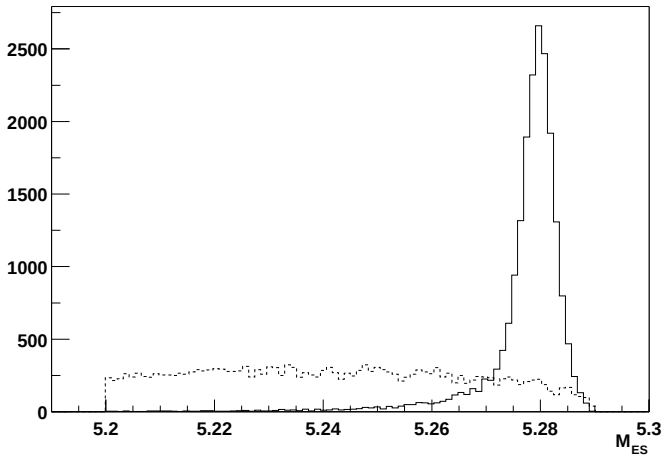

Figure 6.6: M_{ES} variable distributions for off-peak background events (dashed line) and Monte Carlo signal events.

Chapter 7

Signal yield extraction and measurement of CP time-dependent asymmetry in the $B \to \eta' K$ decay

7.1 Introduction

In this chapter will be presented the analysis for the signal yield extraction and measurement of CP time-dependent asymmetry in the $B \to \eta' K$ decay. In this decay channel we consider the following sub-decays of η' and K^0_S mesons:

- η'in $\eta\pi\pi$ and $\rho^0\gamma$ with $\eta \to \gamma\gamma$ and $\eta \to \pi^0\pi^+\pi^-$
- K^0_S in $K^0_S \to \pi^+\pi^-$ and $K^0_S \to \pi^0\pi^0$

We consider as main sub-decays the ones with η' in $\rho\gamma$, $\eta(\gamma\gamma)\pi\pi$ and $K^0_S \to \pi^+\pi^-$ because they have a higher statistics. In this thesis work our goal is to add events from sub-decays with η' in $\eta(\pi^0\pi^+\pi^-)\pi\pi$ and $K^0_S \to \pi^0\pi^0$ to increase the number of signal events used in the Time-Dependent CP violation analysis. So in this thesis we have studied the following decays:

- $B^0 \to \eta' K^0_S$ with η' in $\eta\pi\pi$ (η in $\pi^0\pi^+\pi^-$) and K^0_S in $\pi^+\pi^-$
- $B^0 \to \eta' K^0_S$ with η' in $\rho^0\gamma$ and K^0_S in $\pi^0\pi^0$
- $B^0 \to \eta' K^0_S$ with η' in $\eta\pi\pi$ (η in $\gamma\gamma$) and K^0_S in $\pi^0\pi^0$
- $B^\pm \to \eta' K^\pm$ with η' in $\eta\pi\pi$ (η in $\pi^0\pi^+\pi^-$)

These channels are interesting for the CP violation studies: the tree diagrams contribution is expected to be little and so the interference between these diagrams and the penguin ones can allow CP violation. The difference between the measurement of CKM matrix phase obtained by these channels and the one obtained by *charmed* channels can be considered as evidence of new physics. The analysis has been done through extended maximum likelihood technique (EML) and it's divided in two steps. In the first step we determine the signal event number in the *on-peak* sample. In this case tagging and Δt informations aren't used to avoid any result alterations. Before extracting the number of signal events we have to choose useful variables, optimized cuts, corrections, PDFs etc.: this is a very important part of the analysis. Once obtained the number of signal and background events, we determine the S and C parameters. In this second step we introduce tagging and Δt informations and the B mesons decay rate PDF. The result of the fit is represented by mean value and by the errors of S and C parameters.

The analysis, following collaboration choices, has been done in two parts. First one consists in a *blind* phase where all decisions are taken without operating on data we want to extract signal yields. Then, we pass to the second (*unblind*) phase, where we analyze the taken data at the $\Upsilon(4\mathrm{S})$ resonance energy (*onpeak*) and it's not possible to modify all the things done before. This way to work can erase the possibility to introduce distortions in the results due to prejudices or corrections to push results in a predefined direction. For the measurement of CP time-dependent asymmetry in the *blind* phase we analyze *onpeak* sample to determine statistic and systematic errors. The *blind* procedure in this case consists in moving of a certain unknown quantity the results obtained by the fit for both CP-violating S and C parameters, leaving the same errors.

In August *BABAR* measured these terms and they had been submitted to ICHEP2004 [15]:

$$S_{\eta' K^0_S} = 0.27 \pm 0.14\ (\mathrm{stat}) \pm 0.03\ (\mathrm{syst}) \qquad S_{\eta' K^+} = -0.10 \pm 0.07\ (\mathrm{stat})$$
$$C_{\eta' K^0_S} = -0.21 \pm 0.10\ (\mathrm{stat}) \pm 0.03\ (\mathrm{syst}) \qquad C_{\eta' K^+} = -0.05 \pm 0.06\ (\mathrm{stat})$$

All the results obtained and described in this chapter have to be contextualized in the Milan working group on behalf *BABAR* collaboration; analysis of these decay channels is described in B.A.D.(**B**abar **A**nalysis **D**ocument) #907 [29] and in B.A.D. #906 [28]. These results have been presented at "Meeting of APS, Division of Particles and Fields", Tampa FL(USA), April 16th 2005.

7.2 Data sample

The analysis presented in this work is based on the data taken by *BABAR* in the period 1999-2004 ("Summer2004" sample composed by Run1-4). Results in this thesis are based on the following samples:

- On-resonance data:
  - 210.9 fb^{-1}, (232.0 ± 2.5) million of $B\overline{B}$ pairs.
- Off-resonance data:
  - 11.7 fb^{-1}.
- $B\overline{B}$ Monte Carlo:
  - 206.6 millions events for the $B^0\overline{B}^0$.
  - 207.4 millions events for the B^+B^-.
- Signal Monte Carlo: statistics used for the different modes can be seen in Table 7.1.

$\eta'_{\rho\gamma}K^0_S$ $(K^0_S \to \pi^0\pi^0)$	$\eta'_{\eta(\gamma\gamma)\pi\pi}K^0_S(K^0_S \to \pi^0\pi^0)$	$\eta'_{\eta(3\pi)\pi\pi}K^0_S(K^0_S \to \pi^+\pi^-)$	$\eta'_{\eta(3\pi)\pi\pi}K^+$
65000	67000	96000	105000

Table 7.1: SP6 Monte Carlo signal events

7.3 Extended maximum likelihood analysis

7.3.1 Input to Maximum Likelihood

An unbinned multivariate maximum likelihood (ML) analysis has been done, using MiFit [30]. The events, after the initial selection with the reconstruction cuts described in the Sec.5.2, are selected with further cuts. We summarize all cuts to produce the input to maximum likelihood. All the energies and momenta are given in the lab frame. The cuts done at ntuple level are:

- a minimum number of charged tracks in the event equal to the number of charged tracks of B candidates plus 1;
- $|\cos\theta_{\rm T}| < 0.9$;
- $E_\gamma > 0.050$ GeV for for $\eta \to \gamma\gamma$, $E_\gamma > 0.030$ GeV for the γ in π^0 and $E_\gamma > 0.100$ GeV for $\eta' \to \rho^0\gamma$;
- $5.25 < M_{ES} < 5.29$ GeV/c^2;
- $|\Delta E| < 0.2$ GeV;
- Charged tracks from η' candidates satisfy electron, kaon and proton vetoes;
- π^0 mass between 0.120 and 0.150 GeV/c^2 (between 0.100 and 0.155 GeV/c^2 for $K^0_S \to \pi^0\pi^0$ analysis) ;
- $E_{\pi^0} > 0.200$ GeV;
- ρ^0 mass between 0.510 and 1.000 GeV/c^2;
- for $K^0_S \to \pi^+\pi^-$ we consider K^0_S mass between 0.486 and 0.510 GeV/c^2, fit probability $\chi^2 > 0.001$ and flight lenght $> 3\sigma$; for $K^0_S \to \pi^0\pi^0$ analysis, K^0_S mass is between 0.468 and 0.528 GeV/c^2;
- the ρ^0 helicity $\mathcal{H}^0_\rho = \cos\theta_H$ (cosine of the vector meson's rest frame decay angle of a pion respect to η' flight direction) with $|\mathcal{H}^0_\rho| < 0.9$;
- η mass between 0.490 and 0.600 GeV/c^2 for $\eta \to \gamma\gamma$ GeV/c^2 and between 0.520 and 0.570 GeV/c^2 for $\eta \to \pi^+\pi^-\pi^0$;
- η' mass between 0.930 and 0.980 GeV/c^2 for $\eta' \to \rho^0\gamma$ and between 0.945 and 0.970 for $\eta' \to \eta\pi^+\pi^-$;
- Fisher discriminant: $-4 < \mathcal{F} < 5$;

The cuts done for Time Dependent analysis are:

- $|\Delta t| < 20$ ps ;
- $\sigma_{\Delta t} < 2.5$ ps ;

For charged B we have also done at ntuple level the following cuts:

- bachelor track satisfies electron and proton vetoes;
- number of measured DIRC Cherenkov photons (N_γ) for bachelor track at least equal to 5;
- kaon DIRC hypothesis pull ($pullK$) inside the range $[-5, +2]$. The pulls have been corrected for momentum, polar angle, charge and run number dependences with a prescription for DIRC thetaC resolutions and offset from expected values for kaons and pions [31]. We show in Fig. 7.1 the DIRC pull for $\eta'_{\eta\pi\pi}K^{\pm}$ and $\eta'_{\eta\pi\pi}\pi^{+}$ for kaon hypotesis. In the distribution the area has been normalized to 1 and we applied a cut between $[-6, 6]$. This pull has been cut between $[-5, +2]$

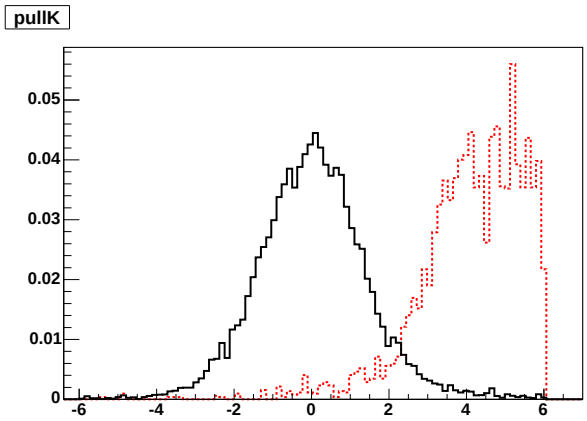

Figure 7.1: DIRC pull for $B^+ \to \eta' K^+$ (black solid line) and $B^+ \to \eta' \pi^+$ (red dashed line) in kaon hypothesis.

for pion and badly reconstructed candidates rejection.

If an event has multiple combinations, the program selects the best one using a χ^2 quantity computed with η' mass and also η mass in the $\eta\pi^+\pi^-$ modes.

All efficiencies after successive cuts are shown in Table 7.2, Table 7.3, Table 7.4, Table 7.5.

7.3.2 "Self-Cross-Feed"

Due to the presence of neutrals and soft tracks, some of the signal events are misreconstructed: it could happen that there is a permutation between two tracks or gammas coming from signal events (denoted as PP) or a particle reconstructed taking a fake

	Signal MC	on-res	off-res	B^+B^-	$B^0\overline{B}^0$
# Events Generated or Integrated Luminosity					
	65000	110.8 fb^{-1}	11.7 fb^{-1}	$32.3 \cdot 10^6$	$64.5 \cdot 10^6$
# Candidates after the preliminary cuts					
	19684	164618	17517	1371	1488
Candidates after the following cuts (%)					
e, K, p vetoes	95.61	64.01	63.93	51.13	59.74
$0.510 < m_{\rho^0} < 1.000$ GeV/c^2	98.66	91.22	91.52	94.29	91.23
$0.468 < m_{K^0_S} < 0.528$ GeV/c^2	84.52	61.83	62.10	60.21	62.89
$0.100 < m_{\pi^0} < 0.155$ GeV/c^2	100.0	100.0	100.0	100.0	100.0
$p_{\pi^0} > 0.200$ GeV/c	98.20	95.05	94.93	91.71	96.08
$E_\gamma > 0.200$ GeV	75.90	62.72	63.08	46.03	48.57
$\lvert\mathcal{H}^0_\rho\rvert < 0.9$	97.25	89.60	89.92	85.71	88.66
$0.910 < m_{\eta'} < 0.990$ GeV/c^2	94.96	74.74	74.20	76.39	76.30
# Events Input to ML fit (with the best candidate chosen)					
	8476	18270	1930	83	134

Table 7.2: Candidate yields after successive selection criteria in the sub-decay $\eta'_{\rho\gamma} K^0_S$ ($K^0_S \to \pi^0\pi^0$) .

	Signal MC	on-res	off-res	B^+B^-	$B^0\overline{B}^0$
# Events Generated or Integrated Luminosity					
	67000	110.8 fb^{-1}	11.7 fb^{-1}	$32.2 \cdot 10^6$	$67.4 \cdot 10^6$
# Candidates after the preliminary cuts					
	21163	11068	1186	52	69
Candidates after the following cuts (%)					
e, K, p vetoes	97.59	73.59	73.44	67.31	62.32
$0.468 < m_{K^0_S} < 0.528$ GeV/c^2	84.81	62.68	57.63	57.14	76.74
$0.100 < m_{\pi^0} < 0.155$ GeV/c^2	100.0	100.0	100.0	100.0	100.0
$p_{\pi^0} > 0.200$ GeV/c	98.10	95.20	94.22	100.0	96.97
$0.490 < m_\eta < 0.600$ GeV/c^2	89.92	75.74	75.26	95.00	53.12
$0.930 < m_{\eta'} < 0.990$ GeV/c^2	90.96	60.42	55.62	57.89	52.94
# Events Input to ML fit (with the best candidate chosen)					
	9774	1545	150	7	8

Table 7.3: Candidate yields after successive selection criteria in the sub-decay $\eta'_{\eta(\gamma\gamma)\pi\pi} K^0_S$ ($K^0_S \to \pi^0\pi^0$) .

	Signal MC	on-res	off-res	B^+B^-	$B^0\overline{B}^0$
# Events Generated or Integrated Luminosity					
	96000	110.8 fb^{-1}	11.7 fb^{-1}	$278 \cdot 10^6$	$275 \cdot 10^6$
# Candidates after the preliminary cuts					
	206691	9870	1031	297	925
Candidates after the following cuts (%)					
e, K, p vetoes	95.31	62.92	59.26	27.95	60.22
$0.120 < m_{\pi^0} < 0.150$ GeV/c^2	64.08	58.37	56.63	71.08	57.27
$p_{\pi^0} > 0.200$ GeV/c	92.13	91.89	84.68	96.61	87.77
$0.488 < m_{K^0_S} < 0.508$ GeV/c^2	95.49	84.75	89.42	70.18	86.07
$0.520 < m_\eta < 0.570$ GeV/c^2	54.28	48.07	42.75	30.00	42.74
$0.930 < m_{\eta'} < 0.990$ GeV/c^2	89.27	75.46	63.39	58.33	49.51
# Events Input to ML fi t (with the best candidate chosen)					
	17143	413	35	4	25

Table 7.4: Candidate yields after successive selection criteria in the sub-decay $\eta'_{\eta(3\pi)\pi\pi}K^0_S$ ($K^0_S \to \pi^+\pi^-$) .

	Signal MC	on-res	off-res	B^+B^-	$B^0\overline{B}^0$
# Events Generated or Integrated Luminosity					
	105000	110.8 fb^{-1}	11.7 fb^{-1}	$277 \cdot 10^6$	$264 \cdot 10^6$
# Candidates after the preliminary cuts					
	265168	99620	11267	5554	2808
Candidates after the following cuts (%)					
e, K, p vetoes	94.04	56.64	58.45	45.89	45.41
$0.120 < m_{\pi^0} < 0.150$ GeV/c^2	63.91	58.46	57.61	61.28	62.51
$p_{\pi^0} > 0.200$ GeV/c	92.17	90.87	89.62	92.64	93.60
$0.520 < m_\eta < 0.570$ GeV/c^2	54.44	46.04	45.76	44.92	42.46
$0.930 < m_{\eta'} < 0.990$ GeV/c^2	89.31	73.70	74.16	63.85	56.33
$N_\gamma > 5$	87.79	85.34	86.83	87.23	88.20
$-5 < pullK < 2$	90.52	39.74	36.33	34.53	13.38
# Events Input to ML fi t (with the best candidate chosen)					
	18114	1419	153	56	9

Table 7.5: Candidate yields after successive selection criteria in the sub-decay $\eta'_{\eta(3\pi)\pi\pi}K^+$.

one from rest of event (ROE) (denoted as self-cross-feed or SXF). Since those events still contain useful CP information, we retain and model them separately from true signal. In Table 7.6 we summarized, after choosing the best candidate, the number of input events, the events with fake B and an η' or a K meson correctly reconstructed and between them the events reconstructed with PP (gammas for K_S^0 and pions for η and η') and SXF.

	$\eta'_{\eta(\gamma\gamma)\pi\pi}K_S^0$	$\eta'_{\rho\gamma}K_S^0$	$\eta'_{\eta(3\pi)\pi\pi}K_S^0$	$\eta'_{\eta(3\pi)\pi\pi}K^+$
Input to maximum likelihood				
	9063	9326	13820	15778
B Truth (%)				
	58.7	56.8	62.5	61.6
Events with fake K and η' correctly reconstructed (%)				
	32.7	33.3	1.0	0.0
PP events	14.7	14.5	–	–
SXF events	18.0	18.8	1.0	0.0
Events with fake η' and K correctly reconstructed (%)				
	4.1	5.0	36.0	38.4
PP events	–	–	18.0	9.6
SXF events	4.1	5.0	18.0	28.8
Events with fake η' and K (%)				
	4.6	5.0	0.6	0.0
PP events	0.6	0.9	0.2	–
SXF events	4.0	4.1	0.4	0.0
SXF fraction for all events (%)				
	26.1	27.9	19.4	28.8

Table 7.6: Signal input and self-cross-feed results.

For $\eta'_{\eta\pi\pi}K_S^0$ we studied all the possible combination to reconstruct a fake K_S^0 considering PP events (the possible permutations between gammas coming from η, η' or from the two π^0 in decay $K_S^0 \to \pi^0\pi^0$) and SXF events, i.e. a gamma taken from rest of event. The results are shown in Table 7.7. In the last row of this table we considered cases where a K_S^0 is reconstructed taken more that one gamma from η, η' or ROE.

	$\eta'_{\eta\pi\pi}K^0_S$	$\eta'_{\rho\gamma}K^0_S$
$Total\ Input\ To\ ML\ Fit$	9063	9326
$Ks\ Truth\ (\%)$	62.7	61.8
$Gammas\ Permuted\ (\%)$	15.3	15.5
$One\ Gamma\ From\ ROE\ (\%)$	20.6	21.7
$One\ Gamma\ From\ \eta$ or $\eta'\ (\%)$	1.4	1.0

Table 7.7: K^0_S cross feed study

In our ML fit we consider the two components for signal events:

- **MC truth events**: the sum of signal correctly reconstructed and of signal events reconstructed with permutated gammas or pions (PP events);
- **SXF events**: the SXF fraction will be fixed in our fits.

7.3.3 Fit description

In our sample of events we have considered three components: signal, "self-cross-feed" (see section 7.3.2) and continuum background. For $\eta' \to \rho^0\gamma$ sub-decay is necessary to add a $B\overline{B}$ background component. We will indicate with the index j the species of the event. The discriminating variables used in the fits are: M_{ES} , ΔE , $\mathcal{F}$ and Δt . In the Tag04 tagger we have 6 tagging categories plus the untagged events (which we call category 0)(for more details see Sec.7.4.1). We use the index c = (0, 1, 2, 3, 4 ,5 ,6) to indicate that the event belongs to one specific category. For each species j and each category c, we define a total PDF for the events i as:

$$\mathcal{P}^i_{j,c} = \mathcal{P}_j(M_{ES}{}^i) \cdot \mathcal{P}_j(\Delta E{}^i) \cdot \mathcal{P}_j(\mathcal{F}{}^i) \cdot \mathcal{P}_j(\Delta t^i, \sigma^i_{\Delta t}, c) \tag{7.1}$$

where the index j is the species of the event. If with n_{sig} we indicate the number of signal events and with $f_{sig,c}$ the fraction of signal events for each category, then the number of events for each different category is:

$$n_{sig,c} = n_{sig} f_{sig,c}. \tag{7.2}$$

Introducing the "self-cross-feed" (SXF) events category, we defined the fraction of SXF events respect to total signal events as f_{SXF}; so for each input event i belonging to a specific tag category c, the likelihood function is defined as:

$$\mathcal{L}^i_c = n_{sig} f_{sig,c}(1 - f_{SXF})\mathcal{P}^i_{sig,c} + n_{sig} f_{sig,c} f_{SXF} \mathcal{P}^i_{SXF,c} + n_{q\overline{q},c}\mathcal{P}^i_{q\overline{q}}. \tag{7.3}$$

We fixed in our fits SXF fractions obtained from MC studies. The extended likelihood function for all events belonging to category c is:

$$\mathcal{L}_c = \frac{\exp\left(-\sum_j n_{j,c}\right)}{N_c!} \prod_i^{N_c} \mathcal{L}^i_c \tag{7.4}$$

where N_c is the total number of input events in category c.

Finally the total likelihood function for all categories can be written as:

$$\mathcal{L} = \prod_{c=0}^{6} \mathcal{L}_c \tag{7.5}$$

To fit two (or more) different sub-decay modes, the total likelihood becomes:

$$\mathcal{L} = \prod_{d} \mathcal{L}^d \tag{7.6}$$

where the index d runs over the fitted sub-decay modes. Our fitter minimizes the expression $-\ln \mathcal{L}$ with respect to a set of free parameters.

7.3.4 Discriminating Variables and their Probability Distribution Functions

The discriminating variables used in the ML fits are: M_{ES} , ΔE , $\mathcal{F}$. In this section we describe the PDFs of the discriminating variables for signal, SXF and background. PDFs for signal, SXF and $B\overline{B}$ background have been done using Monte Carlo simulated events. PDFs for continuum background have been done using on-peak sidebands, defined as:

- *Grand Side Band* (GSB): $5.25 < M_{ES} < 5.27$ GeV/c^2
- ΔE *Side Band* (DESB): $0.1 < |\Delta E\,| < 0.2$ GeV

The values of background PDFs parameters obtained in these fits are used as initial values in the ML fits where they are floating. Appendix A shows PDFs plots and correlations between input variables. The parameters for the M_{ES} background distributions are determined by fits to DESB sidebands, while the other parameters are determined from GSB data. The Table 7.8 reports the parametrization chosen for the different PDF(G is for Gaussian, A for Argus, CH for Chebychev polynomial, K for KEYS [22]). From control sample studies, we apply these MC/data matching corrections for signal PDF parameters when we fit on real data:

- we scale the sigma of core Gaussian of ΔE PDFs by 1.05;
- we shift the central value of core Gaussian of M_{ES} PDFs by (MeV/c^2): $+0.8$, $+0.6$, $+0.4$, $+0.1$ for Run1, Run2, Run3 and Run4 data, respectively.

	ΔE	M_{ES}	$\mathcal{F}$
SIGNAL (without SXF) PDF parametrisation			
$\eta'_{\rho\gamma}K^0_S$	double G	double G	asymmetric G
$\eta'_{\eta(\gamma\gamma)\pi\pi}K^0_S$	double G	double G	asymmetric G
$\eta'_{\eta(3\pi)\pi\pi}K^0_S$	double G	double G	G + asymmetric G
$\eta'_{\eta(3\pi)\pi\pi}K^+$	double G	double G	asymmetric G
SXF PDF parametrisation			
$\eta'_{\rho\gamma}K^0_S$	G	double G	asymmetric G
$\eta'_{\eta(\gamma\gamma)\pi\pi}K^0_S$	G	double G	asymmetric G
$\eta'_{\eta(3\pi)\pi\pi}K^0_S$	1^{st} order CH + G	G + asymmetric G	double G
$\eta'_{\eta(3\pi)\pi\pi}K^+$	double G	double G	asymmetric G
CONTINUUM BACKGROUND PDF parametrisation			
$\eta'_{\rho\gamma}K^0_S$	1^{st} order CH	A	1^{st} order CH + asymmetric G
$\eta'_{\eta(\gamma\gamma)\pi\pi}K^0_S$	1^{st} order CH	A	1^{st} order CH + asymmetric G
$\eta'_{\eta(3\pi)\pi\pi}K^0_S$	1^{st} order CH	A	asymmetric G
$\eta'_{\eta(3\pi)\pi\pi}K^+$	1^{st} order CH	A	1^{st} order CH + asymmetric G
$B\overline{B}$ BACKGROUND PDF parametrisation			
$\eta'_{\rho\gamma}K^0_S$	K	K	asymmetric G

Table 7.8: PDF used for signal, SXF and background parametrisation.

7.3.5 Correlations among Discriminating Variables

The likelihood function we are using in our fits is based on the assumption that the variables used in the fit are uncorrelated. We show in Appendix A the correlation coefficients for all pairs of M_{ES} , ΔE , $\mathcal{F}$, Δt and $\sigma_{\Delta t}$ in Monte Carlo signal events and in side band on-resonance data. As you can see the correlations are below 10% so we can assume that our initial assumption is correct.

7.4 Time-dependent *CP* fitting

7.4.1 Overview

Defining $\Delta t \ = t_{CP} - t_{\rm tag}$, where t_{CP} and $t_{\rm tag}$ are the proper decay times of the CP and tagged B's, respectively, the decay rate distribution $f_+ \, (f_-)$ for $B_{CP} \to f$ when $B_{\rm tag}$ is a $B^0 \, (\overline{B}^0)$ is given by

$$f_{\pm}(\delta t) = \frac{e^{-|\Delta t|/\tau}}{4\tau} \left[1 \pm S_f \sin(\Delta m_d \Delta t) \mp C_f \cos(\Delta m_d \Delta t)\right], \tag{7.7}$$

where τ is the average B^0 lifetime, Δm_d is the mixing frequency, and

$$S_f = \frac{2\mathcal{I}m\lambda}{1+|\lambda|^2} \quad \text{and} \quad C_f = \frac{1-|\lambda|^2}{1+|\lambda|^2}. \tag{7.8}$$

λ is defined as:

$$\lambda \equiv \frac{q}{p}\frac{\overline{A}_f}{A_f} = \eta_f e^{-2i\beta}\frac{\overline{A}_{\overline{f}}}{A_f}, \tag{7.9}$$

where $e^{-2i\beta}$ is the mixing phase, $A_f \, (\overline{A}_{\overline{f}})$ is the amplitude for the decay $B^0 \to f \, (\overline{B}^0 \to \overline{f})$, η_f is the CP eigenvalue of the final state. No CP violation in mixing ($|q/p| = 1$) is assumed. CP violation effects can arise from interference between different decay amplitudes ($\left|\overline{A}_{\overline{f}}/A_f\right| \neq 1$) and interference between the mixing and decay weak phases. C_f parameter measures direct CP violation and if we assume $C_f = 1$, we obtain $S_f = \sin 2\beta$, where β is an angle of unitary triangle.

In the case of imperfect tagging, Eq. 7.7 must be modified to include the mistag probabilities:

$$f_{B^0\,\rm tag} \ = \ (1 - w_{B^0}) f_+ + w_{\overline{B^0}} f_-,$$

$$f_{\overline{B}^0\,\mathrm{tag}} = (1 - w_{\overline{B^0}}) f_- + w_{B^0} f_+, \tag{7.10}$$

where w_{B^0} ($w_{\overline{B^0}}$) is the probability that a true B^0 ($\overline{B}^0$) meson is tagged as a $\overline{B}^0$ (B^0). Defining the average mistag $\langle w \rangle$, and the mistag difference Δw,

$$\begin{aligned} \langle w \rangle &= \frac{w_{B^0} + w_{\overline{B^0}}}{2}, \\ \Delta w &= w_{B^0} - w_{\overline{B^0}}, \end{aligned} \tag{7.11}$$

the decay rate distributions, assuming perfect vertex resolution, are then

$$\begin{aligned} f_{B^0\,\mathrm{tag}} &= \frac{e^{-|\Delta t|/\tau}}{4\tau} \left[1 - \Delta w + (1 - 2\langle w \rangle) \left(S_f \sin(\Delta m_d \Delta t) - C_f \cos(\Delta m_d \Delta t)\right)\right], \\ f_{\overline{B}^0\,\mathrm{tag}} &= \frac{e^{-|\Delta t|/\tau}}{4\tau} \left[1 + \Delta w - (1 - 2\langle w \rangle) \left(S_f \sin(\Delta m_d \Delta t) - C_f \cos(\Delta m_d \Delta t)\right)\right] \end{aligned} \tag{7.12}$$

The final (observed) distribution $F(\Delta t)$ is the convolution of $f(\Delta t)$ with the signal vertex resolution function $\mathcal{R}_{\mathrm{sig}}(\Delta t)$

$$\begin{aligned} F_{B^0\,\mathrm{tag}} &= f_{B^0\,\mathrm{tag}} \otimes \mathcal{R}_{\mathrm{sig}}, \\ F_{\overline{B}^0\,\mathrm{tag}} &= f_{\overline{B}^0\,\mathrm{tag}} \otimes \mathcal{R}_{\mathrm{sig}}. \end{aligned} \tag{7.13}$$

For the time-dependence fit, we proceed as discussed in the section 1.2, while adding the quantity Δt and its error. We require $|dt| < 20$ ps and $\sigma_{\Delta t} < 2.5$ ps.

In our fits we fix the values of Δm_d and the B lifetimes to the PDG values [11]: $\Delta m_d = 0.502 \pm 0.007$ ps^{-1}, $\tau_{B^+} = 1.671 \pm 0.018$ ps, and $\tau_{B^0} = 1.536 \pm 0.014$ ps.

In order to tag the flavour of the "tag" side of the event, we use a tagger called “Tag04”. This tagging algorithm is designed to tag the flavor of the B in two stages: first of all the information relative to a particular physics precess are combined in a Neural Network to obtain a sub-tagger; then all the sub-taggers are combined in a larger Neural Network that determines the probability for the entire event. Based on the output of the various neural nets, each event is assigned to a physics category. The algorithm uses 9 input sub-taggers and has 6 output Physics Categories:*Lepton, Kaon I, Kaon II, Kaon&Pion, Pion, Others* . *Lepton* contains the events in which flavor identification is possible through a lepton identification or if present a kaon. Events with kaons or weak pions with opposite charge but similar flight direction are assigned to *Kaon I* category. Events with only a kaon tag are assigned to *Kaon I*

or *Kaon II* category following the probability of an uncorrected identification. *Kaon II* category contains the residual events with a weak pion. *Kaon&Pion* category has events where both a charged kaon and a slow pion candidates are present. Tag is assigned by requiring a kaon and a slow pion tag with agree (i.e. the kaon and the slow pion candidate must have opposite charge) and additionally exploiting the angular correlation between the two tracks. Events coming from slow pions are assigned as *Pion* category. All the other events are assigned to *Others* category or excluded *no Tag* if the probability of an uncorrected identification is too high. We also include the untagged events in the fit, with mistag fraction fixed to 0.5 and mistag difference fixed to zero. We split several quantities according to these tagging categories: signal fraction, mistag fractions and mistag differences, background yields, and core offset of the signal Δt resolution function.

The signal fraction, mistag fractions and mistag differences, and the parameters of signal Δt resolution model are obtained from fits to the BReco samples with the same PDF strategy used in previous BReco fits. BReco sample is a data sample with events completely reconstructed useful to determine B^0 flavor.

7.4.2 Fits on BReco data

We fit on BReco data to obtain the signal fraction, mistag fractions and mistag differences, and the parameters of signal Δt resolution model in order to fix them in our CP fit for our decay modes. We fit on both MC and real data. We use M_{ES} distribution to discriminate between signal and background events. As signal PDF we use a double Gaussian obtained from fit on MC signal events, while for backgorund we use an Argus function. We find the Argus shape parameter separately for each tagging category, and leave them floating in the fit. We fit the Δt for both signal and background using the BMixing physics model convoluted with a resolution model. The BMixing physics model uses as parameters six quantities: lifetime, Δm_d, mistag fraction, mistag difference, tag and reco efficiency differences. We have four components for Δt :

- **signal**
  The lifetime and Δm_d are fixed to their PDG values for neutral B. We use a triple Gaussian as resolution model (core, tail and outlier), where the core and tail biases and resolutions are scaled to $\sigma_{\Delta t}$ (with the tail scale factor fixed at 3.0),

and the outlier Gaussian has mean value fixed at zero and width fixed at 8 ps. The signal efficiency, mistag fraction, mistag difference, tag efficiency difference for each tagging category are listed in Table 7.9 for real data and Table 7.13 for MC events. The signal resolution parameters are given in Table 7.11 for real data and Table 7.14 for MC events.

- **peaking background**
  The lifetime is fixed to his PDG value for charged B and Δm_d is fixed to zero. The mistag differences are fixed at zero. We fix the fraction of peaking background to signal component at 1.5 %. The resolution model, tag and reco efficiency differences are the same of the signal component.

- **lifetime background**
  The mistag differences, Δm_d and tag and reco efficiency differences are fixed to zero. The mistag fractions and the background lifetime are listed in Table 7.10. We use a double Gaussian resolution model (core and outlier) where the core bias and resolution are scaled to $\sigma_{\Delta t}$ and the outlier Gaussian again has a fixed mean and width. The background resolution parameters are shown in Table 7.12.

- **prompt background** (*i.e.* zero lifetime)
  The lifetime, mistag differences, Δm_d and tag and reco efficiency differences are fixed to zero. The resolution model is the same of lifetime background component. The fraction of prompt background and background mistag fractions are listed in Table 7.10.

Table 7.9: Breco signal tagging fractions (f), mistag fractions ($\langle w \rangle$), mistag differences (Δw) and tag efficiency difference (μ) for each tagging category determined from fit to the neutral Breco sample. The reco efficiency difference is $\nu = 0.0019 \pm 0.0056$.

Category	f_{sig}	$\langle w \rangle$	Δw	μ
`Lepton`	0.0873 ± 0.0011	0.0187 ± 0.0048	-0.0015 ± 0.0087	0.0030 ± 0.0157
`KaonI`	0.1089 ± 0.0013	0.0521 ± 0.0051	-0.0197 ± 0.0092	-0.0276 ± 0.0151
`KaonII`	0.1716 ± 0.0016	0.1415 ± 0.0056	-0.0148 ± 0.0092	-0.0042 ± 0.0136
`KorPI`	0.1368 ± 0.0015	0.2182 ± 0.0070	-0.0022 ± 0.0110	-0.0109 ± 0.0156
`Pions`	0.1433 ± 0.0015	0.3215 ± 0.0074	0.0658 ± 0.0110	-0.0208 ± 0.0157
`Other`	0.1005 ± 0.0013	0.4004 ± 0.0091	0.0447 ± 0.0132	0.0105 ± 0.0185
`Untagged`	0.2516 ± 0.0034	0.5	0	0

Table 7.10: Fit results for Breco prompt background and lifetime mistag fractions and the fraction of prompt background for the neutral Breco sample. The fit background lifetime is 1.202 ± 0.032 ps.

Category	f_P	$\langle w_L \rangle$	$\langle w_P \rangle$
`Lepton`	0.3067 ± 0.0942	0.4788 ± 0.0758	0.0774 ± 0.1350
`KaonI`	0.6738 ± 0.0222	0.2377 ± 0.0276	0.1880 ± 0.0133
`KaonII`	0.6850 ± 0.0166	0.3097 ± 0.0201	0.2457 ± 0.0096
`KorPI`	0.6728 ± 0.0190	0.3595 ± 0.0235	0.3435 ± 0.0119
`Pions`	0.6892 ± 0.0173	0.4550 ± 0.0233	0.4255 ± 0.0111
`Other`	0.7311 ± 0.0182	0.4930 ± 0.0295	0.4613 ± 0.0118
`Untagged`	0.7589 ± 0.0122	0.5	0.5

Table 7.11: Summary of Breco signal resolution function parameters.

Parameter	B^0
Scale (core)	1.0199 ± 0.0277
$\delta(\Delta t$) `Lepton` (core)	-0.0294 ± 0.0422
$\delta(\Delta t$) `KaonI` (core)	-0.0975 ± 0.0422
$\delta(\Delta t$) `KaonII` (core)	-0.1814 ± 0.0331
$\delta(\Delta t$) `KorPI` (core)	-0.2177 ± 0.0350
$\delta(\Delta t$) `Pions` (core)	-0.1953 ± 0.0341
$\delta(\Delta t$) `Other` (core)	-0.1419 ± 0.0407
$\delta(\Delta t$) `Untagged` (core)	-0.1918 ± 0.0266
Scale (tail)	3.0 (fixed)
f (tail)	0.1147 ± 0.0114
$\delta(\Delta t$) (tail)	-1.1510 ± 0.1590
f (outlier)	0.0044 ± 0.0008
Scale (outlier)	8.0 (fixed)
$\delta(\Delta t$) (outlier) (ps)	0.0 (fixed)

Table 7.12: Summary of Breco background resolution function parameters.

Parameter	B^0
Scale (core)	1.3147 ± 0.0093
$\delta(\Delta t$) (core)	-0.0205 ± 0.0070
f (core)	0.9802 ± 0.0012
Scale (outlier)	8.0 (fixed)
$\delta(\Delta t$) (outlier) (ps)	0.0 (fixed)

Table 7.13: BReco signal tagging fractions (f), mistag fractions ($\langle w \rangle$), mistag differences (Δw) and tag efficiency difference (μ) for each tagging category determined from fit to the neutral MC BReco sample. The reco efficiency difference is $\nu = 0.0043 \pm 0.0047$.

Category	f_{sig}	$\langle w \rangle$	Δw	μ
`Lepton`	0.0879 ± 0.0010	0.0098 ± 0.0040	-0.0020 ± 0.0071	-0.0163 ± 0.0137
`KaonI`	0.1127 ± 0.0011	0.0570 ± 0.0046	0.0008 ± 0.0076	0.0014 ± 0.0127
`KaonII`	0.1709 ± 0.0013	0.1429 ± 0.0061	-0.0061 ± 0.0075	-0.0145 ± 0.0113
`KorPI`	0.1401 ± 0.0012	0.2540 ± 0.0083	-0.0216 ± 0.0090	0.0035 ± 0.0128
`Pions`	0.1494 ± 0.0012	0.3416 ± 0.0061	0.0751 ± 0.0089	-0.0358 ± 0.0127
`Other`	0.0987 ± 0.0010	0.4330 ± 0.0075	0.0554 ± 0.0110	-0.0050 ± 0.0154
`Untagged`	0.2403 ± 0.0028	0.5	0	0

Table 7.14: Summary of MC BReco signal resolution function parameters.

Parameter	B^0
Scale (core)	1.1337 ± 0.0239
$\delta(\Delta t)$ `Lepton` (core)	-0.0345 ± 0.0370
$\delta(\Delta t)$ `KaonI` (core)	-0.2037 ± 0.0353
$\delta(\Delta t)$ `KaonII` (core)	-0.1978 ± 0.0277
$\delta(\Delta t)$ `KorPI` (core)	-0.2602 ± 0.0289
$\delta(\Delta t)$ `Pions` (core)	-0.2360 ± 0.0275
$\delta(\Delta t)$ `Other` (core)	-0.2376 ± 0.0335
$\delta(\Delta t)$ `Untagged` (core)	-0.2371 ± 0.0216
Scale (tail)	3.0 (fixed)
f (tail)	0.0795 ± 0.0121
$\delta(\Delta t)$ (tail)	-1.4997 ± 0.2670
f (outlier)	0.0056 ± 0.0007
Scale (outlier)	8.0 (fixed)
$\delta(\Delta t)$ (outlier) (ps)	0.0 (fixed)

7.4.3 Δt Parametrization

The vertex of the fully reconstructed B has been determined using the `GeoKin` algorithm [32]. The decay vertex of the tagged B is determined with the `VtxTagBtaSelFit` algorithm [32], with the full beam-constraint. The time interval Δt is determined from the vertex separation Δz between B_{tag} and B_{CP} using the *average* τ_B *approximation* [32].

Vertex resolution is independent of the reconstructed B decay mode so parameters of the Δt resolution function can be taken from fit on BReco sample.

For our CP sample we use the CP model PDF convoluted with the resolution function described in Eq. 7.14. The resolution function $\mathcal{R}_{\rm sig}(t)$ is the same triple Gaussian as described for BReco (naturally since the parameters are in common):

$$\begin{aligned} \mathcal{R}_{\rm sig}(t) &= (1 - f_{\rm tail} - f_{\rm out})\, G\left(t, s^{\mu}_{\rm core}\sigma_t, s^{\sigma}_{\rm core}\sigma_t\right) + f_{\rm tail} G\left(t, s^{\mu}_{\rm tail}\sigma_t, s^{\sigma}_{\rm tail}\sigma_t\right) \\ &+ f_{\rm out} G\left(t, \mu_{\rm out}, \sigma_{\rm out}\right) \end{aligned} \tag{7.14}$$

where $G(x, x_0, \sigma)$ is a Gaussian with bias x_0 and standard deviation σ.

The $q\overline{q}$ background Δt distribution is modelled using on-peak sideband data, defined as $5.25 < M_{ES} < 5.27$ GeV/c^2 and $|\Delta E| < 0.2$ GeV. It is parameterized as the sum of three Gaussians. For $B\overline{B}$ background, we use a Triple Gaussian fitted on $B\overline{B}$ MC events.

The PDF for both $q\overline{q}$ background and $B\overline{B}$ background distributions are shown in Appendix A.

7.4.4 Vertexing Validation

To check and validate the K^0_S vertexing reconstruction we made a comparison on vertexing resolution between charged and neutral K^0_S decay mode ($K^0_S \to \pi^0\pi^0$ and $K^0_S \to \pi^+\pi^-$) using MC truth signal events. We fit the distributions of z_{CP}, z_{CP} pull on MC truth events with a triple gaussian for z_{CP} . The results are shown in Table 7.15 and 7.16.

The results for neutral K^0_S decay are in good agreement with the ones for the charged K^0_S decay, so we verify that the vertexing reconstruction depends mostly from the informations on the η' meson.

		$\eta'_{\eta\pi\pi}K^0_S\,(\pi^0\pi^0)$	$\eta'_{\eta\pi\pi}K^0_S\,(\pi^+\pi^-)$
MC events		38000	67000
B_{CP}	μ_{core}	-0.0009 ± 0.0006	-0.0001 ± 0.0001
	σ_{core}	0.0099 ± 0.0013	0.0062 ± 0.0002
B_{CP} Pull	μ_{core}	0.0056 ± 0.0161	-0.0006 ± 0.0094
	σ_{core}	0.8605 ± 0.0166	0.9708 ± 0.0096
Δt Pull	μ_{core}	-0.1612 ± 0.0198	-0.2100 ± 0.0111
	σ_{core}	1.0555 ± 0.0188	1.0409 ± 0.0119

Table 7.15: Results for vertexing validation.

		$\eta'_{\rho\gamma}K^0_S\,(\pi^0\pi^0)$	$\eta'_{\rho\gamma}K^0_S\,(\pi^+\pi^-)$
MC events		39000	67000
B_{CP}	μ_{core}	0.0003 ± 0.0002	0.0001 ± 0.0002
	σ_{core}	0.0058 ± 0.0003	0.0133 ± 0.0004
B_{CP} Pull	μ_{core}	0.0404 ± 0.0168	-0.0032 ± 0.0085
	σ_{core}	0.9224 ± 0.0153	0.9381 ± 0.0080
Δt Pull	μ_{core}	-0.1819 ± 0.0226	-0.2323 ± 0.0110
	σ_{core}	1.0706 ± 0.0231	1.0766 ± 0.0110

Table 7.16: Results for vertexing validation.

7.4.5 Effects of SXF on CP asymmetry parameters

We made some checks in order to understand how the SXF events contribute to the CP asymmetry parameters. Because the vertexing reconstruction is made using the information on the η' meson for the neutral channels and η' together with K^+ for the charged channel, we study the Δt resolution for signal events with η' misreconstructed ($i.e.$ reconstructed with particles not belonging to the true η', denoted as SXF$_{\eta'}$ events) and with η' true or with permutated daughters. Due to the fact that most of the SXF$_{\eta'}$ contributions come from the decays with $\eta' \to \eta_{3\pi}\pi\pi$, we decided to study these subdecays.

We show in Fig. 7.2 , 7.3, 7.4 and 7.5 the Δt and $\sigma_{\Delta t}$ distributions. There isn't any significant difference between the distributions.

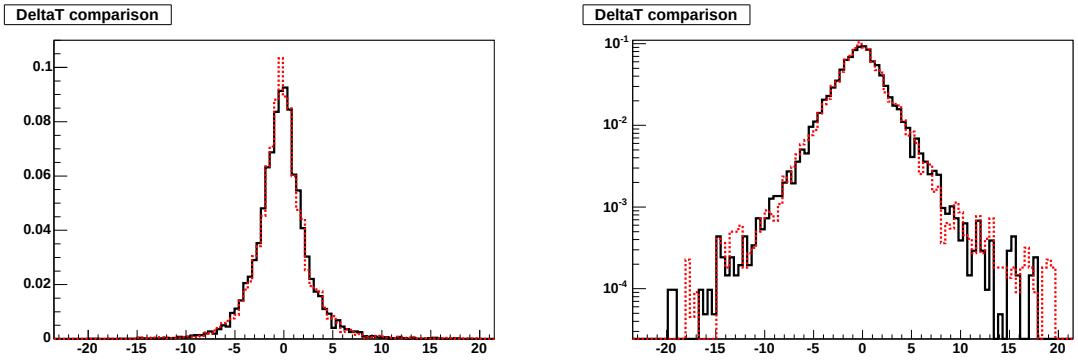

Figure 7.2: Δt distributions (left: linear, right: logarithmic) for true events (black continuos line) and SXF$_{\eta'}$ events (red dashed line) in $\eta'_{\eta(3\pi)\pi\pi}K^0_S$.

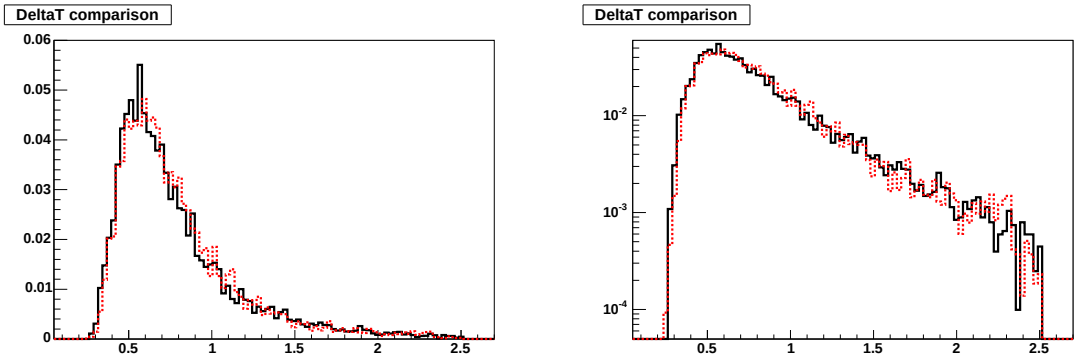

Figure 7.3: $\sigma_{\Delta t}$ distributions (left: linear, right: logarithmic) for true events (black continuos line) and SXF$_{\eta'}$ events (red dashed line) in $\eta'_{\eta(3\pi)\pi\pi}K^0_S$.

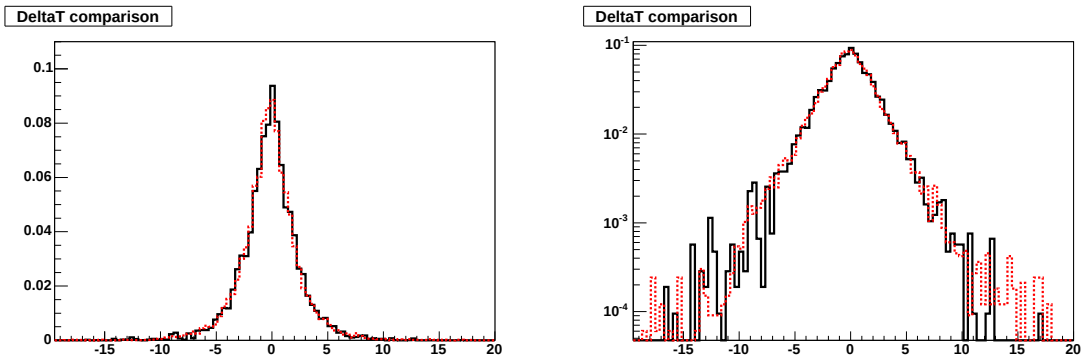

Figure 7.4: Δt distributions (left: linear, right: logarithmic) for true events (black continuos line) and SXF$_{\eta'}$ events (red dashed line) in $\eta'_{\eta(3\pi)\pi\pi}K^+$.

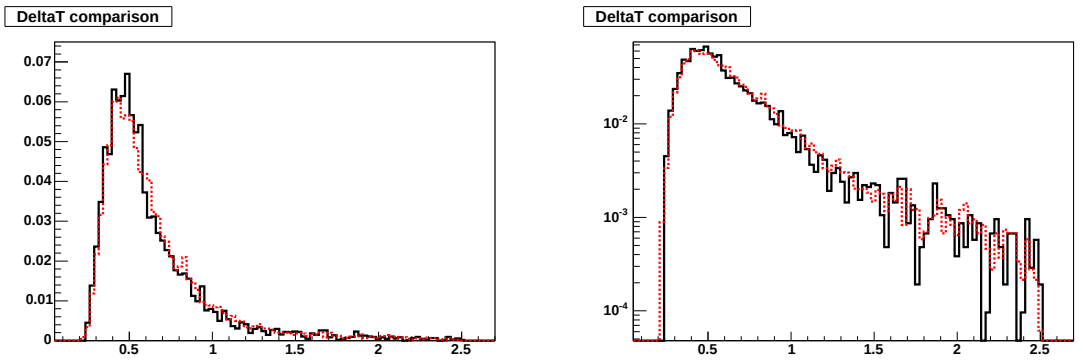

Figure 7.5: $\sigma_{\Delta t}$ distributions (left: linear, right: logarithmic) for true events (black continuos line) and SXF$_{\eta'}$ events (red dashed line) in $\eta'_{\eta(3\pi)\pi\pi}K^+$.

We calculate and fit with a double Gaussian the Δt pull in the channels with $\eta' \to \eta\pi^+\pi^-$ and $\eta \to \pi^+\pi^-\pi^0$ for events with and without SXF$_{\eta'}$ contribution. The results are shown in Table 7.17. The Δt pull distributions are shown in Fig. 7.6 and 7.7.

Table 7.17: Results for vertexing validation.

		$\eta'_{\eta(3\pi)\pi\pi}K^0_S$	$\eta'_{\eta(3\pi)\pi\pi}K^+$
Δt Pull SXF	μ_{core}	-0.2080 ± 0.0184	-0.2048 ± 0.0125
Δt Pull no SXF	μ_{core}	-0.1994 ± 0.0104	-0.1936 ± 0.0106
Δt Pull SXF	σ_{core}	0.9873 ± 0.0209	0.9265 ± 0.0128
Δt Pull no SXF	σ_{core}	0.9809 ± 0.0106	0.8369 ± 0.0115

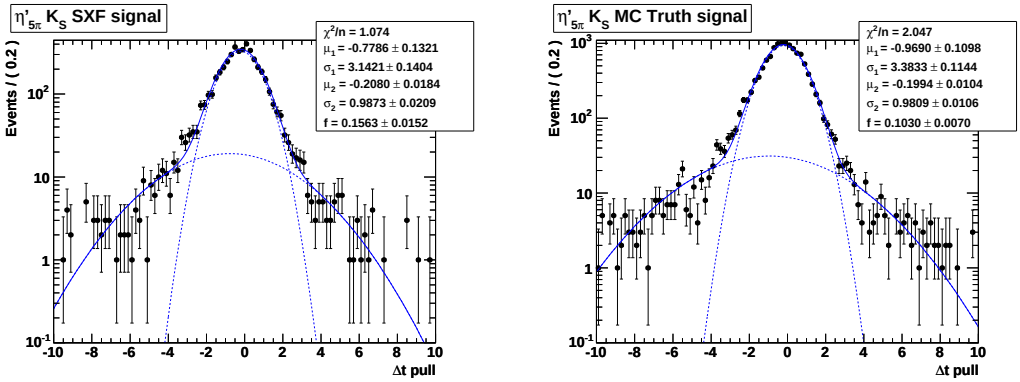

Figure 7.6: Δt pull with (left) and without (right) SXF$_{\eta'}$ fraction in $\eta'_{\eta(3\pi)\pi\pi}K^0_S$.

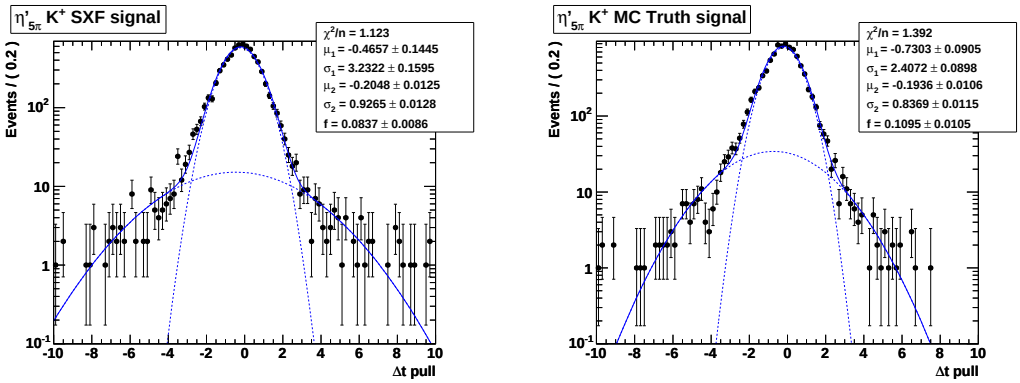

Figure 7.7: Δt pull with (left) and without (right) SXF$_{\eta'}$ fraction in $\eta'_{\eta(3\pi)\pi\pi}K^+$.

We also check Δt residual for no $SXF_{\eta'}$ and $SXF_{\eta'}$ signal events. Both events are fitted using PDF defined as Eq.7.14. Results are shown in Tab 7.18 and 7.19.

Parameter	$\eta'_{\eta(3\pi)\pi\pi}K^0_S$	
	no $SXF_{\eta'}$ events	$SXF_{\eta'}$ events
Scale (core)	1.1550 ± 0.0119	1.1802 ± 0.0242
$\delta(\Delta t$) `Lepton` (core)	-0.0994 ± 0.0370	-0.1866 ± 0.0886
$\delta(\Delta t$) `KaonI` (core)	-0.2209 ± 0.0348	-0.2182 ± 0.0790
$\delta(\Delta t$) `KaonII` (core)	-0.2297 ± 0.0300	-0.1437 ± 0.0559
$\delta(\Delta t$) `KorPI` (core)	-0.2668 ± 0.0335	-0.3994 ± 0.0613
$\delta(\Delta t$) `Pions` (core)	-0.2665 ± 0.0321	-0.3457 ± 0.0586
$\delta(\Delta t$) `Other` (core)	-0.2865 ± 0.0394	-0.1996 ± 0.0677
$\delta(\Delta t$) `Untagged` (core)	-0.1968 ± 0.0254	-0.2285 ± 0.0430
Scale (tail)	3.0 (fixed)	3.0 (fixed)
f (tail)	0.1009 ± 0.0075	0.1151 ± 0.0156
$\delta(\Delta t$) (tail)	-1.3357 ± 0.1327	-1.1962 ± 0.2198
f (outlier)	0.0107 ± 0.0015	0.0260 ± 0.0038
Scale (outlier)	8.0 (fixed)	8.0 (fixed)
$\delta(\Delta t$) (outlier) (ps)	0.0 (fixed)	0.0 (fixed)

Table 7.18: Δt residual parameters for no SXF signal and SXF events.

Parameter	$\eta'_{\eta(3\pi)\pi\pi}K^+$	
	no $SXF_{\eta'}$ events	$SXF_{\eta'}$ events
Scale (core)	1.1157 ± 0.0127	1.1660 ± 0.0157
$\delta(\Delta t$) `Lepton` (core)	-0.1207 ± 0.0423	-0.1249 ± 0.0630
$\delta(\Delta t$) `KaonI` (core)	-0.2146 ± 0.0365	-0.2823 ± 0.0520
$\delta(\Delta t$) `KaonII` (core)	-0.3038 ± 0.0301	-0.2980 ± 0.0391
$\delta(\Delta t$) `KorPI` (core)	-0.2441 ± 0.0367	-0.2515 ± 0.0453
$\delta(\Delta t$) `Pions` (core)	-0.3379 ± 0.0355	-0.2715 ± 0.0452
$\delta(\Delta t$) `Other` (core)	-0.2347 ± 0.0456	-0.1776 ± 0.0565
$\delta(\Delta t$) `Untagged` (core)	-0.2787 ± 0.0276	-0.3494 ± 0.0336
Scale (tail)	3.0 (fixed)	3.0 (fixed)
f (tail)	0.0828 ± 0.0071	$0.0906 \pm 0.0.0089$
$\delta(\Delta t$) (tail)	-1.0538 ± 0.1462	-0.3573 ± 0.1608
f (outlier)	0.0048 ± 0.0010	0.0062 ± 0.0015
Scale (outlier)	8.0 (fixed)	8.0 (fixed)
$\delta(\Delta t$) (outlier) (ps)	0.0 (fixed)	0.0 (fixed)

Table 7.19: Δt residual parameters for no SXF signal and SXF events.

We calculate the CP parameters C and S for MC signal events, considering separately events with SXF (where the cross feed regards now all the particles in the reconstructed event, as it's defined in Sec 7.3.2) and without SXF. The results are shown in Table 7.20. As shown in the table, the CP asymmetry parameters are quite similar for the two categories, so the effect of the SXF events on S and C is negligible. For this reason we decide to fit the asymmetry parameters with the same S and C value for both kind of event.

Decay mode	S	C
$\eta'_{\rho\gamma}K^0_S$		
SXF events	0.744 ± 0.156	-0.022 ± 0.102
no SXF events	0.639 ± 0.058	0.046 ± 0.040
$\eta'_{\eta(\gamma\gamma)\pi\pi}K^0_S$		
SXF events	0.648 ± 0.138	-0.006 ± 0.089
no SXF events	0.640 ± 0.062	0.027 ± 0.040
$\eta'_{\eta(3\pi)\pi\pi}K^0_S$		
SXF events	0.658 ± 0.068	0.011 ± 0.048
no SXf events	0.687 ± 0.031	0.003 ± 0.022
$\eta'_{\eta(3\pi)\pi\pi}K^+$		
SXF events	-0.063 ± 0.054	-0.007 ± 0.039
no SXf events	0.009 ± 0.034	0.031 ± 0.024

Table 7.20: CP asymmetry parameters for signal and SXF events.

7.5 Background sources

From the fits on $B\overline{B}$ generic samples, off-peak data and from our previous analyses [33, 34], we know that in our target decays the main source of background is continuum $udsc$ events. While for the decays with $\eta' \to \eta\pi^+\pi^-$ this is the only source of background, in the decays with $\eta' \to \rho^0\gamma$ we have a contribution from non continuum $B\overline{B}$ background. The procedure followed in the analysis of such background consists in the definition of the categories which can contribute to cross feed by looking at the pattern of $B\overline{B}$ events seen in the input of the ML fit of the $B\overline{B}$ generic MC samples and in the introduction of a $B\overline{B}$ term in the ML fit for these specific decay modes. We have done a carefully study of $B\overline{B}$ background for $B^0 \to \eta'_{\rho\gamma}K^0_S$ decay mode with $K^0_S \to \pi^+\pi^-$ and we have done the assumption that the $B\overline{B}$ background is the same if you consider the sub-decays with $K^0_S \to \pi^0\pi^0$. So we use what we have done for $K^0_S \to \pi^+\pi^-$ sub-decay in sub-decay with $K^0_S \to \pi^0\pi^0$. We have run MC $B^0\overline{B}^0$ generic events (274.5 millions) and B^+B^- generic events (260.7 millions) to reconstruct $B^0 \to \eta'_{\rho\gamma}K^0_S$ with $K^0_S \to \pi^+\pi^-$. From visual inspection of these events entering in our ML input, we have defined a class of different kinds of $B\overline{B}$ decay modes able to give some contribution to our ML input sample. For each of these decay modes we have reconstructed the specific MC events. Then the reconstructed events of the categories have been summed together, taking into account the total number of input MC signal events, reconstruction efficiencies and branching fractions. Finally these summed events have been used to prepare the $B\overline{B}$ PDFs. The results are shown in Tables 7.21 and 7.22. We took best central value for branching fractions for each decays, taken from HFAG groups [35]. In the last column of these table we have put the estimated numbers of $B\overline{B}$ for each sub-decays that we should have in our on-peak sample.

These $B\overline{B}$ PDFs are able to eliminate all $B\overline{B}$ background in Monte Carlo $B\overline{B}$ simulated events (see Yields Verification Tests).

B^+B^- decays	MC ϵ (%)	$\prod \mathcal{B}_i$ (%)	$\epsilon \times \prod \mathcal{B}_i$ (%)	$\mathcal{B}(\times 10^{-6})$	# $B\overline{B}$bkg
$B^+ \to a_1^+ K^0$	1.74	50.0	0.87	15.0 †	15.9
$B^+ \to K^{*+}(K_S^0\pi^+)\rho^0\ long.$	2.83	22.9	0.65	10.6	8.4
$B^+ \to \rho^+ K^0$	1.14	50.0	0.57	2.5	1.7
$B^+ \to \eta'(\rho^0\gamma)K^{*+}(K_S^0\pi^+)$	2.61	6.7	0.17	6.3	1.3
$B^+ \to K^{*+}(K_S^0\pi^+)K^0$	1.06	16.7	0.18	1	0.2
$B^+ \to \phi(\pi^+\pi^-\pi^0)K^{*+}(K_S^0\pi^+)$	0.23	3.5	0.01	9.7	0.1
$B^+ \to \omega K^{*+}(K_S^0\pi^+)\ long.$	0.11	20.4	0.02	3.5	0.1
$B^+ \to a_0^+(\eta(\gamma\gamma)\pi^+)K^0$	0.90	13.5	0.12	1	0.1
$B^+ \to K^{*+}(K^+\pi^0)K^0$	0.23	16.7	0.04	1	0.1

Table 7.21: B^+B^- background categories. † Branching ratio estimates from $B^0 \to a_1^+(\rho^0\pi^+)K^-$.

$B^0\overline{B}^0$ decays	MC ϵ (%)	$\prod \mathcal{B}_i$ (%)	$\epsilon \times \prod \mathcal{B}_i$ (%)	$\mathcal{B}(\times 10^{-6})$	# $B\overline{B}$bkg
$B^0 \to \rho^0 K^0$	5.02	50.0	2.51	5	16
$B^0 \to \phi(\pi^+\pi^-\pi^0)K^0(\pi^+\pi^-)$	8.08	5.35	0.43	8.3	4.4
$B^0 \to K^{*+}(K_S^0\pi^+)\pi^-$	0.45	33.3	0.16	15.3	2.8
$B^0 \to \omega K^0(\pi^+\pi^-)$	1.11	30.64	0.34	5.5	2.3
$B^0 \to \eta'(\eta\pi^+\pi^-)K^0(\pi^+\pi^-)$	0.34	6.02	0.02	65	1.6
$B^0 \to \phi(\pi^+\pi^-\pi^0)K^{*0}(K_S^0\pi^0)$	0.26	1.8	0.01	10.7	0.1

Table 7.22: $B^0\overline{B}^0$ background categories.

7.6 Verification Tests

In the *blind* phase, to check if the fitting model is right and if the program works well, we made some checks on the exctraction of signal yield and S and C. For the yield and CP-violating parameters we used some repeated Monte Carlo tests (so called *Toy Experiments*) to verify how data were reproduced.

7.6.1 Yield Verification Tests

We decided to check our SXF fractions leaving them floating when we fit events MC signal and we compare the results with the estimated values obtained in Table 7.6. We found a good agreement. The results are shown in Table 7.23.

Decay Mode	Input	Fit output			
		Signal	$q\overline{q}$ bkg.	$B\overline{B}$ bkg.	SXF (%)
$\eta'_{\eta\pi\pi}K^0_S$	9063	$9016.3^{+96.2}_{-95.5}$	$46.7^{+15.8}_{-14.0}$	$-$	24.7 ± 1.1
$\eta'_{\rho\gamma}K^0_S$	9326	$9091.1^{+109.8}_{-110.6}$	$85.5^{+19.1}_{-17.7}$	$149.4^{+52.5}_{-51.3}$	22.8 ± 1.3
$\eta'_{\eta(3\pi)\pi\pi}K^0_S$	13820	$13669.7^{+119.2}_{-118.6}$	$150.3^{+25.7}_{-24.1}$	$-$	14.5 ± 0.5
$\eta'_{\eta(3\pi)\pi\pi}K^+$	15778	$15457.2^{+126.8}_{-126.5}$	$320.8^{+30.5}_{-29.3}$	$-$	29.8 ± 0.9

Table 7.23: Yield verification tests on MC signal to estimate SXF fraction.

Furthermore, in the first step of the analysis when not all the data were avalaible, we had made verification tests for the charged and neutral decay modes on off-peak, B^+B^-, $B^0\overline{B}^0$ and Monte Carlo signal events with SXF fixed. Results of this analysis are shown in Tables 7.24. In this case we do not fit using the Δt and tagging information.

The number of background events found as signal by the fitter in these samples can be considered compatible with zero.

From the results shown in Tables 7.24 we can conclude that our fitter is able to extract correctly signal and background events.

Decay Mode	Event Sample	Input	Fit output		
			Signal	$q\overline{q}$ continuum	$B\overline{B}$
$\eta'_{\eta\pi\pi}K^0_S$	Off-peak	150	$0.0^{+0.6}_{-0.0}$	$150.0^{+12.6}_{-11.9}$	–
	B^+B^-	7	$0.0^{+0.5}_{-0.0}$	$7.0^{+3.0}_{-2.3}$	–
	$B^0\overline{B}^0$	8	$0.0^{+0.7}_{-0.0}$	$8.0^{+3.2}_{-2.5}$	–
	MC signals	9774	$9726.1^{+99.2}_{-98.8}$	$48.0^{+11.8}_{-10.6}$	–
$\eta'_{\rho\gamma}K^0_S$	Off-peak	1930	$0.0^{+1.2}_{-0.0}$	$1930.0^{+44.3}_{-43.6}$	$0.0^{+15.2}_{-11.6}$
	B^+B^-	83	$0.0^{+0.7}_{-0.0}$	$58.7^{+9.9}_{-9.1}$	$24.3^{+8.0}_{-7.0}$
	$B^0\overline{B}^0$	134	$0.0^{+3.2}_{-0.0}$	$79.5^{+12.4}_{-11.7}$	$54.5^{+11.3}_{-10.6}$
	MC signals	8476	$8290.0^{+95.6}_{-95.8}$	$16.1^{+12.1}_{-10.1}$	$170.3^{+37.5}_{-36.3}$
$\eta'_{\eta(3\pi)\pi\pi}K^0_S$	Off-peak	35	$0.0^{+0.5}_{-0.0}$	$35.0^{+6.3}_{-5.6}$	–
	B^+B^-	4	$0.0^{+0.5}_{-0.0}$	$4.0^{+2.4}_{-1.7}$	–
	$B^0\overline{B}^0$	25	$0.3^{+3.1}_{-0.0}$	$24.7^{+5.6}_{-5.2}$	–
	MC signals	17143	$17110^{+131.5}_{-130.9}$	$32.7^{+12.7}_{-11.2}$	–
$\eta'_{\eta(3\pi)\pi\pi}K^+$	Off-peak	153	$0.0^{+1.0}_{-0.0}$	$153.0^{+12.7}_{-12.0}$	–
	B^+B^-	56	$0.0^{+2.4}_{-0.0}$	$56.0^{+8.0}_{-7.2}$	–
	$B^0\overline{B}^0$	9	$0.0^{+0.9}_{-0.0}$	$9.0^{+3.3}_{-2.7}$	–
	MC signals	18114	$18034.3^{+135.0}_{-135.1}$	$79.9^{+17.5}_{-15.8}$	–

Table 7.24: Yields verification tests with SXF fixed.

7.6.2 Yield Pure Toy Test

We check how data are reproduced by toy Monte Carlo generated events. We have generated 500 experiments for each decay mode, each experiment with the number of signal and background events as found in data. Events were generated from the PDFs used in the data fit; we don't generate $B\overline{B}$ events. We fit the distributions of signal yields and their errors using a Gaussian. We show in Tables 7.25 the central values of these Gaussians. We show also the values of mean and sigma of the pull distributions fitted with a Gaussian.

Fit on the generated events agree well with input data and no biases are seen.

Decay Mode	# Sg.	# Bkg	Sg Value	Sg Err.	Pull Mean	Pull σ.
$\eta'_{\eta\pi\pi}K^0_S$	29	1545	29.4 ± 0.4	7.56 ± 0.04	0.02 ± 0.05	1.03 ± 0.05
$\eta'_{\rho\gamma}K^0_S$	44	18270	42.7 ± 0.7	13.96 ± 0.06	-0.07 ± 0.05	0.96 ± 0.04
$\eta'_{\eta(3\pi)\pi\pi}K^0_S$	46	413	45.6 ± 0.3	7.79 ± 0.03	-0.02 ± 0.05	0.97 ± 0.04
$\eta'_{\eta(3\pi)\pi\pi}K^+$	161	1419	160.8 ± 0.7	14.56 ± 0.03	-0.06 ± 0.05	0.96 ± 0.04

Table 7.25: 500 Pure Toy experiments (Run1+Run2+Run3 data sample).

7.6.3 Yield MC Toy Test

We have generated 500 experiments for each decay mode, each experiment with the number of signal and background events as found in data. In this case the signal events are taken from MC events while the background events are generated from PDFs and we don't generate $B\overline{B}$ background. We fit the distributions of signal yields and their errors using a Gaussian. We show in Tables 7.26 the central values of these Gaussians.

Decay Mode	# Sg.	# Bkg	Sg Value	Sg Err.
$\eta'_{\eta\pi\pi}K^0_S$	29	1545	29.2 ± 0.2	7.50 ± 0.03
$\eta'_{\rho\gamma}K^0_S$	44	18270	44.2 ± 0.5	13.61 ± 0.06
$\eta'_{\eta(3\pi)\pi\pi}K^0_S$	46	413	46.5 ± 0.2	8.09 ± 0.02
$\eta'_{\eta(3\pi)\pi\pi}K^+$	161	1419	158.9 ± 0.4	14.42 ± 0.02

Table 7.26: 500 MC Toy experiments (Run1+Run2+Run3 data sample).

7.6.4 CP Verification Tests

We fitted the asymmetries parameters on MC signal events using MC BReco parameters. Monte Carlo signal events are simulated with $S = 0.7$ and $C = 0.0$ for neutral modes while $S = 0.0$ and $C = 0.0$ for the charged ones. The results are shown in Table 7.27.

Decay Mode	Input	Fit output		
		Signal	S	C
$\eta'_{\eta\pi\pi}K^0_S$	8326	8281.7 ± 91.7	0.690 ± 0.041	0.025 ± 0.026
$\eta'_{\rho\gamma}K^0_S$	8943	8863.8 ± 102.6	0.668 ± 0.035	0.012 ± 0.024
$\eta'_{\eta(3\pi)\pi\pi}K^0_S$	13347	13282.2 ± 116.3	0.724 ± 0.028	-0.016 ± 0.020
$\eta'_{\eta(3\pi)\pi\pi}K^+$	15332	15046.1 ± 124.2	0.008 ± 0.026	0.023 ± 0.019

Table 7.27: Time dependent verification tests on MC signal events.

7.6.5 CP Pure Toy Studies

We performed several different analyses in order to validate the ability of our fitter to extract correctly time-dependent asymmetry present in data and Monte Carlo simulated events. We performed pure toy experiments for the neutral channels $\eta'_{\rho\gamma}K^0_S$, $\eta'_{\eta\pi\pi}K^0_S$, $\eta'_{\eta(3\pi)\pi\pi}K^0_S$ and for the charged channel $\eta'_{\eta(3\pi)\pi\pi}K^+$ with the number of signal and background events as found in the data. The events are generated according to the PDFs shown in Appendix A. We don't generate $B\overline{B}$ events.

We have performed 500 toy experiments for each sub-decay with $C = 0.0$ and $S = 0.7$ ($S = 0.0$ for charged channel). We summarize in Table 7.28 the mean values, the errors on mean value, and pull for the signal yield and for the asymmetry parameters with corresponding errors obtained from a Gaussian fit of their distributions.

$\eta'_{\eta\pi\pi}K^0_S$			
Signal events	44		
Bkg. events	458		
	Sg	S	C
Value	44.1 ± 0.4	0.732 ± 0.037	-0.039 ± 0.023
Value Error	8.89 ± 0.03	0.720 ± 0.008	0.457 ± 0.004
Pull Mean	0.01 ± 0.04	0.06 ± 0.05	-0.09 ± 0.05
Pull σ	0.92 ± 0.03	1.02 ± 0.05	1.01 ± 0.04
$\eta'_{\rho\gamma}K^0_S$			
Signal events	94		
Bkg. events	12461		
	Sg	S	C
Value	100.4 ± 0.9	0.729 ± 0.031	0.031 ± 0.038
Value Error	20.89 ± 0.07	0.544 ± 0.006	0.624 ± 0.011
Pull Mean	0.21 ± 0.05	0.18 ± 0.06	0.01 ± 0.05
Pull σ	0.97 ± 0.04	1.14 ± 0.06	1.14 ± 0.04
$\eta'_{\eta(3\pi)\pi\pi}K^0_S$			
Signal events	54		
Bkg. events	106		
	Sg	S	C
Value	52.7 ± 0.3	0.704 ± 0.029	0.011 ± 0.018
Value Error	8.11 ± 0.02	0.538 ± 0.005	0.354 ± 0.002
Pull Mean	-0.07 ± 0.03	0.01 ± 0.05	0.06 ± 0.05
Pull σ	0.74 ± 0.03	1.05 ± 0.04	1.09 ± 0.05
$\eta'_{\eta(3\pi)\pi\pi}K^+$			
Signal events	205		
Bkg. events	373		
	Sg	S	C
Value	204.7 ± 0.6	0.012 ± 0.012	0.001 ± 0.009
Value Error	15.43 ± 0.02	0.246 ± 0.001	0.179 ± 0.001
Pull Mean	-0.02 ± 0.04	0.09 ± 0.05	0.06 ± 0.05
Pull σ	0.80 ± 0.03	0.97 ± 0.04	1.04 ± 0.04

Table 7.28: Mean values of CP violating parameters and their errors for pure toy experiments.

7.6.6 CP MC Toy Studies

We performed MC toy experiments for the neutral channels $\eta'_{\rho\gamma}K^0_S$, $\eta'_{\eta\pi\pi}K^0_S$, $\eta'_{\eta(3\pi)\pi\pi}K^0_S$ and for the charged channel $\eta'_{\eta(3\pi)\pi\pi}K^+$. The signal events are taken from MC events while background events are generated according to the PDFs shown in Appendix A. We don't generate any $B\overline{B}$ background. The number of events for each toy experiment is the measured value in the data. We use MC BReco parameters for resolution and fitting models. We summarize in Table 7.29 the mean values of signal yield and of the asymmetries parameters with corresponding errors, obtained from Gaussian fit of their distributions.

$\eta'_{\eta\pi\pi}K^0_S$			
Signal events	44		
Bkg. events	458		
	Sg	S	C
Value	45.5 ± 0.3	0.753 ± 0.038	-0.001 ± 0.021
Value Error	8.93 ± 0.02	0.721 ± 0.007	0.432 ± 0.003
$\eta'_{\rho\gamma}K^0_S$			
Signal events	94		
Bkg. events	12461		
	Sg	S	C
Value	100.3 ± 0.8	0.683 ± 0.027	-0.001 ± 0.012
Value Error	20.35 ± 0.06	0.509 ± 0.005	0.361 ± 0.003
$\eta'_{\eta(3\pi)\pi\pi}K^0_S$			
Signal events	54		
Bkg. events	106		
	Sg	S	C
Value	53.9 ± 0.2	0.748 ± 0.026	-0.010 ± 0.017
Value Error	8.19 ± 0.01	0.505 ± 0.005	0.328 ± 0.002
$\eta'_{\eta(3\pi)\pi\pi}K^+$			
Signal events	205		
Bkg. events	373		
	Sg	S	C
Value	196.7 ± 0.3	0.014 ± 0.012	0.008 ± 0.008
Value Error	15.12 ± 0.01	0.242 ± 0.001	0.178 ± 0.001

Table 7.29: Mean values of CP violating parameters and their errors for MC toy experiments.

7.7 Results

After all checks, we extract the results for the onpeak sample. We show in Tables 7.30 and 7.31 the numbers of events to fit, the numbers of signal yield, the various efficiencies and the product of branching fractions and, in the bottom part of the tables, the results of Time-Dependent analysis.

Quantity	$\eta'_{\rho\gamma} K^0_S$ $(\pi^0\pi^0)$	$\eta'_{\eta\pi\pi} K^0_S$ $(\pi^0\pi^0)$
Yield-only fits:		
Events into fit	13505	564
Fit yield	69 ± 25	51 ± 11
$B\overline{B}$ Fit yield	38 ± 27	–
MC Combinations/event	1.29	1.31
On-Peak Data Combinations/event	1.30	1.33
ML-fit ϵ (%)	100.5	100.7
MC ϵ (%)	14.3	13.5
$\prod \mathcal{B}_i$ (%)	9.16	5.42
TD fits:		
Events into fit	12555	502
Fit yield	94 ± 23	44 ± 9
$B\overline{B}$ Fit yield	47 ± 22	–
S	-0.45 ± 0.68	-0.04 ± 0.57
C	0.41 ± 0.40	-0.65 ± 0.42

Table 7.30: Summary of ML fit results for the decays $\eta'_{\rho\gamma} K^0_S$ and $\eta'_{\eta\pi\pi} K^0_S$ for Final Run1-4 dataset.

Quantity	$\eta'_{\eta(3\pi)\pi\pi} K^0_S$ $(\pi^+\pi^-)$	$\eta'_{\eta(3\pi)\pi\pi} K^+$
Yield-only fits:		
Events into fit	165	596
Fit yield	55 ± 8	215 ± 16
MC Combinations/event	2.23†	1.61†
On-Peak Data Combinations/event	2.45	2.34
ML-fit ϵ (%)	101.1	98.7
MC ϵ (%)	14.4	15.0
$\prod \mathcal{B}_i$ (%)	6.90	10.01
TD fits:		
Events into fit	160	578
Fit yield	54 ± 8	205 ± 16
S	0.79 ± 0.47	-0.17 ± 0.23
C	0.11 ± 0.35	0.05 ± 0.17

Table 7.31: Summary of ML fit results for the decays $\eta'_{\eta(3\pi)\pi\pi} K^0_S$ and $\eta'_{\eta(3\pi)\pi\pi} K^+$ for Final Run1-4 dataset. † Multiple candidates with η' permutated daughters counted as single candidate.

7.7.1 Projections

We have done the M_{ES} and ΔE projections. To reduce the contribution of continuum background, we make a cut on the quantity:

$$R = \frac{P_{sig}}{P_{sig} + P_{bkg}}, \tag{7.15}$$

where P_{sig} and P_{bkg} are the probability for the event to be a signal or a background respectively. These probabilities are calculated from PDFs, excluding in the computation the variable being plotted. The optimal cut for R has been determined using MC signal events and offpeak events. These projections are shown in Fig. 7.8. Fit curves shown are not a fit to the data in the histogram but the projection of the overall fit scaled to take into account the effect of the cut on R.

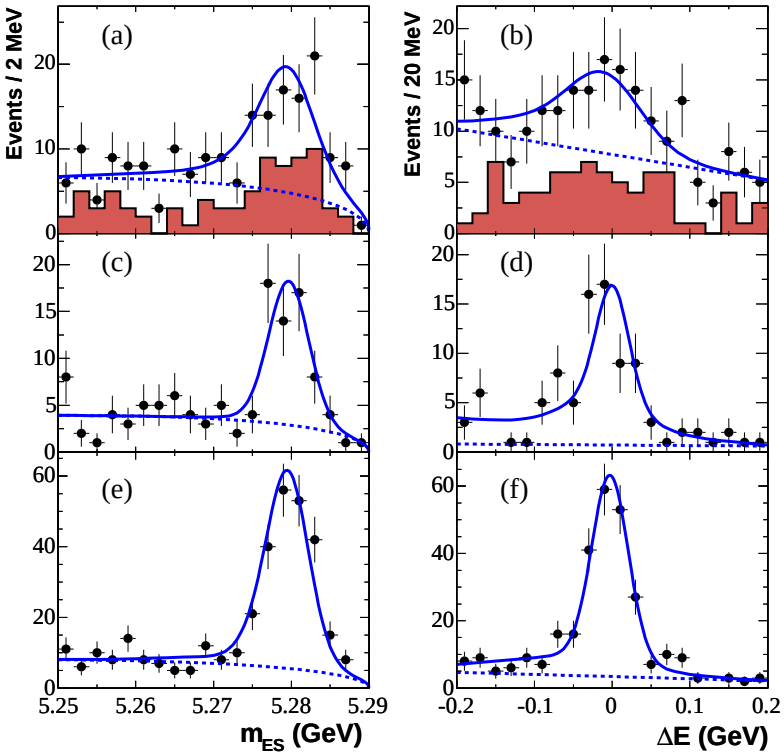

Figure 7.8: The B candidate M_{ES} and ΔE projections for $B^0 \to \eta' K^0$ with $K^0_S \to \pi^0\pi^0$ (a, b), $B^0 \to \eta'_{\eta(3\pi)\pi\pi} K^0_S$ with $K^0_S \to \pi^+\pi^-$ (c, d) and $B^+ \to \eta'_{\eta(3\pi)\pi\pi} K^+$ (e, f). Points with errors represent the data, solid curves the full fit functions, and dashed curves the background functions. The shaded histogram represents the $\eta'_{\eta(\gamma\gamma)\pi\pi} K^0_S$ subset.

7.8 Systematic Uncertainties for the Time-Dependent Asymmetry Fit

Because we merge the signal yield obtained in this analysis with the one from main sub-decays, due to a higher statistics with respect to the latter, we have studied the following contributions to the systematic errors only for the main sub-decays:

- For PDF shapes, we estimate the errors principally by variation of the fit parameters. In Table 7.32, we summarize all of the variations and their results. All changes are combined in quadrature to obtain an error which we round to 0.01 for both S and C.

- We correct for a possible dilution of S due to $B\overline{B}$ background and assign an uncertainty of 0.01 in S due to the uncertainty in this correction.

- Toy studies show that there are no significant biases in S and C other than the $B\overline{B}$ background issue just discussed. We assign an uncertainty of 0.01 for the modeling of the signal to cover the statistical uncertainties of these toy studies.

- We vary the SVT alignment parameters in the signal Monte Carlo events by the size of mis-alignment found in the real data [36], and assign the resulting shift in the fit results as the systematic errors. There are five different SVT configurations which are considered. Four configurations simulate time dependent mis-alignment and one (labeled “boost") simulates the radius-dependent z shift of entire layers. The difference for each configuration between the nominal values of S and C and those from the mis-aligned configuration are presented in Table 7.33. The nominal value was extracted by running signal MC in refit mode with a perfect SVT alignment. We take an uncertainty of 0.01 on both S and C.

- We vary the beam-spot y position and error in the signal Monte Carlo events. The values of the change were provided by Max Baak and are considered realistic for real data. The variations in the beam-spot parameters and the changes in S and C are presented in Table 7.34. We take an uncertainty of 0.01 on both S and C.

- The effect of interference between the CKM-suppressed $\overline{b} \to \overline{u}c\overline{d}$ amplitude with the favored $b \to c\overline{u}d$ amplitude for some tag-side B decays [37]. This is negligible for S, but contributes an uncertainty of 0.012 to C.

Table 7.32: Results of systematic variations. We show the nominal values, the amount that we vary these, the source of this variation amount, and the change of S and C for this amount of variation. We group similar quantities together after combining their variations in quadrature.

Quantity	Nominal	$\pm$ variation	Source of variation	Change in S	Change in C
Δm_d	0.502	0.007	PDG	0.0044	0.0002
τ_B	1.536	0.014	PDG	0.0007	0.0002
w	Table 4	Table 4	Table 4	0.0030	0.0016
δw	Table 4	Table 4	Table 4	0.0011	0.0067
Signal $f_{\rm cat}$	Table 4	Table 4	Table 4	0.0055	0.0025
Signal Δt	Table 6	Table 6	Table 6	0.0005	0.0002
Total				0.0078	0.0074

Table 7.33: The change in S and C due to different SVT configurations. The overall is calculated by taking the largest positive and negative contributions of the four time dependent configurations adding them in quadrature to the "Boost" contribution.

	$\eta'_{\eta\pi\pi}K^0$		$\eta'_{\rho\gamma}K^0$	
Configuration	Change in S	Change in C	Change in S	Change in C
Time1	0.0070	0.0006	0.0006	-0.0027
Time2	0.0084	0.0003	0.0037	0.0008
Time3	0.0075	-0.0035	0.0001	-0.0008
Time4	0.0056	-0.0010	0.0014	-0.0005
"Boost"	0.0071	-0.0014	0.0000	0.0000
Overall	$^{+0.0110}_{-0.0000}$	$^{+0.0006}_{-0.0037}$	$^{+0.0037}_{-0.0000}$	$^{+0.0008}_{-0.0027}$

Table 7.34: The Beam Spot y position was varied by $\pm 20\,\mu m$ and the error on y was independently increased to $20\,\mu m$. The Overall contribution to the systematics was evaluated by averaging the absolute contributions from the shift in y and adding that in quadrature to the contribution from the error on y.

	$\eta'_{\eta\pi\pi}K^0$		$\eta'_{\rho\gamma}K^0$	
Beam spot	Change in S	Change in C	Change in S	Change in C
position $y + 20\,\mu m$	-0.0046	0.0035	0.0043	-0.0059
position $y - 20\,\mu m$	0.0011	0.0056	0.0073	-0.0050
error on y $20\,\mu m$	0.0011	0.0041	0.0079	-0.0054
Overall	± 0.0031	± 0.0061	± 0.0098	$\pm - 0.0077$

For the channels studied in this thesis work, we have to add another contribution to the systematic error coming from SXF fraction. We made fits for S and C by varying the SXF fraction by $\pm$ 1 σ. Results of this analysis are shown in Table 7.35. We find

Decay Mode	Bias on S		Bias on C	
	$f_{SXF} + 1\sigma$	$f_{SXF} - 1\sigma$	$f_{SXF} + 1\sigma$	$f_{SXF} - 1\sigma$
$\eta'_{\rho\gamma}K^0_S$ $(\pi^0\pi^0)$	$+0.003$	-0.003	$+0.002$	-0.002
$\eta'_{\eta\pi\pi}K^0_S$ $(\pi^0\pi^0)$	0.000	$+0.001$	0.000	$+0.001$
$\eta'_{\eta(3\pi)\pi\pi}K^0_S$ $(\pi^+\pi^-)$	$+0.001$	$+0.002$	0.000	0.000

Table 7.35: Results of systematic variations due to SXF fraction (f_{SXF}) on S and C parameters, when we vary SXF fraction $\pm$ 1 σ.

that the maximum bias for S is 0.003 and for C is 0.002. We take these values as systematics errors due to SXF and we will sum all systematics errors in quadrature we find 0.02 for both S and C.

Chapter 8

Conclusions

The goal of this work was to add events to the main decay modes and reduce the statystical error for the measurement of S and C parameters. So, the previous results for the decays studied in this thesis have been added to the main ones to obtain a combined fit for the CP-violating parameters. The results have been reported below in Table 8.1:

Table 8.1: Results with statistical errors for the $B^0 \to \eta' K^0_S$ time-dependent fits. First result is only for decays with $K^0_S \to \pi^+\pi^-$, the latter is the combined fit for decays with $K^0_S \to \pi^+\pi^-$ and $K^0_S \to \pi^0\pi^0$.

Mode	Signal yield	S	C
$\eta'_{\eta(\gamma\gamma)\pi\pi} K^0_{\pi^+\pi^-}$	188 ± 15	0.01 ± 0.28	-0.18 ± 0.18
$\eta'_{\rho\gamma} K^0_{\pi^+\pi^-}$	430 ± 26	0.44 ± 0.19	-0.30 ± 0.13
$B \to \eta' K^0_S$ **(**$K^0_S \to \pi^+\pi^-$**)**	618 ± 30	0.30 ± 0.16	-0.25 ± 0.11
$\eta'_{\eta(3\pi)\pi\pi} K^0_{\pi^+\pi^-}$	54 ± 8	0.79 ± 0.47	0.11 ± 0.35
$\eta'_{\eta(\gamma\gamma)\pi\pi} K^0_{\pi^0\pi^0}$	44 ± 9	-0.04 ± 0.57	-0.65 ± 0.42
$\eta'_{\rho\gamma} K^0_{\pi^0\pi^0}$	94 ± 23	-0.45 ± 0.68	0.41 ± 0.40
Combined fit	804 ± 40	0.30 ± 0.14	-0.21 ± 0.10

As it's shown in the rows with the results, adding decay modes studied in this thesis work we have an improvement on statistical error. The measured time-dependent CP violation parameters in $B^0 \to \eta' K^0_S$ are $S = 0.30 \pm 0.14 \pm 0.02$ and $C = -0.21 \pm 0.10 \pm 0.02$. Our result for S differs from that measured by *BABAR* in $B^0 \to J/\psi K^0_S$ [14] by 3.0 standard deviations; it also represents an improvement by a factor 2.4 (1.9) in precision over the published results of *BABAR* [38] (Belle [39]). All these measurements

supersede our previous published results [38].

These results have been presented “Meeting of APS, Division of Particles and Fields”, Tampa FL(USA), 16th April 2005 and published on PRL [16].

Appendix A

PDF libraries

We show here for each decay mode the signal and background PDFs used in ML fits. We show also the correlation coefficients between the input variables used in the ML fits.

Signal PDFs are determinated from MC signal events. For continuum background PDFs we have used on-peak sidebands. For $B\overline{B}$ background PDFs we have used MC events.

A.1 $\eta'_{\rho\gamma} K^0_S$ $(K^0_S \to \pi^0\pi^0)$

	M_{ES}	ΔE	$\mathcal{F}$	Δt	$\sigma_{\Delta t}$
M_{ES}	1.000				
ΔE	0.060	1.000			
$\mathcal{F}$	-0.039	-0.017	1.000		
Δt	0.005	0.014	0.013	1.000	
$\sigma_{\Delta t}$	-0.018	-0.026	0.002	-0.029	1.000

Table A.1: Correlation matrix for MC signal.

	M_{ES}	ΔE	$\mathcal{F}$	Δt	$\sigma_{\Delta t}$
M_{ES}	1.000				
ΔE	-0.005	1.000			
$\mathcal{F}$	0.006	-0.059	1.000		
Δt	0.003	0.009	0.008	1.000	
$\sigma_{\Delta t}$	-0.016	0.014	-0.103	0.034	1.000

Table A.2: Correlation matrix for on-peak side band data.

Floating Parameter	FinalValue +/- Error
bMass_xi_bg	-1.4461e+01 +/- 2.27e+00
dE_c1_bg	-3.8897e-01 +/- 1.45e-02
deltaT_frac1_bg	3.1856e-01 +/- 1.78e-02
deltaT_frac2_bg	3.1169e-02 +/- 2.69e-03
deltaT_mu1_bg	1.9638e-02 +/- 1.07e-02
deltaT_mu2_bg	1.2741e-01 +/- 3.80e-02
deltaT_sigma1_bg	6.9959e-01 +/- 1.56e-02
deltaT_sigma2_bg	1.9311e+00 +/- 6.01e-02
fisher_Mu1_bg	1.5242e+00 +/- 2.15e-02
fisher_Sigma1_bg	8.0508e-01 +/- 1.50e-02
fisher_Sigma2_bg	9.4038e-01 +/- 1.45e-02

Final values for the parameters which were allowed to float in the fit.

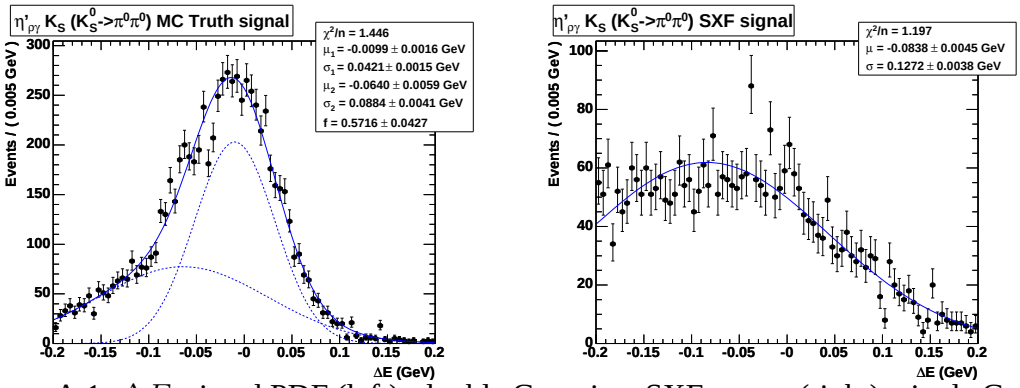

Figure A.1: ΔE signal PDF (left): double Gaussian; SXF events (right): single Gaussian.

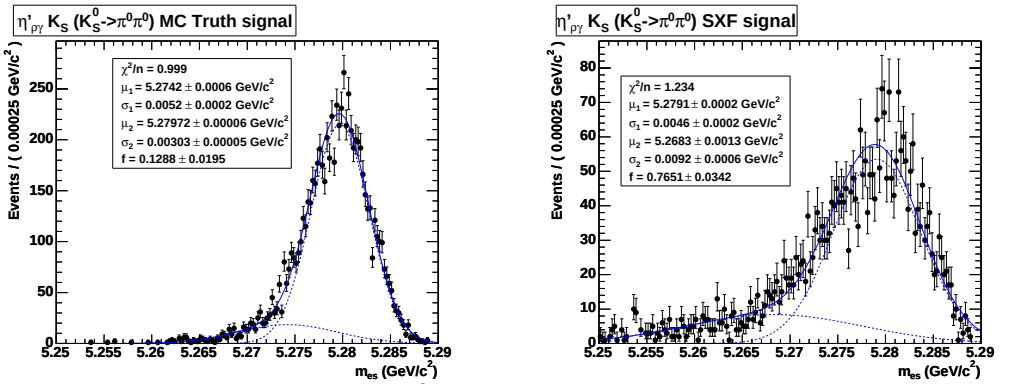

Figure A.2: Signal M_{ES} PDF (left): double Gaussian; SXF events (right): double Gaussian.

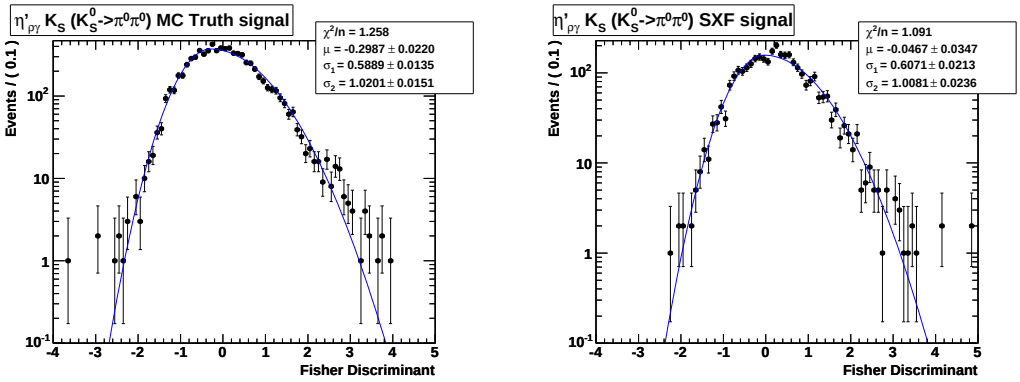

Figure A.3: Signal $\mathcal{F}$ Fisher PDF (left): asymmetric Gaussian ; SXF events (right): asymmetric Gaussian .

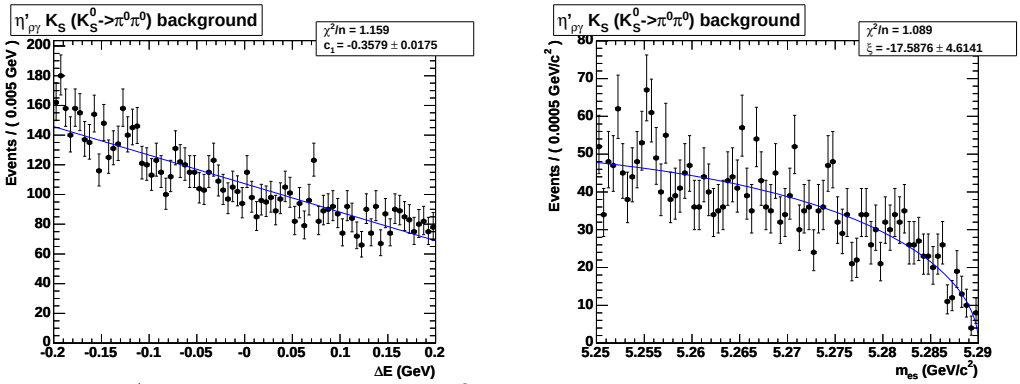

Figure A.4: ΔE background PDF (left): linear Chebyshev polynomial; M_{ES} background PDF (right): Argus.

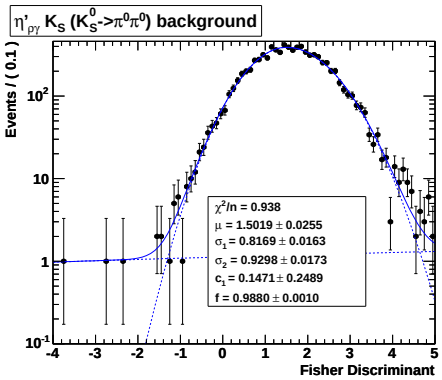

Figure A.5: $\mathcal{F}$ Fisher background PDF: an asymmetric Gaussian plus a linear Chebyshev polynomial.

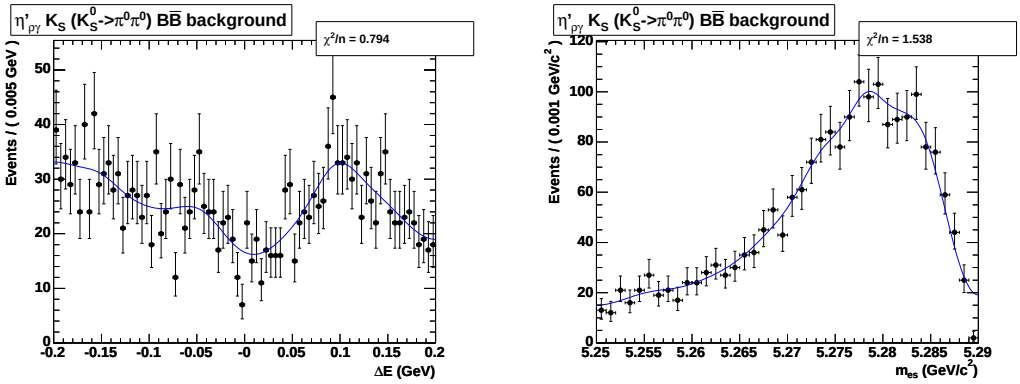

Figure A.6: $B\overline{B}$ data ΔE PDF (left): KEYS; $B\overline{B}$ data M_{ES} PDF (right): KEYS.

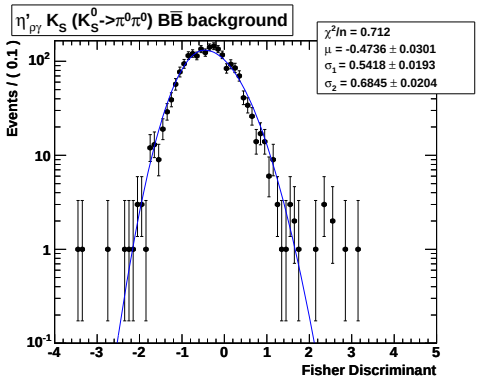

Figure A.7: $B\overline{B}$ data $\mathcal{F}$ Fisher PDF: asymmetric Gaussian.

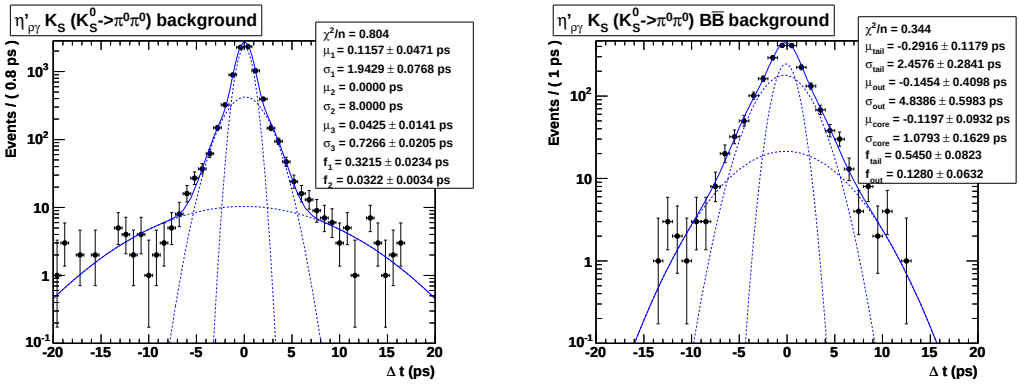

Figure A.8: Δt background PDF (left): Triple Gaussian; $B\overline{B}$ data Δt PDF (right): Triple Gaussian.

A.2 $\eta'_{\eta(\gamma\gamma)\pi\pi} K^0_S$ ($K^0_S \to \pi^0\pi^0$)

	M_{ES}	ΔE	$\mathcal{F}$	Δt	$\sigma_{\Delta t}$
M_{ES}	1.000				
ΔE	0.087	1.000			
$\mathcal{F}$	-0.025	-0.016	1.000		
Δt	-0.004	-0.001	0.001	1.000	
$\sigma_{\Delta t}$	0.001	-0.011	-0.010	-0.008	1.000

Table A.3: Correlation matrix for MC signal.

	M_{ES}	ΔE	$\mathcal{F}$	Δt	$\sigma_{\Delta t}$
M_{ES}	1.000				
ΔE	0.024	1.000			
$\mathcal{F}$	-0.037	-0.024	1.000		
Δt	-0.030	0.002	0.066	1.000	
$\sigma_{\Delta t}$	0.037	0.006	-0.093	0.019	1.000

Table A.4: Correlation matrix for on-peak side band data.

Floating Parameter	FinalValue +/- Error
bMass_xi_bg	-3.3316e+01 +/- 1.18e+01
dE_c1_bg	-2.5201e-01 +/- 7.87e-02
deltaT_frac1_bg	2.7591e-01 +/- 1.17e-01
deltaT_frac2_bg	3.0656e-02 +/- 1.34e-02
deltaT_mu1_bg	7.7064e-02 +/- 8.40e-02
deltaT_mu2_bg	-1.6437e-01 +/- 2.86e-01
deltaT_sigma1_bg	1.0196e+00 +/- 1.11e-01
deltaT_sigma2_bg	2.2574e+00 +/- 3.49e-01
fisher_Mu1_bg	1.3353e+00 +/- 1.14e-01
fisher_Sigma1_bg	6.0339e-01 +/- 7.59e-02
fisher_Sigma2_bg	8.3322e-01 +/- 8.01e-02

Final values for the parameters which were allowed to float in the fit.

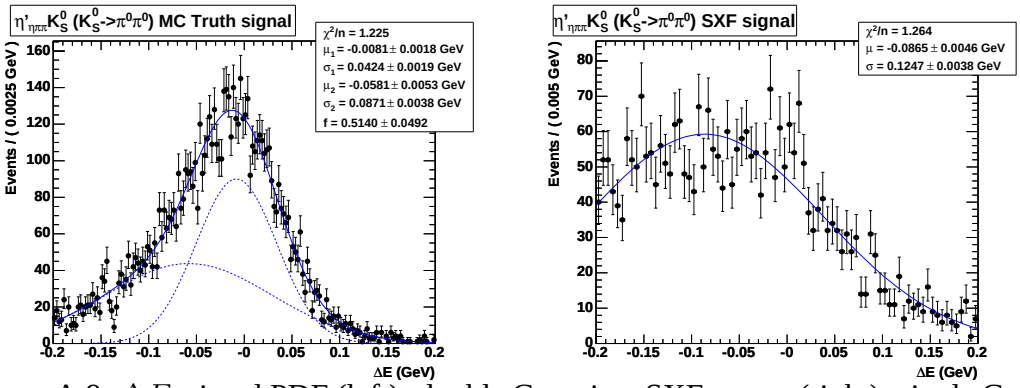

Figure A.9: ΔE signal PDF (left): double Gaussian; SXF events (right): single Gaussian.

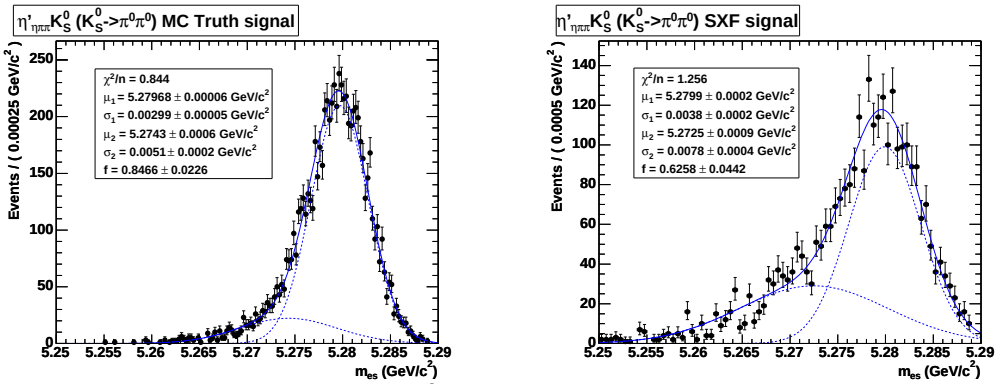

Figure A.10: Signal M_{ES} PDF (left): double Gaussian; SXF events (right): double Gaussian.

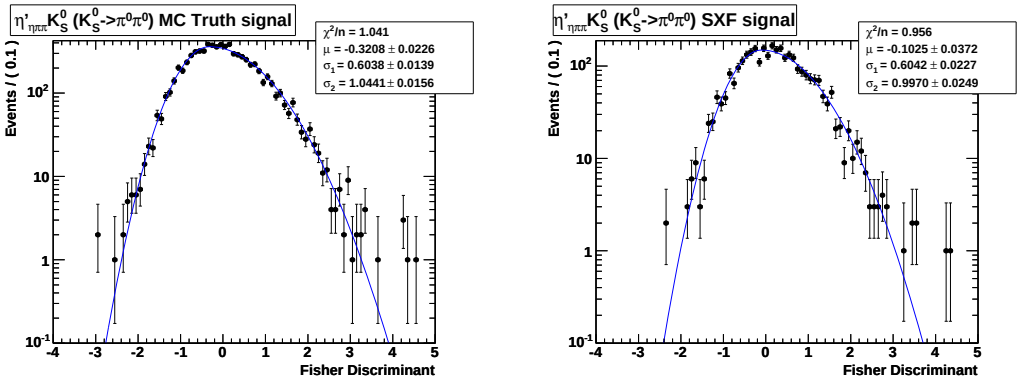

Figure A.11: Signal $\mathcal{F}$ Fisher PDF (left): asymmetric Gaussian; SXF events (right): asymmetric Gaussian.

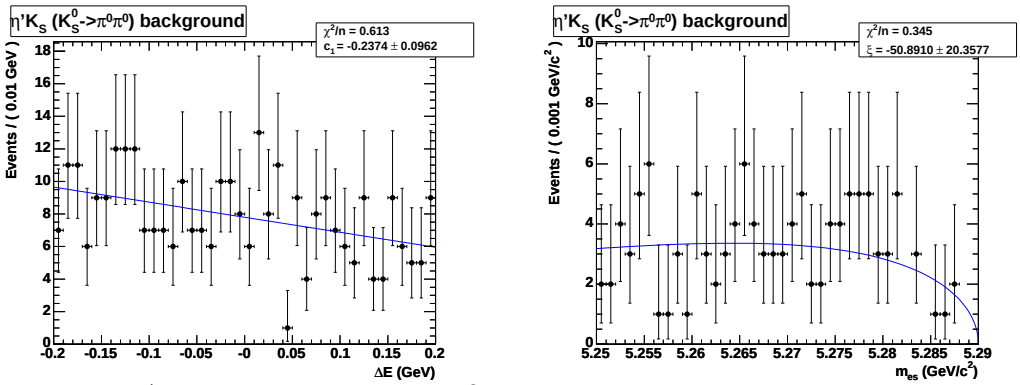

Figure A.12: ΔE background PDF (left): linear Chebyshev polynomial; M_{ES} background PDF (right): Argus.

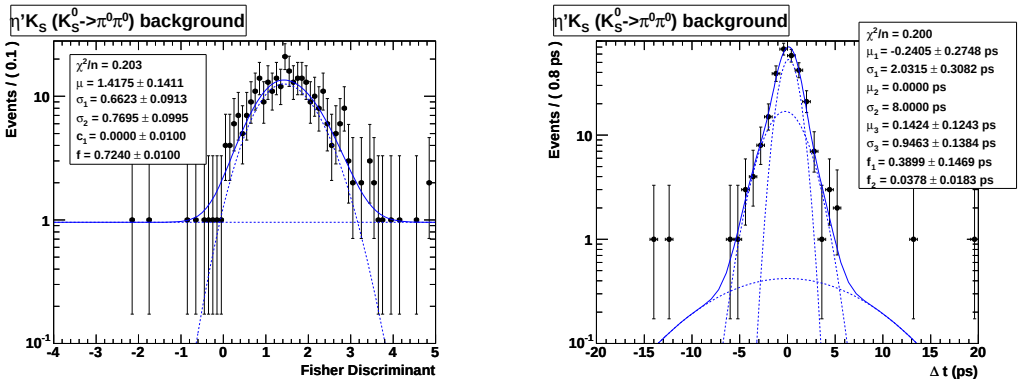

Figure A.13: $\mathcal{F}$ Fisher background PDF (left): linear Chebyshev polynomial plus asymmetric Gaussian. Δt background PDF (right): Triple Gaussian.

A.3 $\eta'_{\eta(3\pi)\pi\pi}K^0_S$ ($K^0_S \to \pi^+\pi^-$)

	M_{ES}	ΔE	$\mathcal{F}$	Δt	$\sigma_{\Delta t}$
M_{ES}	1.000				
ΔE	0.113	1.000			
$\mathcal{F}$	-0.063	-0.051	1.000		
Δt	-0.025	-0.004	0.015	1.000	
$\sigma_{\Delta t}$	-0.015	-0.006	-0.009	-0.008	1.000

Table A.5: Correlation matrix for MC signal.

	M_{ES}	ΔE	$\mathcal{F}$	Δt	$\sigma_{\Delta t}$
M_{ES}	1.000				
ΔE	-0.140	1.000			
$\mathcal{F}$	0.011	-0.022	1.000		
Δt	0.115	-0.085	0.024	1.000	
$\sigma_{\Delta t}$	0.089	0.005	-0.110	-0.049	1.000

Table A.6: Correlation matrix for on-peak side band data.

Floating Parameter	FinalValue +/-	Error
dE_c1_bg	-3.3808e-01 +/-	1.64e-01
deltaT_frac1_bg	2.6707e-01 +/-	1.27e-01
deltaT_mu1_bg	6.4950e-02 +/-	2.06e-01
deltaT_mu2_bg	-3.7289e-01 +/-	1.73e-01
deltaT_sigma1_bg	1.5175e+00 +/-	1.91e-01
deltaT_sigma2_bg	4.4026e-01 +/-	1.63e-01
fisher_Mu1_bg	7.4112e-01 +/-	4.31e-01
fisher_Sigma1_bg	6.3659e-01 +/-	2.42e-01
fisher_Sigma2_bg	1.5181e+00 +/-	2.87e-01

Final values for the parameters which were allowed to float in the fit.

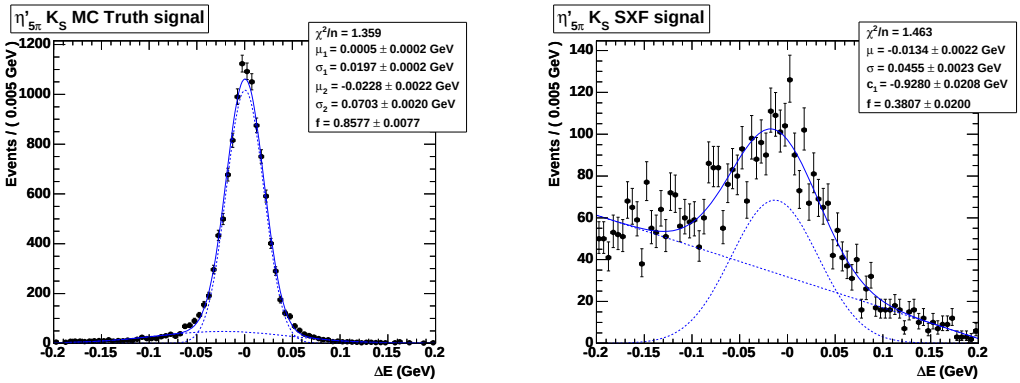

Figure A.14: ΔE signal PDF (left): double Gaussian; SXF events (right): single Gaussian plus linear Chebyshev polynomial.

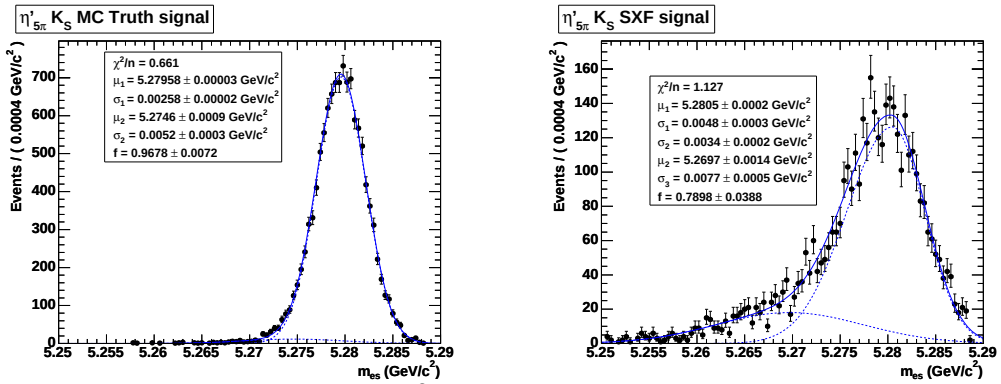

Figure A.15: Signal M_{ES} PDF (left): double Gaussian; SXF events (right): an asymmetric Gaussian plus a single Gaussian.

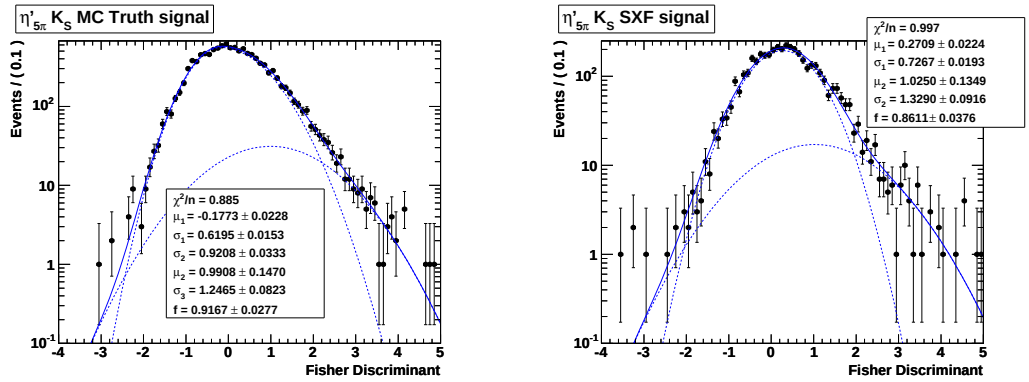

Figure A.16: Signal $\mathcal{F}$ Fisher PDF (left): an asymmetric Gaussian plus a single Gaussian; SXF events (right): a double Gaussian.

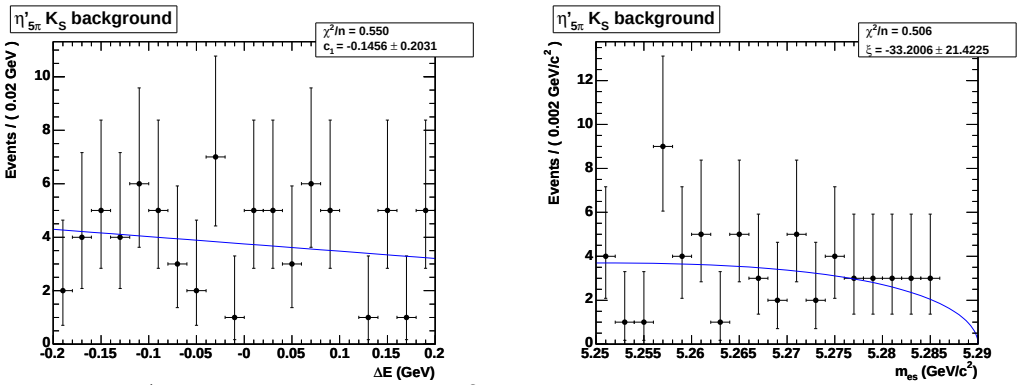

Figure A.17: ΔE background PDF (left): linear Chebyshev polynomial; M_{ES} background PDF (right): Argus.

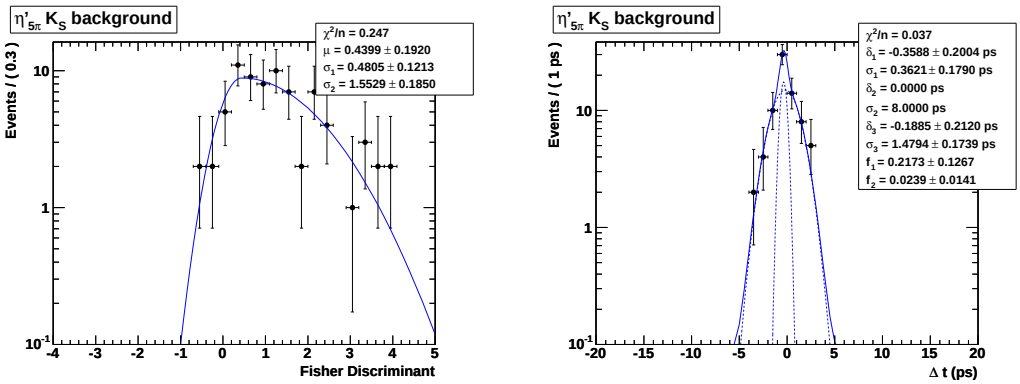

Figure A.18: $\mathcal{F}$ Fisher background PDF (left): asymmetric Gaussian. Δt background PDF (right): Triple Gaussian.

A.4 $\eta'_{\eta(3\pi)\pi\pi}K^+$

	M_{ES}	ΔE	$\mathcal{F}$	Δt	$\sigma_{\Delta t}$
M_{ES}	1.000				
ΔE	0.129	1.000			
$\mathcal{F}$	-0.057	-0.036	1.000		
Δt	0.004	0.014	-0.002	1.000	
$\sigma_{\Delta t}$	-0.020	-0.012	-0.023	-0.011	1.000

Table A.7: Correlation matrix for MC signal.

	M_{ES}	ΔE	$\mathcal{F}$	Δt	$\sigma_{\Delta t}$
M_{ES}	1.000				
ΔE	-0.115	1.000			
$\mathcal{F}$	-0.079	0.016	1.000		
Δt	-0.054	0.075	-0.019	1.000	
$\sigma_{\Delta t}$	0.026	-0.000	-0.046	0.095	1.000

Table A.8: Correlation matrix for on-peak side band data.

Floating Parameter	FinalValue +/- Error
bMass_xi_bg	-5.1398e+00 +/- 1.35e+01
dE_c1_bg	-4.5049e-01 +/- 8.58e-02
deltaT_frac1_bg	1.1508e-01 +/- 6.81e-02
deltaT_frac2_bg	1.5135e-02 +/- 1.26e-02
deltaT_mu1_bg	7.5036e-03 +/- 5.35e-02
deltaT_mu2_bg	-3.6210e-01 +/- 4.56e-01
deltaT_sigma1_bg	7.5084e-01 +/- 5.77e-02
deltaT_sigma2_bg	2.0088e+00 +/- 8.05e-01
fisher_Mu1_bg	1.5253e+00 +/- 1.31e-01
fisher_Sigma1_bg	7.6652e-01 +/- 9.27e-02
fisher_Sigma2_bg	8.0308e-01 +/- 8.97e-02

Final values for the parameters which were allowed to float in the fit.

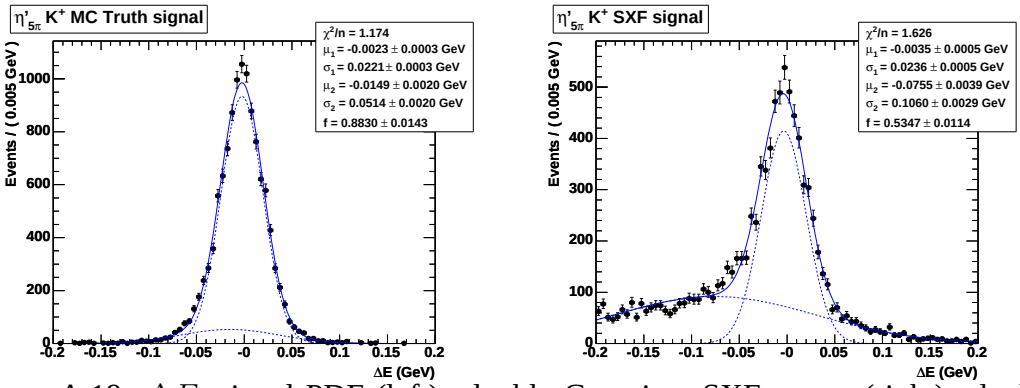

Figure A.19: ΔE signal PDF (left): double Gaussian; SXF events (right): double Gaussian.

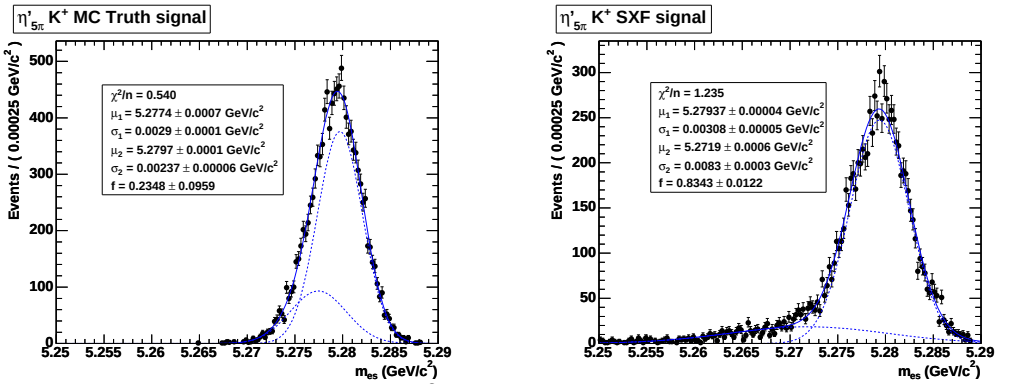

Figure A.20: Signal M_{ES} PDF (left): double Gaussian; SXF events (right): double Gaussian.

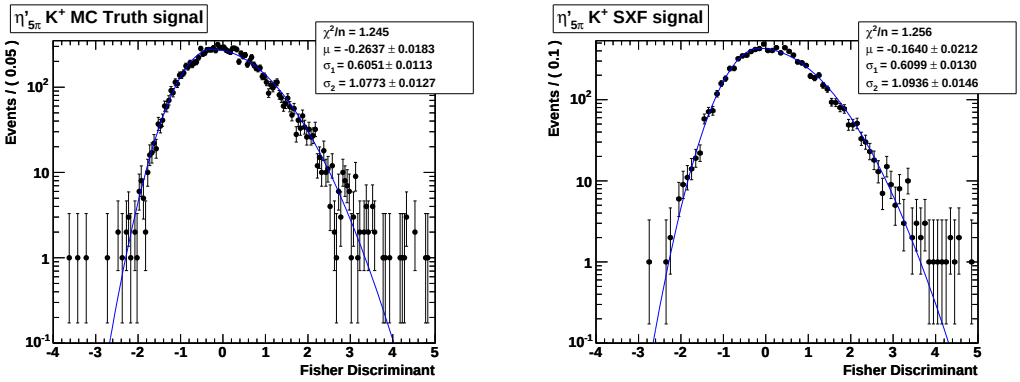

Figure A.21: Signal $\mathcal{F}$ Fisher PDF (left): asymmetric Gaussian; SXF events (right): asymmetric Gaussian.

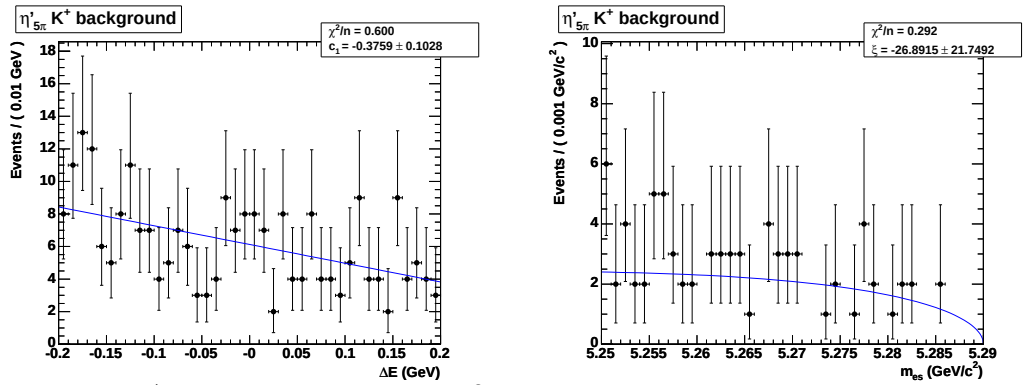

Figure A.22: ΔE background PDF (left): linear Chebyshev polynomial; M_{ES} background PDF (right): Argus.

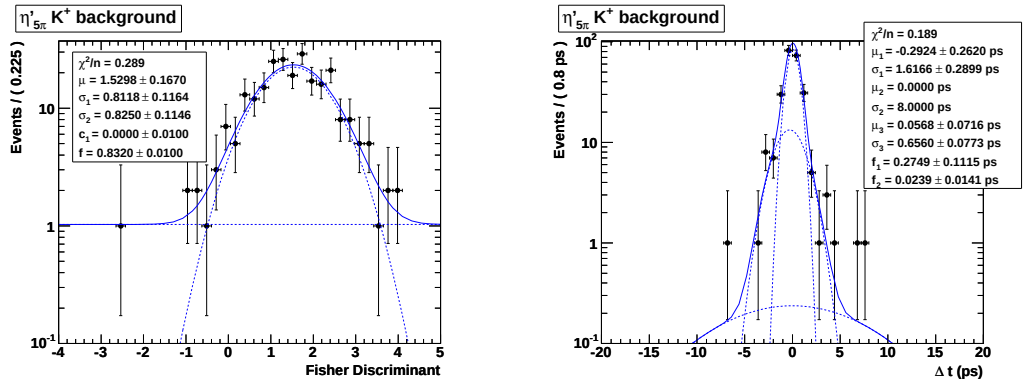

Figure A.23: $\mathcal{F}$ Fisher background PDF (left): linear Chebyshev polynomial plus asymmetric Gaussian. Δt background PDF (right): Triple Gaussian.

Appendix B

Toy experiments distributions

B.1 $\eta'_{\rho\gamma} K^0_S$ $(K^0_S \to \pi^0\pi^0)$

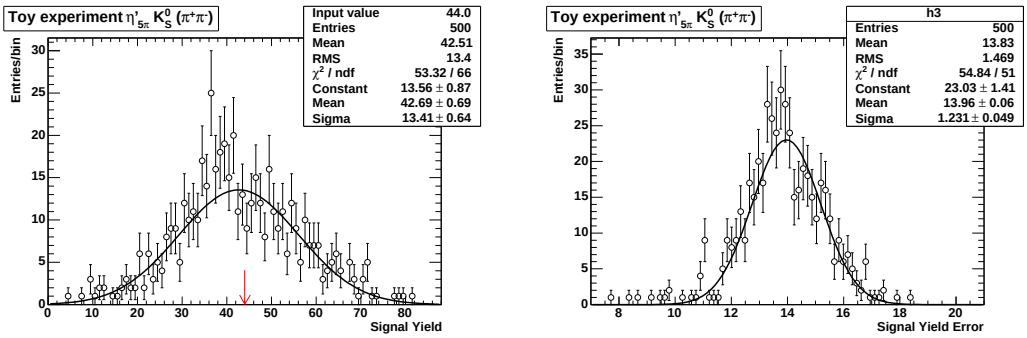

Figure B.1: 500 yield pure toy experiments: signal yield (left), error on signal yield (right).

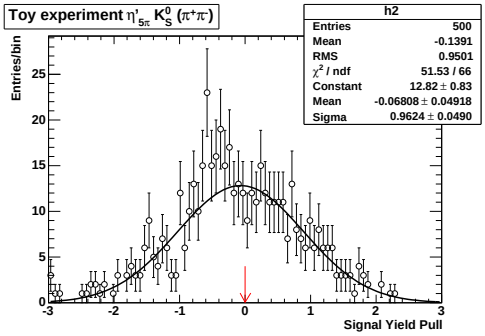

Figure B.2: 500 yield pure toy experiments: pull value and sigma distribution.

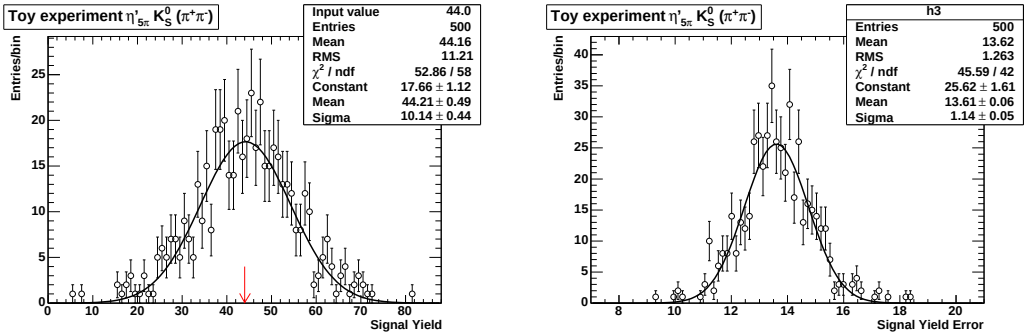

Figure B.3: 500 yield MC toy experiments: signal yield (left), error on signal yield (right).

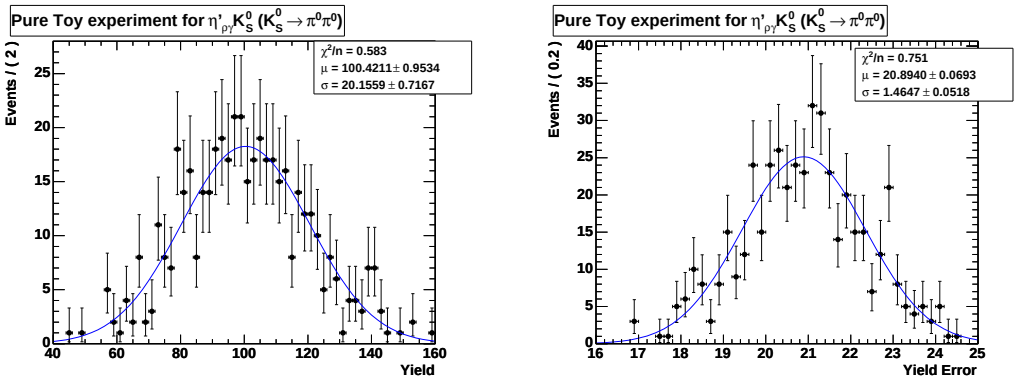

Figure B.4: 500 CP pure toy experiments: signal yield (left), error on signal yield (right).

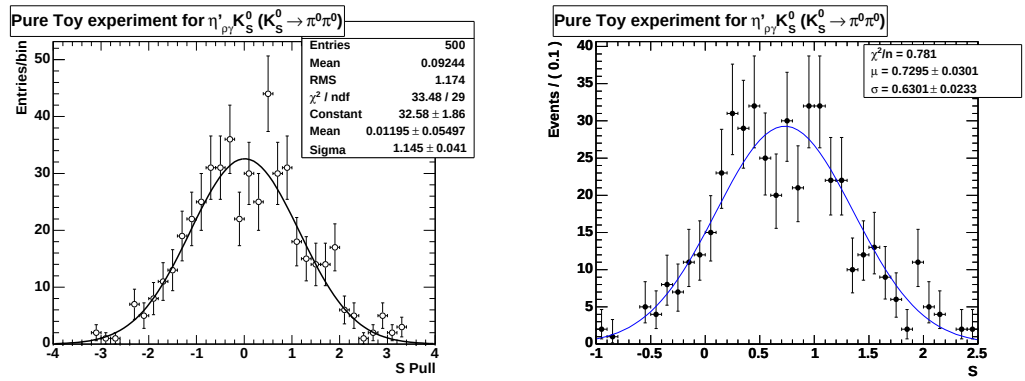

Figure B.5: 500 CP pure toy experiments: pull value and sigma for signal (left), S parameter value (right).

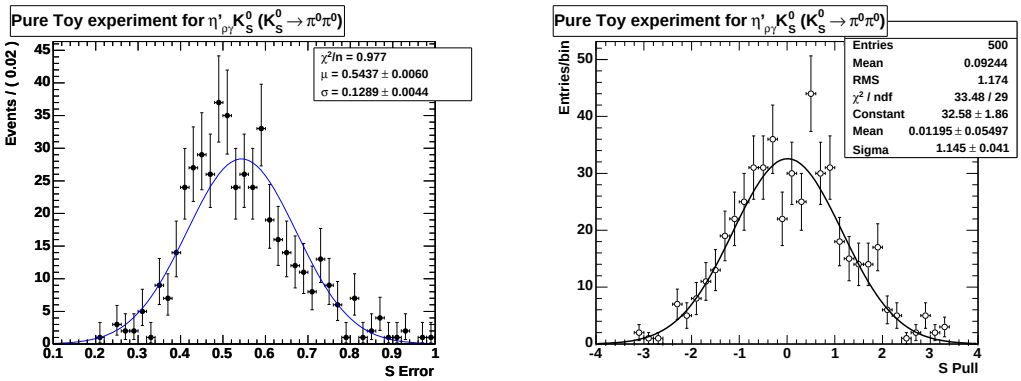

Figure B.6: 500 CP pure toy experiments: error on S (left), pull value and sigma for S (right).

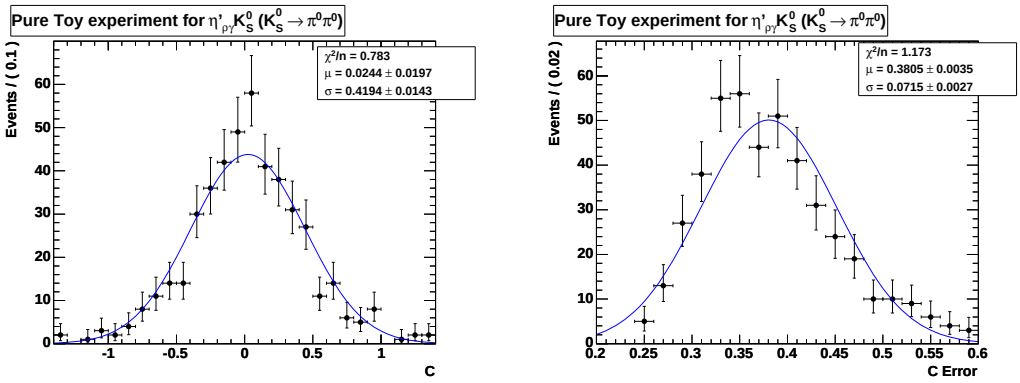

Figure B.7: 500 CP pure toy experiments: C parameter value (left), error on C (right).

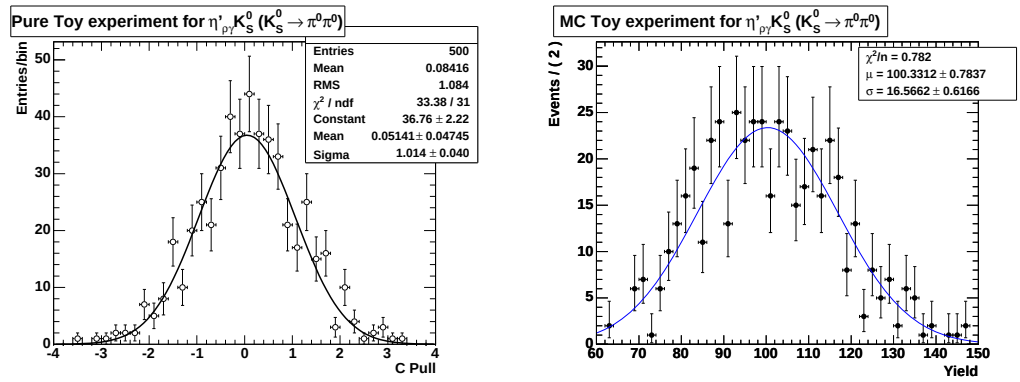

Figure B.8: 500 CP pure toy experiments: pull value and sigma for C (left); 500 CP MC toy experiments: signal yield (right).

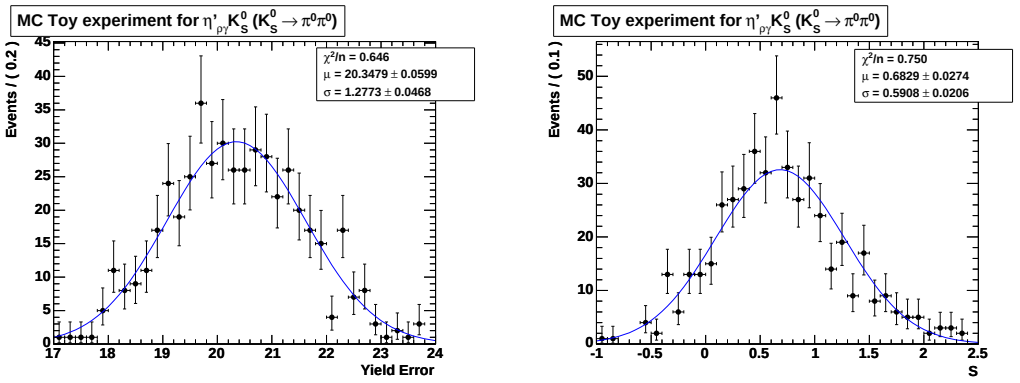

Figure B.9: 500 CP MC toy experiments: pull value and sigma for signal (left); 500 CP MC toy experiments: S parameter value (right).

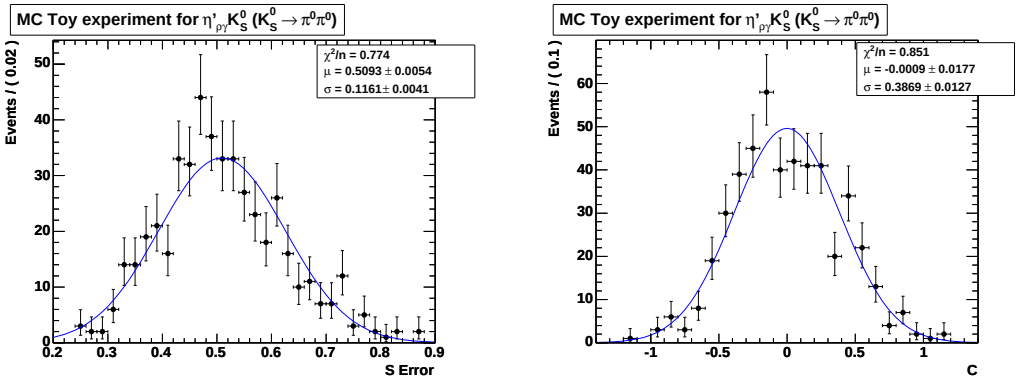

Figure B.10: 500 CP MC toy experiments: error on S (left); 500 CP MC toy experiments: C parameter value (right).

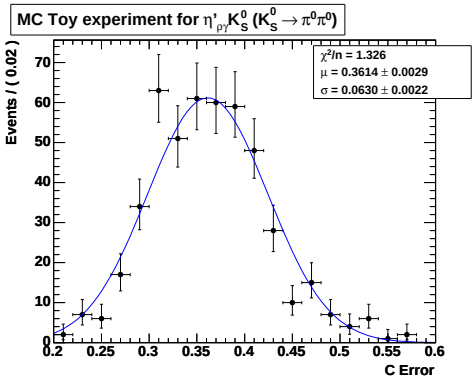

Figure B.11: 500 CP MC toy experiments: error on C.

B.2 $\eta'_{\eta(\gamma\gamma)\pi\pi} K^0_S\,(K^0_S \to \pi^0\pi^0)$

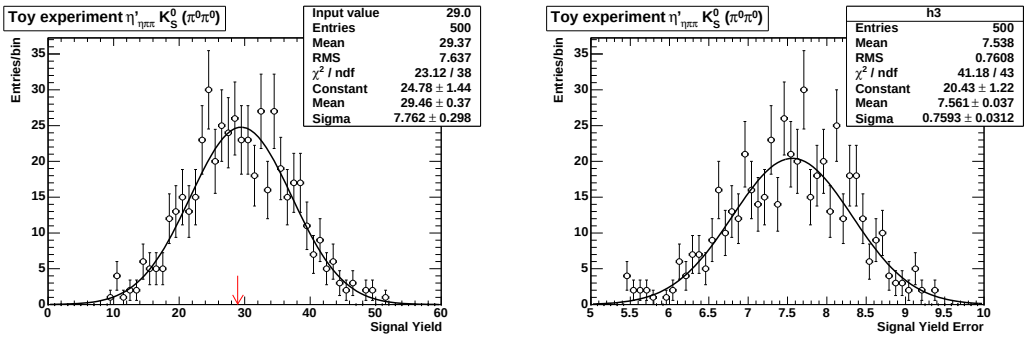

Figure B.12: 500 yield pure toy experiments: signal yield (left), error on signal yield (right).

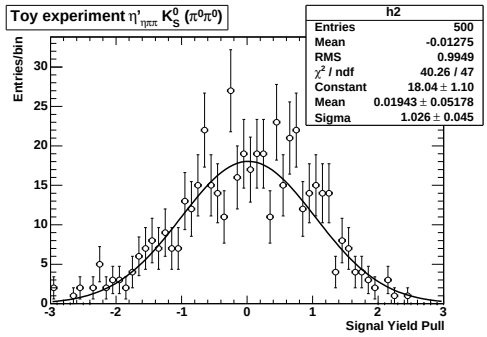

Figure B.13: 500 yield pure toy experiments: pull value and sigma distribution.

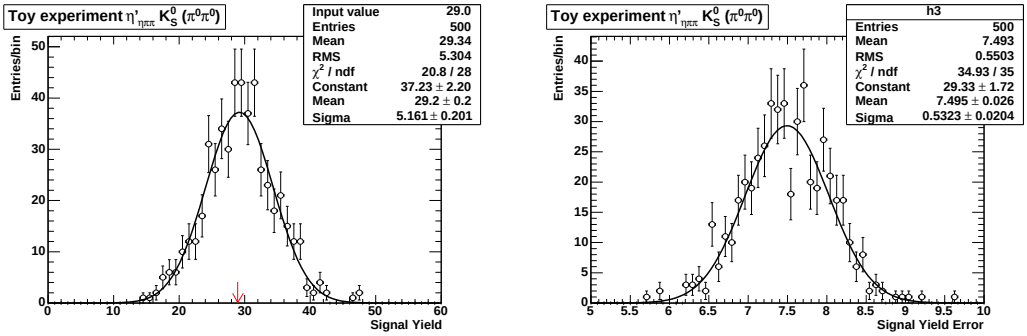

Figure B.14: 500 yield MC toy experiments: signal yield (left), error on signal yield (right).

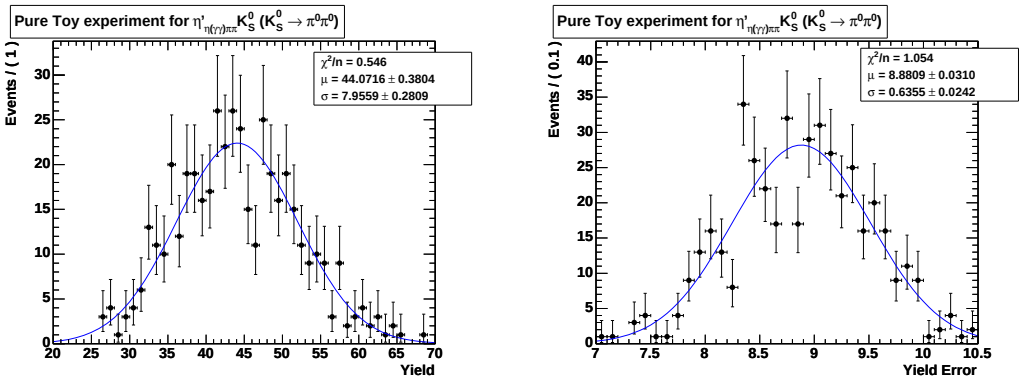

Figure B.15: 500 CP pure toy experiments: signal yield (left), error on signal yield (right).

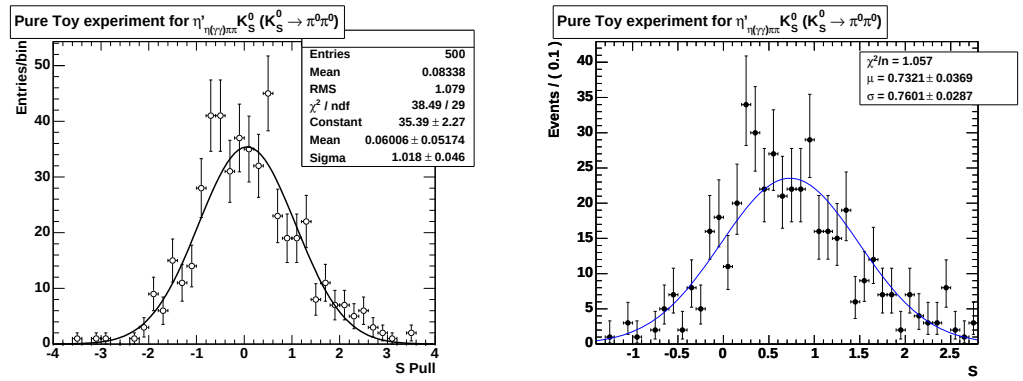

Figure B.16: 500 CP pure toy experiments: pull value and sigma for signal (left), S parameter value (right).

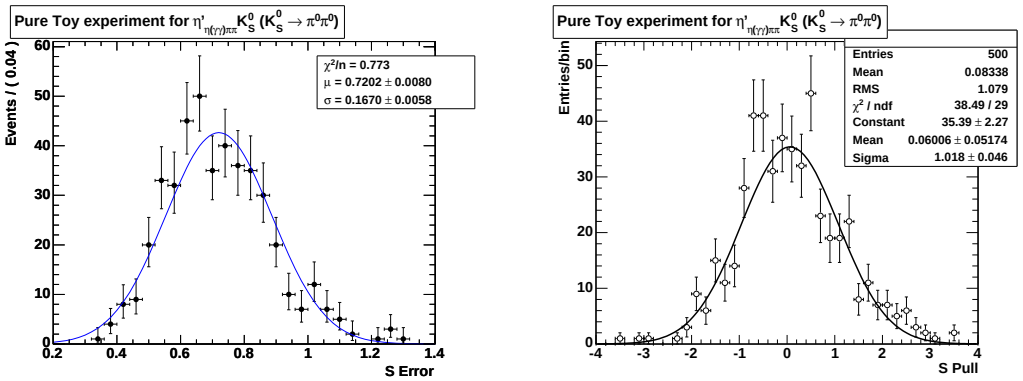

Figure B.17: 500 CP pure toy experiments: error on S (left), pull value and sigma for S (right).

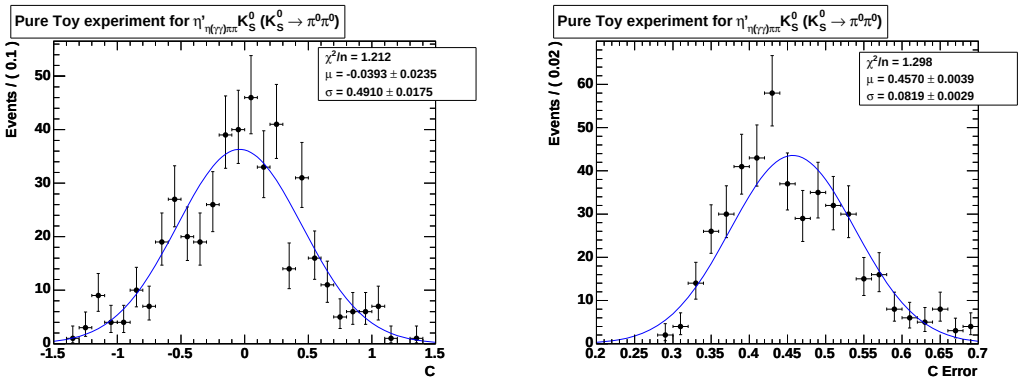

Figure B.18: 500 CP pure toy experiments: C parameter value (left), error on C (right).

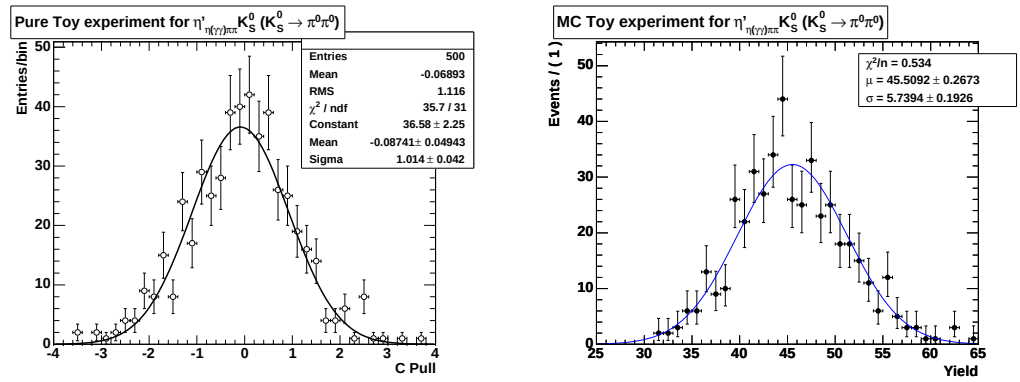

Figure B.19: 500 CP pure toy experiments: pull value and sigma for C (left); 500 CP MC toy experiments: signal yield (right).

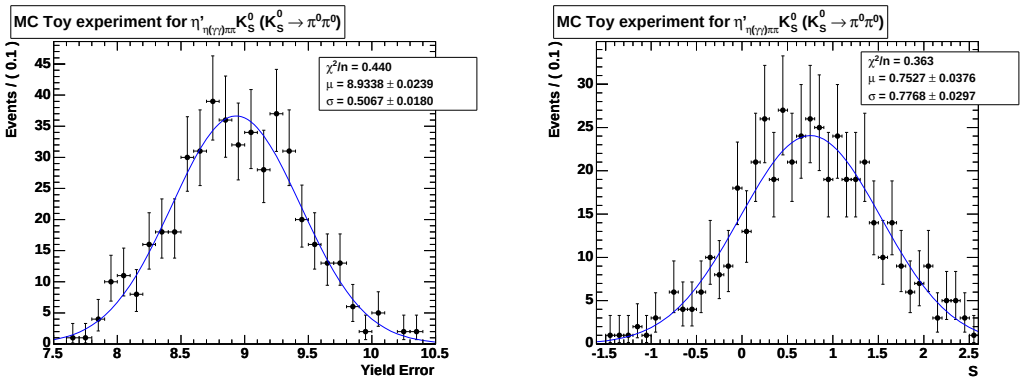

Figure B.20: 500 CP MC toy experiments: pull value and sigma for signal (left); 500 CP MC toy experiments: S parameter value (right).

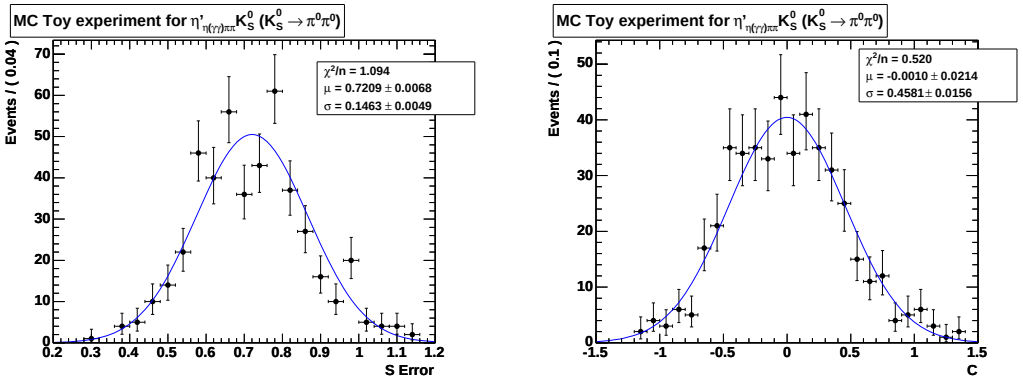

Figure B.21: 500 CP MC toy experiments: error on S (left); 500 CP MC toy experiments: C parameter value (right).

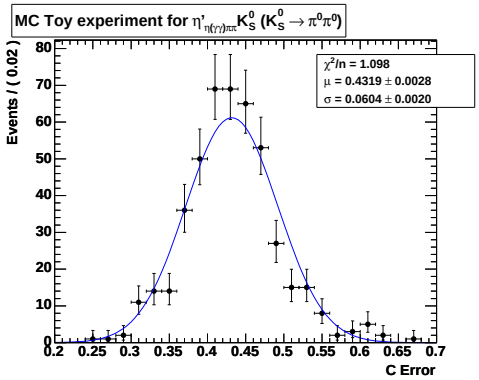

Figure B.22: 500 CP MC toy experiments: error on C.

B.3 $\eta'_{\eta(3\pi)\pi\pi} K^0_S\,(K^0_S \to \pi^+\pi^-)$

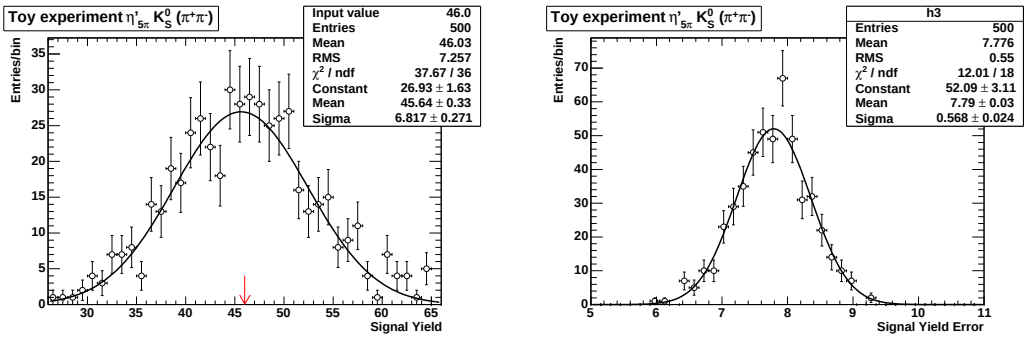

Figure B.23: 500 yield pure toy experiments: signal yield (left), error on signal yield (right).

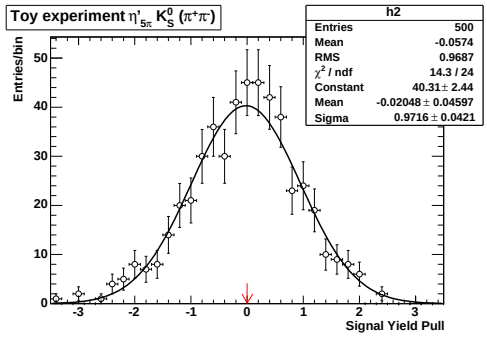

Figure B.24: 500 yield pure toy experiments: pull value and sigma distribution.

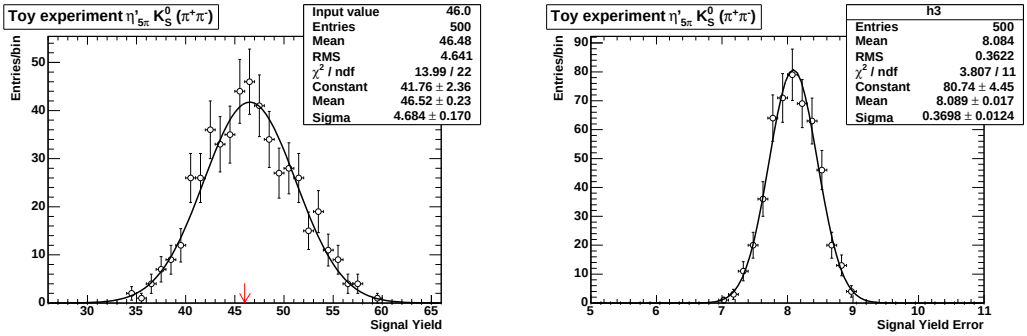

Figure B.25: 500 yield MC toy experiments: signal yield (left), error on signal yield (right).

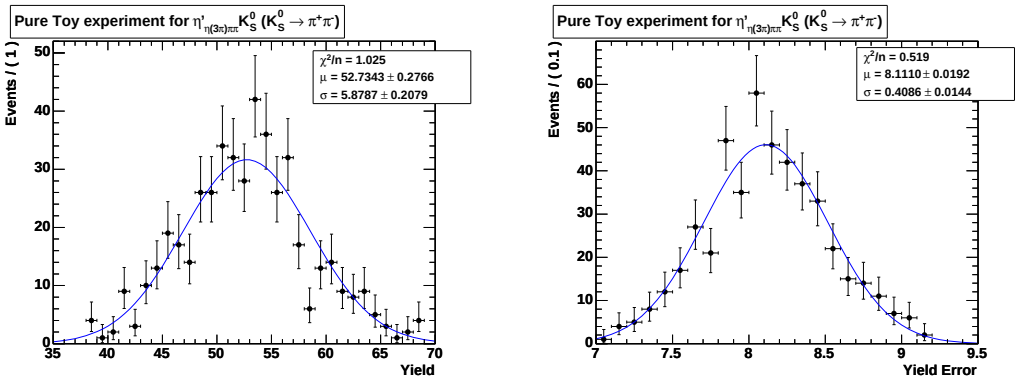

Figure B.26: 500 CP pure toy experiments: signal yield (left), error on signal yield (right).

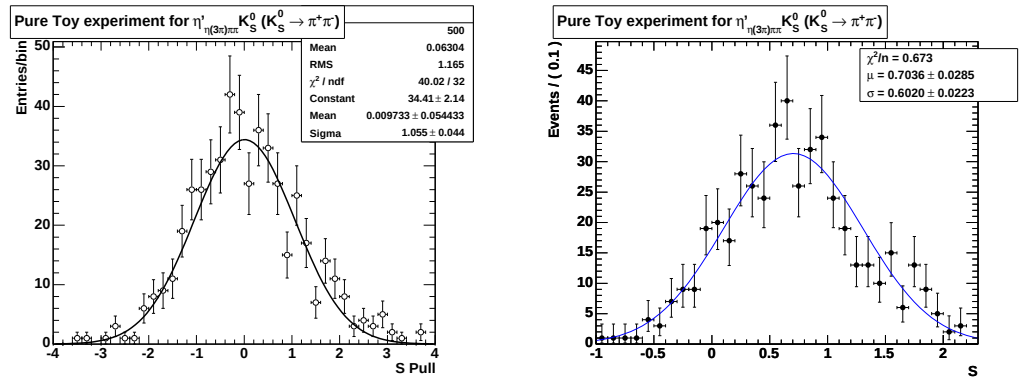

Figure B.27: 500 CP pure toy experiments: pull value and sigma for signal (left), S parameter value (right).

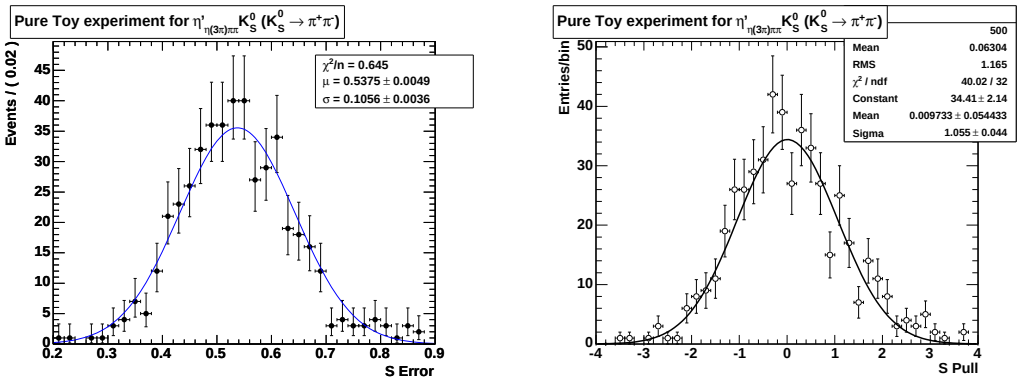

Figure B.28: 500 CP pure toy experiments: error on S (left), pull value and sigma for S (right).

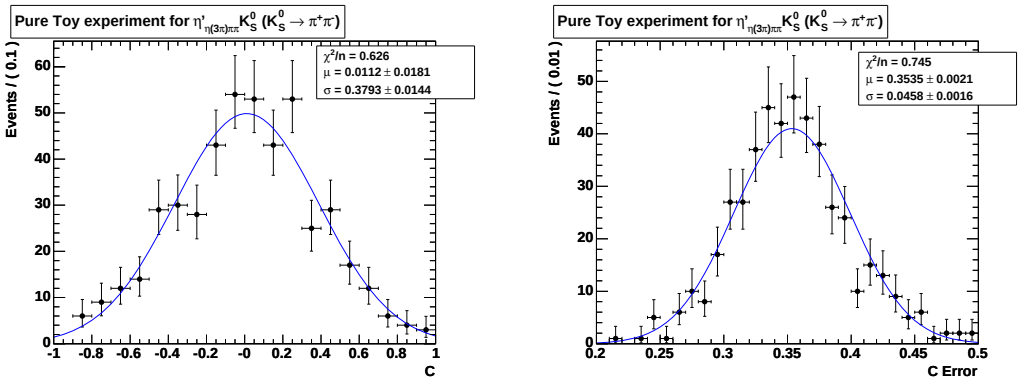

Figure B.29: 500 CP pure toy experiments: C parameter value (left), error on C (right).

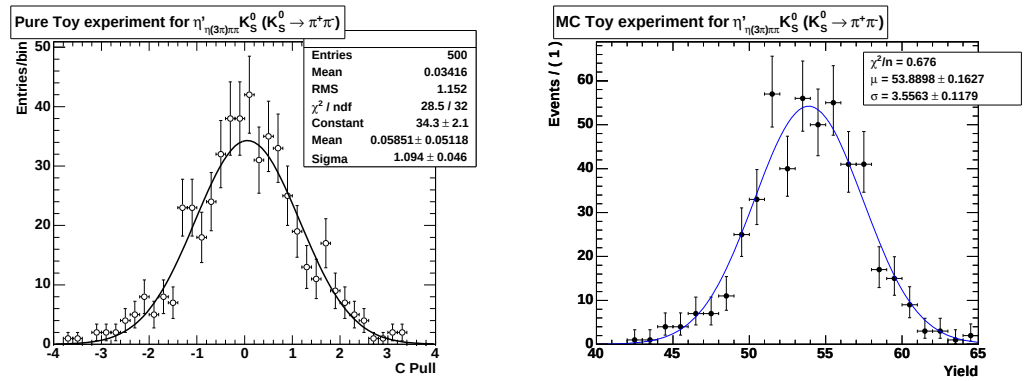

Figure B.30: 500 CP pure toy experiments: pull value and sigma for C (left); 500 CP MC toy experiments: signal yield (right).

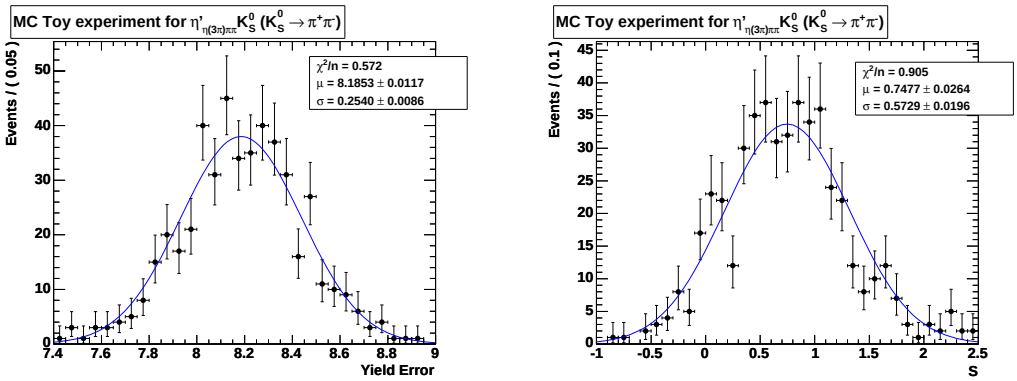

Figure B.31: 500 CP MC toy experiments: pull value and sigma for signal (left); 500 CP MC toy experiments: S parameter value (right).

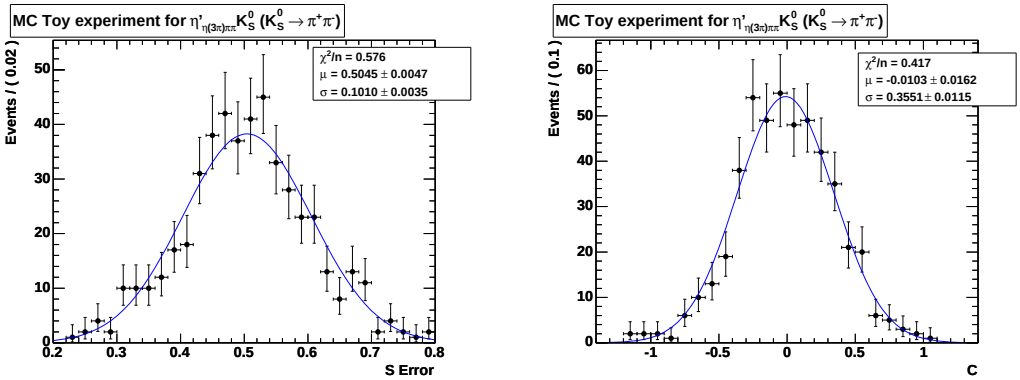

Figure B.32: 500 CP MC toy experiments: error on S (left); 500 CP MC toy experiments: C parameter value (right).

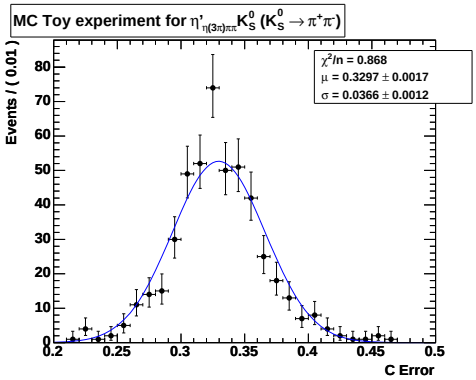

Figure B.33: 500 CP MC toy experiments: error on C.

B.4 $\eta'_{\eta(3\pi)\pi\pi}K^+$

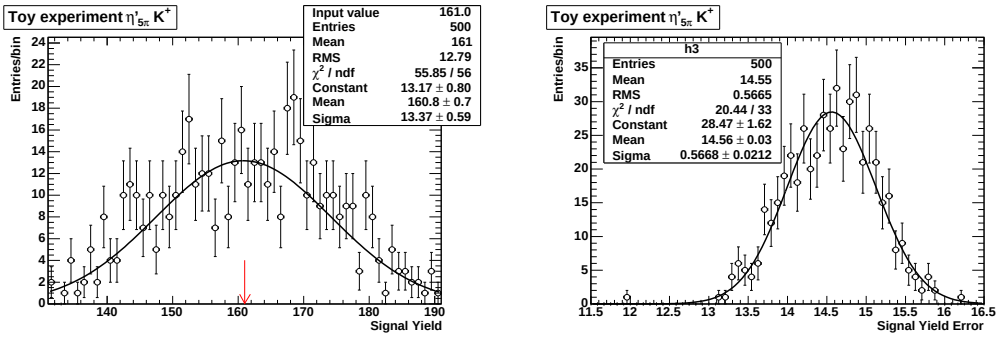

Figure B.34: 500 yield pure toy experiments: signal yield (left), error on signal yield (right).

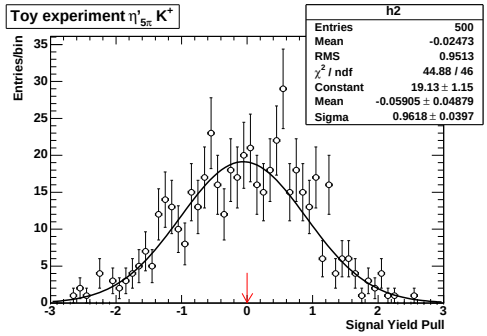

Figure B.35: 500 yield pure toy experiments: pull value and sigma distribution.

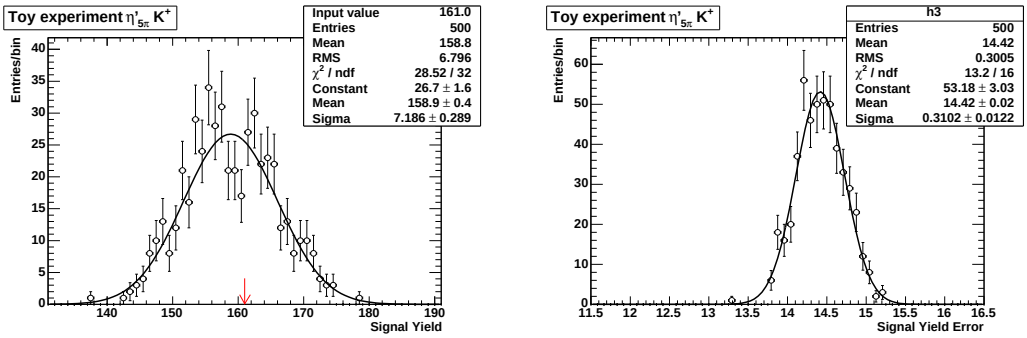

Figure B.36: 500 yield MC toy experiments: signal yield (left), error on signal yield (right).

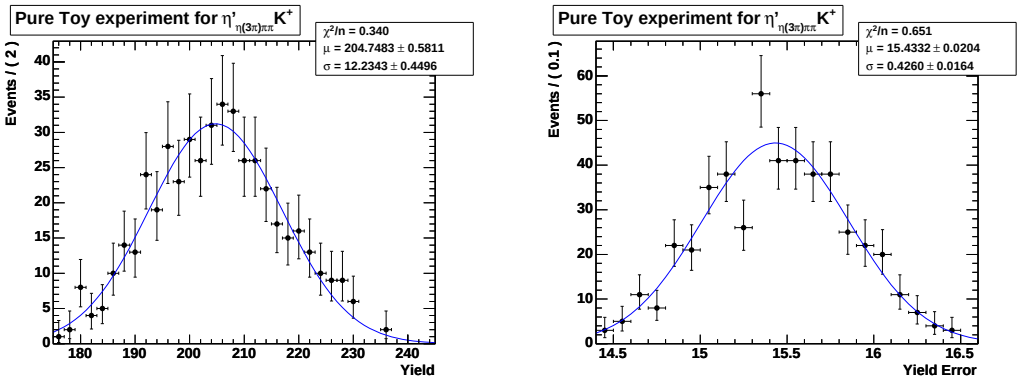

Figure B.37: 500 CP pure toy experiments: signal yield (left), error on signal yield (right).

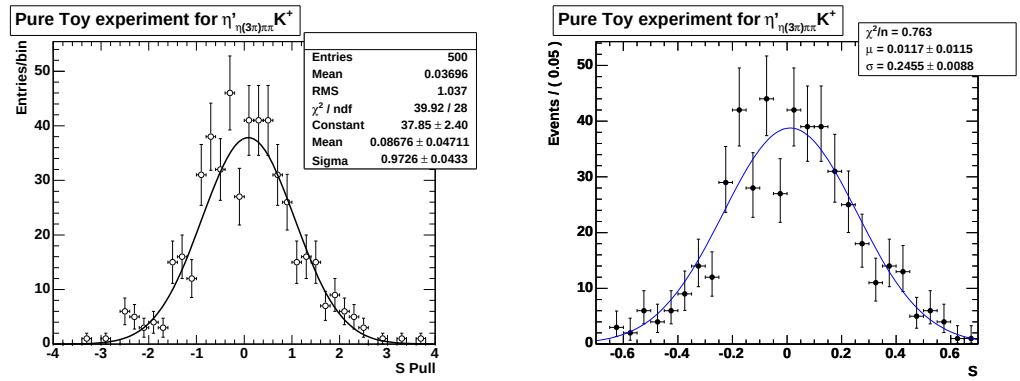

Figure B.38: 500 CP pure toy experiments: pull value and sigma for signal (left), S parameter value (right).

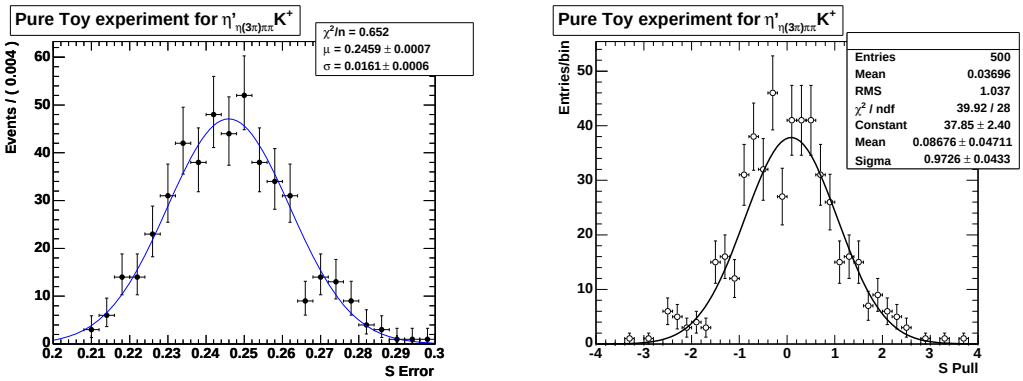

Figure B.39: 500 CP pure toy experiments: error on S (left), pull value and sigma for S (right).

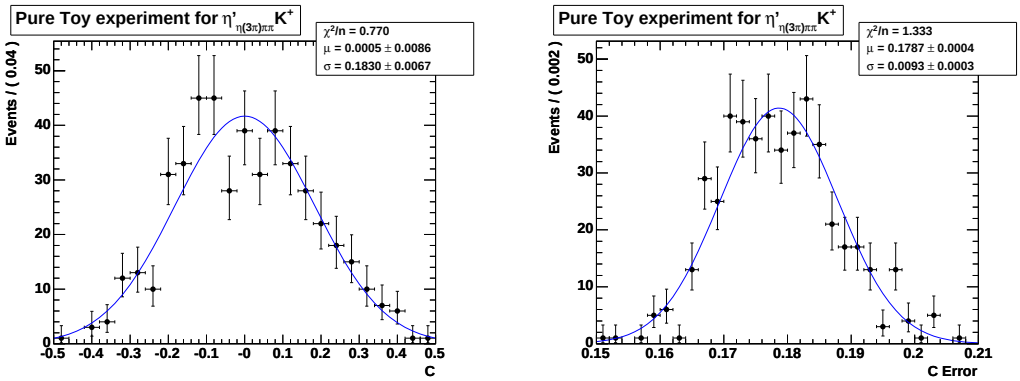

Figure B.40: 500 CP pure toy experiments: C parameter value (left), error on C (right).

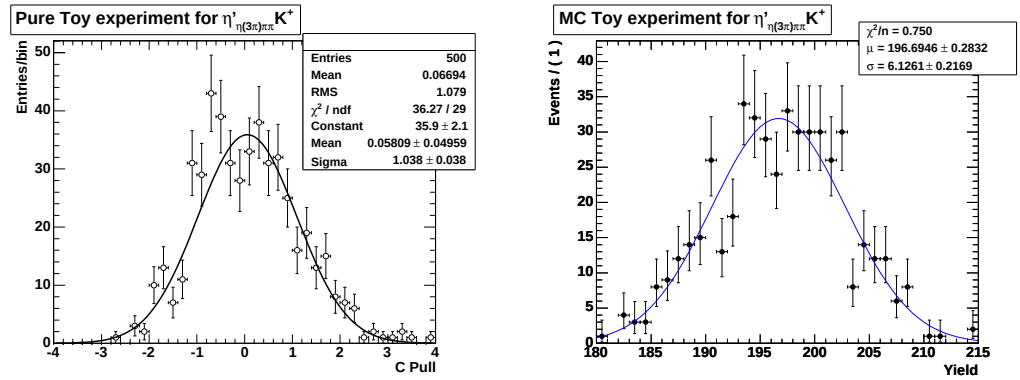

Figure B.41: 500 CP pure toy experiments: pull value and sigma for C (left); 500 CP MC toy experiments: signal yield (right).

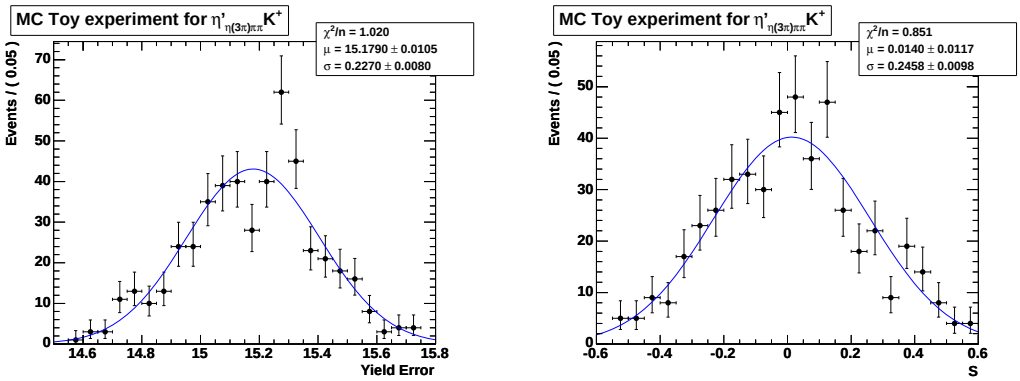

Figure B.42: 500 CP MC toy experiments: pull value and sigma for signal (left); 500 CP MC toy experiments: S parameter value (right).

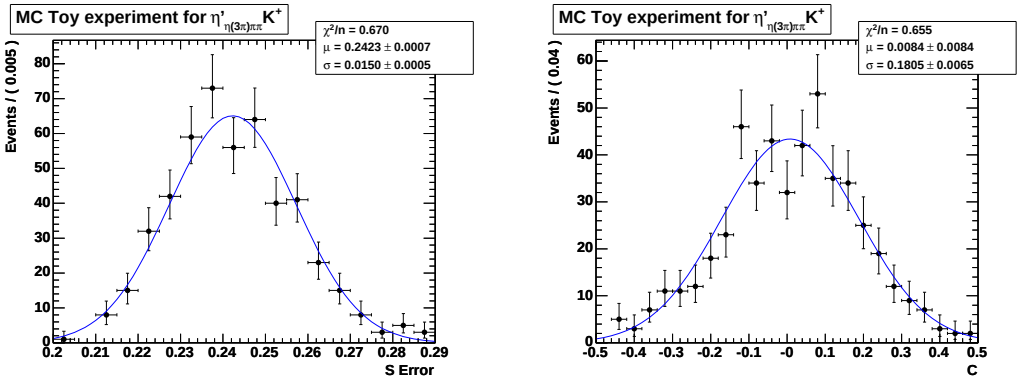

Figure B.43: 500 CP MC toy experiments: error on S (left); 500 CP MC toy experiments: C parameter value (right).

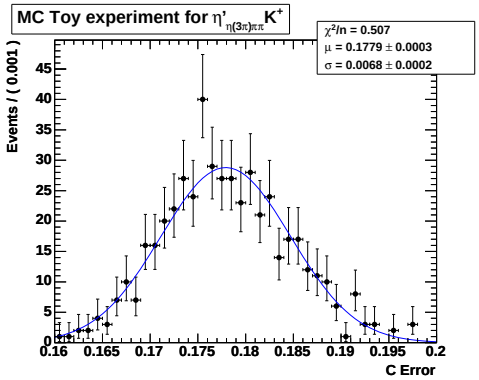

Figure B.44: 500 CP MC toy experiments: error on C.

Bibliography

[1] T. D. Lee and C. N. Yang, *Phys. Rev.* **104** (1956) 254.

[2] C. S. Wu *et al.*, *Phys. Rev.* **105** (1957) 1413.

[3] J.H. Christensen, J.W. Cronin, V.L. Fitch, and R. Turlay, *Phys. Rev. Lett.* **13** (1964) 138.

[4] M. Kobayashi and T. Maskawa, *Prog. Th. Phys.* **49** (1973) 652.

[5] V. Fitch, in Nobel Lectures (Physics) World Scientific, Singapore (1991), lecture for 1980 prize.

[6] S. Weinberg, Phys. Rev. Lett. **19**, pag. 1264 (1967).

[7] A. Salam, *Elementary Particle Physics*, ed. by N. Svartholm (Almquist and Wiksells, Stockhol 1968), p. 367

[8] S. Weinberg, Phys. Rev. Lett. **37**, pag. 657 (1976).

[9] M. Gell-Mann and A. Pais, Phys. Rev. **97** (1955) 1387.

[10] S. L. Glashow, J. Iliopoulis, and L. Maiani, *Phys. Rev. D* **2** (1970) 1285.

[11] K. Hagiwara *et al.*, Phys. Rev. **D66**, 010001-1 (2004).

[12] M. Peskin and D. Schroeder, An Introduction to Quantum Field Theory Addison-Wesley, New York (1995).

[13] P. F. Harrison, H. R. Quinn, *The* BABAR *Physics Book*, SLAC-REP-504 (2004).

[14] *BABAR* Collaboration, B. Aubert *et al.*, hep-ex/0408127, submitted to *Phys. Rev. Lett.* .

[15] F. Blanc *et al.*, *Measurements of CP-violating Asymmetries and Branching Fractions in B Meson Decays to* $\eta' K$, BABAR Note 1093 (2005).

[16] B. Aubert *et al.*, *Measurements of Branching Fractions and Time-Dependent CP-Violating Asymmetries in* $B \to \eta' K$ *Decays*, Phys. Rev. Lett. **94**, 191802 (2005).

[17] S. Patton, *Object Oriented Programming (For a novice, by a novice*), CSN 95-341 C3S 95-003 (1995).

[18] Please see ROOT home page at CERN:
`http://root.cern.ch`.

[19] R. T. Hamilton *et al.*, *DataFlow Reference Manual* BABAR Note 387 (1999).

[20] F. Martinez-Vidal, R. Faccini, Composition Tools User's Guide:
`http://www.slac.stanford.edu/BFROOT/www/Physics/Tools/Vertex/CompGuide/index.html`.

[21] Please see the home page of the project:
`http://root.cern.ch/root/Cint.html`.

[22] D. Kirkby *et al.*, *A User's Guide to the RooFitTools Package for Unbinned Maximum Likelihood Fitting*, BAD 18 (2001).

[23] Si veda la home page del progetto:
`http://www.slac.stanford.edu/BFROOT/www/Computing/Offline/ROOT/RooFit`.

[24] ARGUS Collaboration (H. Albrecht *et al.*) Phys. Lett. **B241**, 278 (1990); **254**, 288 (1991).

[25] F.James, MINUIT, CERN Program Library Long Writeup D506.

[26] M. Pivk *et al.*, *Background fighting in charmless two-body analysis* , BABAR Note 346 (2002).

[27] F. Blanc *et al.*, *Measurements of branching fractions and charge and time-dependent asymmetries for* $B \to \eta' K$, BABAR Note 490 (2003).

[28] F. Blanc *et al.*, *Time-Dependent CP-violating Asymmetries in B meson Decays to* $etapr K$, BABAR Note 906 (2004).

[29] G. Cerizza *et al., Study of B meson Decays to $\eta' K$ in new sub-decay modes of η' and K^0_S*, BABAR Note 907 (2004).

[30] For a description of MiFit program see:

`http://pcbabar4.mi.infn.it/lazzaro/MiFit`

[31] Carlo Dallapiccola , "New DIRC thetaC parameterization", Charmless Hadronic B Decays AWG, Msg # 359

[32] F. Martinez-Vidal *et al.*, *The BABAR vertexing*, BABAR Note 102 (2001). (2002)

[33] A. Lazzaro and F. Palombo ,*Time-Dependent and Direct CP-Violating Asymmetries and Branching Fractions Measurements in B Meson Decays to $\eta' K$*, BABAR Note 444 (2003).

[34] A. Lazzaro and F. Palombo , *B meson decay to $\eta' K^0$ with η' to $\eta\pi\pi$ and eta to 3 π*, BABAR Note 488 (2003).

[35] `http://www.slac.stanford.edu/xorg/hfag/rare/pre_winter04/charmless/OUTPUT/TABLES/charmless.pdf`

[36] D. Brown *et al.*, *Local Alignment of the SVT*, BABAR Note 486 (2003).

[37] Owen Long, Max Baak, Robert N. Cahn, and David Kirkby, *Phys. Rev. D* **68**, 034010 (2003). See also new work on this subject in Ref. [**?**].

[38] *BABAR* Collaboration, B. Aubert *et al.*, *Phys. Rev. Lett.* **91**, 161801 (2003).

[39] Belle Collaboration, K. Abe *et al.*, *Phys. Rev. Lett.* **91**, 261602 (2003).

[40] N. Cabibbo, Phys. Rev. Lett. **10**, pag. 531 (1963).

[41] Fermilab E288 Collaboration, S. W. Herb *et al.*, Phys. Rev. Lett. **39**, 252 (1977); W. R. Innes *et al.*, Phys. Rev. Lett. **39**, 1240,1640(E) (1977).

[42] CDF Collaboration, F. Abe *et al.*, Phys. Rev. D **50**, 2966 (1994); **51**, 4623 (1994); **52**, 2605 (1995); Phys. Rev. Lett. **73**, 225 (1994); **74**, 2626 (1995); D0 Collaboration, S. Abachi *et al.*, Phys. Rev. Lett. **72**, 2138 (1994); **74**, 2422 (1995); **74**, 2632 (1995); Phys. Rev. D **52**, 4877 (1995).

[43] B. Aubert *et al.*, *Observation of Direct CP Violation in* $B^0 \to K^+\pi^-$ *Decays* , BABAR Note 1020 (2004).

[44] *BABAR* Collaboration (B. Aubert *et al.*) *Observation of* CP *violation in the* B^0 *meson system*, Phys. Rev. Lett. **87**, 091801 (2001).

[45] *BABAR* Collaboration (B. Aubert *et al.*) *Measurement of* CP*-violating asymmetries in* B^0 *decays to CP eigenstates*, Phys. Rev. Lett. **86**, 2515–2522 (2001).

[46] *BABAR* Collaboration (B. Aubert *et al.*) BABAR-CONF-02/01, SLAC-PUB-9153, hep-ex/0203007, 2002.

[47] BELLE Collaboration (K. Abe *et al.*) Phys. Rev. Lett. **87**, 091802 (2001).

[48] G. Buchala, A. J. Buras, Phys. Lett. B **333**, 221 (1994)

[49] G. Buchala, A. J. Buras, Phys. Rev. D **54**, 6782 (1996)

[50] S. Bergmann, G. Perez, JHEP **0008**, 034 (2000)

Acknowledgements

Voglio ringraziare Fernando per avermi seguito nel lavoro di analisi e il Dott. Lazzaro, the MiFit creator, per il paziente lavoro di revisione della tesi. Grazie al mio mentore e amico Alfio che mi ha insegnato tantissimo, al fratello **V**inci, all'amico S**i**mo e alla sua bergamasca simpatia, a Meghido e alle sue foto sado&fetish, Riky dai bei capelli e Umberto per gli ultimi anni di corso trascorsi insieme. Inoltre **v**oglio rigraziare particolarmente l**a** Dani per avermi sopportato durante (e non solo) l'anno di tesi. Grazie. Poi ci sono tutti i pisto**l**a di matematica che mai una volta che si**a** una, mi hanno aiutato nell'esame di Metodi Matematici: l'analista Zambo (sempre e solo HV1903), il Lanci, Raf**f**a, Mauro, Albi, Anna, Chiara, Daniel, Tati, lo Ste biondo, Andrea "che sa tutte le battute dei film", Antuan, Pino "the fox", Parrucca, Arbac**i**, Brasu, Rocco, Mari, Tizi, la Anto sorella di Mari, Ciccio, Vale, Oscar, Paolo, Laura sorella di Anna e gli altri che se mi sono dimenticato vuol dire che non sono importanti. Scherzo.
Ci sono poi quelli di novebraccia.net che nell'ultimo anno mi hanno fatto divertire di brutto e a cui sono legato: il grande Dario LB, N3ddo, la Sere, Eman, Nick, la Sarita e la Meekee, Cranio, il mitico Pietro e per ultimo ma non per importanza Dave Trielina. Un ringraziamento speciale a John Lo Secco e ai suoi fit, Bim, al pipistrello, uccello.jpe**g**, Gaetanuccio nostro, al porco di Maurizio, il Baba, il Penguin, Mr. Bistecca, the ghost, Boscolo, il becchino dall'occhio di vetro, Gambalf il bianco, Danny De Vito, Kasparov, Play Mobil, grotte di Toir**a**no e Marco Pappagallo (chi?).

This thesis is written in LaTeX 2_ε

Milan, July 1st 2005.